Chemical and Kinematical Evolution in Nearby Dwarf Spheroidal Galaxies

Inauguraldissertation

zur Erlangung der Würde eines Doktors der Philosophie
vorgelegt der
Philosophisch-Naturwissenschaftlichen Fakultät
der Universität Basel

von

Andreas Koch

aus Bremen (Deutschland)

Basel, 2006

Genehmigt von der Philosophisch-Naturwissenschaftlichen Fakultät

auf Antrag von
Prof. Dr. Eva K. Grebel und Dr. Mark I. Wilkinson

Basel, den 19. September 2006

Prof. Dr. Hans-Jakob Wirz
Dekan

Thesis Abstract:
Chemical and kinematical evolution in nearby dwarf spheroidal galaxies

Dwarf spheroidal (dSph) galaxies are the least massive and luminous objects known to exist. These galaxies are often considered as the fossil building blocks of massive systems predicted by some cosmological models. Nonetheless, evidence has been mounting that this idea of hierarchical assembly may be too simplistic a picture, since a number of the dSphs' characteristics, such as the α-element abundance patterns, stand in contradiction to the properties of stars in the Galactic halo. Further, yet unsolved, puzzles include the missing satellite problem, the influence of feedback and reionization, and the nature of dark matter. How then do the dSphs form, to what extent do they contribute to the build-up of massive galaxies, what can we say about their dark matter content and how can one characterize their role in cosmology and galactic evolution? These systems' intriguing properties, such as the omnipresence of old stellar populations, their gas deficiency, their high velocity dispersion and flat dispersion profiles provide stringent tests of the paradigm of galaxy formation and render these systems important benchmarks for studying galactic evolution from the earliest epochs on. In particular, the proximity of the dSphs in the Local Group (LG) allows us to resolve their stellar populations and to pursue near-field cosmology on the smallest scales.

In this Thesis I address several evolutionary aspects of these galaxies by concentrating on three Galactic satellites and additionally investigating the global satellite galaxy system of the Andromeda galaxy, M 31.

In this context, I spectroscopically analyzed the Carina dSph, which stands out among the LG dSphs because of its unusual, *episodic* star formation (SF) history. Carina bears evidence of at least three prominent stellar populations. Hence, I aimed at studying the metallicity spread of such systems, investigating potential age-metallicity relations, searching for spatial gradients and exploring its evolutionary history accounting for chemical enrichment. This was achieved by obtaining medium-resolution spectroscopy of $\sim$1200 targets in Carina. Based on the near-infrared calcium triplet as a well established metallicity indicator, I was able to compile the metallicity distribution function (MDF) of this galaxy from a large sample of stars. Despite the wide spread in stellar ages present in Carina, originating from its episodic SF, it exhibits a remarkably narrow red giant branch (RGB). On the other hand, I found a wide spread in the metallicities, reaching from -3 dex to near-solar. Hence, I could show that age and metallicity conspire to produce old, metal poor stars at the same locus on the RGB as young, metal rich ones. This manifestation of an age-metallicity degeneracy generically explains the observed narrowness of Carina's RGB. In addition, I could also derive the age of each single red giant from isochrone fits. The resultant age distribution indicates the presence of three major peaks, with a prevailing intermediate-age population. These populations may in fact be related to Carina's three well established SF episodes. By correlating metallicities and spatial information, I could confirm a radial population gradient in the metallicities, in the sense that more metal rich stars are found towards the center of the galaxy. This phenomenon points to a deep central potential well in the dSphs, where gas is longer retained for SF and enrichment. In order to analyze the shape of the observed MDF, several simple models of chemical evolution were calculated, which support the view that the galaxy's early SF must have occurred from pre-enriched gas. Moreover, all the models in use tend to overestimate the number of metal poor stars, i.e., there is a persistent G-dwarf problem.

This medium-resolution study was complemented by measurements of iron- and α-element abundance ratios from high-resolution spectra of ten stars in Carina. These elements are important tracers of SF and thus reflect the evolutionary status of any stellar system. It could be shown that the calibration of the metallicity [Fe/H] via the calcium triplet reproduces the "true" stellar iron abundance well for moderately metal-poor stars, but the calibration tends to fail towards the most metal-poor populations. Carina's $[\alpha/\mathrm{Fe}]$-ratios are well consistent with those measured in other dSphs of the LG and confirm that they are systematically lower than those in Galactic halo stars of comparable metallicities. The overall abundance patterns are not inconsistent with an episodic SF, but the accuracy and small number statistics of such measurements impedes quantifying the underlying evolution. It is, however, safe from the present data to say that also Carina inheres the typical characteristics of other dSphs in terms of a low SF efficiency and the occurrence of strong galactic winds.

In an analoguous manner I determined metallicities in the remote Galactic satellite Leo II. The resulting MDF also shows a deficiency in very metal-poor stars. Furthermore it turns out to be rather asymmetric, with a rapid decline towards higher metallicities. By comparing my measurements with model predictions of LG dSphs I illustrated that Leo II's MDF bears resemblence to the UMi and Scl dSphs, albeit none of the models succeed in reproducing all features of the MDF simultaneously. By additionally determining the ages of the RGB stars in Leo II, I showed that the age-metallicity relation in this galaxy is essentially flat over a long time interval, while there is evidence for an enrichment during the last 2–4 Gyr. The overall wide spread in ages present in this dSph support earlier views that Leo II is in fact a galaxy with a prominent old and a prevalent intermediate-age population. Contrary to Carina, I could not detect any radial metallicity nor age gradient in Leo II.

Another important aspect of the nature and evolution of dSphs is the study of their kinematical properties. These low-mass galaxies are believed to be the smallest cosmological structures containing dark matter. By measuring radial velocities in the remote dSph Leo I I showed that the resulting velocity dispersion profile is essentially flat out to the nominal tidal radius. The non-detection of any apparent velocity gradient across the galaxy supports the negligible role of Galactic tides in the course of its whole evolution. The application of dynamical modeling under the assumption of an isotropic velocity distribution then yielded mass and density profiles. Moreover, the behaviour of the velocity anisotropy was analysed. The resulting high mass to light ratio of Leo I is supportive of the idea that *all* dSphs share a common dark halo mass-scale of $\sim 4 \times 10^7 \mathrm{M}_\odot$, so that the pure velocity (dispersion) information of such a system

is a direct proxy for mass. All this argues in favour of a general dark matter dominance in the dSphs and renders the hypothesis that these systems are of tidal origin less likely.

Lastly, information about the origin and evolution of the dSphs can be gleaned by examining their spatial distribution around their host galaxies. It has often been reported that, in the Milky Way system, the dSphs are aligned along one or more great circles or polar planes. Hence, I reconstructed the three-dimensional distribution of the entire M31 satellite sample. By applying detailed statistical methods I could demonstrate that seven out of 16 satellites are located within a thin polar sheet. One reason for this planar alignment can be the break up of a common progenitor, which was orbiting M31. Also plausible is that the dSphs fell in along the filamentary dark matter structure of the cosmic web, which is underscored by the fact that the plane extends in the direction of nearby galaxy groups.

All in all, my studies of the chemical and kinematical properties of a sample of nearby dSph galaxies do confirm that these are dark matter dominated systems, which are governed by highly complex chemical enrichment processes and thus warrant detailed investigations. These turn out to be invaluable for drawing a global picture of galaxy formation in a cosmological context.

◆

Zusammenfassung der Arbeit: Chemische und kinematische Entwicklung in nahen sphäroidalen Zwerggalaxien

Sphäroidale Zwerggalaxien (im Engl. dwarf spheroidals, dSphs) sind die vermutlich masseärmsten und leuchtschwächsten Objekte überhaupt. Diese Galaxien werden oft als die archetypischen Bausteine massereicher Systeme angesehen, die von manchen kosmologischen Theorien vorhergesagt werden. Nichtsdestotrotz häufen sich seit den letzten Jahren die Anzeichen, dass dieses Bild der hierarchischen Strukturbildung zu simpel sein könnte: Demzufolge stehen einige der Eigenschaften der dSphs, wie z.B. ihre α-Elementhäufigkeiten im Widerspruch zu den Eigenschaften galaktischer Halosterne. Weitere noch ungelöste Fragen betreffen die Diskrepanz zwischen der Anzahl beobachteter und vorhergesagter Satelliten, die Rolle der Reionisation und Rückführung von Gas sowie die Beschaffenheit der dunklen Materie. Wie entstehen nun die dSphs, in welchem Masse tragen sie zum Aufbau massereicher Galaxien bei, was kann man über ihren Gehalt an dunkler Materie aussagen und welche Rolle spielen sie für die Kosmologie und Galaxienentwicklung? Die faszinierenden Eigenschaften dieser Galaxien, wie die Allgegenwart alter Sternpopulationen, ihr Mangel an jeglichem Gas, sowie ihre hohen Geschwindigkeitsdispersionen und abflachenden Dispersionsprofile stellen effiziente Mittel zum Erforschen der Galaxienentstehung dar und ermöglichen es, die Entwicklung solcher Systeme von den frühesten Epochen an zu verfolgen. Insbesondere die Nähe zu den dSphs der Lokalen Gruppe erlaubt es uns, ihre Sternpopulationen einzeln aufzulösen und damit Kosmologie auf kleinsten Skalen zu betreiben.

In dieser Arbeit werden verschiedene Aspekte zur Entwicklung dieser Galaxien angesprochen, wobei ich mich auf drei galaktische Satelliten konzentriert und zusätzlich das globale Satellitensystem um M31 untersucht habe.

In diesem Zusammenhang analysierte ich Spektren der dSph Carina, die eine herausragende Rolle unter den dSphs der Lokalen Gruppe innehält und sich durch eine ungewöhnliche, *episodische* Sternentstehungsgeschichte auszeichnet. In Carina finden sich Anzeichen für wenigstens drei ausgeprägte stellare Populationen. Infolgedessen ist es interessant, die Metallizitätsstreuung eines solchen Systems und eventuelle Alters-Metallizitätsrelationen zu untersuchen, nach radialen Gradienten zu suchen, sowie ihre Entwicklungsgeschichte im Hinblick auf chemische Anreicherungsprozesse zu betrachten. Dies wurde anhand von niedrig-aufgelöster Spektroskopie von etwa 1200 Sternen in Carina in Angriff genommen. Mithilfe des nahinfraroten Kalziumtripletts, einem gängigen Metallizitätsindikator, konnte ich die Metallizitätsverteilung (MV) dieser Galaxie anhand einer grossen Anzahl von Sternen etablieren. Trotz der breiten Altersstreuung in Carina, die von ihrer episodischen Sternentstehung herrührt, weist diese Galaxie einen bemerkenswert schmalen roten Riesenast auf. Andererseits konnte ich einen gleichermassen weiten Bereich an Metallizitäten nachweisen, der sich von ca. -3 dex bis zu nahezu solaren Werten erstreckt. Dadurch konnte ich zeigen, dass Alters- und Metallizitätseffekte gegeneinander agieren, so dass alte, metallarme Sterne an der gleichen Stelle auf dem roten Riesenast zu liegen kommen wie die jungen und metallreichen. Durch die so geartete Alters-Metallizitätsentartung lässt sich unmittelbar der beobachtete schmale rote Riesenast erklären. Zusätzlich konnte ich anhand von Isochronenfits jedem roten Riesen ein Alter zuweisen. Die resultierende Altersverteilung deutet ebenfalls auf drei Komponenten hin, wobei die intermediäre Population überwiegt. Es ist nicht auszuschliessen, dass diese Populationen in Zusammenhang mit den drei etablierten Sternentstehungsepisoden in Carina stehen. Durch die Kombination von Metallizitäten und räumlicher Information konnte ich einen radialen Populationsgradienten bestätigen. In diesem Zuge befinden sich mehr metallreiche Sterne im Zentrum der Galaxie. Diese Phänomen deutet auf einen tiefen Potentialtopf in den Zentralbereichen hin, in dem sich das Gas aufstauen und über einen längeren Zeitraum hinweg Sternentstehung und chemische Anreicherung aufrechterhalten kann. Um die genaue Form der MV zu analysieren wurden verschiedene einfache chemische Entwicklungsmodelle berechnet. Demzufolge muss Carinas früheste Sternentstehung aus einem vorangereicherten Gasreservoir vonstatten gegangen sein. Ausserdem sagen all diese Modelle eine zu hohe Anzahl an metallarmen Sternen vorher, was einem ausgeprägten G-Zwerg Problem entspricht.

Diese Ergebnisse aus niedrig-aufgelöster Spektroskopie wurden durch die Messung von Eisen- und α-Elementhäufigkeiten aus hochaufgelösten Spektren von zehn roten Riesen in Carina ergänzt. Diese Elemente stellen wichtige Indikatoren für Sternentstehung dar und zeichnen somit die Entwicklungszustand eines Sternsystems nach. Dadurch konnte ich zeigen, dass die Kalibration der Metallizität [Fe/H] über die Kalzium Triplettlinien die "wahre" Eisenhäufigkeit im Falle von mässig metallarmen Sternen verhältnismässig gut wiederspiegelt, jedoch für die metallärmsten Objekte stark abweicht. Die [α/Fe]-Häufigkeiten in Carina stimmen gut mit denen in anderen dSphs der Lokalen Gruppe überein und bestätigen somit, dass diese Elemente in den dSphs systematisch niedrigere Häufigeitsverhältnisse aufweisen als Sterne vergleichbarer Metallizität im galaktischen Halo. Insgesamt schliesst die beobachtete Elementhäufigkeitsverteilung ein episodisches Sternentstehungsszenario nicht aus. Jedoch vehindern es die Messgenauigkeit und die geringe Anzahl an Sternen in derartigen Datensätzen, die ursprüngliche Entwicklungsgeschichte zu quantifizieren. Allerdings lassen die gegenwärtigen Messungen den Schluss zu, dass auch Carina von den typischen Prozessen dominiert ist, wie die übrigen dSphs, zu denen eine niedrige Sternentstehungseffizienz und das Auftreten starker galaktischer Winde gehören.

Auf die gleiche Art und Weise analysierte ich Metallizitäten in der dSph Leo II, einem entfernten Begleiter der Milchstrasse. Die sich ergebende MV ist ebenfalls verarmt an äusserst metallarmen Sternen. Des weiteren ist die Verteilung asymmetrisch, wobei sie zu den metallreicheren Sternen hin stark abfällt. Durch einen Vergleich meiner Messungen mit Modellvorhersagen über andere dSphs der Lokalen Gruppe konnte ich demonstrieren, dass die MV von Leo II Ähnlichkeit mit denen der dSphs UMi und Scl aufweist, obgleich keines der Modelle gleichzeitig alle Merkmale der beobachteten Verteilung reproduzieren kann. Anhand der Altersbestimmung der roten Riesen in Leo II konnte ich nachweisen, dass die Alters-Metallizitätsrelation dieser Galaxie im Wesentlichen über einen langen Zeitraum hinweg flach verläuft. Darüberhinaus gibt es Hinweise auf eine Metallanreicherung während der vergangenen 2–4 Gyr. Insgesamt lassen sich durch die beobachtete breite Altersstreuung der Sterne in Leo II frühere Vermutungen belegen, denen zufolge diese Galaxie eine ausgeprägte alte Sternpopulation aufweist und durch die vorherschenden Sterne intermediären Alters geprägt ist. Im Unterschied zu Carina liess sich in Leo II weder ein radialer Alters- noch ein Metallizitätstrend nachweisen.

Kinematische Studien liefern einen weiteren wichtigen Aspekt für das Verständnis des Ursprungs und der Entwicklung der dSphs. Diese massearmen Galaxien sind wahrscheinlich die kleinsten kosmologischen Strukturen, die dunkle Materie enthalten. Indem ich Radialgeschwindigkeiten von roten Riesen in der entfernten dSph Leo I bestimmte, konnte ich nachweisen, dass das entsprechende Geschwindigkeitsdispersionsprofil bis hinaus zum Gezeitenradius im Wesentlichen flach verläuft. Dieses gilt hinaus bis zu grossen Abständen vom Zentrum, soweit die Daten noch Messungen zuliessen. Dass galaktische Gezeiten keine merkliche Rolle in der Entwicklung von Leo I spielten spiegelt sich im Fehlen jeglicher scheinbarer Geschwindigkeitsgradienten wieder. Durch das Anwenden von Modellen unter der Annahme dynamischen Gleichgewichts und Geschwindigkeitsisotropie konnte ich ein Masse- und Dichteprofil dieser dSph erstellen. Ebenso bestimmte ich das radiale Verhalten der Geschwindigkeitsanisotropie. Das resultierende hohe Masse/Leuchtkraft Verhältnis unterstützt die These, dass *allen* dSphs ein dunkler Materiehalo der typischen Grössenordung von $\sim 4 \times 10^7 \mathrm{M}_\odot$ gemein ist. Insofern drücken sich in der reinen Beobachtungsgrösse der Radialgeschwindigkeit (und -dispersion) die gemeinsamen Masseeigenschaften dieser Systeme aus. All dies spricht dafür, dass die dSphs in der Tat von dunkler Materie dominiert sind und stellt die Hypothese in Frage, dass sie ihren Ursprung ebenso gut in Gezeitenwechselwirkungen haben könnten.

Zuguterletzt lassen sich zusätzliche wichtige Informationen über den Ursprung und die Entwicklung der dSphs aus ihrer räumlichen Verteilung um ihre Muttergalaxien gewinnen. Von den dSphs des Milchtrassensystems ist schon seit längerem bekannt, dass sie sich auf einem oder mehreren Grosskreisen, bzw. auf polaren Ebenen anordnen. Daher rekonstruierte ich die dreidimensionale räumliche Verteilung des Satellitensystems der Andromedagalaxie. Durch die Verwendung detaillierter statistischer Methoden konnte ich demonstrieren, dass sieben der 16 dSph Satelliten um M31 sich innerhalb einer schmalen polaren Struktur ansammeln. Ein Grund für diese Ausrichtung in einer Ebene kann das Aufbrechen einer gemeinsamen Vorgängergalaxie sein, die sich um M31 bewegte. Ebenso ist es möglich, dass die dSphs entlang von kosmologischen Filamenten auf M31 einfallen. Hierfür spricht, dass sich die Ebene in Richtung naher massereicher Galaxiengruppen erstreckt. Abschliessend lässt sich sagen, dass meine Untersuchungen zu den chemischen und kinematischen Eigenschaften von nahen sphäroidalen Zwerggalaxien in der Tat belegen, dass diese Objekte durch dunkle Materie domiert sind und komplexen Anreicherungsprozessen unterliegen. Somit verdienen sie genaueste Beobachtungen, die unerlässlich für das Gewinnen eines umfassenden Bildes zur Galaxienentstehung im kosmologischen Kontext sind.

◆

“Il n’est pas de destin qui ne se surmonte par le mépris.”
(Albert Camus, *Le Mythe de Sisyphe*)

Contents

List of Figures

List of Tables

Chapter 1

Introduction

> "*It's better to look at the sky than live there. Such an empty place; so vague. Just a country where the thunder goes and things disappear.*"
> — Truman Capote, *Breakfast at Tiffany's*

1.1 Dwarf Spheroidal Galaxies

Dwarf galaxies come in many flavors ranging from gas-rich to gas-poor, from irregular in shape to ellipsoidal, from actively star-forming to quiescent (Grebel 2001). The least massive, least luminous galaxies known to exist are the dwarf spheroidal (dSph) galaxies, which constitute the majority of the galaxies in the Local Group (LG). They are characterized by absolute V-band luminosities $\mathrm{M}_V \gtrsim -14$ mag, surface brightnesses of $\mu_V \gtrsim 22$ mag arcsec^{-2}, low H I masses of $M_{\mathrm{HI}} \lesssim 10^5 M_\odot$, estimated dynamical total masses M_{tot} of a few times $10^7 M_\odot$, have shallow projected radial light profiles and tend not to be rotationally supported (see Grebel, Gallagher, & Harbeck 2003 and references therein). Because of their high velocity dispersion, their velocity dispersion profiles, their morphology and their lack of depth extent many dSphs are believed to be dominated by dark matter (e.g., Mateo 1997; Odenkirchen et al. 2001; Klessen, Grebel, & Harbeck 2003; Wilkinson et al. 2004). Moreover, dSphs are often considered as the fossil building blocks of massive galaxies predicted by some cosmological models. However, over the past few years, evidence has been mounting that the building block scenario is too simplistic a picture, as a number of the dwarfs' properties stand in contradiction to the characteristics of stars in the Galactic halo. In particular, observed chemical abundances in dSphs, predominantly those of the α-elements, are at variance with the halo patterns, apparently ruling out their major contribution as building blocks (e.g., Venn et al. 2004). Other unsolved puzzles include the missing satellite problem (Moore et al. 1999), the impact of reionization and feedback (Grebel & Gallagher 2004), and the nature of dark matter.

In galaxy groups the gas-poor late-type dSphs are usually found within ~ 300 kpc around more massive galaxies like the Milky Way or M31, whereas the gas-rich early-type dwarfs, primarily the dwarf irregular (dIrr) galaxies, show a less concentrated distribution and are also common at larger distances (see, e.g., Grebel, Gallagher, & Harbeck 2003; Fig. 1 in Grebel 2005). This distinct morphology-density relation may be explained by the occurrence of (ram-pressure or tidal) stripping effects by the massive primary or a high Galactic UV flux and points to the importance of the dwarf galaxies' environment for their evolutionary paths.

The dSph census in the Local Group remains incomplete owing to the intrinsically low surface brightnesses of these gas-deficient galaxies. The last three years alone saw the discovery of 13 new Local Group dSph candidates (Zucker et al. 2004, Zucker et al. 2006a, 2006b, 2006c; Willman et al. 2005; Belokurov et al. 2006a, 2006b, Martin et al. 2006), seven of which are new Milky Way companions. This increases the number of known Galactic dSph satellites to 15, omitting accreted companions and additional objects whose nature remains yet to be confirmed (Grebel, Gallagher, & Harbeck 2006).

How then do dwarf galaxies form and evolve, how much do they contribute to the build-up of more massive galaxies, what is the shape and extent of their dark matter distribution, and what is their role in cosmology and galaxy evolution? In this Thesis I will address several of these issues. The advantage of the dSphs of the LG is that they are sufficiently close and luminous so that they can be actually resolved into individual stars. In this context, the multiplexing capabilities of present-day multi-object spectrographs on 4–10 m class telescopes have opened a window to study dSph galaxies in unprecedented detail by enabling one to gather data sets for a large number of individual stars. Hence, these data are able to provide stringent tests of the paradigm of galaxy formation and to pursue "near-field cosmology".

1.2 Chemical evolution: Stellar populations

The gas deficiency of dSphs remains an unsolved puzzle – dSphs typically contain even less gas than expected from red giant mass loss over time scales of several Gyr. Searches for neutral and ionized gas usually only lead to low upper limits on the gas content (e.g., Gallagher et al. 2003 and references therein), which are estimated to be of the order of $M_{\rm HI} \lesssim 10^5\,M_\odot$. It has been suggested that external effects such as tidal or ram pressure stripping in the gaseous corona of the Milky Way (MW; likewise for M 31) or the early Galactic UV radiation field may have affected their evolution and effectively had expelled most of their gas (Grebel 1997; van den Bergh 1994; Grebel et al. 2003).

Our current knowledge of the detailed evolutionary history of nearby dwarf galaxies is mainly based on photometry supplemented by rather sparse spectroscopic information (e.g., Grebel 1999). Such analyses are well able to account for estimates of the overall modes of star formation (SF), but may be hampered by photometric uncertainties and do not provide detailed insight into the predominant timescales for enrichment and SF, nor their governing processes.

However, currently it is becoming possible to take the crucial step further, i.e., to break undesirable age-metallicity degeneracies that plague purely photometric colour-magnitude diagram analyses. When the metallicity of individual stars can be measured independently via spectroscopy, this information can be added to constrain photometric determinations of the star formation history. Within the observational errors this will permit us to assign ages to each star, thus providing vital ingredients to the understanding of galaxy evolution. Ultimately, one may be able to derive detailed age-metallicity relations.

For gas-deficient galaxies like dSphs, our primary sources of metallicity information are their red giants, which are now easily accessible for ground-based 8 to 10m-class telescopes. Spectroscopic information for a sizable number of stars is gradually becoming available for an increasing number of dwarf galaxies (e.g., Côté, Oke, & Cohen 1999a; Smecker-Hane et al. 1999; Guhathakurta, Reitzel, & Grebel 2000; Tolstoy et al. 2001; Pont et al. 2004). The study of detailed chemical abundance ratios via high resolution spectroscopy allows one then to proceed further and to analyze the galactic evolution via the well-established principal chemical tracers of SF, i.e., the investigation of α-elements, r-process and s-process and other heavy elements. This "chemical tagging" (Freeman & Bland-Hawthorn 2002) is the most viable method to elucidate the different phases of galaxy evolution including the earliest epochs via the imprint of nucleosynthetic products, originating in the stars and released in supernovae, in the interstellar medium out of which the subsequent stellar generations will be born.

DSphs are typically dominated by either very old populations (> 10 Gyr) or by intermediate-age populations ($1-10$ Gyr). Very few show more recent star formation. All dSphs (and all other dwarfs) studied in sufficient detail so far have been shown to contain ancient populations that are indistinguishable in age with the oldest age-datable populations in the Milky Way (Grebel 2000, Grebel & Gallagher 2004). The detailed star formation histories and the metal enrichment of dwarf galaxies including dSphs vary widely and no two dwarfs are alike (e.g., Grebel 1997, Mateo 1998). In particular the fraction of intermediate-age stars apparently relates to the distance to the respective massive galaxy (the MW or M 31). The dSphs usually show continuous star formation with some amplitude variations and declining rates at more recent times (Grebel 1997; Grebel et al. 2006). A number of dSphs are entirely dominated by old populations, for instance, Draco and Ursa Minor.

On the other hand, in the Galactic dSph Carina, there is evidence of at least three well-separated star formation bursts, intermitted by quiescent phases. What could cause such an episodic onset and cessation of SF has not yet been satisfyingly resolved. The chemical evolution of this intriguing galaxy will be discussed in detail in terms of its metallicity distribution and elemental abundances in Chapters 2 and 3. Leo II, on the other hand, has experienced continuous SF with an indication of a prominent intermediate-age population. This MDF and evolution of this dSph will be the subject of Chapter 4.

In those dSphs of the Local Group, in which both old and intermediate-age stellar populations have been detected, the younger components often are more strongly centrally concentrated. In a number of dSphs with predominantly old populations, population gradients have been found in the sense that red HB stars are more centrally concentrated than blue HB stars (e.g., Da Costa et al. 1996; Hurley-Keller et al. 1999; Harbeck et al. 2001). This trend is then also mirrored by a central concentration of the presumably more metal-rich red giants (Harbeck et al. 2001). This tendency is generally ascribed to the deeper central potential wells, in which the gas is longer retained compared to the outer regions and thus allows for longer ongoing star formation.

On the other hand, due to the overall comparably shallow potential, dSphs are unlikely to accrete large amounts of matter. On the contrary, these systems are generally believed to be strongly affected by galactic winds (Mac Low & Ferrara 1999; Dong et al. 2003; Lanfranchi & Matteucci 2004). In the light of their orbits around their massive host galaxies, they are likely to constantly lose blown-out gas to the Galaxy (e.g., Tolstoy et al. 2003), whence their evolution is strongly influenced by their vicinity to the Galaxy. To what extent the more distant of these stellar systems, like the remote Leo I and Leo II dSphs are affected by the presence of the MW, will be investigated by analyzing their metallicity distributions in Chapters 4 and 5.

1.3 Kinematic properties: Dark matter or tidal origin?

DSphs are possibly the most dark-matter-dominated objects in the Universe. The origin and nature of these systems is still poorly understood. This makes it particularly interesting to understand their evolutionary histories and renders the dSphs the subject of intense research.

Cold dark matter (CDM) simulations of galaxy formation predict the existence of a large number of sub-haloes surrounding larger galaxies, such as the Milky Way or M 31 (e.g., Moore et al. 1999). The correctness of this prediction remains a subject of debate: the number of observed dSphs is much less, though several have been discovered very recently, indicating that the known sample is incomplete (Belokurov 2006a, 2006b; Martin et al. 2006; Zucker et al. 2006a, 2006b, 2006c). The correspondence between prediction and observation more importantly requires masses, so that dynamical studies of the dSphs are critical.

As a result of large observational programs employing the current state-of-the-art multi-object spectrographs, the systemic velocities of the majority of the LG dSphs are known (tabulated in the reviews by Grebel 1997; Mateo 1998; van den Bergh 1999; and more recent measurements as quoted in, e.g., Evans et al. 2000, 2003). Moreover, high-precision radial velocity data for many individual stars in all the known dSphs are being obtained. These serve as the kinematical input for detailed dynamical studies (Mateo et al. 1998b; Côté et al. 1999; Kleyna et al. 2001, 2003, 2004; Łokas et al. 2002; Wilkinson et al. 2004; Tolstoy et al. 2004; Chapman et al. 2005; Muñoz et al. 2005; Walker et al. 2006a, 2006b; Wilkinson et al. 2006a,b; and references therein), which are determining the spatial distribution of dark matter on the smallest available scales:

It is nowadays well established that dSphs have high central stellar radial velocity dispersions, typically of order $10\,\mathrm{km\,s^{-1}}$ (Aaronson 1983; Mateo 1998). Together with their globular-cluster-like low luminosities (Gallagher & Wyse 1994; Mateo 1998) and their large core size – hundreds of parsecs rather than the few parsecs of star clusters – such dispersion values demonstrate that the dSphs are most likely dominated by dark matter at all radii (Mateo et al. 1997; Wilkinson et al. 2004, 2006a). This deduction presumes the dSphs are in a state of dynamical equilibrium, a presumption supported by direct evidence that the dSphs are not highly disrupted along our lines of sight (e.g., Odenkirchen et al. 2001; Mackey & Gilmore 2003; Klessen et al. 2003). This assumption merits careful test, however, especially in the outer-most parts of the dSph, where Galactic tides might become significant.

The inferred high mass-to-light ratios (M/L), obtained under the assumption of dynamical equilibrium, are as large as $500\,(M/L)_\odot$ or more, making dSphs the smallest observable objects available to study the properties of dark matter halos. Available measurements suggest that the dark matter in dSphs has some common properties, including a minimum halo mass scale of $\sim 4\times10^7$ $\mathrm{M}_\odot$, a small range in central (dark) mass densities, and a minimum length (core radius) scale of order 100 pc (e.g., Gallagher & Wyse 1994; Odenkirchen et al. 2001; Kleyna et al. 2001; Klessen, Grebel, & Harbeck 2003; Wilkinson et al. 2004, 2006a). If established, these are the first characteristic properties of dark matter.

According to a second plausible scenario, the large observed velocity dispersions may be explained if dSphs are unbound tidal remnants that underwent tidal disruption while orbiting the Milky Way (Kuhn 1993; Kroupa 1997; Klessen & Kroupa 1998; Klessen & Zhao 2002; Fleck & Kuhn 2003; Majewski et al. 2005), and all happen to be aligned to mimic a bound system. Predictions following from this scenario include a large depth extent and elongation along the line of sight (Klessen & Kroupa 1998; Klessen & Zhao 2002). However, in two of the closest Milky Way companions, the Draco dSph (Klessen et al. 2003) and the Fornax dwarf (Mackey & Gilmore 2003) direct evidence against such effects is available. Other arguments against dSphs being unbound tidal remnants without dark matter include that they all experienced extended star formation histories with considerable enrichment and that they follow a metallicity-luminosity relation (see Grebel et al. 2003 for details).

The subject of tides in the context of dSph galaxies suffers from a rather controversial literature. In large part this follows from an historical labelling issue. Specifically, it used to be fashionable to fit the projected surface brightness distributions of dSph galaxies with King models. A King (1962) model has two named linear scales: an inner scale, frequently called a ‘core radius’ and an outer truncation radius, called a ‘tidal radius’. While these labels have some relevance in their historical application to models of globular clusters of stars truncated by Galactic tides, they have no general physical interpretation in a different context. In general, dSph stellar populations are not single-component, and there is no astrophysical reason to assume ab initio that the distribution function is simply isothermal. Some form of numerically tractable functional fit to a projected surface brightness profile is required in the dynamical analysis, but a more sophisticated analysis is required than fitting functions to surface brightness profiles before the possible importance of tides can be investigated. It is sometimes suggested that high-frequency ‘distorted’ photometric structure and the progressively reported presence of stars outside the formal King tidal radius is indicative of tidal damage, but no available numerical simulations support this view: rather, if tides are important, they produce smooth systematic distortions in the outer parts of a system. One test, applicable in some circumstances, is detection of apparent rotation associated with such a distortion. Some of these relevant issues are discussed further by Read & Gilmore (2005), and by Read et al. (2006a, 2006b).

I will address the questions related to the still unresolved and controversial origin and dominant nature of the dSphs by investigating the kinematic properties and of the Galactic dSph companion Leo I in Chapter 5. In the light of its large Galactocentric distance, this galaxy is well suited as a test of the possible importance of tidal perturbations.

1.4 Kinematic evolution: Great circles, planes and streams

The galaxies of the LG are not randomly distributed, but exhibit a number of distinct patterns. Firstly, there is a pronounced morphology-density relation. That is, gas-poor late-type dwarf galaxies are mainly found in close proximity to one of the two dominant spirals in the LG, the MW and M31. Typically these dwarfs have distances of less than 300 kpc from the closest spiral and comprise dwarf elliptical (dE) and dSph galaxies. Gas-rich early-type dwarf galaxies (primarily dwarf irregular (dIrr) galaxies, but also so-called transition-type dIrr/dSph galaxies; see Grebel, Gallagher, & Harbeck 2003 for details), on the other hand, show a less concentrated distribution and are also common at larger distances (e.g., Fig. 3 in Grebel 1999 and Fig. 1 in Grebel 2000). Secondly, the satellites of the Milky Way show an anisotropic distribution in the sense that locations around the polar axis, well away from the Galactic plane, are preferred, resembling the Holmberg effect (Holmberg 1969). Thirdly, the companions of the Milky Way and some of the outer halo globular clusters lie close to one or two polar great planes (e.g., Lynden-Bell 1976; Kunkel & Demers 1976; Kunkel 1979; Lynden-Bell 1982; Majewski 1994; Fusi Pecci et al. 1995; Kroupa, Theis, & Boily 2005). There may be additional “streams” comprising only one or a few satellites and outer halo globular clusters (e.g., Lynden-Bell & Lynden-Bell 1995; Palma, Majewski, & Johnston 2002).

It is curious that essentially all of the Milky Way satellites appear to be located in one or two great planes. A number of studies showed that the probability of such planar alignments to have occurred by chance is very low (e.g., Kunkel 1979; Kroupa et al. 2005). Several suggestions were put forward to explain the non-isotropic, planar distribution of the satellites. According to one of these scenarios, the Galactic satellites may be remnants of one or two larger, previously disrupted galaxies and orbit the Milky Way within the great planes defined by their original parents (e.g., Kunkel 1979, Lynden-Bell 1982; Palma et al. 1992). Whether the orbits of all these satellites do indeed lie within the planes is at present still unclear. For some, the proper motions seem to agree with motion within the plane of apparent alignment, whereas this is apparently ruled out for other objects (e.g., Schweitzer et al. 1995; Dauphole et al. 1996; Grebel 1997; Schweitzer, Cudworth, & Majewski 1997; Palma et al. 2002; Piatek et al. 2002, 2003, 2005; Dinescu et al. 2004). However, the uncertainties of the proper motion measurements are at present still uncomfortably large and will have to await more accurate measurements with forthcoming astrometric space missions such as ESA's Gaia and NASA's SIM (Space Interferometry Mission). Another scenario suggests that satellites follow their massive host's dark matter distribution. Kang et al. (2005) demonstrate that in this case satellites may exhibit planar distributions as observed for the Milky Way satellites although they find a distribution almost perpendicular to the stellar Galactic plane to be unexpected. Hartwick (1996; 2000) argues that the Galaxy's dark halo has "an extended prolate triaxial distribution highly inclined to the Galactic plane", thus accounting for the satellites' polar alignment. In a third, related scenario Knebe et al. (2004) suggest that satellites retain the alignment with the massive primary that they had when they first fell into the group or cluster along a filament. Zentner et al. (2005) and Libeskind et al. (2005) point out that cold dark matter (CDM) hierarchical structure formation scenarios lead to highly anisotropic collapse along filaments, naturally resulting in planar configurations aligned with the major axis of the dark matter distribution. Both groups share the view that the Galactic stellar disk should be approximately perpendicular to the major axis of the dark matter distribution, an orientation supported by recent disk galaxy formation simulations (Navarro, Abadi, & Steinmetz 2004), which may provide a natural explanation also for the Holmberg effect. All these scenarios have one idea in common: They all suggest that the planar alignment reflects the plane of motion of the satellites.

Is the Milky Way exceptional in having its satellites located in one or two great planes? If such alignments are common, are they preferentially polar? If one or several of the the above scenarios hold, then similar great planes (possibly even polar great planes) should also be found for the satellite systems of other galaxies. I will turn to an analysis of possible alignments in the M 31 satellite system, which covers a comparable range in distances as the MW companions, in Chapter 6.

Chapter 2

Complexity on Small Scales: The Metallicity Distribution of the Carina Dwarf Spheroidal Galaxy

> *“Lang ist*
> *Die Zeit, es ereignet sich aber*
> *Das Wahre.”*
> — Friedrich Hölderlin, *Mnemosyne*

Abstract

The Carina dSph is the only galaxy of this type that shows clearly episodic star formation separated by long pauses. In this Chapter we present metallicities for 437 radial velocity members of this Galactic satellite. The metallicities and radial velocities were measured from medium-resolution spectroscopy obtained with ESO/VLT’s multi-object spectrograph FLAMES. Our target red giants cover the entire projected surface area of Carina. Our spectra are centered at the near-infrared Ca II triplet, which is a well-established metallicity indicator for old and intermediate-age red giants. The resulting data sample provides the largest collection of spectroscopically derived metallicities for a Local Group dwarf spheroidal to date. Four of our likely radial velocity members of Carina lie outside of this galaxy’s nominal tidal radius, supporting earlier claims of the possible existence of such stars beyond the main body of Carina. We find a mean metallicity of [Fe/H] ~ -1.7 dex on the metallicity scale of Carretta & Gratton (1997) for Carina. The formal full width at half maximum of the metallicity distribution function is 0.92 dex, while the full range of metallicities is found to span $\sim -3.0 <$ [Fe/H] < 0.0 dex. The metallicity distribution function might be indicative of several subpopulations distinct in metallicity. There appears to be a mild radial gradient such that more metal-rich populations are more centrally concentrated, matching a similar trend for an increasing fraction of intermediate-age stars (Harbeck et al. 2001). This as well as the photometric colours of the more metal-rich red giants suggest that Carina exhibits an age-metallicity relation. Indeed the age-metallicity degeneracy seems to conspire to form a narrow red giant branch despite the considerable spread in metallicity and wide range of ages. The metallicity distribution function is not well-matched by a simple closed-box model of chemical evolution. Qualitatively better matches are obtained by chemical models that take into account also infall and outflows. A G-dwarf problem remains for all of these models.

2.1 Introduction

The Galactic dSph Carina stands out among the dSphs in the Local Group because of its unusual, episodic star formation history. In no other dSph clear evidence for well-separated episodes of star formation has been found. Carina was discovered in 1977 (Cannon, Hawarden, & Tritton 1977) on an ESO/SRC(J) Southern Sky Survey plate. Carina is located at a heliocentric distance of 94 ± 5 kpc and belongs to the fainter dSphs ($M_V = -9.4$, $\mu_V = 25.5 \pm 0.4$; see Grebel 2000 for references). First indications that Carina is not a purely old, globular-cluster-like system came from the discovery of carbon stars (Cannon, Niss, & Norgaard-Nielsen 1981; Mould et al. 1982). Subsequent deep photometry revealed a younger main sequence (Mould & Aaronson 1983; Mighell 1990a,b) and showed that the bulk of the stars in Carina is of intermediate age (i.e., younger than 10 Gyr). However, an old population (traced by a horizontal branch and RR Lyrae stars, e.g., Saha, Monet, & Seitzer 1986) is present as well. Mighell's (1990a,b) data show two distinct main-sequence turnoffs. Smecker-Hane et al.'s (1994) colour-magnitude diagram (CMD) of Carina reveals a morphologically distinct, prominent red clump of an intermediate-age population next to a well-defined red and blue horizontal branch. Mighell and Smecker-Hane et al. concluded that Carina must have undergone at least two separate episodes of star formation.

The episodic nature of the star formation in Carina was then confirmed by deeper photometry: Smecker-Hane et al. (1996) presented a colour-magnitude diagram (CMD) that reached $R \sim 25$ mag. Three well-defined, distinct main-sequence turn-offs (MSTOs) corresponding to ages of 2, 3–6, and 11–13 Gyr are visible in these data. Smecker-Hane et al. note that each of the three MSTOs connects to the same narrow red giant branch and conclude that "regardless of age, Carina stars are metal-poor with [Fe/H] ~ -1.86 dex and a spread in metal abundance of $\sigma_{\mathrm{[Fe/H]}} \leq 0.2$ dex." Mighell (1997), Hurley-Keller, Mateo, & Nemec (1998), Monelli et al. (2003), and Rizzi et al. (2003) arrive at similar conclusions based on additional deep CMDs[1] Hurley-Keller et al. (1998) argue that only 10–20% of Carina's stars formed very early on, while the majority formed approximately 7 Gyr ago and $\sim 30\%$ about 3 Gyr ago. (Note that differences in the derived ages or times of the extended episodes of star formation are mainly caused by the use of different isochrone models). Monelli et al. (2003) suggest that the blue plume stars of Carina may be as young as 1 Gyr, and that the anomalous Cepheids of Carina may belong to an even younger population with an age of ~ 0.6 Gyr (see also Mateo, Hurley-Keller, & Nemec 1998; Poretti 1999; and McNamara 2000 for the identification and the discussion of these stars). The younger populations of Carina are more centrally concentrated than the extended distribution of the old stars (Harbeck et al. 2001; Monelli et al. 2003), similar to the trend seen in other dSphs.

Smecker-Hane et al. (1999) obtained Ca II triplet (CaT) metallicities for 52 red giants in Carina. These authors argue that the narrow red giant branch of Carina results from an age-metallicity conspiracy in the sense that more metal-rich, but younger stars come to lie at the same location in the colour-magnitude plane as older, metal-poor stars, and that photometry alone underestimates the true metallicity spread in Carina. Based on a photometric study, Rizzi et al. (2003) suggest that the narrow red giant branch is a consequence of the contribution of the dominant intermediate-age star-formation episode, while the contribution of the ancient episode is almost negligible.

All these findings underline the highly complex star formation history of Carina. There is not yet a satisfactory explanation why Carina would have experienced episodic star formation with

---

[1] We will not discuss here star formation histories of Carina derived from HST photometry since the field coverage and the number of stars are too small to do so reliably.

extended quiescent episodes in between, and why its evolution was so different from that of other dSphs. As pointed out by Smecker-Hane et al. (1996), episodic accretion of fresh gas would be difficult given the inferred mass of Carina's dark matter halo, and cooling and sinking back of previously ejected gas should have led to higher enrichment.

In the current comprehensive study we add spectroscopic metallicities for several hundred red giants in the enigmatic dSph galaxy Carina in order to analyze its overall metal content. This will allow us to investigate several of the questions raised in Section 1.2 and the previous paragraphs. In particular, we wish to measure the true, spectroscopic mean metallicity and metallicity spread of Carina, derive its metallicity distribution function, investigate whether age and metallicity do indeed conspire, search for possible spatial gradients, and explore its evolutionary history taking into account its chemical enrichment by envisaging some simple models of chemical evolution. Hence, the present Chapter only deals with the measurement of overall stellar metallicities, whereas individual element abundance ratios in stars, which enable one to impose strong constraints on the modes of star formation in galaxies, will be derived and discussed in Chapter 3.

2.2 Observations and reduction

In the course of the ESO Large Programme 171.B-0520(A) (PI: Gilmore), which is dedicated to the analysis of kinematic and chemical characteristics of Galactic dSphs, we observed five fields in Carina. These fields were selected such that we cover most of the area of Carina, but also go a bit beyond its nominal tidal radius. In these fields we obtained spectra of red giants with the goal of determining their metallicities through the well-established CaT method and of measuring their radial velocities to constrain the dark matter profile of Carina. In addition four globular clusters (NGC 3201, 4147, 4590 and 5904) were observed in order to permit us to place our CaT measurements on a scale of known reference metallicities (Rutledge et al. 1997a).

2.2.1 Target selection

Targets in Carina were chosen from photometry and astrometry obtained by the ESO Imaging Survey (EIS; see Nonino et al. 1999 for details) during the Pre-FLAMES era using the Wide Field Imager (WFI) at the 2.2 m telescope at La Silla, Chile. In the framework of EIS a number of different targets and fields was observed, including a region of four WFI fields, comprising approximately 1 deg^2, located at the center of the Carina dSph. The reduced and transformed photometry is available from the EIS web pages at `http://www.eso.org/science/eis/`. For our spectroscopic study, we need to pick sufficiently bright objects. Moreover, the CaT method is only calibrated for intermediate-age and old red giants (Cole et al. 2004), so we chose luminous red giant branch (RGB) stars for the present work.

We selected our targets to cover magnitudes ranging from the tip of the RGB down to 3 mag below the RGB tip, thus down to 20.3 mag in V-band apparent magnitude. This corresponds to an absolute magnitude $M_V \approx 0.3$ at an adopted apparent V-band distance modulus of 20.05 and a reddening of 0.05 (Mighell 1997). The actual values of the distance and reddening are not critical for the analysis in this paper, since we utilize apparent magnitudes relative to the horizontal branch (HB) locus. This differential approach also reduces the problems inherent in the EIS photometry, which go back to intrinsic problems of WFI photometry (see, e.g., Koch et al. 2004a,b). Our chosen RGB magnitude range is such that even for the faintest stars one is generally able to achieve high signal-to-noise ratios (S/N $\sim$ 25) within a reasonable integration time and under good observing conditions (see below). Furthermore, we selected stars across the full width of the RGB (approximately 0.2 mag in B−V) in order to ensure that we were unbiased with respect to metallicity or age, and include also potential extremely metal-poor and metal-rich giants (see the CMD in Fig. 2.1). With these constraints and with the limitations in possible positions on the fiber plate in order to avoid fiber crossings, a total number of 1257 stars was targeted. However, our photometric selection is inevitably contaminated by Galactic foreground stars.

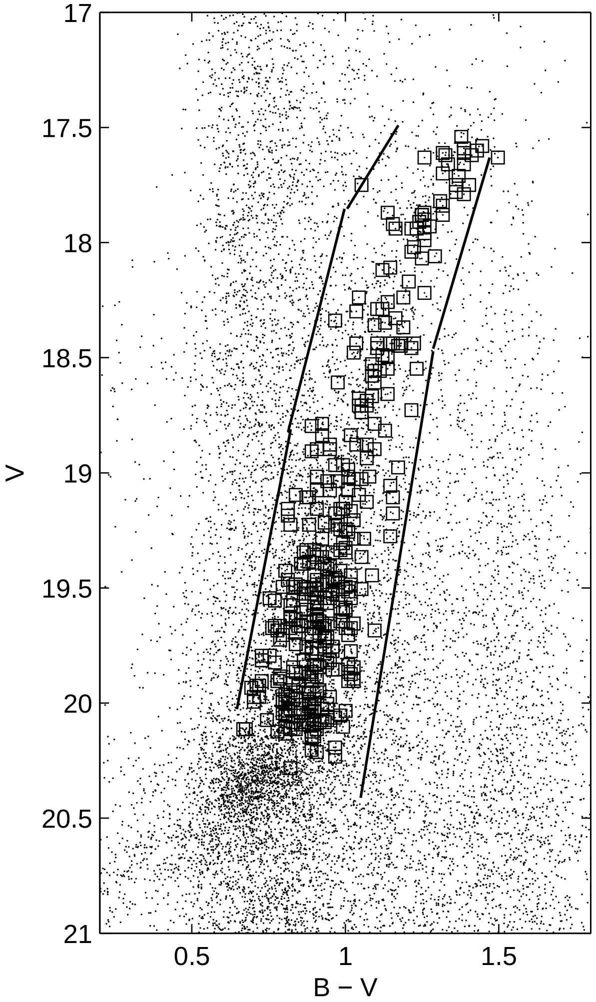

Figure 2.1: Region of the red giant branch in Carina, from which our targets were selected. The photometry shown here is EIS photometry transformed into the Landolt-Stetson *UBVRI* system. The solid lines delineate the colour cuts imposed to select the targets and open squares denote the confirmed radial velocity members of Carina.

For our calibration clusters, we used the standard fields of Stetson (2002). More than 80 red giant candidates altogether were picked from Stetson's B- and V-band photometry. These clusters range in metallicity from approximately −1.1 dex to ∼ −2 dex in [Fe/H] (see Table 2.1 for details). The available photometry of Carina targets is, in contrast to the Stetson list, in the Johnson-Cousins system provided by the EIS. Because of differences in the filter curves, this system differs

Cluster	α	δ	[Fe/H]	[Fe/H]	(m−M)$_V$	E (B−V)	V$_{HB}$	[Ca/Fe]
	(J2000)		ZW,R97	CG,R97				
NGC 3201	10 17 36.8	−46 24 40	−1.53 ± 0.03	−1.24 ± 0.03	14.21	0.21	14.74 ± 0.07	0.11
NGC 4147	12 10 06.2	+18 32 31	−1.77 ± 0.04	−1.50 ± 0.06	16.48	0.02	16.95 ± 0.10	...
NGC 4590	12 39 28.0	−26 44 34	−2.11 ± 0.04	−2.00 ± 0.03	15.19	0.04	15.75 ± 0.05	0.32
NGC 5904	15 18 33.8	+02 04 58	−1.38 ± 0.05	−1.12 ± 0.03	14.46	0.03	15.13 ± 0.05	0.21

Table 2.1: Globular clusters used for calibration of the metallicity scale. Metallicities [Fe/H] are those from Rutledge et al. (1997) and horizontal branch magnitudes V_{HB} were taken from Ferraro et al. (1999). [Ca/Fe] values are cited after Carney (1996). All other parameters were adopted from the compilation of Harris (1996).

from the standard Johnson-Cousin system as defined by Landolt's (1992) and Stetson's (2000) *UBVRI* standard stars. Conveniently, the observed EIS fields overlap with a standard star field in Carina (Stetson 2000) allowing a direct comparison between the EIS photometry and that provided by Stetson. We obtained a linear transformation using the 258 stars in common, and used this to place both the calibration clusters and the science targets on Stetson's homogeneous photometric standard system, avoiding any offsets between the different sets of photometry.

2.2.2 Data acquisition

Our observations were performed in visitor mode with the FLAMES (Fibre Large Array Multi Element Spectrograph) facility at the Very Large Telescope UT2 of the European Southern Observatory on Cerro Paranal in Chile. We observed during 22 nights spread over two semesters in 2003 and 2004 (as detailed in Table 2.2). We used the GIRAFFE spectrograph with both MEDUSA[2] fiber slits in "low-resolution" mode. We observed with grating L8 centered at the near-infrared CaT. This set-up provides a nominal resolving power of R=6500 at the center of the spectra and covers the wavelength range 8206–9400 Å. Each pointing is designed to handle 132 fibers, distributed across a field of view of $25'$ diameter. We dedicated about 20 fibers per configuration to blank sky for sky subtraction purposes.

We observed five different fields in and around the center of Carina (Table 2.3), which we observed with several configurations of the fiber positioning plates in order to maximize the number of targeted stars. The location of our fields is displayed in Fig. 2.2. The total required exposure time per configuration in Carina was six hours in order to reach a nominal S/N of at least 20. This S/N is needed to obtain highly accurate equivalent width (EW) measurements at our spectral resolution. The observations were split into single exposures of approximately one hour each to facilitate cosmic ray removal.

Most of the nights were clear and good sky conditions resulted in a typical seeing of $0\farcs5$-$0\farcs7$, although the first run in 2003 February was hampered by non-photometric conditions and seeing reached values as bad as $2''$. Spectra with low S/N ratios were excluded from the chemical abundance analysis, where the lower limit for marginally measuring EWs is at ≈ 10, but were still useful for the kinematic analysis (Wilkinson et al. 2006a).

---

[2] For details on the individual components of the FLAMES spectrograph see `http://www.eso.org/instruments/FLAMES/`

Date	Field [3] (Configuration)	Total exp. time [s]
21 Feb 2003	Center	1560
	NGC 3201	627
22 Feb 2003	Center	9900
	NGC 4147	2400
03 Mar 2003	Center	9497
04 Mar 2003	Center	7800
	NGC 5904	3600
05 Mar 2003	Center	7800
	NGC 4590	1800
	NGC 3201	1200
22 Dec 2003	NE (1c)	14981
	NE (1b)	12975
23 Dec 2003	Center (2b)	13630
	Center (2a)	13213
24 Dec 2003	SW (1e)	14401
	SW (1d)	13172
25 Dec 2003	NW (1e)	14333
	NW (1d)	13113
26 Dec 2003	NE (2b)	14470
	NE (2a)	13001
27 Dec 2003	SE (1e)	20488
	SE (1d)	13333
28 Dec 2003	SW (2a)	19469
	SW (2b)	235
	NW (1e)	7933
29 Dec 2003	SW (2b)	13421
	Center (1e)	13553
30 Dec 2003	Center (1d)	13694
	Center (2a)	13393
21 Feb 2004	SE (2a)	19677
22 Feb 2004	SE (2b)	15162
	NGC 4590	4794
	NGC 3201	3598
23 Feb 2004	NW (2a)	10824
	NGC 4590	6596
24 Feb 2004	NW (2b)	10833
	NGC 3201	7196
25 Feb 2004	NE (1d)	23481
26 Feb 2004	NE (1e)	10884
27 Feb 2004	NE (2a)	10931
28 Feb 2004	NE (2b)	10635

Table 2.2: Observation log. Only nights relevant for Carina observations are listed – see also Chapter 4.

2.2.3 Data reduction

In the course of ESO's standard calibration exposures, bias frames, fiber flatfield exposures and Th-Ar spectra from a calibration lamp were taken automatically during daytime. We reduced our data using version 1.09 of the FLAMES data-reduction system, *girbldrs*, and the respective pipeline *girbldrs-pipe-1.05* (Blecha et al. 2000). The basic steps comprise bias correction as well as fiber localization and successive adjustment via the flatfield exposures.

Our spectra were extracted by summing up the pixel values along a virtual slit with a width of one pixel. The final re-binning to linear wavelength space was obtained with the master wavelength solution from the calibration Th-Ar spectra, which were reduced and extracted analogously to the science spectra. All spectra were flatfielded using the fiber flatfield exposures. The dedicated skyfibers were employed to calculate an average sky spectrum. This sky spectrum was then subtracted from the science spectra using the IRAF-task *skytweak*[4]. The resulting accuracy (the dispersion, in a 68% confidence interval, of the medians of the sky subtracted spectra in any exposure divided by the median sky) was typically better than 2%.

Finally, the dispersion-corrected, sky-subtracted spectra were co-added to enhance the S/N using *scombine*, where the frames were weighted by their individual S/N. The resulting frames were then continuum-normalized or rectified by a polynomial fit to the regions excluding the Ca and other stronger absorption lines. Thus the median S/N ratio obtained in this way lies at 33 pixel^{-1}, reaching $\approx$200 pixel^{-1} for the brightest stars. Sample spectra of stars representative of our sample are shown in Fig. 2.3.

---

[3] Labels in brackets refer to different configurations on the fiber positioning plates, thus aiming at different

Field	α (J2000)	δ (J2000)
Center	06 41 36.8	−50 57 58
NW	06 41 00.8	−50 45 06
NE	06 42 51.1	−50 52 50
SW	06 39 50.0	−51 04 49
SE	06 42 05.3	−51 10 00
NGC 3201	10 17 36.8	−46 24 40
NGC 4147	12 10 09.6	+18 35 511
NGC 4590	12 39 28.0	−26 44 33
NGC 5904	15 18 03.5	+02 06 41

Table 2.3: Observed fields in Carina and the calibration clusters

2.2.4 Membership: Radial velocities

In order to assess the membership of each target star, we made use of the individual radial velocities. The determination of accurate velocities by means of template spectra is detailed in a paper that concentrates on the kinematic aspects of Carina (Wilkinson et al. 2006a). For the present work it should suffice to note that the Carina dSph galaxy clearly stands out against the Galactic foreground contamination, at a systemic heliocentric radial velocity of ~ 220 km s^{-1}.

Membership probabilities were derived by performing an error-weighted maximum likelihood fit of a Gaussian velocity distribution between 150 km s^{-1} and 300 km s^{-1}. Rejecting $3\,\sigma$-outliers, the fit was iterated until convergence was reached, resulting in a mean heliocentric radial velocity of 223.9 km s^{-1} and a dispersion of 7.5 km s^{-1} (see Fig. 2.4). Taking into account our measurement uncertainties, this agrees very well with previous results. For example, Mateo (1998) quotes a systemic velocity of 224±3 km s^{-1} and a central velocity dispersion of 6.8±1.6 km s^{-1} (based on 17 centrally located stars). Majewski et al. (2005) find a mean velocity of 222.8 km s^{-1} from 61 stars that extend out to 1.5 nominal tidal radii.

Depending on the chosen probability selection[5] to define a member, the total number of stars belonging to Carina varies from 471 ($2\,\sigma$), 501 ($2.5\,\sigma$) to 510 ($3\,\sigma$). The number of high-probability member stars with spectra sufficiently high to be useful for abundance determinations, as opposed to radial velocity determinations, is somewhat lower, namely 409 ($2\,\sigma$), 433 ($2.5\,\sigma$) and 437 ($3\,\sigma$).

Membership of red giants in the four calibration clusters was also determined via radial velocities. Only five stars (N4147-S370 and N4147-D57 in NGC 4147; M68-S155 and M68-S164 in NGC 4590; and M5-1046 in the cluster NGC 5904) were rejected due to their strongly discrepant ($> 8\sigma$) velocities.

2.3 Calibration of the metallicity scale

Determinations of accurate spectroscopic abundances require a well calibrated and widely applicable reference scale. The infrared lines of the singly ionized calcium ion at $\lambda\lambda$ 8498, 8542, 8662 Å have become one of the spectral features of choice. These triplet lines are relatively easy to be distinguished, since they provide the strongest absorption lines in the near-infrared regime of RGB spectra. They also lie at a wavelength range where many CCDs have fairly high sensitivity,

---

targets.

[4] IRAF is distributed by the National Optical Astronomical Observatory.

[5] In the present representation the 2σ, 2.5σ and $3\,\sigma$ limits correspond to membership probabilities of $p >$0.0072, 0.0023 and 0.0006.

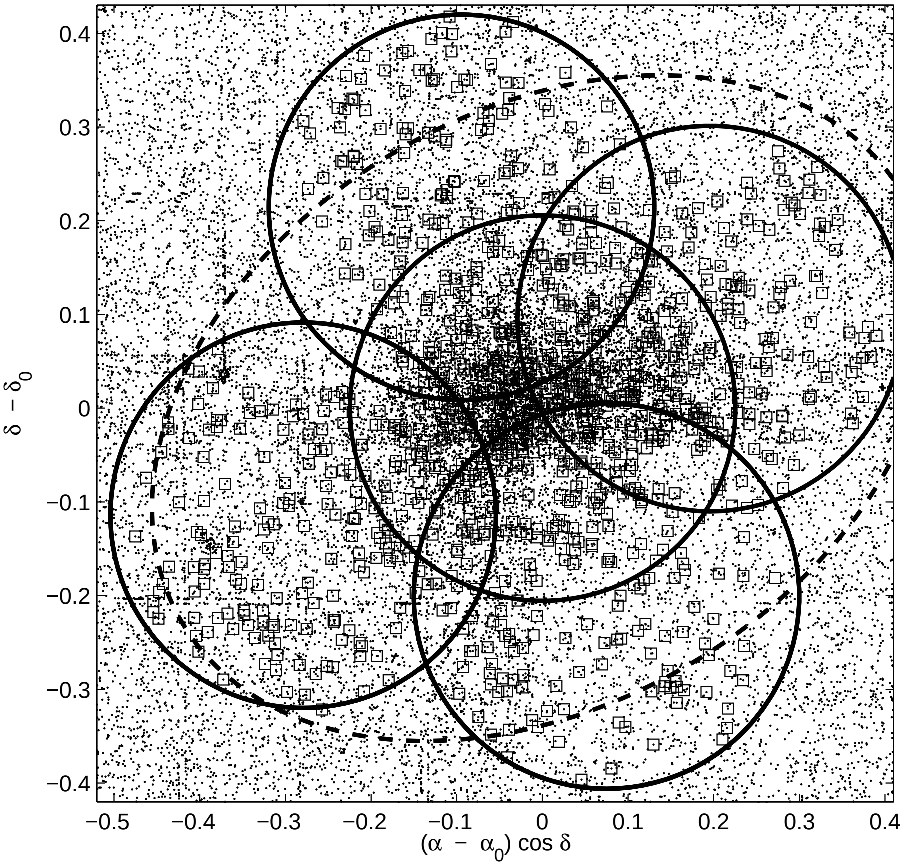

Figure 2.2: Location of our targets (shown as open squares) relative to Carina's geometric centre (α_0,δ_0), superposed on a stellar map of the galaxy and its surroundings. The circles circumscribe the field of view of the FLAMES spectrograph of 25′. The ellipse indicates the nominal tidal radius, ellipticity, and position angle of Carina as inferred by Irwin & Hatzidimitriou (1995).

an advantage when trying to measure faint sources within reasonable exposure times. However, the CaT lines are generally considerably affected by strong night-sky emission lines, hampering accurate measurements for abundances in faint stars.

The use of the CaT for measuring metallicities of red giants in old, metal-poor populations was first established for simple stellar populations such as globular clusters (Armandroff & Zinn 1988; Armandroff & Da Costa 1991; Rutledge et al. 1997a). It was then also employed for mixed populations beyond the Milky Way halo, such as in dSphs (e.g., Suntzeff et al. 1993, Côté et al. 1999a; Smecker-Hane et al. 1999; Guhathakurta et al. 1999; Tolstoy et al. 2001; Pont et al. 2004) and in irregular galaxies (e.g., Cole et al. 2005). Based on the comprehensive catalog of CaT data from Rutledge et al. (1997a), Rutledge, Hesser & Stetson (1997b) established a seminal calibration of Galactic globular cluster metallicities to the scales of Zinn & West (1984, hereinafter ZW) and Carretta & Gratton (1997, hereafter CG). Nevertheless, this empirical linear calibration is strictly valid only for old and metal poor red giants with [Fe/H] below −0.5 dex and ages no younger than 10 Gyr, since this is the parameter range covered by their calibrating globular clusters.

Smecker-Hane et al. (1999) carried out CaT spectroscopy of 52 red giants in Carina and

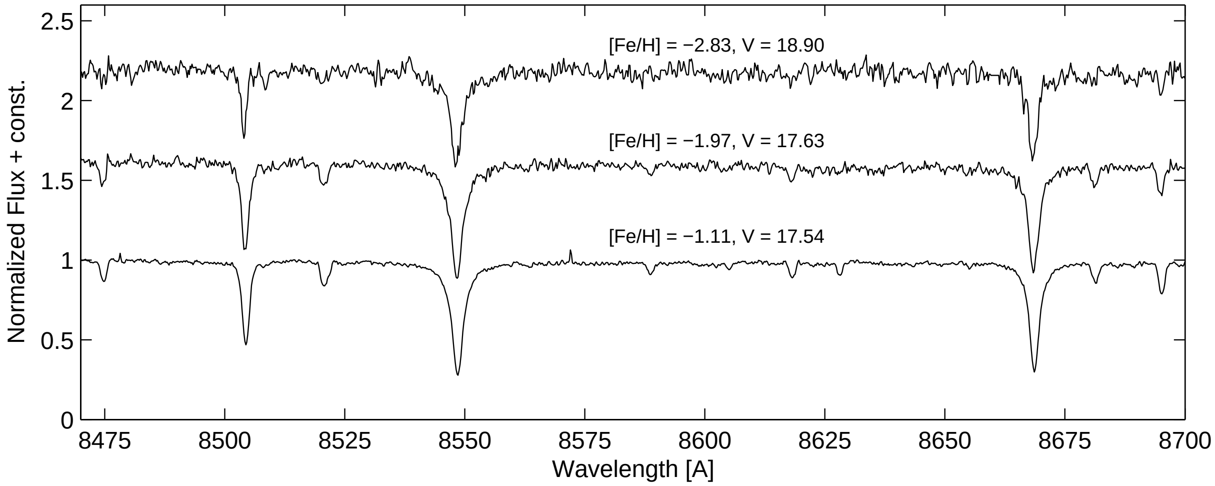

Figure 2.3: Sample spectra of Carina red giants centered on the near-infrared Ca II triplet region. The three spectra are representative of the observed range in metallicities.

found that most of the Carina RGB stars belong to a metal poor population around −2 dex. Still, the occurrence of a wide range of ages, particularly the dominant intermediate-age populations (Hurley-Keller et al. 1998; Rizzi et al. 2003), hence raises the question of an unbiased applicability of the CaT-technique to our Carina sample. However, recently the CaT calibration was extended to ages as young as 2.5 Gyr: Based on spectroscopy of red giants in Galactic globular and open clusters Cole et al. (2004) have shown that the CaT method has very little age sensitivity and can be reliably applied to composite populations with a range of ages. Since the dominant populations in the Carina dSph lie in the range of validity of the CaT method, we can trust that our measurements will yield consistent results for this galaxy.

2.3.1 Equivalent widths and reduced width

Equivalent widths of the three CaT lines were measured by means of the software kindly provided by A. Cole, which is a modified version of G. Da Costa's EWPROG-program (see Cole et al. 2004). We followed Suntzeff et al. (1993) in using line and continuum bandpasses as defined in Armandroff & Zinn (1988). These were shifted to take account of our derived radial velocities. As was proposed by Cole et al. (2004), each CaT line is best fit by the sum of a Gaussian and a Lorentz profile with a common nominal line center, which yields a progressively better fit to the line wings. Theoretical models show that the wings are most sensitive to changes in stellar parameters (e.g., Smith & Drake 1990). The final width was then derived by summing up the flux in the fit profile across the bandpass and errors were calculated automatically from the residuals of the fit.

In order to perform a self-consistent analysis of our calibration clusters and of the Carina data, we have to re-derive the relation between line strength and metallicities. We chose to exclude the weakest of the three lines at 8498 Å in order to minimize the errors in the final metallicity measurements. Thus we define the Ca linestrength as

$$\Sigma W = EW_{8542} + EW_{8662}.$$

The overall width ΣW of the CaT lines is not only a strong function of metallicity, but is

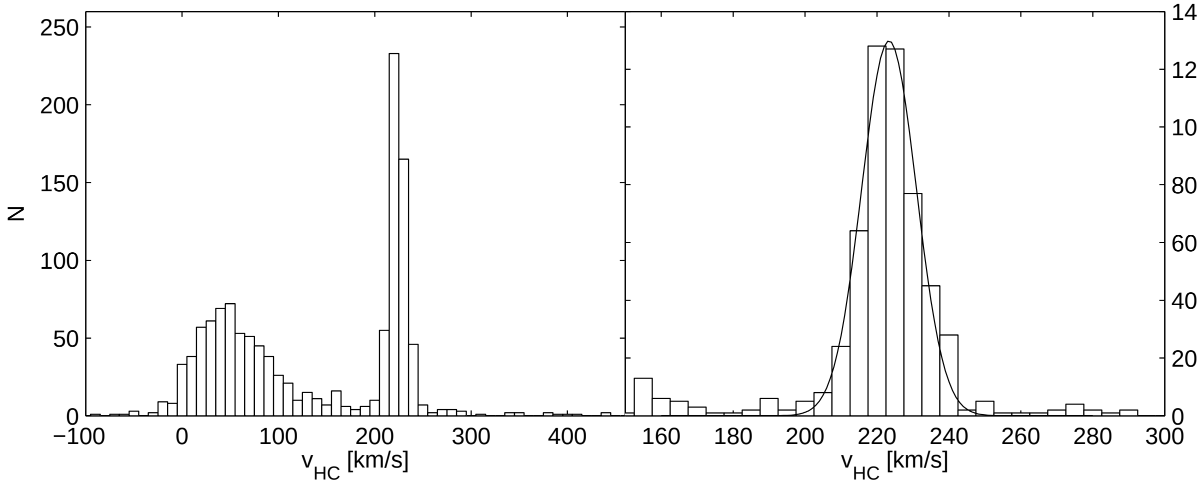

Figure 2.4: Left panel: Distribution of radial velocities for all stars in our sample. Right panel: The region around Carina's systemic velocity of ∼223 km s^{-1}. Also indicated is the best fit of a single Gaussian.

also affected by stellar effective temperature and surface gravity. Isolating the strong sensitivity of the linestrength to metallicity is commonly achieved by defining a *reduced* equivalent width, which effectively removes the signature of surface gravity and effective temperature from the CaT strength (Rutledge et al. 1997b and references therein). Basically, correcting the linestrength for a star's V-magnitude overcomes the sensitivity to gravity, since a given star on the RGB can have a range of radii depending on its evolutionary phase, although its mass remains nearly constant. The increase in radius toward the tip of the RGB results in a progressively lower surface gravity (and effective temperature), where the relation between gravity and V magnitude is close to linear (e.g., Cole et al. 2000). The additional introduction of the apparent magnitude of the horizontal branch, V_{HB}, and the subsequent measurement of the difference between the apparent V-band magnitude of a given red giant and of V_{HB} removes any remaining dependence on systemic distance and reddening.

As a comparison with the maps of Schlegel, Finkbeiner & Davis (1998) reveals, the Galactic foreground extinction toward the region of Carina is rather constant, with an r.m.s. scatter around the mean E(B−V) of less than 0.01 mag across the projected area of the galaxy (see Fig. 2.5).

Thus differential reddening is unlikely to significantly falsify the use of a single HB magnitude throughout this dSph. In a gas- and dust-deficient dSphs like Carina the internal reddening may be neglected. Furthermore, since the colour range across the RGB is small and since we are using Johnson-Cousins colours, any extinction-induced magnitude differences for stars of different surface temperature may be entirely ignored (Grebel & Roberts 1995). Hence the reduced width, defined as

$$W' = \Sigma W + \beta (V - V_{HB}),$$

is basically the CaT-linestrength of an RGB star with the luminosity that it would have if it were located on the HB. This parameter is a very convenient metallicity indicator (Rutledge et al. 1997b), since in this form it is *purely* a function of metallicity.

Fig. 2.6 shows a plot of the measured linestrengths for each of the calibration clusters versus the respective magnitudes above their HBs. We adopted the HB magnitudes of our calibrators from

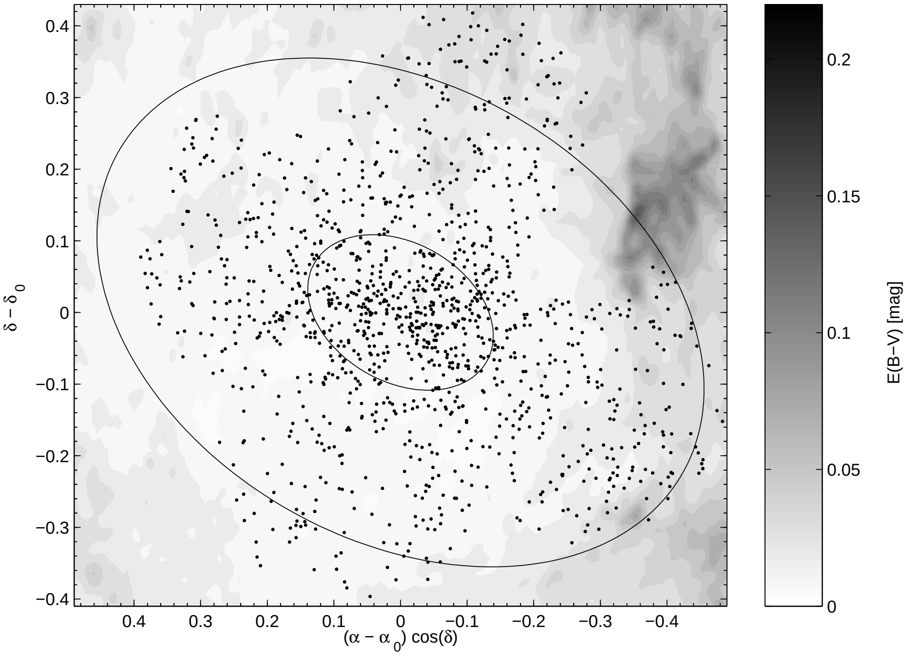

Figure 2.5: Extinction map around Carina after Schlegel, Finkbeiner & Davis (1998). Points denote all targets; the inner and outer circles circumfer Carina's core and tidal radius.

Ferraro et al. (1999) in order to place all measurements on a consistent scale. Likewise, we defined the HB level of Carina via the magnitude of the lower envelope of the observed HB distribution in the region with $0.2 < B\text{-}V < 0.6$. Hence we consistently use the determined V_{HB} magnitude of 20.88 mag. This is the HB of the *old* population in the Carina dSph; the core-Helium-burning stars of the (dominant) younger/intermediate-age population form the prominent red clump at $V \sim 20.5$ (see Monelli et al. 2003; Smecker-Hane et al. 1994). As was demonstrated by Cole et al. (2004) using the HB location of the old HB is perfectly acceptable also for intermediate-age populations. We discuss the (small) expected amplitude of the resulting systematic effect in the metallicities of the intermediate-age stars below.

A linear, error-weighted least-squares fit to the line measurements of all remaining 72 stars in the four globular clusters leads to the parameterization of the reduced width, W′, as

$$W' = \Sigma W + (0.55 \pm 0.02)\,(V - V_{HB}), \tag{2.1}$$

with an r.m.s. scatter around this averaged slope of 0.18 Å. In this equation, the given slope is the error-weighted mean of the individual slopes of each of the four clusters. The value for the slope derived by us is shallower than the one obtained in the original calibrations by Rutledge et al. (1997a), who measured it to be (0.64 ± 0.02) Å mag^{-1} based on the CaT line strengths in 52 Galactic globular clusters. The more recent analysis of Cole et al. (2004), who included metal-rich open clusters, obtained an even steeper slope of 0.73 ± 0.04. They suggest that the difference is due to an increase of slope with the mean metallicity of the calibrating clusters. Indeed, the mean metallicity of our four calibrating clusters, at -1.47 dex on the CG scale (-1.70 dex on the ZW scale), is $\sim 0.2 - 0.4$ dex more metal-poor than the entire sample used by Rutledge et al. (1997a,b) (mean metallicities of -1.25 dex on the CG scale, -1.33 dex on the ZW scale,

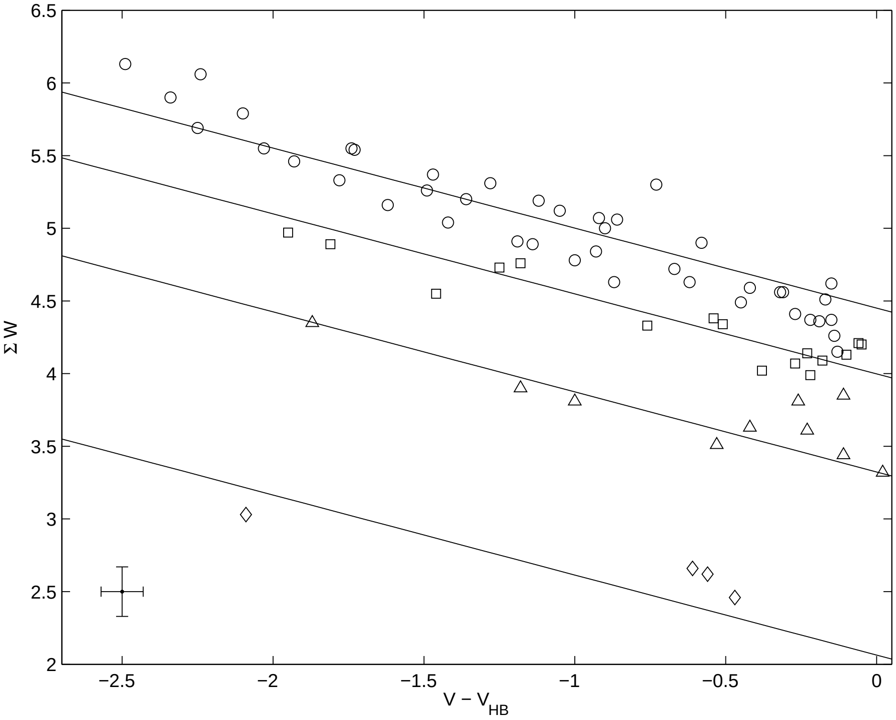

Figure 2.6: Equivalent widths of red giant branch stars in our four calibrating globular clusters plotted against their magnitude above their respective horizontal branches. Shown as a solid line is the best-fitting line for each cluster, based on a common slope of 0.55Å mag^{-1}. The symbols denote NGC 5904 (open circles), NGC 3201 (open squares), NGC 4147 (open triangles) and NGC 4590 (open diamonds). A representative 1σ errorbar is indicated at the lower left. The metallicities of the globular clusters decrease from top to bottom. See Table 2.1 for their [Fe/H] values on different metallicity scales.

respectively), giving some support to the interpretation of Cole et al. (2004). Our calibrating clusters were selected to cover the expected metallicity range of the Carina dSph. Further, our analysis is based on only the two stronger CaT lines and uses a different line profile to that used by Rutledge et al. (1997a). In this paper, we shall consistently use our own calibration.

2.3.2 The metallicity scale

One of our observed globular clusters, NGC 4147, was not included in the common scale of Carretta & Gratton (1997). In order to exploit the maximum number of calibrators at hand, we nevertheless retained this cluster in our analysis by adopting the reference metallicities by Rutledge et al. (1997b), who also measured this cluster. These authors calibrated their sample of globular clusters to both the ZW and CG scales, and we also apply calibrations to both scales for the sake of consistency. Another calibration scale is provided by Kraft & Ivans (2003), who derive globular cluster metallicities based on the equivalent widths of Fe II lines from high-resolution spectroscopy. Their scale yields metallicities that are about 0.2 dex more metal poor than those on the CG scale. However, we will present our results later on in terms of the calibration of Rutledge et al. (1997b) on the scale of CG unless stated otherwise, since this is the most common representation nowadays.

As Fig. 2.7 implies our observations yield well-defined linear relations between the reduced width W′ and [Fe/H] on both scales. We can thus infer the metallicities of our target stars using

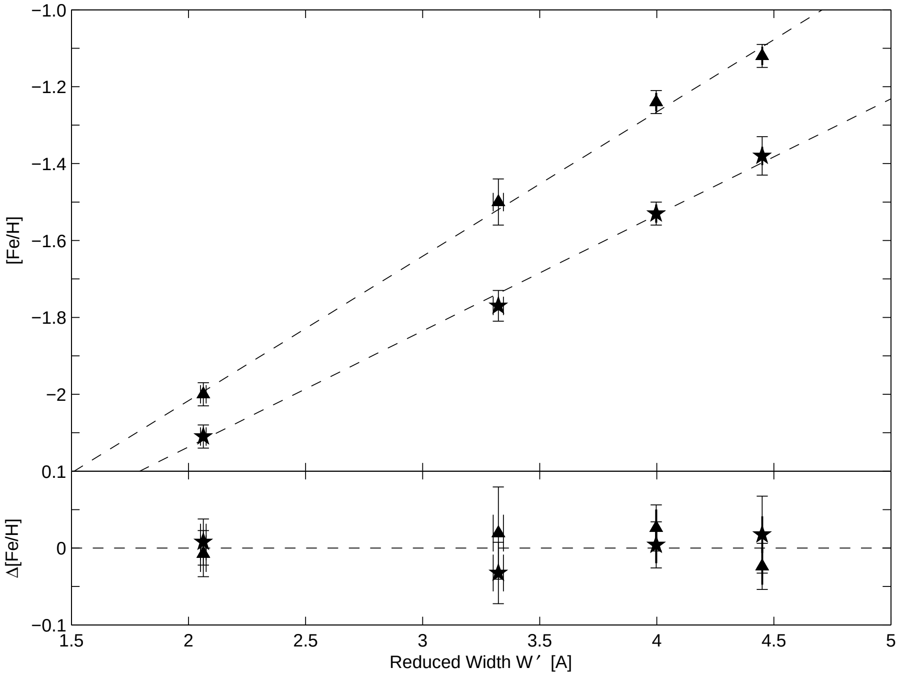

Figure 2.7: The top panel displays the metallicity of the four calibration clusters against their reduced width, both calibrated against the reference values of Rutledge et al. (1997b) on the scale of Zinn & West (stars) and Carretta & Gratton (triangles). The residuals of the linear best fit (dashed lines) are plotted in the bottom panel.

the following equations, which were obtained by an error-weighted least-squares fit:

$$[\mathrm{Fe/H}]_{R97,CG} = (-2.77 \pm 0.06) + (0.38 \pm 0.02)\,W' \qquad (2.2)$$

$$[\mathrm{Fe/H}]_{R97,ZW} = (-2.74 \pm 0.06) + (0.30 \pm 0.02)\,W' \qquad (2.3)$$

The bottom panel of Fig. 2.7 shows that there is only little scatter around the best-fit line. The r.m.s. scatter was calculated to be 0.02 dex for both metallicity scales. The uncertainties of our metallicities were estimated by propagation using the measurement errors in the EWs and uncertainties in the calibration (eqs. 2.1–2.3). The mean measured uncertainty in our metallicities amounts to 0.17 dex.

Red giants that were observed in Carina are shown in the V,ΣW-plane of Fig. 2.8, together with some isometallicity lines to guide the eye. The wide range of values in the diagram already indicates a large spread in metallicities.

2.3.3 The possible impact of Ca abundance variations

The "metallicity" of a galaxy is customarily represented by its iron abundance [Fe/H] (or [Me/H]). Strictly speaking, Ca does not necessarily trace Fe as such, and Ca and Fe are formed in different

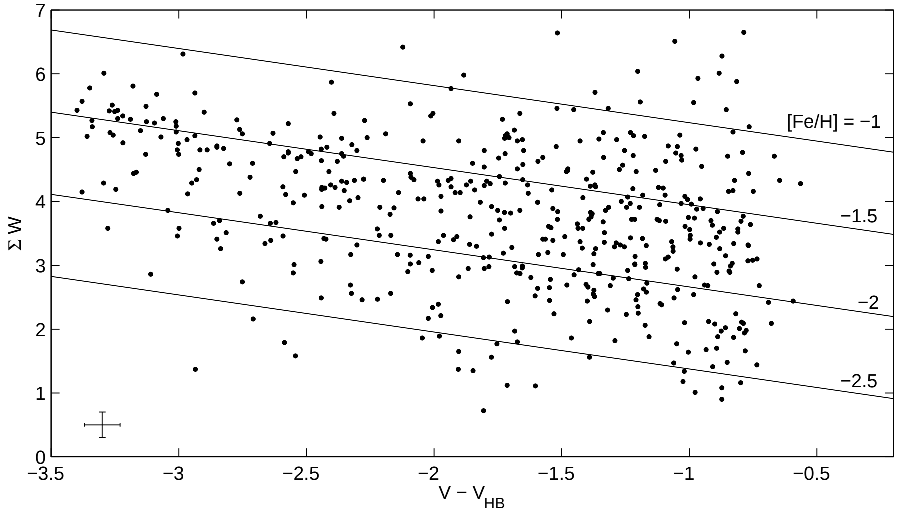

Figure 2.8: Distribution of the Carina targets in the V,ΣW-plane. As the lines of constant metallicity indicate, the galaxy exhibits a large spread in [Fe/H]. A typical errorbar is shown left.

nucleosynthesis processes. A potential inconsistency in applying the CaT technique to derive metallicities in a dSph in terms of [Fe/H] is the likely variation of the [Ca/Fe] ratio, both within the composite population of the dSph, and in between the calibrating clusters and the dSph stars. When converting from Ca to Fe abundances, one has to consider the different dependencies of [Fe/H] and [Ca/Fe] on the detailed star formation histories of the galaxy. It is far from straightforward to determine an unambiguous metallicity scale from single element measurements, particularly in a galaxy with a strongly episodic star formation history like Carina (see Cole et al. 2000; Tolstoy et al. 2001 for a detailed discussion and Gilmore & Wyse 1991 for models).

The measured [Ca/Fe] ratios for stars in globular clusters tend to be higher than the solar value (see the compilation in Carney 1996). Indeed, the values for three of our calibrating clusters (each based on only a handful of stars; Carney 1996) are (see also Table 2.1): [Ca/Fe] = +0.11 ± 0.04 (NGC 3201); [Ca/Fe] = +0.32 (NGC 4590; only two stars); [Ca/Fe] = +0.21 ± 0.02 (NGC 5904). The few published elemental abundances for stars in the Carina dSph show some stars with similar values, but a tendency toward the lower values as expected for an extended star-formation history and incorporation of Fe from Type Ia supernovae. Shetrone et al. (2003) analyzed five stars that are known to be members from the radial velocity measurements of Mateo et al. (1993). They obtained values for [Ca/Fe] of: +0.14, −0.10, +0.20, +0.12 and −0.02, with a typical uncertainty of 0.05 (see Table 2.4).

The values of [Fe/H] that were based on Fe lines in Shetrone et al.'s (2003) high-resolution spectra for these bright stars are: −1.60, −1.64, −1.60, −1.40 and −1.94 respectively.

We note that uncertainties resulting from the unknown variations in the values of [Ca/Fe] for our target stars are likely to be up to 0.2 dex, based on these measured values. Such effects may in the future be overcome by calibrating W′ directly onto [Ca/H] (Bosler et al. 2002), making calibrations independent of star formation history, unlike the present technique. Our own high-resolution UVES spectra for ten stars will provide more elemental abundance information, which

---

[6] Metallicities given for the Shetrone et al. (2003) stars are the weighted means from [Fe I/H] and [Fe II/H].

Star ID (Mateo 1993)	EIS-ID	$[Fe/H]_{\rm high\,res}$ (Shetrone et al. 2003)^6	$[Fe/H]_{\rm CaT,ZW}$ (This work)	$[Fe/H]_{\rm CaT,CG}$
M2	LG04a_003764	-1.60 ± 0.02	-1.67 ± 0.09	-1.43 ± 0.09
M3	LG04a_001419	-1.65 ± 0.02	-2.00 ± 0.08	-1.84 ± 0.07
M4	LG04a_001673	-1.59 ± 0.02	-1.65 ± 0.09	-1.41 ± 0.09
M10	LG04d_006644	-1.94 ± 0.02	-2.16 ± 0.07	-2.04 ± 0.07
M12	LG04a_007126	-1.40 ± 0.02	-1.33 ± 0.11	-1.01 ± 0.10

Table 2.4: Stars in common with Shetrone et al. (2003).

can be used to obtain an improved statistical estimate of the metallicity uncertainty (see also Chapter 3).

The high-resolution measurements from Shetrone et al. (2003) quoted above in fact also provide an external check of our metallicity estimates. Comparing their results with our data permits us to assess the internal precision of our measurements. Table 2.4 gives a comparison of [Fe/H] values from our analysis with the respective high-resolution data. The mean offset between both analyses is 0.09 dex (our CG scale) and 0.13 dex (ZW). After adjusting the individual deviations by these mean offsets, the absolute average difference amounts to 0.18 (0.25) dex. This offset is comparable to the order of uncertainty introduced by the [Ca/Fe] variations with respect to Galactic globular clusters as mentioned above, as well as our random measurement errors. Since we here juxtapose our Ca-based metallicities with the true iron abundances from Shetrone et al. (2003), the above quoted average difference well reflects the calibration uncertainty.

2.3.4 Additional potential sources of uncertainty

Furthermore, while ideally one would like to associate each RGB star with the appropriate HB level corresponding to a population of the age and metallicity of that RGB star, in practice we do not have sufficient information. Our adoption of a single HB for all the stars has the advantage of providing us with a well-defined magnitude and allows us to estimate the associated uncertainties. Since we adopted the HB appropriate for the oldest stars, and hence the least luminous HB, there will be a systematic effect. The expected result from normalizing with an HB of apparent magnitude $V_{HB,\,true} + \Delta V_{HB}$, with $V_{HB,\,true}$ the appropriate HB level for a given star, can be seen by the appropriate substitution in the relations for reduced width and [Fe/H] (eqs. 2.1,2.3). We find a resulting error in [Fe/H] of $-0.55 \times 0.38 \times \Delta V_{HB}$ dex. As noted earlier, the core He-burning phase of the intermediate-age population in the Carina dSph forms a prominent red clump, some 0.4 mag brighter than the old HB used in the normalization; thus for these stars $\Delta V_{HB} \sim 0.4$. The resulting bias in [Fe/H] is -0.07 dex, i.e., we estimate that these stars may be -0.07 dex too metal-poor.

The small amplitude of this effect is confirmed by the analysis of Cole et al. (2004), where they experiment by assigning HB levels (absolute magnitudes) randomly to stars in different clusters. The variation in the luminosity of the clusters' HB levels is 0.4 mag (see their Table 1). Using their derived slopes for the calibration relations, we find that the total amplitude of the change in metallicity estimates from using the appropriate HB level is 0.1 dex. This is just what is seen in their Figure 6. Basically the variation of HB level with age and metallicity amounts to ~ 0.1 dex in metallicity uncertainty, and in our case for most of the stars results in an underestimate by this amount. Of course we cannot say for which stars we are underestimating the metallicity without having age information. As we discuss below, in principle, with robust accurate models of the upper RGB, one could iteratively solve for age and metallicity. We did not attempt this procedure since the maximum amplitude of the effect, ~ 0.1 dex, is within the uncertainties of the models.

Of the target stars in the central field, 46 were observed repeatedly, i.e., during all of the runs. In these cases the finally quoted metallicity is the value derived from a combined spectrum, including all of the respective single spectra. However, in order to get an estimate of the random errors of the measurements, we compare in Fig. 2.9 the metallicities determined from spectra obtained on the individual observing runs in 2003 February and March to metallicities derived from combined spectra from all the available observations (see also Table 2.5). Some of the entries have metallicity estimates from the two runs differing by several sigma.

Table 2.5: Stars measured in different observing runs.

Star	$[\mathrm{Fe/H}]_{CG}$ first run	$[\mathrm{Fe/H}]_{CG}$ second run	$\Delta[\mathrm{Fe/H}]_{CG}$	$[\mathrm{Fe/H}]_{CG}$ combined spectra
LG04a_000030	-1.49 ± 0.11	-1.77 ± 0.10	0.28	-1.58 ± 0.08
LG04a_000377	-1.45 ± 0.11	-1.45 ± 0.11	0.00	-1.45 ± 0.08
LG04a_000451	-1.95 ± 0.10	-1.45 ± 0.11	-0.50	-1.51 ± 0.08
LG04a_001042	-1.53 ± 0.11	-1.36 ± 0.12	-0.17	-1.49 ± 0.08
LG04a_001111	-1.60 ± 0.11	-1.75 ± 0.10	0.15	-1.62 ± 0.08
LG04a_001142	-2.01 ± 0.09	-1.61 ± 0.11	-0.40	-1.85 ± 0.07
LG04a_001170	-1.62 ± 0.11	-1.53 ± 0.11	-0.09	-1.62 ± 0.08
LG04a_001234	-0.91 ± 0.14	-1.53 ± 0.11	0.62	-1.44 ± 0.08
LG04a_001298	-0.79 ± 0.14	-2.32 ± 0.09	1.53	-2.09 ± 0.07
LG04a_001313	-1.06 ± 0.13	-2.24 ± 0.09	1.18	-2.13 ± 0.07
LG04a_001364	-1.61 ± 0.11	-1.57 ± 0.11	-0.04	-1.68 ± 0.08
LG04a_001390	-1.68 ± 0.10	-1.62 ± 0.11	-0.06	-1.39 ± 0.09
LG04a_001426	-1.92 ± 0.10	-1.58 ± 0.11	-0.34	-1.68 ± 0.08
LG04a_001556	-1.40 ± 0.12	-1.41 ± 0.12	0.01	-1.41 ± 0.09
LG04a_001558	-1.81 ± 0.10	-1.40 ± 0.12	-0.41	-1.62 ± 0.08
LG04a_001608	-1.49 ± 0.11	-1.67 ± 0.10	0.18	-1.80 ± 0.07
LG04a_001734	-1.80 ± 0.10	-1.93 ± 0.10	0.13	-1.78 ± 0.07
LG04a_001875	-1.53 ± 0.11	-2.48 ± 0.08	0.95	-2.00 ± 0.07
LG04a_001899	-1.55 ± 0.11	-2.01 ± 0.09	0.46	-1.92 ± 0.07
LG04a_001910	-1.50 ± 0.11	-1.61 ± 0.11	0.11	-1.56 ± 0.08
LG04a_001917	-1.45 ± 0.11	-1.66 ± 0.11	0.21	-1.60 ± 0.08
LG04a_002065	-1.37 ± 0.12	-1.55 ± 0.11	0.18	-1.52 ± 0.08
LG04a_002169	-1.50 ± 0.11	-1.52 ± 0.11	0.02	-1.51 ± 0.08
LG04a_002181	-1.44 ± 0.11	-1.37 ± 0.12	-0.07	-1.39 ± 0.09
LG04a_003952	-1.25 ± 0.12	-1.68 ± 0.10	0.43	-1.64 ± 0.08
LG04a_004179	-1.80 ± 0.10	-1.92 ± 0.10	0.12	-1.93 ± 0.07
LG04b_002633	-1.25 ± 0.12	-2.10 ± 0.09	0.85	-1.87 ± 0.07
LG04b_005294	-1.22 ± 0.12	-1.90 ± 0.10	0.68	-1.51 ± 0.08
LG04c_000626	-1.91 ± 0.10	-2.11 ± 0.09	0.20	-2.06 ± 0.07
LG04c_000710	-1.44 ± 0.11	-1.24 ± 0.12	-0.20	-1.19 ± 0.09
LG04c_003085	-1.12 ± 0.13	-1.16 ± 0.13	0.04	-0.96 ± 0.10
LG04c_004153	-1.70 ± 0.10	-1.61 ± 0.11	-0.09	-1.56 ± 0.08
LG04c_004227	-2.32 ± 0.09	-2.53 ± 0.08	0.21	-2.31 ± 0.06
LG04c_004308	-2.08 ± 0.09	-2.13 ± 0.09	0.05	-2.15 ± 0.07
LG04c_006477	-1.25 ± 0.12	-1.75 ± 0.10	0.50	-1.55 ± 0.08
LG04c_006479	-1.51 ± 0.11	-1.75 ± 0.10	0.24	-1.65 ± 0.08
LG04c_006573	-1.52 ± 0.11	-1.42 ± 0.11	-0.10	-1.45 ± 0.08
LG04c_006593	-1.34 ± 0.12	-1.36 ± 0.12	0.02	-1.39 ± 0.09
LG04c_006601	-1.52 ± 0.11	-1.53 ± 0.11	0.01	-1.54 ± 0.08

Continued on next page

Table 2.5 – *Carina stars, continued*

Star	$[\mathrm{Fe/H}]_{CG}$ first run	$[\mathrm{Fe/H}]_{CG}$ second run	$\Delta[\mathrm{Fe/H}]_{CG}$	$[\mathrm{Fe/H}]_{CG}$ combined spectra
LG04c_006788	-1.08 ± 0.24	-1.42 ± 0.11	0.34	-1.38 ± 0.09
LG04c_007260	-1.58 ± 0.11	-1.49 ± 0.11	-0.09	-1.52 ± 0.08
LG04d_003625	-2.01 ± 0.09	-1.60 ± 0.11	-0.41	-1.68 ± 0.07
LG04d_004311	-1.90 ± 0.10	-2.14 ± 0.09	0.24	-1.85 ± 0.07
LG04d_004565	-1.65 ± 0.11	-2.06 ± 0.09	0.41	-2.05 ± 0.07
car1_t100	-2.12 ± 0.09	-1.90 ± 0.10	-0.22	-2.01 ± 0.07
car1_t102	-1.62 ± 0.11	-1.53 ± 0.11	-0.09	-1.55 ± 0.08

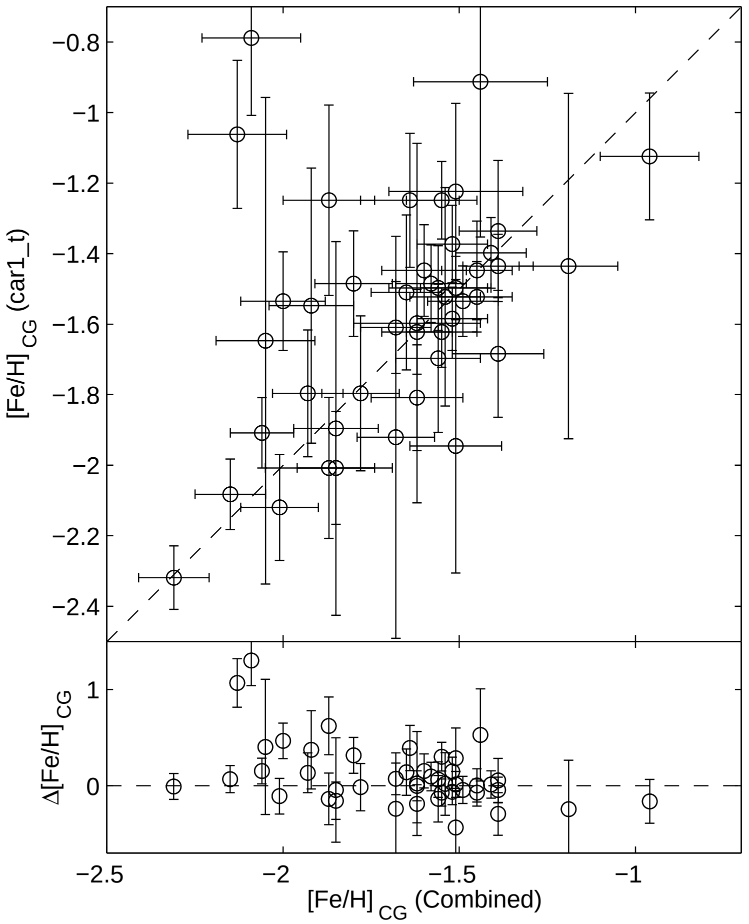

Figure 2.9: Comparison of the stars observed during different observing runs: Shown are metallicities derived from spectra of the first run (labeled *car1_t*) versus [Fe/H] as measured from the combined spectra of all runs. The dashed line is unity and the bottom panel displays the respective residuals.

It turns out that the median difference ([Fe/H] (1st run) − [Fe/H] (2nd run)) between individual metallicity estimates amounts to 0.08 dex and the r.m.s. scatter of the different estimates from both runs totals 0.57 dex. Rejecting those objects deviating more than two standard deviations, namely two targets with particularly low S/N, from the sample we find a respective r.m.s. of 0.3 dex. This is larger than our overall random error estimate of 0.17 dex. But as noted before, this is mainly due to the first run being plagued by poor weather conditions, which was taken into account by weighting spectra by their S/N ratio during the co-addition. Consequently, the mean uncertainty of 0.24 dex for the targets observed during the first run compares to 0.13 dex for the same objects targeted in the second run.

2.4 The metallicity distribution

Metallicities and reduced widths derived for each individual star are given in the Table in the Appendix to this Chapter. The resultant MDFs (see Fig. 2.10) turn out to be almost indistinguishable when using different membership selections (i.e., cutting at different σ levels in the radial velocity distributions), except for the varying total number. We used both a K-S test and the Kuiper statistics (Press et al. 1992) to test how different the MDFs are for different selection criteria. The Kuiper statistics is more sensitive to differences in the MDFs' tails. The MDFs resulting from a 1σ, 2σ, and 3σ-cut are consistent with each other at a level of greater than 99.9%. Hence we chose to maintain the limit of $3\,\sigma$ as our membership criterion.

2.4.1 The width of the MDF

Histograms of the resulting metallicities on each of the two calibration scales for the sample of the 437 Carina red giants are displayed in Fig. 2.10.

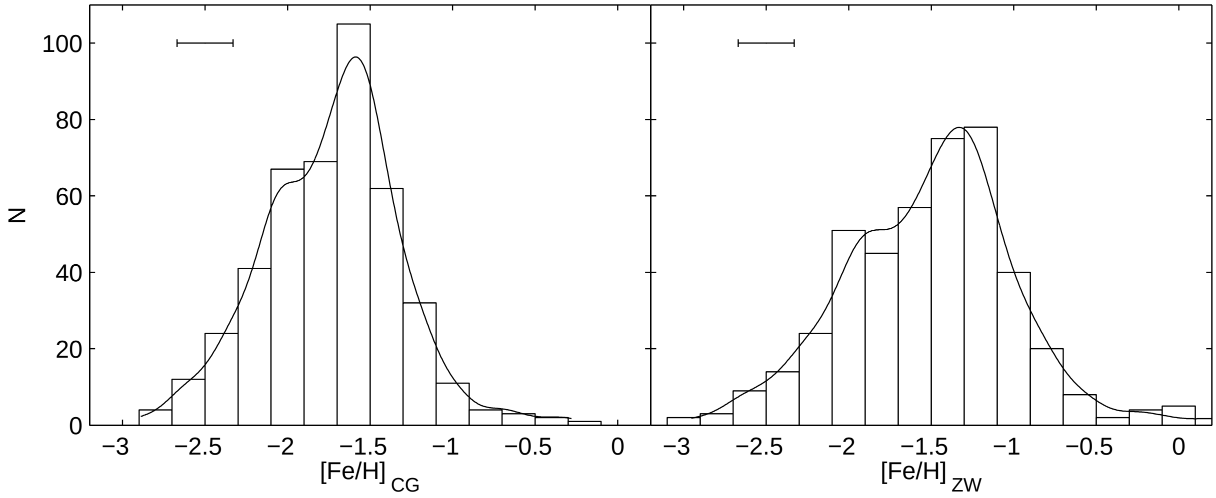

Figure 2.10: Histograms for metallicities of the RGB stars in Carina. The histogram in the left panel uses the scale of CG, the right one refers to the scale of ZW. The line at the top right indicates the median measurement error of 0.17 dex. Overplotted as solid lines are MDFs, convolved by the respective errors.

These show a broad distribution, with a mean metallicity of -1.72 ± 0.01 dex (CG scale) or -1.90 ± 0.01 (ZW scale), respectively. The peak of the MDF is, however, more pronounced for the case of the CG-scale. The entire distribution's *formal* full width at half maximum is 0.92 dex. The full metallicity range is $\sim$ 3.0 dex, as can be seen in Fig. 2.10. This spread can in part be attributed to the measurement uncertainties, but also an occurrence of several subpopulations with different peak metallicities cannot be rejected as a further source of the broadening (see below).

The formal 1 σ-width of the distribution is 0.39 dex, but since a best-fit single Gaussian is simply a mathematically convenient description, some of this width will also be due to measurement and calibration uncertainties. Subtracting our best estimates of these, namely 0.17 dex for the measurement error and 0.02 uncertainty in the slope of the calibration in quadrature, we estimate the width of our distribution to be $\sigma = 0.33$ dex. One should keep in mind, however, that the combined effects of calibration uncertainties from the [Fe/H] calibration via reference clusters through systematic effects due to varying [Ca/Fe] and normalizing the HB level may amount up to 0.22 dex in total. Accounting also for these systematic errors, we obtain an estimate of the width of the MDF of $\sigma = 0.25$ dex. Furthermore, we recall that the dominant population in Carina is of intermediate age, reducing the possibility of star-to-star random variations of uncertainties introduced by the chosen HB level. Thus the width of the distribution is in fact dominated by physical variations in metallicity.

In the extreme tails of the MDF we find stars with metallicities approaching -3 dex and near-solar metallicity, respectively. Note that our calibrating globular clusters only cover the initially expected range of metallicities in Carina, i.e., metallicities from ~ -2 to ~ -1 dex (Table 2.1). Hence the metallicities for the stars in the tails of the MDF are based in extrapolation of our calibration. Follow-up spectroscopy of these stars would be desirable in order to check whether this extrapolation yields reliable results and to further elucidate the chemical properties of these stars. If the overall [Fe/H] values for these stars are correct, they would be as metal-poor as the most metal-poor red giants found in other nearby dwarf galaxies (e.g., Shetrone et al. 2001). At the metal-rich end, a handful of them would be as metal-rich as the metal-rich population in the Sgr dSph (Bonifacio et al. 2004).

2.4.2 Comparison with previous studies

We can now compare the results of our large sample with previous results for large samples of red giants in Carina. From a sample of 52 RGB stars using the same method as here, Smecker-Hane et al. (1999) found the mean spectroscopic metallicity of Carina to be -1.99 ± 0.08 dex (CG scale). These authors have not published individual metallicities, so we cannot perform a direct comparison between stars in common to both samples. Rizzi et al. (2003) analyzed the colour distribution across the RGB, including a statistical correction for the star-formation history inferred from the main sequence turn-off region. They derived a photometry-based average metallicity of -1.91 ± 0.18 dex on the scale of ZW. These results on Carina are in reasonable agreement with our data if the quoted uncertainties and the widths of the distributions are taken into account.

Yet, metallicity estimates via purely photometrical isochrone fitting of RGB stars without age information lead to mean values that are typically more metal-rich by approximately 0.2 dex, as, e.g., in Monelli et al. (2003). These authors obtain their result by a direct comparison with the Galactic globular cluster NGC 1904, a single-age, single-metallicity system. For this object, different values for [Fe/H] are found in the literature, reaching from -1.37 dex (Rutledge et al. 1997b on the CG scale) to -1.69 dex (loc. cit., ZW-scale), whereas Harris (1996) cites an average metallicity of -1.57 dex from all available sources. Still, one has to keep in mind that such a purely photometric fit to the RGB, without any input from an age distribution and age-metallicity relation, is subject to large uncertainties, as is underscored by Fig. 2.11. An additional source of uncertainty is the ability (or lack thereof) of many isochrone models to correctly reproduce the slopes of the red giant branch for very low or high metallicities (e.g., Fig. 5 in Grebel 1997 and Fig. 5 in Grebel 1999).

2.4.3 The shape of the MDF

The complex morphology of the CMD of the Carina dSph – both the multiple turn-off regions and the different He-burning phases – is compelling evidence for strongly varying star formation rates, in fact even for distinct episodes. The metallicity distribution of low-mass stars, as derived here, is rather insensitive to the details of the star formation history, particularly if elements dominated by massive stars are used (cf. Pagel 1997, Section 8.3.7). However, we have calibrated our CaT metallicities onto *iron* (assuming the same [Ca/Fe] in the calibrators as in our stars), which in systems with extended star formation can have a significant contribution from long-lived stars through Type Ia supernovae. Thus one can have enrichment in Fe without accompanying star formation. Hence with a star-formation history that consists of bursts of star formation with a real hiatus between the bursts, the Fe distribution can have "gaps" (no stars formed while Type Ia supernovae enriched the gas, prior to the next burst; cf. Gilmore & Wyse 1991). In order to test whether any substructure reflected in the MDF may provide evidence of star formation events, we applied the Shapiro-Wilk test for normality of a distribution (e.g., Royston 1995) to our observed binned MDF. As a result we can reject the hypothesis of an underlying single Gaussian normal distribution with a significance of 96%. On the other hand, the observed MDF is not expected to be strictly Gaussian, since star formation events do not naturally produce such normal distributions. In addition, we applied a KMM test for multiple populations imprinted in the MDF (Ashman, Bird, & Zepf 1994) to our unbinned data. Again, given our measurement uncertainties and the non-normality of astrophysical star formation events, one has to keep in mind that such a decomposition into multiple single Gaussian sub-populations is purely a formal procedure at this stage that does not necessarily have a physical meaning. We find that the case of four populations is significantly preferred against a one-population model at the 98.1% confidence level. Such a potential multi-population star formation history could also easily account for the MDF's metal-rich extension. Yet a proper interpretation of the observed metallicities requires detailed modeling of the chemical evolution to which we will return in Sect. 6 below.

2.4.4 An age-metallicity relation?

The (lack of a) relation between the colour of our targets and their metallicity is demonstrated in Fig. 2.11.

This figure shows that there is no obvious trend in the sense that predominantly metal-poor stars are not concentrated along the blue ridgeline of the RGB, and the metal-rich stars are not concentrated at the red ridgeline (in contrast to the LMC data of Cole et al. 2005, where such a trend is clearly visible). A metallicity-colour trend would have been expected to result from a direct comparison with fiducials of globular clusters of known metallicities, i.e., for populations of roughly the same age but different metallicities, as indicated by the RGB fiducials for four globular clusters of Sarajedini & Layden (1997) in Fig. 2.11 (left panel). The ridgelines from Sarajedini & Layden cover a wide range of colours in the CMD, corresponding to a metallicity range from -2.02 to -0.78 dex for old and nearly coeval populations. On the right-hand side we show three isochrones with ages and metallicities that roughly correspond to what may be expected from the three main star formation episodes in Carina. Again there is no clear correlation with the data points. Hence it is clear that one cannot derive the metallicity of an individual star from

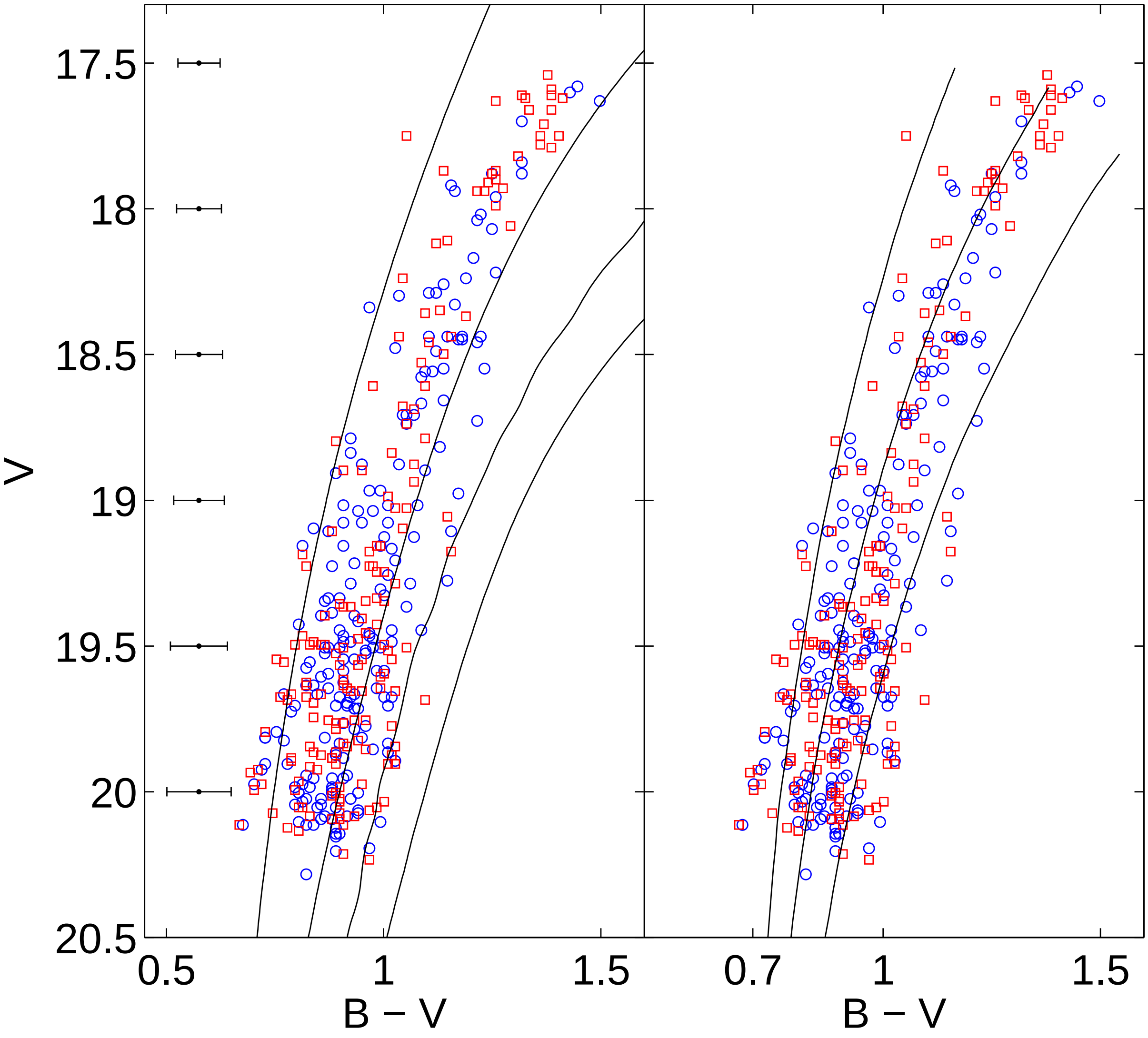

Figure 2.11: Left panel: Distribution of metallicities across the RGB. Red squares depict the metal-poor RGB stars with $[\mathrm{Fe/H}]_{\mathrm{CG}} \leq -1.68$, whereas blue circles refer to the metal-rich tail of the distribution ($[\mathrm{Fe/H}]_{\mathrm{CG}} > -1.68$). Also indicated as solid lines are globular cluster fiducials from Sarajedini & Layden (1997) at the respective $[\mathrm{Fe/H}]_{\mathrm{CG}}$, from left to right: M15 (-2.02), NGC 6752 (-1.24), NGC 1851 (-1.03) and 47 Tuc (-0.78). Representative colour errorbars are indicated in the left panel. — Right panel: The same data points shown with Yonsei-Yale isochrones (solid lines; Yi, Kim, & Demarque 2003). From left to right, the isochrones have the following parameters: [Fe/H] $= -2.3$ dex and 12.6 Gyr, -1.7 dex and 6.3 Gyr, -1.3 dex and 3.2 Gyr. The choice of parameters corresponds roughly to the three main episodes of an assumed star formation history of Carina. Comparing the location of the isochrones with the red giant branch fiducials on the left-hand side illustrates the effects of the age-metallicity degeneracy.

its colour and magnitude on the RGB when dealing with a mixed-age population as present in Carina, nor can a metallicity distribution directly be inferred from the colour distribution in this case.

The existence of an age-metallicity relation can be inferred from the fact that the giants appear to be equally widely spread across the RGB regardless of their metallicity. At a given age, metal-poor stars are in general bluer than their metal-rich counterparts owing to the reduced opacity in their photospheres. Conversely, the older stars tend to have redder colours at a given [Fe/H]. Hence, in order to produce the counteracting trend with both metal-rich and metal-poor stars at the same locus in the CMD, the metal-poor stars necessarily have to be older, whereas the more metal-rich giants have to be of younger age.

If one had reliable models of the upper RGB in the observational plane, one could in principle derive age estimates for our stars of known metallicity, from finding the best-matched isochrone at that metallicity. However, the small offset in colour with age at the relevant intermediate ages, combined with sensitivity to the largely unknown elemental abundance mix and He content limits the usefulness of this exercise. An age distribution and age-metallicity relations are better derived from turn-off stars, provided that the photometry is at a sufficient level of accuracy.

2.5 Radial variations

Previous analyses based on wide-area photometric surveys and thus derived CMDs have shown that the stellar populations in the Carina dSph feature different spatial distributions. Mighell (1997) proposed a strong central concentration of intermediate-age stars from a comparison between a deep HST CMD of the center and ground-based data that covered a wider area. This was confirmed by Harbeck et al. (2001) via wide-field photometry. Harbeck et al. found a pronounced central concentration of the prominent intermediate-age red clump stars in comparison to the old HB. This was subsequently also seen in the photometric study of Monelli et al. (2003). Harbeck et al. (2001) discarded the presence of a significant radial gradient in Carina's old HB morphology out to its nominal tidal radius.

Our large data set allows us to address the issue of population gradients by looking for radial gradients in the MDFs. For this purpose we investigated the MDFs as a function of elliptical radius $r = [x^2 + y^2/(1-\varepsilon)^2]^{1/2}$, where x and y denote the distances along the major and minor axis, respectively. For Carina we adopted a position angle of $(65 \pm 5)^\circ$ and an ellipticity of $\varepsilon = 0.33 \pm 0.05$ (Irwin & Hatzidimitriou 1995). There is no obvious strong radial gradient in the resulting scatter plot of metallicity against elliptical radial coordinate, as shown in Fig. 2.12 (top panel). A simple linear fit yields a gradient of $(-0.0047 \pm 0.0008)\,\mathrm{dex\,arcmin}^{-1}$.

However, as Fig. 2.12 (bottom left) implies, there is a clear radial tendency in the respective MDFs to be seen when the data are split into three radial bins. The annuli have been chosen to cover everything within one core radius ($\mathrm{r}_c = 8\overset{\prime}{.}8$), then everything within r_c to $2\mathrm{r}_c$, and from $2\mathrm{r}_c$ to the nominal tidal radius at $28\overset{\prime}{.}8$. The ratio of the total number of stars in the annuli is approximately 5:4:1.

Fig. 2.12 shows the single MDFs, represented by normalized generalized histograms, which were obtained from the density distributions of our [Fe/H] measurements by convolution with a Gaussian distribution accounting for the individual measurement errors.

The MDF of the innermost region is already rather broad with a suggestion of both lower and higher metallicities and an indication of a secondary population around approximately -2 dex. However, the MDF of the middle annulus is peaked at a metallicity that is at least 0.1 dex lower

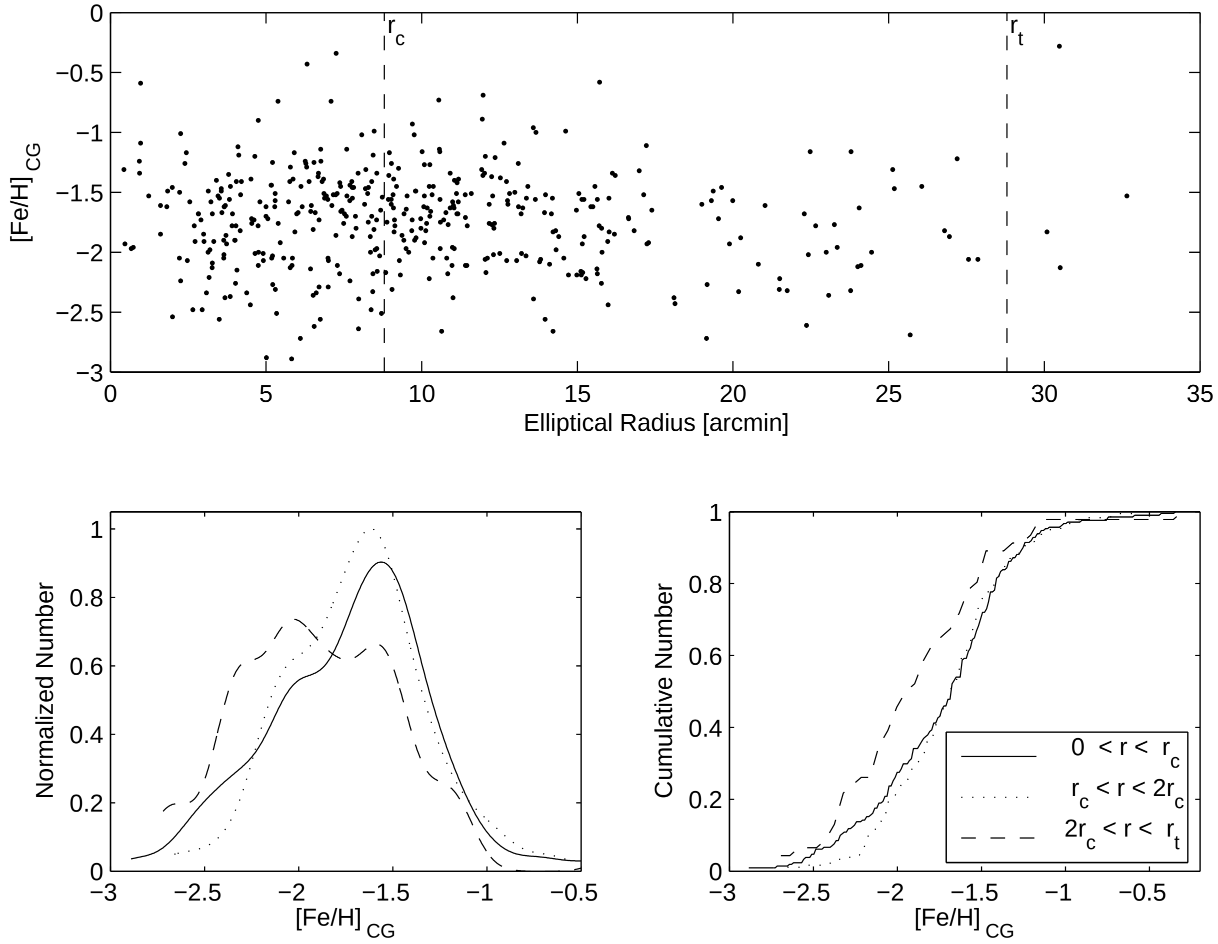

Figure 2.12: CaT metallicities of the 437 red giants versus their elliptical radius in Carina (top). Nominal core and tidal radii are also denoted. The bottom left panel shows MDFs for three regions at different radii. These density distributions were convolved by the individual measurement errors in [Fe/H]. A weak trend of the MDF to become more metal-poor when proceeding outwards is visible and also reflected in the cumulative distribution (bottom right).

than in the inner region and shows an increase of the potential secondary peak at ~ -2 dex. Considering the overall uncertainties in the metallicity measurements, a shift by, e.g., 0.1 dex may not appear significant. However, if we take into account that the uncertainties of the metallicity measurements should be the same everywhere in Carina and that there is no obvious reason why these uncertainties should introduce systematic offsets from one bin to another, these differences may be meaningful.

A K-S test revealed a probability of 98.2% that the MDF from the innermost ring is drawn from the same parent population as the entire sample. Based on the same statistical test, we cannot reject the hypothesis that also the middle annulus is drawn from the same population as the innermost annulus and the entire sample, respectively (at significances of 35% and 50%).

The MDF of the outermost region, on the other hand, shows several peaks, the broadest and most distinct of which is more metal-poor by $\sim$0.3 dex than that the one seen in the innermost region. In contrast, the location of a second peak at an [Fe/H] of -1.6 dex is consistent with the

MDFs' peaks in the inner parts of the galaxy to within the measurement uncertainties. Using a K-S test we find that the probability that the outer and inner MDFs are drawn from the same distribution is less than 4% and we can therefore reject this hypothesis. Moreover, the probability of the outer region being compatible with the entire sample is at the 6% level. Hence there do seem to be indications of spatial (and indeed radial) variations in Carina's stellar populations.

This gradient is also reflected in the cumulative metallicity distributions shown in the bottom right panel of Fig. 2.12. In a complementary manner, a cumulative plot of the giants' galactocentric radii clearly indicates a preferential central concentration of the metal-rich component (Fig. 2.13) compared to the more metal-poor population – a K-S yields a probability that the metal-poor and metal-rich populations take the same spatial distributions of 10%.

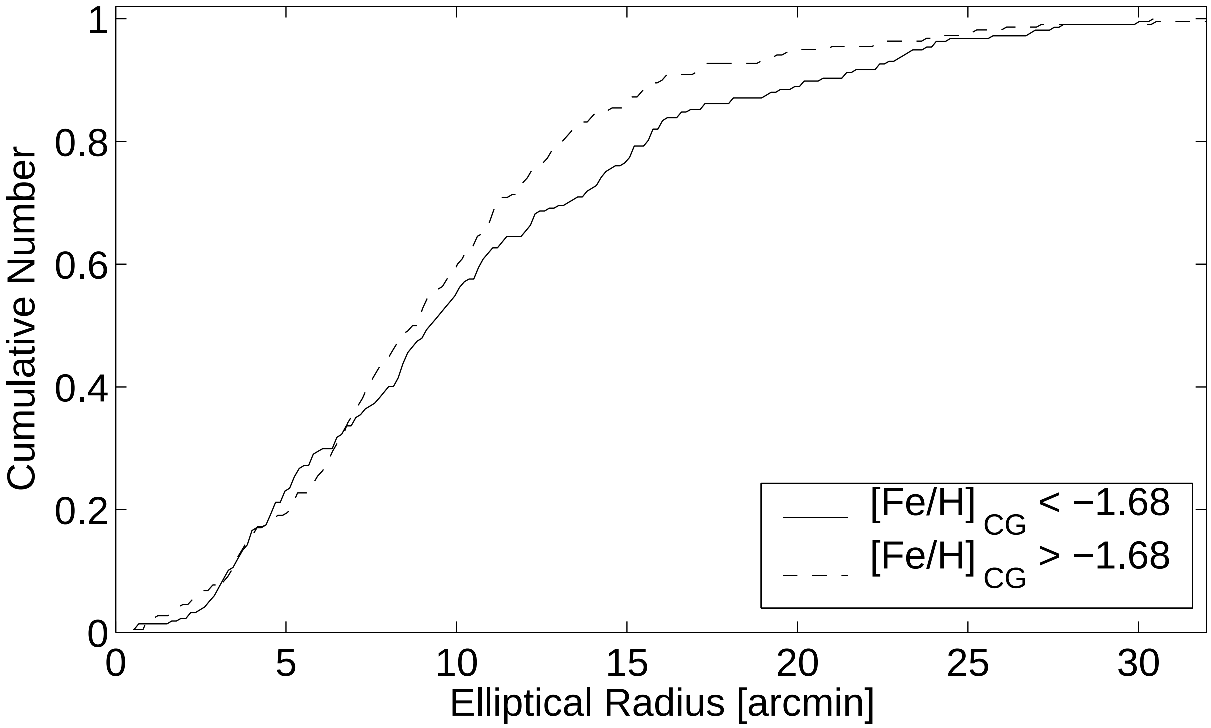

Figure 2.13: Cumulative number distributions for elliptical radii of the metal-poor population ([Fe/H]<-1.68, solid line) and the more metal-rich component (dashed line). The latter is more centrally concentrated.

The evidence of a concentration of the metal-rich component in Carina that we found is consistent with earlier findings that the intermediate-age stars favor the inner regions, in particular if one takes into consideration that we have likely underestimated their metallicity by ~ 0.1 dex due to the adoption of the old HB in the reduced CaT width. Thus, if the metal-rich component can be attributed to the intermediate-age population and, vice versa, the metal-poor RGB stars in Carina are to be identified as predominantly belonging to an old population, then the radial variations and progressive shifts of the peaks found in the spectroscopically determined MDFs underscore previous findings of centrally concentrated starbursts based on CMD analyses (Harbeck et al. 2001). A reason for such a concentration could be stronger cooling and dissipation of more metal-enriched gas. It may also indicate that star-forming material can be more easily retained at the center of a dSph's shallow potential well.

2.6 Ages

With the accurate metallicity measurements at hand, it is possible to additionally derive an age for each star based on its position in the CMD. For this purpose, we employed a set of Yonsei-Yale (Y^2; Yi et al. 2001) isochrones with no α-enhancement. Each star was assigned isochrones of its individual metallicity as derived above. As Fig. 2.14 implies, also the age-distribution exhibits several peaks.

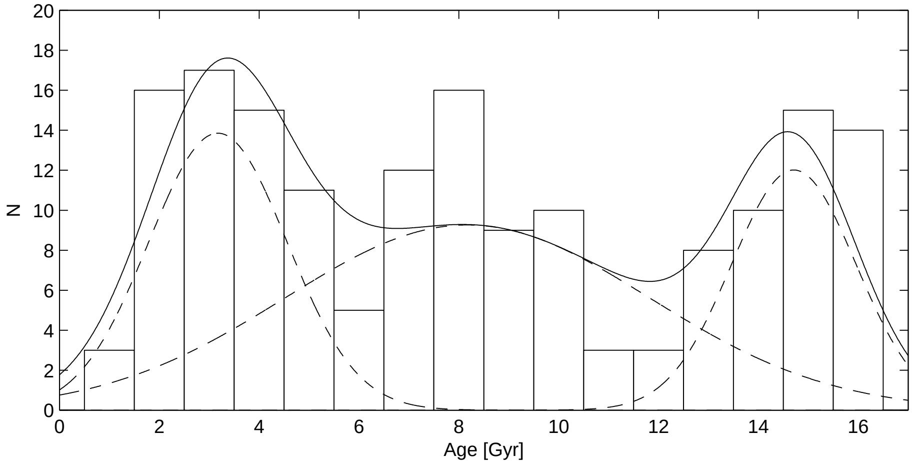

Figure 2.14: Age distribution from Y^2 isochrones. The dashed lines indicate the best KMM decomposition into three subpopulations and the solid line is the sum of the three curves.

A KMM-decomposition into single Gaussians reveals the presence of a young population at 2.5 Gyr (with 13% of all stars), a rather old population at approximately 15 Gyr (populated with 23%) and the major part (65 per cent) of the red giants belong to an intermediate-age population with ages around 7.8 Gyr. Such a decomposition into three components is preferred over the one component scenario at a confidence level compatible with 100%, whereas the likelihood of two and four (or more) peaks is ruled out at a similarly high significance. Both the young and old population appear to be rather narrow, with a formal width of 0.8 Gyr, whereas the dominant intermediate-age population spans a range of at least 3 Gyr. In this context, the age-distribution is consistent with Carina's SFH from photometric studies as it reveals the presence of several distinct populations, which possibly relate to its prominent SF episodes. Also the approximate location and widths of the populations from our data are comparable to those found from photometric studies and CMD modeling: According to Hurley-Keller et al. (1998), the majority of stars (∼50–60%) formed about 7 Gyr ago, while approximately 10–20% of Carina's stellar populations can be associated with old ages (15 Gyr) and the remaining ∼30% of SF occurred more recently, ∼3 Gyr ago. Other authors come up with comparable values (e.g., Smecker-Hane et al. 1994, 1996; Mighell 1997; Monelli et al. 2003; Rizzi et al. 2003), which differ in the exact peak of the SF episodes and their duration, but are still in compliance with the distribution from our data, if one considers the limited accuracy of our isochrone fits.

Moreover, we do not detect any apparent trend in our age distribution with radial distance. Such a radial population gradient has been photometrically reported to exist in Carina based on a central concentration of the prominent intermediate age population compared to the old HB stars (Harbeck et al. 2001; see also Section 2.5). We note, however, that the present age determinations should be taken with caution and may be hampered by large observational errors due to the limitations of the photometric accuracy of the data provided by the EIS (Nonino et al. 1999; P. Lynam [EIS-team] 2003, private communication).

2.7 Implications for chemical evolution

As the present-day observed MDF of a stellar system reflects its entire integrated history it is relatively insensitive to the star-formation history (SFH). The SFH cannot be unequivocally derived unless these data are combined with accurate ages (and preferably also individual elemental abundances to constrain the actual modes of star formation, see, e.g., Shetrone, Côté, & Sargent 2001). However, the gross properties of the MDF can provide insight into certain aspects of the chemical evolution of a system, such as the importance of gas flows. Following long-standing practice, we gain a basic insight by consideration of variants of the simple model of chemical evolution (e.g., Pagel 1997, Chapter 8) and refer the detailed stochastic modeling to a future paper (Wyse et al., in preparation).

In such basic models, the mean metallicity of long-lived stars at late stages (close to gas exhaustion) is representative of the true nucleosynthetic yield, p, if all metals are retained in the system. If the system is not closed and if outflows are possible, the mean metallicity reflects the 'effective yield", a combination of true yield and effects of loss of metals (see Hartwick 1976): outflows at a constant factor c times the star-formation rate reduce the mean metallicity below the true yield by approximately this factor c, $p_{\rm eff} \sim p/c$. Thus, assuming an invariant stellar initial mass function (and thus invariant true yield p), the low peak metallicity of our derived MDF, compared to say the G dwarfs in the solar neighborhood, which peaks at ~ -0.2 dex (e.g., Nordström et al. 2004 and references therein) suggests a strong influence of outflows, presumably driven by Type II supernovae. Indeed, this has been the basic model for the evolution of gas-poor dwarf galaxies since Sandage (1965).

2.7.1 Outflows

A modified simple model with flows overpredicts the number of metal-poor stars (leading to a "G-dwarf problem" just as in applications of this model to the solar neighborhood). Having normalized the fit of our models in Fig. 2.14 to the total number of stars observed, the discrepancies between the prediction and observations are marginal at -2.5 dex, but become significant below -2.7 dex, where the deviations progressively exceed the $2\,\sigma$-level. The fit may be improved by adopting some non-zero initial metallicity (or prompt initial enrichment (PIE), e.g., Tinsley 1975), understood in the present-day context as being from pre-galactic Population III stars. The predicted metallicity distributions for a simple model with outflows, and with PIE, are shown compared to the full Carina data set in Fig. 2.14.

The respective best-fit parameters to our data are $p_{eff} = 0.028\,Z_{\odot}$ for the simple model, and $p_{eff} = 0.029\,Z_{\odot}$ and $Z_{init} = 0.0013\,Z_{\odot}$ in the case of PIE. One should note that these models retain the instantaneous recycling approximation and so are not expected to provide a perfect fit to our iron-based MDF. Further, the radial variations discussed in Section 5 imply that the system is not in fact well-mixed at all times, another assumption inherent to the simple model. Given these caveats, the models provide an adequate fit. There are still some discrepancies present, such as the prominent main peak at $[\mathrm{Fe/H}]_{CG} \sim -1.7$ dex, which deviates by more than 2σ (taken as $\sqrt{N}$) from the model curves and a single Gaussian. Note, however that this peak is not distinct in the MDF on the ZW scale. As noted above, any potential substructure may reflect variations

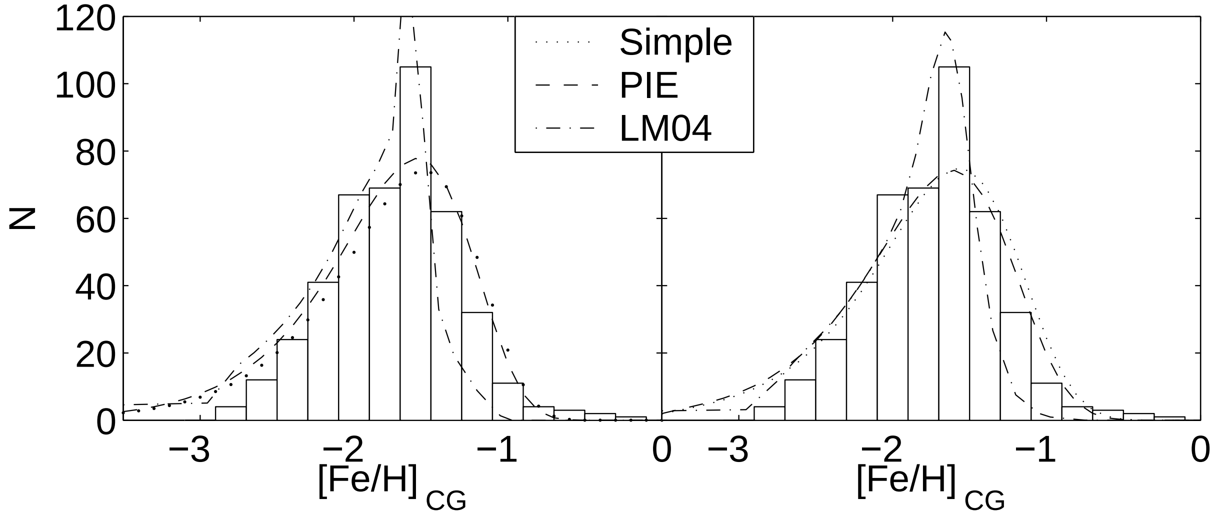

Figure 2.15: Fits of basic models (modified simple closed box with outflows and prompt initial enrichment (PIE)) overplotted on the frequency distribution of the observed metallicities, where the dash-dotted line refers to the predicted distribution for Carina from Lanfranchi & Matteucci (2004, LM04), scaled to match the total number of stars. The right panel is the analogous plot where the models were convolved by the observational errors.

in star formation activity. That such variations must have occurred is obvious from the presence of multiple main-sequence turn-offs and the decline in star formation activity in between. Indeed, not just outflows are implicated, but also inflows to sustain star formation over many Gyr (see, e.g., Silk, Wyse & Shields 1987, Lin & Murray 1998; Carigi, Hernandez & Gilmore 2002; Dong et al. 2003).

2.7.2 Infall and the gravitational potential

Mac Low & Ferrara (1999) investigated starburst-driven mass loss from dwarf galaxies. They distinguish between gas that is blown out but retained by the gravitational potential well of their host galaxy, and gas that is entirely blown away and lost from the galaxy. Lin & Murray (1998) and Dong et al. (2003) present a model for episodic star formation in dwarf galaxies like Carina according to which enriched gas is blown out but eventually re-accreted once it has cooled down sufficiently, leading to a new episode of star formation. Smecker-Hane et al. (1996) argued that episodic accretion of fresh gas seemed unlikely since the mass of Carina's dark halo seemed to be too low; also Carigi et al. (2002) note that in the case of external accretion the previously measured tidal radius (Irwin & Hatzidimitriou 1995) needs to be larger, i.e., the potential well needs to be deeper to permit the accretion of external gas.

Odenkirchen et al. (2001) demonstrated that tidal radii inferred from photographic data may underestimate the angular extent and nominal limiting radius of dwarf galaxies. For Carina we may expect a firmer limit on the dark matter halo from the analysis of its radial velocity dispersion profile (Wilkinson et al. 2006a). Here we note that our spectroscopic data indicate that four red giants whose radial velocities are consistent with membership in Carina lie beyond of its nominal limiting stellar radius (Fig. 2.11, top panel). Three of these stars have metallicities consistent with the trend seen in the outskirts of Carina. Claims suggesting the existence of "extratidal" stars around Carina have also been made by Kuhn, Smith, & Hawley (1996) and Majewski et al. (2000, 2005). Whether this implies that Carina is not in virial equilibrium and in the process of losing/having lost substantial amounts of mass as suggested in these studies is beyond the scope of the present Chapter. However, if Carina were a remnant of a once substantially more massive galaxy then the simple chemical models discussed here would need to be modified.

2.7.3 A model with outflows and infall

A more sophisticated model (Lanfranchi & Matteucci 2004) is also plotted in Fig. 2.14. This special model uses as input a SFH consistent with the CMD and hence incorporates two major epochs of outflows and respective winds associated with two main star formation episodes, each with a duration of 3 Gyr. The crucial model parameters were fit such as to reproduce Carina's total stellar mass, the gas content and observed [α/Fe] abundance ratio for five stars. The distribution resulting from this model holds strictly for the true elemental iron abundance as measured from high-resolution spectroscopy, rather than overall metallicity that we derived from our CaT measurements (but see the discussion in Sections 2.3 and 3.5). The Lanfranchi & Matteucci model for Carina shows one dominant metallicity peak, demonstrating the insensitivity of the resulting MDF to the details of the SFH, even for Fe. There is again acceptable agreement between this particular model (in a non-instantaneous recycling approximation) and our observations, particularly when observational uncertainties are included (right panel, Fig. 2.14). However, as before there are also remaining discrepancies, e.g., associated with the metal-rich and metal-poor tails (with a persisting G-dwarf problem).

The Carina model of Lanfranchi & Matteucci tries to reproduce individual element abundance measurements for five stars and has hence constraints only over the narrow metallicity range of these five stars. Lanfranchi & Matteucci's "best" model (see Fig. 2.14) requires a wind efficiency of some seven times the SFR and high star formation efficiency, leading to solar metallicities within only a few Gyr. This is at odds with our MDF in combination with the photometrically inferred ages of the different star formation episodes in Carina (e.g., Hurley-Keller et al. 1998; Monelli et al. 2003). Lanfranchi & Matteucci point out that their results also differ from the SFH derived by Tolstoy et al. (2003) on the basis of the five stars mentioned before. Adding more data points should aid in imposing stronger constraints.

The spatial variation of the SFH of the Carina dSph and other dSphs (e.g., Harbeck et al. 2001), plus evidence for cold sub-structures in dSphs (e.g., Kleyna et al. 2004; Wilkinson et al. 2004) suggest that star formation and chemical evolution should be modeled on small scales. We will present the details of such models in a future paper (Wyse et al., in preparation).

2.8 Summary and Discussion

Carina is the only dSph known to have undergone distinct, well-separated episodic star formation. The dominant episodes of star formation took place at intermediate ages. It is not yet understood what caused the repeated cessation and delayed re-start of star formation in this enigmatic dSph. In the framework of a VLT Large Programme aiming exploring the chemical evolution, kinematics, and dark matter content of Galactic dSphs, we have derived CaT metallicities for 437 red giants in the Galactic dSph Carina. Our spectroscopic sample exceeds the previously largest published data set (Smecker-Hane et al. 1999) by a factor of ~ 8. Our targets cover the entire surface area of Carina and allow us to investigate also radial metallicity variations.

While we are using Ca as a tracer of overall metallicity ("[Fe/H]"), we are well-aware of the different dependencies of [Fe/H] and [Ca/Fe] on the detailed star-formation history of a galaxy, and of possible differences between Ca and Fe abundances in globular clusters and dwarf galaxies. We compare our results to direct Fe measurements from the few existing high-resolution spectra in the literature and arrive at the same conclusions as previous authors: The widely used CaT method is indeed a powerful tool for efficient measurements of *overall* metallicities and for studies of overall trends in the metallicity distribution of intermediate-age and old populations in nearby galaxies as presented here. However, uncertainties in the metallicity measurements for *individual* red giants may amount to up to more than 0.2 dex when using the CaT method.

The resulting metallicity distribution function shows a wide range of metallicities spanning ~ 3.0 dex in [Fe/H]. The MDF peaks at a mean metallicity of -1.72 ± 0.01 dex (CG scale) or -1.90 ± 0.01 (ZW scale), respectively. Our mean metallicity on the CG scale is slightly more metal-rich as compared to earlier spectroscopic CaT studies (e.g., Smecker-Hane et al. 1999). The entire distribution's *formal* full width at half maximum is 0.92 dex. We proposed that some of this spread might be attributed to the occurrence of an extended SF and self-enrichment, resulting in several subpopulations with different peak metallicities. The question whether these subpopulations of different metallicities are manifestations of corresponding distinct episodes of SF requires a combination of deep photometric and spectroscopic data and detailed modeling and will not be pursued in this work. It is worth noticing, however, that also the age distribution that we derived from isochrone fits to each individual star appears to exhibit three distinct peaks, with younger, intermediate-age and old SF peaks. The MDF and its peaks change as one goes to larger distances from Carina's center. Generally, it shows a trend for more pronounced metal-poor subpopulations with increasing distance.

We found a higher concentration of metal-rich, presumably intermediate-age stars toward the inner regions of the galaxy as compared to more metal-poor stars. Metal-poor stars are, however, detected throughout the entire galaxy. This trend matches the observed central concentration of intermediate-age stars in Carina (Harbeck et al. 2001), supporting that the more metal-rich stars are also the younger ones. Another argument in support of an age-metallicity relation in Carina is the location of the more metal-rich stars on the RGB: Their metallicities in combination with their photometric colours are inconsistent with these stars belonging to the old population.

Our data thus confirm earlier suggestions that Carina shows an age-metallicity degeneracy in the sense that higher metallicities counteract the effects of younger ages. This conspiracy in turn leads to the observed narrow RGB. These findings and the considerable metallicity spread rule out scenarios in which Carina's unusual episodic star formation history was caused by the repeated accretion of pristine, unenriched gas.

Comparing our MDFs to simple chemical evolution models such as a closed-box model and prompt initial enrichment reveals a G-dwarf problem at low metallicities, but a fairly close approximation of the shape of the MDF at high metallicities. The metallicity peak of the MDF itself is not reproduced by these simple models. One should bear in mind that the peak is most prominent on the CG scale, but does not show up in the MDF based on the scale of ZW. The early star formation in Carina that can still be traced by present-day red giants must have occurred from pre-enriched gas (e.g., by Population III stars). A better match to the MDF can be obtained through more sophisticated models that include infall and outflows. The steep rise toward higher metallicities and its culmination in a prominent peak are qualitatively well reproduced by the models of Lanfranchi & Matteucci (2004), but the subsequent decline toward even higher metallicities is too rapid compared to our observationally derived MDF. Still, the qualitatively good overall agreement between these models and the observations is encouraging. One possible explanation for the repeated onset and cessation of the extended star formation episodes in Carina is the possible re-accretion of previously blown-out, but not blown-away, enriched gas (see, e.g., Lin & Murray 1998; Dong et al. 2003). The predicted time scales for blow-out, cooling, and re-accretion are consistent with the observed long pauses in star formation activity.

Refined chemical evolution models will be presented in a forthcoming paper (Wyse et al., in prep.), complemented by results from high-resolution spectroscopy and a new derivation of the star formation history of Carina that combines spectroscopic and photometric information. This will also lead to a quantitative age-metallicity relation. Furthermore, future work will investigate whether different subpopulations in Carina show different kinematics (Wilkinson et al. 2006a).

A handful of the red giants whose radial velocities make them likely Carina members lie beyond the nominal tidal radius of Carina. Spectroscopic evidence for potential "extratidal" stars has also been found by Majewski et al. (2000, 2005), raising the question whether Carina is a dark-matter-dominated, bound dSph with an even larger limiting radius than previously thought (see, e.g., Odenkirchen et al. 2001) or a disrupted remnant. Carina's orbit as inferred from its proper motion indicates that its perigalactic distance to the Milky Way is rather close (~ 20 kpc), suggesting that Carina needs to be strongly dark-matter dominated in order to have survived these passages (Piatek et al. 2003). The radial velocity dispersion profiles that will be derived as part of of our VLT Large Programme will help to elucidate the extent of Carina's dark matter halo (Wilkinson et al. 2006a).

In spite of its unusual star formation history, Carina fits in well with the metallicity-luminosity relation of other dSph galaxies. The metallicity-luminosity relation of dSphs is offset from that of dIrrs such that dSphs have higher mean stellar metallicities for a fixed optical luminosity. This offset suggests that star formation in young dSphs was more vigorous than in young dIrrs (Grebel et al. 2003). As is the case for other dSphs, Carina is thus unlikely to simply be a stripped former irregular galaxy. However, Piatek et al. suggest that Carina is currently near apogalacticon and that its pericentric passages bring it very close to the Milky Way, while its star formation history does not seem to be correlated with its orbital motion. Nonetheless, Carina's orbit would seem to suggest that in addition to intrinsic effects such as feedback, its evolution must also have been influenced by externally induced mass loss. Such mass loss may have been induced through tidal interactions with the Milky Way and/or through ram pressure stripping when passing through the denser regions of the Galaxy's gaseous halo. There appears to be a correlation between present-day Galactocentric distance and the fraction of intermediate-age populations (van den Bergh 1994; Grebel 1997, 1999). Carina with its distance of 94 kpc and its prominent intermediate-age population seems to fit into this correlation rather well. However, one may ask whether this is merely fortuitous for this galaxy, if one considers Carina's proposed short pericentric distance and the resulting eccentric orbit. Clearly, a comprehensive exploration of Carina's history will have to take into account both internal and external influences, its detailed chemical evolution, its age structure, its mass and mass distribution, its internal kinematics and its orbit.

Acknowledgments This Chapter resulted from a collaboration with Eva K. Grebel, Rosemary F.G. Wyse, Jan T. Kleyna, Mark Wilkinson, Gerry Gilmore, Daniel Harbeck and N. Wyn Evans. It has been published as *Koch et al. 2006, AJ, 131, 895* and the ages were published in *Koch et al. 2005, IAU Colloq. 198, 119.* I would like to thank Andrew Cole for providing me his version of the Equivalent Width code, Gustavo Lanfranchi for sending me his Carina models and Michael Odenkirchen for preparing parts of the fiber configurations.

Appendix 2.A
Target stars in Carina

Table 2.A: Derived properties of targeted stars in Carina. Only those stars, for which EWs could be determined are listed.

Star[7]	α	δ	r	V	B−V	Σ W	[Fe/H]	[Fe/H]	log p
	(J2000)		[']			[Å]	R97,ZW	R97,CG	
LG04a_000002	06 42 59	−51 00 06	15.4	19.50	0.86	3.82	−1.82± 0.16	−1.62± 0.16	−1.31
LG04a_000008	06 42 31	−50 59 59	10.6	18.55	1.13	3.99	−1.93± 0.09	−1.75± 0.09	−1.31
LG04a_000017	06 42 26	−50 59 43	9.6	19.71	0.94	2.69	−2.13± 0.39	−2.00± 0.39	−1.32
LG04a_000030	06 41 58	−50 59 32	4.8	17.93	1.27	4.79	−1.79± 0.10	−1.58± 0.10	−1.27
LG04a_000039	06 41 28	−50 59 16	2.0	19.73	0.99	5.63	−1.23± 0.12	−0.89± 0.12	−105.07
LG04a_000046	06 40 52	−50 59 12	7.4	19.56	0.83	2.29	−2.27± 0.20	−2.18± 0.20	−1.46
LG04a_000061	06 41 30	−50 58 54	1.4	19.14	1.06	4.84	−1.57± 0.16	−1.31± 0.16	−76.00
LG04a_000064	06 42 52	−50 58 48	13.4	19.86	0.84	4.07	−1.68± 0.33	−1.45± 0.33	−1.31
LG04a_000074	06 42 21	−50 58 28	7.9	17.67	1.18	6.58	−1.29± 0.15	−0.96± 0.15	−108.19
LG04a_000083	06 42 49	−50 58 15	12.7	19.79	1.00	4.64	−1.52± 0.16	−1.25± 0.16	−12.92
LG04a_000094	06 41 45	−50 58 05	1.4	18.47	1.05	4.57	−1.76± 0.13	−1.55± 0.13	−87.58
LG04a_000111	06 41 04	−50 57 41	5.8	19.57	0.83	2.63	−2.17± 0.47	−2.05± 0.47	−1.30
LG04a_000115	06 42 08	−50 57 32	5.2	19.70	0.90	2.61	−2.15± 0.11	−2.03± 0.11	−1.55
LG04a_000118	06 43 35	−50 57 23	20.4	17.55	1.50	3.43	−2.27± 0.09	−2.17± 0.09	−51.43
LG04a_000126	06 43 36	−50 57 14	20.5	18.01	1.51	4.00	−2.02± 0.34	−1.86± 0.34	−50.52
LG04a_000160	06 41 56	−50 56 51	3.3	19.29	0.92	3.16	−2.06± 0.10	−1.91± 0.10	−1.29
LG04a_000178	06 43 04	−50 56 24	14.7	18.68	1.00	5.52	−1.44± 0.10	−1.15± 0.10	−35.96
LG04a_000189	06 41 27	−50 56 05	3.6	18.84	1.02	4.05	−1.86± 0.21	−1.67± 0.21	−1.56
LG04a_000201	06 42 19	−50 55 49	7.0	19.22	0.93	2.83	−2.17± 0.12	−2.05± 0.12	−1.61
LG04a_000217	06 41 32	−50 55 27	3.9	18.86	0.89	5.15	−1.52± 0.33	−1.25± 0.33	−83.69
LG04a_000219	06 41 13	−50 55 26	6.3	19.93	0.85	4.54	−1.53± 0.30	−1.26± 0.30	−1.28
LG04a_000223	06 42 01	−50 55 21	4.8	19.58	0.99	2.76	−2.13± 0.38	−2.00± 0.38	−1.42
LG04a_000224	06 41 17	−50 55 15	5.8	19.07	0.96	0.67	−2.85± 0.12	−2.89± 0.12	−1.39
LG04a_000237	06 42 31	−50 54 42	9.2	19.13	0.87	4.08	−1.80± 0.13	−1.60± 0.13	−123.83
LG04a_000238	06 41 53	−50 54 43	4.6	19.70	0.91	3.41	−1.91± 0.15	−1.73± 0.15	−1.69
LG04a_000243	06 43 26	−50 54 33	18.1	19.42	0.94	1.84	−2.44± 0.38	−2.38± 0.38	−1.28
LG04a_000263	06 43 17	−50 54 04	16.7	19.89	0.82	4.48	−1.55± 0.16	−1.29± 0.16	−74.00
LG04a_000264	06 41 53	−50 54 06	5.3	19.99	0.83	3.41	−1.86± 0.21	−1.67± 0.21	−14.26
LG04a_000284	06 42 38	−50 53 38	10.6	18.79	1.09	4.37	−1.77± 0.09	−1.56± 0.09	−1.36
LG04a_000290	06 42 26	−50 53 29	9.0	18.01	1.21	3.62	−2.13± 0.08	−2.00± 0.08	−186.59
LG04a_000298	06 41 45	−50 53 23	6.2	18.53	0.92	5.15	−1.58± 0.35	−1.32± 0.35	−153.01
LG04a_000309	06 41 23	−50 53 16	7.7	19.71	1.01	2.05	−2.32± 0.40	−2.24± 0.40	−1.31
LG04a_000311	06 43 53	−50 53 07	22.7	19.82	0.72	3.22	−1.95± 0.17	−1.78± 0.17	−1.29
LG04a_000319	06 41 24	−50 53 04	7.9	19.41	0.85	4.40	−1.66± 0.17	−1.42± 0.17	−78.19
LG04a_000322	06 44 01	−50 52 45	24.0	19.29	0.85	5.69	−1.29± 0.11	−0.96± 0.11	−58.63
LG04a_000335	06 42 12	−50 52 25	8.4	19.86	0.89	1.33	−2.52± 0.36	−2.48± 0.36	−1.38

Continued on next page

Table 2.A – *Carina stars, continued*

Star[7]	α	δ	r	V	B−V	Σ W	[Fe/H]	[Fe/H]	log p
	(J2000)		[′]			[Å]	R97,ZW	R97,CG	
LG04a_000357	06 41 59	−50 51 43	8.6	19.33	1.00	3.62	−1.91± 0.10	−1.73± 0.10	−1.49
LG04a_000377	06 42 00	−50 51 13	9.2	17.78	1.36	5.21	−1.68± 0.10	−1.45± 0.10	−1.30
LG04a_000412	06 43 03	−50 50 11	15.7	20.11	0.68	3.05	−1.95± 0.16	−1.78± 0.16	−1.58
LG04a_000413	06 43 05	−50 50 10	16.0	18.76	1.22	4.49	−1.74± 0.12	−1.52± 0.12	−134.92
LG04a_000451	06 41 42	−50 48 44	12.8	18.46	1.10	4.68	−1.73± 0.13	−1.51± 0.13	−1.58
LG04a_000479	06 42 19	−50 48 02	13.8	19.51	0.99	2.59	−2.19± 0.32	−2.08± 0.32	−1.81
LG04a_000494	06 42 09	−50 47 43	13.9	18.32	1.24	5.29	−1.57± 0.10	−1.31± 0.10	−147.92
LG04a_000506	06 43 00	−50 47 18	17.6	19.51	0.82	5.65	−1.26± 0.11	−0.93± 0.11	−81.30
LG04a_000538	06 40 53	−50 46 06	20.5	18.74	0.91	4.79	−1.65± 0.10	−1.41± 0.10	−20.35
LG04a_000564	06 41 58	−50 45 22	17.1	19.10	1.12	5.26	−1.45± 0.14	−1.16± 0.14	−134.61
LG04a_000576	06 41 26	−50 44 50	19.2	19.37	0.98	5.14	−1.44± 0.14	−1.15± 0.14	−136.38
LG04a_000613	06 41 11	−50 43 26	22.4	17.42	1.44	5.41	−1.68± 0.09	−1.45± 0.09	−134.09
LG04a_000628	06 41 20	−50 42 56	22.3	18.88	0.98	5.25	−1.49± 0.11	−1.21± 0.11	−105.31
LG04a_000635	06 43 38	−50 42 32	25.5	17.96	1.28	5.28	−1.63± 0.10	−1.39± 0.10	−188.07
LG04a_000742	06 42 05	−50 38 39	26.3	18.54	1.00	5.54	−1.46± 0.13	−1.17± 0.13	−112.96
LG04a_000754	06 41 22	−50 38 07	29.0	18.34	1.14	4.06	−1.94± 0.10	−1.77± 0.10	−110.66
LG04a_000999	06 42 49	−51 00 04	13.8	18.89	1.16	5.08	−1.54± 0.13	−1.27± 0.13	−141.51
LG04a_001001	06 42 26	−51 00 04	9.8	19.01	1.09	5.01	−1.54± 0.15	−1.27± 0.15	−154.71
LG04a_001014	06 43 25	−50 59 51	19.7	19.36	0.83	5.49	−1.33± 0.13	−1.02± 0.13	−11.71
LG04a_001017	06 41 17	−50 59 56	3.7	19.64	0.83	2.91	−2.07± 0.20	−1.93± 0.20	−1.83
LG04a_001020	06 41 52	−50 59 54	4.4	18.75	1.12	5.45	−1.45± 0.12	−1.16± 0.12	−92.25
LG04a_001024	06 41 27	−50 59 52	2.7	18.13	1.43	5.82	−1.44± 0.12	−1.15± 0.12	−162.26
LG04a_001034	06 41 16	−50 59 48	3.8	17.75	1.36	5.50	−1.60± 0.09	−1.35± 0.09	−1.33
LG04a_001042	06 41 48	−50 59 44	3.6	18.11	1.15	4.93	−1.72± 0.10	−1.49± 0.10	−1.28
LG04a_001044	06 40 59	−50 59 45	6.2	17.68	1.59	5.38	−1.65± 0.26	−1.41± 0.26	−176.87
LG04a_001062	06 42 26	−50 59 36	9.4	19.36	1.05	3.73	−1.87± 0.12	−1.68± 0.12	−1.67
LG04a_001068	06 41 30	−50 59 35	2.3	20.05	0.85	1.86	−2.32± 0.44	−2.24± 0.44	−1.42
LG04a_001073	06 41 18	−50 59 33	3.3	18.95	1.13	5.85	−1.29± 0.11	−0.97± 0.11	−135.81
LG04a_001074	06 42 01	−50 59 31	5.4	19.91	0.83	5.93	−1.11± 0.31	−0.74± 0.31	−1.34
LG04a_001079	06 42 17	−50 59 28	7.9	18.47	0.98	5.77	−1.40± 0.13	−1.10± 0.13	−144.03
LG04a_001085	06 42 43	−50 59 20	12.3	19.63	0.91	3.27	−1.97± 0.23	−1.80± 0.23	−1.28
LG04a_001104	06 41 26	−50 59 16	2.2	19.48	0.98	2.68	−2.17± 0.13	−2.05± 0.13	−1.45
LG04a_001108	06 41 55	−50 59 14	4.1	19.66	0.79	5.06	−1.42± 0.21	−1.12± 0.21	−2.18
LG04a_001111	06 41 38	−50 59 13	1.8	19.34	0.98	3.91	−1.82± 0.18	−1.62± 0.18	−1.29
LG04a_001126	06 42 16	−50 59 04	7.4	19.06	1.14	3.98	−1.85± 0.10	−1.65± 0.10	−1.89
LG04a_001131	06 41 14	−50 59 06	3.8	19.88	0.88	1.61	−2.43± 0.27	−2.37± 0.27	−1.35
LG04a_001134	06 42 32	−50 59 03	10.2	19.71	0.88	5.03	−1.42± 0.14	−1.12± 0.14	−5.46
LG04a_001137	06 43 09	−50 58 59	16.5	19.40	0.79	5.12	−1.44± 0.11	−1.15± 0.11	−88.17
LG04a_001142	06 41 30	−50 59 02	1.6	18.96	0.97	3.50	−2.01± 0.11	−1.85± 0.11	−1.28
LG04a_001150	06 41 05	−50 59 01	5.3	19.56	0.90	3.91	−1.78± 0.13	−1.57± 0.13	−1.38
LG04a_001154	06 41 24	−50 58 59	2.2	19.64	0.90	4.06	−1.72± 0.20	−1.50± 0.20	−1.35
LG04a_001155	06 41 19	−50 58 58	2.9	19.49	0.92	1.53	−2.52± 0.44	−2.48± 0.44	−1.44
LG04a_001157	06 42 55	−50 58 53	14.0	18.47	0.95	4.70	−1.72± 0.10	−1.50± 0.10	−181.43
LG04a_001164	06 42 12	−50 58 52	6.6	19.88	0.88	3.47	−1.86± 2.10	−1.67± 2.10	−1.36
LG04a_001170	06 41 55	−50 58 47	3.7	18.44	1.15	4.40	−1.82± 0.10	−1.62± 0.10	−1.48
LG04a_001174	06 42 48	−50 58 43	12.8	18.68	1.04	4.32	−1.80± 0.09	−1.60± 0.09	−1.28
LG04a_001184	06 41 04	−50 58 42	5.5	18.76	0.93	4.94	−1.60± 0.28	−1.35± 0.28	−145.01
LG04a_001187	06 42 44	−50 58 37	12.1	19.33	0.90	2.44	−2.27± 0.15	−2.17± 0.15	−1.37
LG04a_001190	06 43 16	−50 58 33	17.6	17.81	1.06	5.04	−1.73± 0.09	−1.51± 0.09	−92.61
LG04a_001194	06 42 46	−50 58 33	12.3	19.82	0.72	3.27	−1.93± 0.14	−1.76± 0.14	−1.51
LG04a_001204	06 41 00	−50 58 32	6.2	19.35	0.96	3.90	−1.82± 0.13	−1.62± 0.13	−1.33
LG04a_001218	06 43 09	−50 58 21	16.2	19.67	0.93	3.11	−2.01± 0.14	−1.85± 0.14	−1.75
LG04a_001223	06 42 36	−50 58 21	10.5	18.16	1.02	5.00	−1.68± 0.09	−1.45± 0.09	−112.85

Continued on next page

Table 2.A – *Carina stars, continued*

Star[7]	α	δ	r	V	B−V	Σ W	[Fe/H]	[Fe/H]	log p
	(J2000)		[′]			[Å]	R97,ZW	R97,CG	
LG04a_001233	06 43 03	−50 58 17	15.2	18.33	1.16	3.00	−2.27± 0.07	−2.17± 0.07	−1.30
LG04a_001234	06 40 52	−50 58 22	7.7	19.10	1.04	4.52	−1.67± 0.19	−1.44± 0.19	−1.51
LG04a_001243	06 42 45	−50 58 15	12.0	19.83	0.94	4.75	−1.48± 0.17	−1.20± 0.17	−1.30
LG04a_001263	06 41 59	−50 58 08	4.0	18.15	1.15	3.92	−2.02± 0.08	−1.86± 0.08	−165.50
LG04a_001275	06 42 41	−50 58 02	11.1	19.48	0.94	4.36	−1.66± 0.11	−1.42± 0.11	−1.32
LG04a_001276	06 41 31	−50 58 05	1.0	19.84	0.92	5.04	−1.39± 0.19	−1.09± 0.19	−1.37
LG04a_001279	06 41 56	−50 58 03	3.5	19.61	0.91	3.99	−1.75± 0.24	−1.53± 0.24	−1.32
LG04a_001288	06 41 51	−50 58 00	2.5	19.87	0.73	3.72	−1.79± 0.17	−1.58± 0.17	−66.22
LG04a_001289	06 41 45	−50 58 00	1.4	19.35	1.02	5.73	−1.26± 0.29	−0.93± 0.29	−142.57
LG04a_001298	06 41 18	−50 57 57	3.3	18.87	0.96	2.91	−2.20± 0.18	−2.09± 0.18	−1.44
LG04a_001313	06 41 04	−50 57 50	5.8	18.55	1.23	2.98	−2.23± 0.14	−2.13± 0.14	−1.41
LG04a_001325	06 41 41	−50 57 40	0.7	19.95	0.84	2.66	−2.10± 0.15	−1.96± 0.15	−1.82
LG04a_001327	06 41 37	−50 57 39	0.4	19.75	0.84	4.50	−1.57± 0.17	−1.31± 0.17	−1.37
LG04a_001330	06 41 38	−50 57 37	0.5	19.15	0.82	3.18	−2.07± 0.11	−1.93± 0.11	−1.32
LG04a_001341	06 40 49	−50 57 34	8.6	19.07	0.91	3.12	−2.10± 0.14	−1.97± 0.14	−1.48
LG04a_001346	06 41 59	−50 57 32	3.7	19.79	0.89	3.68	−1.81± 0.22	−1.61± 0.22	−1.84
LG04a_001349	06 41 27	−50 57 31	2.0	19.86	0.97	1.17	−2.57± 0.48	−2.54± 0.48	−1.37
LG04a_001353	06 40 59	−50 57 30	6.7	19.58	0.81	3.88	−1.79± 0.09	−1.58± 0.09	−180.08
LG04a_001359	06 42 40	−50 57 24	10.8	19.68	1.01	2.23	−2.27± 0.16	−2.18± 0.16	−1.34
LG04a_001364	06 41 20	−50 57 25	3.3	17.96	1.25	4.50	−1.87± 0.10	−1.68± 0.10	−1.32
LG04a_001365	06 43 59	−50 57 15	24.5	19.63	0.78	3.99	−1.75± 0.11	−1.53± 0.11	−47.52
LG04a_001367	06 43 04	−50 57 18	14.9	19.49	0.90	5.50	−1.31± 0.11	−0.99± 0.11	−95.55
LG04a_001371	06 42 07	−50 57 21	5.1	19.81	0.95	3.38	−1.90± 0.15	−1.72± 0.15	−1.29
LG04a_001372	06 41 44	−50 57 22	1.2	19.65	0.91	3.97	−1.75± 0.13	−1.53± 0.13	−1.28
LG04a_001379	06 41 18	−50 57 20	3.6	18.24	1.19	3.36	−2.17± 0.08	−2.05± 0.08	−1.56
LG04a_001386	06 41 58	−50 57 15	3.5	17.88	1.25	4.90	−1.76± 0.09	−1.55± 0.09	−1.58
LG04a_001389	06 42 36	−50 57 12	10.1	18.06	1.29	4.85	−1.75± 0.09	−1.53± 0.09	−1.32
LG04a_001390	06 42 12	−50 57 13	5.9	19.86	0.89	4.23	−1.63± 0.13	−1.39± 0.13	−1.33
LG04a_001391	06 42 11	−50 57 13	5.8	18.12	1.12	5.14	−1.65± 0.10	−1.41± 0.10	−1.75
LG04a_001393	06 42 18	−50 57 12	6.9	19.16	0.98	4.30	−1.73± 0.23	−1.51± 0.23	−1.28
LG04a_001396	06 41 48	−50 57 13	2.0	19.51	1.01	4.23	−1.69± 0.13	−1.46± 0.13	−1.28
LG04a_001403	06 42 33	−50 57 06	9.4	19.71	0.91	2.96	−2.05± 0.14	−1.90± 0.14	−1.33
LG04a_001404	06 42 56	−50 57 05	13.4	19.32	1.05	4.58	−1.62± 0.14	−1.37± 0.14	−134.16
LG04a_001409	06 41 19	−50 57 06	3.6	19.67	0.85	2.98	−2.05± 0.14	−1.90± 0.14	−1.28
LG04a_001410	06 41 46	−50 57 04	1.8	19.62	1.09	5.85	−1.18± 0.11	−0.83± 0.11	−160.17
LG04a_001413	06 42 36	−50 57 01	10.0	19.60	1.00	4.99	−1.45± 0.12	−1.16± 0.12	−2.07
LG04a_001414	06 41 28	−50 57 04	2.2	17.95	1.53	5.47	−1.58± 0.10	−1.32± 0.10	−141.45
LG04a_001416	06 43 09	−50 56 58	15.6	20.08	0.94	2.01	−2.27± 0.26	−2.18± 0.26	−1.51
LG04a_001418	06 41 45	−50 57 02	1.6	20.01	0.88	3.56	−1.81± 0.19	−1.61± 0.19	−1.30
LG04a_001419	06 41 55	−50 57 01	3.0	17.59	1.44	4.26	−2.00± 0.08	−1.84± 0.08	−1.54
LG04a_001423	06 40 56	−50 57 01	7.6	18.45	1.06	4.66	−1.74± 0.11	−1.52± 0.11	−84.87
LG04a_001426	06 41 53	−50 56 57	2.8	19.04	0.94	3.91	−1.87± 0.11	−1.68± 0.11	−1.38
LG04a_001427	06 41 10	−50 56 58	5.2	19.49	0.90	2.09	−2.35± 0.14	−2.27± 0.14	−1.39
LG04a_001432	06 42 16	−50 56 54	6.5	19.66	0.94	4.71	−1.52± 0.15	−1.25± 0.15	−1.50
LG04a_001437	06 40 53	−50 56 53	8.2	19.62	0.91	4.58	−1.57± 0.25	−1.31± 0.25	−1.57
LG04a_001449	06 41 55	−50 56 46	3.2	19.71	0.85	5.43	−1.29± 0.13	−0.97± 0.13	−157.49
LG04a_001458	06 40 54	−50 56 44	8.1	20.05	0.98	5.11	−1.33± 0.29	−1.02± 0.29	−1.82
LG04a_001486	06 41 52	−50 56 23	2.9	19.55	0.91	3.50	−1.91± 0.14	−1.73± 0.14	−2.02
LG04a_001487	06 42 03	−50 56 22	4.5	19.23	0.96	4.58	−1.63± 0.10	−1.39± 0.10	−1.29
LG04a_001489	06 42 15	−50 56 21	6.3	20.09	0.88	6.66	−0.86± 0.31	−0.43± 0.31	−1.30
LG04a_001495	06 42 32	−50 56 17	9.1	19.51	1.03	3.25	−1.99± 0.14	−1.83± 0.14	−72.30
LG04a_001498	06 42 05	−50 56 17	4.7	20.02	0.90	5.44	−1.24± 0.16	−0.90± 0.16	−1.31
LG04a_001501	06 40 49	−50 56 17	9.4	20.04	0.81	2.88	−2.02± 0.67	−1.86± 0.67	−2.43

Continued on next page

Table 2.A – *Carina stars, continued*

Star[7]	α	δ	r	V	B−V	Σ W	[Fe/H]	[Fe/H]	log p
	(J2000)		[′]			[Å]	R97,ZW	R97,CG	
LG04a_001505	06 42 24	−50 56 12	7.9	18.45	1.18	4.18	−1.89± 0.09	−1.70± 0.09	−1.28
LG04a_001507	06 40 52	−50 56 13	8.9	19.02	1.01	3.73	−1.93± 0.11	−1.75± 0.11	−1.32
LG04a_001512	06 41 50	−50 56 11	2.8	18.49	1.12	4.21	−1.87± 0.09	−1.68± 0.09	−1.28
LG04a_001521	06 42 00	−50 56 08	4.2	19.31	0.99	3.39	−1.98± 0.11	−1.82± 0.11	−1.28
LG04a_001524	06 41 23	−50 56 08	4.0	19.39	0.88	3.13	−2.05± 0.15	−1.90± 0.15	−1.30
LG04a_001527	06 41 29	−50 56 07	3.3	20.20	0.89	2.07	−2.23± 0.22	−2.13± 0.22	−1.42
LG04a_001531	06 43 43	−50 55 58	21.3	20.12	0.82	5.21	−1.29± 0.11	−0.97± 0.11	−28.62
LG04a_001534	06 41 45	−50 56 04	2.6	19.13	1.00	1.73	−2.52± 0.10	−2.48± 0.10	−1.61
LG04a_001535	06 41 45	−50 56 02	2.7	19.59	0.88	3.34	−1.95± 0.21	−1.78± 0.21	−1.90
LG04a_001536	06 42 39	−50 56 00	10.3	18.44	1.22	4.19	−1.89± 0.11	−1.70± 0.11	−1.35
LG04a_001538	06 41 17	−50 56 03	5.0	19.44	1.02	3.63	−1.89± 0.25	−1.70± 0.25	−1.28
LG04a_001542	06 41 24	−50 56 01	4.0	19.55	0.93	3.36	−1.95± 0.14	−1.78± 0.14	−1.30
LG04a_001543	06 42 21	−50 55 59	7.3	19.77	0.96	2.36	−2.22± 0.19	−2.11± 0.19	−1.34
LG04a_001556	06 42 17	−50 55 55	6.8	17.82	1.31	5.30	−1.65± 0.10	−1.41± 0.10	−1.28
LG04a_001558	06 41 55	−50 55 55	3.7	18.43	1.04	4.40	−1.82± 0.13	−1.62± 0.13	−1.32
LG04a_001569	06 43 54	−50 55 39	23.1	20.10	1.03	3.19	−1.91± 0.08	−1.73± 0.08	−76.05
LG04a_001572	06 41 56	−50 55 46	3.8	18.21	1.33	6.31	−1.28± 0.12	−0.95± 0.12	−159.39
LG04a_001577	06 41 52	−50 55 43	3.5	20.01	0.88	1.03	−2.58± 0.20	−2.56± 0.20	−1.84
LG04a_001578	06 41 26	−50 55 44	4.1	17.59	1.39	6.01	−1.47± 0.10	−1.19± 0.10	−1.71
LG04a_001583	06 40 48	−50 55 42	9.9	19.04	0.90	3.54	−1.98± 0.16	−1.82± 0.16	−162.71
LG04a_001586	06 40 53	−50 55 42	9.1	19.61	0.86	3.33	−1.95± 0.13	−1.78± 0.13	−1.28
LG04a_001592	06 41 42	−50 55 37	3.2	20.10	0.88	1.92	−2.30± 0.95	−2.21± 0.95	−2.35
LG04a_001600	06 42 35	−50 55 31	9.7	19.65	0.98	3.44	−1.91± 0.10	−1.73± 0.10	−1.29
LG04a_001607	06 42 44	−50 55 27	11.2	18.49	1.06	4.40	−1.81± 0.13	−1.61± 0.13	−182.68
LG04a_001608	06 41 02	−50 55 29	7.9	18.47	1.03	3.90	−1.97± 0.11	−1.80± 0.11	−1.63
LG04a_001615	06 43 01	−50 55 22	13.9	18.76	0.90	6.04	−1.27± 0.11	−0.94± 0.11	−59.22
LG04a_001632	06 41 54	−50 55 19	4.0	19.99	0.88	1.84	−2.34± 0.11	−2.26± 0.11	−1.30
LG04a_001653	06 43 56	−50 55 04	23.3	18.02	1.10	4.23	−1.94± 0.09	−1.77± 0.09	−193.69
LG04a_001672	06 41 24	−50 55 03	5.3	20.07	0.90	3.50	−1.82± 0.20	−1.62± 0.20	−1.51
LG04a_001673	06 41 48	−50 55 01	4.0	17.61	1.39	5.42	−1.65± 0.09	−1.41± 0.09	−1.28
LG04a_001688	06 42 46	−50 54 52	11.5	19.25	0.90	3.02	−2.10± 0.17	−1.97± 0.17	−39.55
LG04a_001692	06 43 59	−50 54 44	23.8	20.10	0.99	1.62	−2.39± 0.22	−2.32± 0.22	−1.42
LG04a_001695	06 44 03	−50 54 42	24.4	19.04	1.05	4.95	−1.55± 0.14	−1.29± 0.14	−91.77
LG04a_001696	06 41 16	−50 54 52	6.5	19.76	0.91	3.70	−1.81± 0.19	−1.61± 0.19	−1.41
LG04a_001700	06 43 35	−50 54 42	19.7	19.35	0.98	5.04	−1.47± 0.13	−1.19± 0.13	−15.69
LG04a_001703	06 41 15	−50 54 46	6.8	20.09	0.83	4.77	−1.43± 0.47	−1.14± 0.47	−1.34
LG04a_001730	06 41 48	−50 54 34	4.6	19.45	0.96	4.96	−1.48± 0.22	−1.20± 0.22	−1.28
LG04a_001734	06 41 39	−50 54 33	4.7	18.26	1.14	4.07	−1.95± 0.11	−1.78± 0.11	−1.31
LG04a_001738	06 42 51	−50 54 26	12.4	19.85	1.03	4.72	−1.49± 0.20	−1.21± 0.20	−1.28
LG04a_001742	06 41 32	−50 54 28	5.3	19.72	0.79	1.86	−2.38± 0.34	−2.31± 0.34	−2.22
LG04a_001744	06 42 00	−50 54 25	5.5	19.90	0.73	2.80	−2.06± 0.25	−1.92± 0.25	−1.76
LG04a_001771	06 42 51	−50 54 07	12.5	19.07	1.10	5.57	−1.36± 0.14	−1.05± 0.14	−138.68
LG04a_001776	06 42 36	−50 54 03	10.2	19.24	1.08	4.83	−1.55± 0.11	−1.29± 0.11	−126.06
LG04a_001779	06 41 24	−50 54 05	6.5	20.01	0.80	0.87	−2.63± 0.13	−2.62± 0.13	−1.29
LG04a_001783	06 42 18	−50 53 58	7.7	19.88	1.02	3.74	−1.78± 0.17	−1.57± 0.17	−1.33
LG04a_001784	06 41 48	−50 53 59	5.4	18.49	0.94	5.12	−1.59± 0.11	−1.34± 0.11	−122.12
LG04a_001817	06 43 16	−50 53 33	16.5	20.07	0.91	4.59	−1.49± 0.12	−1.21± 0.12	−151.06
LG04a_001820	06 44 00	−50 53 28	23.8	19.91	1.02	4.82	−1.45± 0.14	−1.16± 0.14	−2.50
LG04a_001822	06 41 45	−50 53 36	5.9	20.03	0.90	4.72	−1.46± 0.35	−1.17± 0.35	−1.76
LG04a_001827	06 43 19	−50 53 29	17.0	19.97	0.77	4.17	−1.63± 0.18	−1.39± 0.18	−17.21
LG04a_001838	06 44 05	−50 53 20	24.7	18.03	1.01	5.24	−1.63± 0.09	−1.39± 0.09	−118.34
LG04a_001843	06 41 05	−50 53 29	9.5	19.02	1.06	4.32	−1.75± 0.10	−1.53± 0.10	−1.29
LG04a_001875	06 41 18	−50 53 11	8.4	18.90	1.09	3.13	−2.13± 0.12	−2.00± 0.12	−1.39

Continued on next page

Table 2.A – *Carina stars, continued*

Star[7]	α	δ	r	V	B−V	Σ W	[Fe/H]	[Fe/H]	log p
	(J2000)		[']			[Å]	R97,ZW	R97,CG	
LG04a_001879	06 42 40	−50 53 06	11.1	19.40	0.86	4.46	−1.64± 0.11	−1.40± 0.11	−1.28
LG04a_001889	06 42 04	−50 53 03	7.2	19.34	1.01	4.17	−1.74± 0.11	−1.52± 0.11	−1.28
LG04a_001891	06 41 20	−50 53 02	8.3	19.05	1.18	4.09	−1.81± 0.10	−1.61± 0.10	−49.62
LG04a_001894	06 41 29	−50 53 01	7.6	19.88	0.91	3.39	−1.89± 0.72	−1.70± 0.72	−1.37
LG04a_001899	06 41 06	−50 52 59	10.1	19.23	0.88	3.17	−2.06± 0.12	−1.92± 0.12	−1.29
LG04a_001907	06 41 00	−50 52 54	10.9	17.73	1.15	4.79	−1.82± 0.11	−1.62± 0.11	−185.90
LG04a_001909	06 42 41	−50 52 50	11.3	19.00	0.86	4.76	−1.62± 0.11	−1.37± 0.11	−112.85
LG04a_001910	06 41 55	−50 52 51	7.0	18.60	0.98	4.47	−1.77± 0.14	−1.56± 0.14	−1.70
LG04a_001917	06 41 25	−50 52 48	8.2	18.74	1.05	4.29	−1.80± 0.12	−1.60± 0.12	−1.33
LG04a_001928	06 41 03	−50 52 43	10.8	19.49	1.11	5.37	−1.35± 0.11	−1.04± 0.11	−112.05
LG04a_001940	06 43 36	−50 52 27	19.9	19.57	1.03	5.16	−1.40± 0.20	−1.10± 0.20	−104.23
LG04a_001950	06 42 36	−50 52 27	10.9	19.88	0.88	3.58	−1.83± 0.37	−1.63± 0.37	−2.16
LG04a_001961	06 42 11	−50 52 20	8.4	18.44	1.15	4.19	−1.89± 0.09	−1.70± 0.09	−1.42
LG04a_001977	06 42 26	−50 52 12	9.9	18.90	1.06	5.02	−1.55± 0.14	−1.29± 0.14	−127.25
LG04a_001989	06 42 56	−50 52 03	13.8	19.35	0.87	5.79	−1.25± 0.13	−0.91± 0.13	−121.73
LG04a_001990	06 41 55	−50 52 05	8.0	20.14	0.89	1.41	−2.45± 0.18	−2.39± 0.18	−2.54
LG04a_002017	06 41 00	−50 51 45	12.3	18.34	1.14	4.69	−1.75± 0.09	−1.53± 0.09	−1.60
LG04a_002018	06 43 04	−50 51 38	15.1	19.86	1.01	2.10	−2.28± 0.12	−2.19± 0.12	−1.85
LG04a_002021	06 42 59	−50 51 36	14.5	18.63	1.03	4.69	−1.70± 0.11	−1.47± 0.11	−79.44
LG04a_002023	06 43 19	−50 51 31	17.5	19.60	0.93	5.97	−1.15± 0.13	−0.79± 0.13	−90.63
LG04a_002031	06 42 49	−50 51 24	13.2	20.00	0.79	3.51	−1.83± 0.16	−1.63± 0.16	−1.30
LG04a_002032	06 41 49	−50 51 27	8.8	19.19	0.87	33.70	7.23± 0.59	9.54± 0.59	−22.19
LG04a_002038	06 41 46	−50 51 24	9.0	19.53	0.89	5.00	−1.46± 0.14	−1.17± 0.14	−1.75
LG04a_002045	06 42 59	−50 51 16	14.6	20.11	0.91	5.15	−1.31± 0.15	−0.99± 0.15	−1.39
LG04a_002051	06 42 33	−50 51 15	11.5	19.51	0.87	5.57	−1.29± 0.13	−0.96± 0.13	−120.76
LG04a_002065	06 41 15	−50 51 10	11.4	17.62	1.33	5.12	−1.74± 0.10	−1.52± 0.10	−1.33
LG04a_002067	06 41 59	−50 51 07	9.3	20.02	0.82	2.01	−2.28± 0.26	−2.19± 0.26	−1.47
LG04a_002080	06 42 39	−50 50 56	12.3	19.66	0.82	4.69	−1.53± 0.14	−1.26± 0.14	−62.41
LG04a_002087	06 42 51	−50 50 51	13.9	18.45	1.21	4.53	−1.78± 0.09	−1.57± 0.09	−111.07
LG04a_002107	06 42 22	−50 50 43	10.9	19.61	0.99	4.50	−1.59± 0.25	−1.34± 0.25	−1.29
LG04a_002110	06 43 41	−50 50 35	21.0	19.66	1.01	5.70	−1.22± 0.16	−0.88± 0.16	−18.08
LG04a_002126	06 41 00	−50 50 36	13.8	19.82	0.77	2.47	−2.18± 0.12	−2.06± 0.12	−1.31
LG04a_002129	06 42 14	−50 50 33	10.6	19.54	1.02	5.07	−1.43± 0.13	−1.14± 0.13	−1.28
LG04a_002144	06 41 41	−50 50 22	10.6	19.55	0.83	4.72	−1.54± 0.13	−1.27± 0.13	−16.13
LG04a_002156	06 42 21	−50 50 12	11.4	19.25	1.04	4.38	−1.69± 0.13	−1.46± 0.13	−157.28
LG04a_002163	06 43 01	−50 50 06	15.5	19.31	0.92	4.72	−1.58± 0.14	−1.32± 0.14	−44.26
LG04a_002169	06 41 37	−50 50 07	11.1	17.91	1.24	4.98	−1.73± 0.10	−1.51± 0.10	−2.01
LG04a_002181	06 41 40	−50 49 59	11.2	17.62	1.42	5.46	−1.63± 0.10	−1.39± 0.10	−1.47
LG04a_002189	06 43 27	−50 49 48	19.2	18.71	1.07	2.52	−2.35± 0.08	−2.27± 0.08	−2.29
LG04a_002192	06 42 24	−50 49 52	12.0	20.13	0.81	4.16	−1.61± 0.25	−1.36± 0.25	−1.92
LG04a_002208	06 43 04	−50 49 37	16.2	19.29	1.02	4.63	−1.61± 0.17	−1.36± 0.17	−1.46
LG04a_002210	06 40 58	−50 49 40	15.2	19.44	0.98	5.40	−1.35± 0.12	−1.04± 0.12	−90.99
LG04a_002212	06 43 38	−50 49 31	20.9	17.93	1.27	5.35	−1.62± 0.09	−1.37± 0.09	−72.25
LG04a_002213	06 43 39	−50 49 30	21.0	18.98	1.01	4.13	−1.81± 0.11	−1.61± 0.11	−1.31
LG04a_002217	06 42 17	−50 49 30	12.0	20.00	0.70	6.02	−1.07± 0.31	−0.69± 0.31	−1.53
LG04a_002244	06 41 08	−50 49 14	14.7	20.10	0.80	1.97	−2.28± 0.26	−2.19± 0.26	−1.47
LG04a_002255	06 41 38	−50 49 03	12.6	18.81	1.14	5.55	−1.41± 0.28	−1.11± 0.28	−131.52
LG04a_002264	06 42 56	−50 48 51	15.8	18.40	1.10	5.01	−1.64± 0.15	−1.40± 0.15	−101.24
LG04a_002265	06 41 45	−50 48 53	12.5	18.29	1.12	3.44	−2.14± 0.09	−2.01± 0.09	−1.48
LG04a_002278	06 42 49	−50 48 43	15.2	18.00	1.29	6.16	−1.36± 0.20	−1.05± 0.20	−156.63
LG04a_002309	06 42 24	−50 48 27	13.5	19.99	0.91	3.84	−1.73± 0.17	−1.51± 0.17	−5.86
LG04a_002311	06 41 46	−50 48 26	13.1	19.36	0.89	4.85	−1.53± 0.17	−1.26± 0.17	−2.02
LG04a_002317	06 41 54	−50 48 24	13.0	19.85	0.83	3.94	−1.72± 0.19	−1.50± 0.19	−1.28

Continued on next page

Table 2.A – *Carina stars, continued*

Star[7]	α	δ	r	V	B−V	Σ W	[Fe/H]	[Fe/H]	log p
	(J2000)		[']			[Å]	R97,ZW	R97,CG	
LG04a_002318	06 41 53	−50 48 23	13.0	18.41	1.12	5.30	−1.55± 0.10	−1.29± 0.10	−192.89
LG04a_002332	06 41 37	−50 48 14	13.8	19.86	0.81	4.97	−1.41± 0.13	−1.11± 0.13	−72.55
LG04a_002335	06 41 30	−50 48 13	14.2	19.11	0.87	3.47	−1.99± 0.11	−1.83± 0.11	−1.30
LG04a_002361	06 43 46	−50 47 49	22.9	17.70	1.36	5.66	−1.56± 0.10	−1.30± 0.10	−176.26
LG04a_002372	06 42 21	−50 47 45	14.2	20.08	0.94	3.68	−1.76± 0.18	−1.55± 0.18	−1.61
LG04a_002382	06 42 42	−50 47 41	15.5	19.13	0.85	4.68	−1.62± 0.11	−1.37± 0.11	−4.05
LG04a_002399	06 41 54	−50 47 26	14.3	19.64	0.88	2.78	−2.11± 0.31	−1.98± 0.31	−1.34
LG04a_002431	06 43 39	−50 46 57	22.4	17.35	1.68	5.14	−1.78± 0.10	−1.57± 0.10	−135.88
LG04a_002456	06 42 43	−50 46 43	16.6	19.96	0.88	3.32	−1.89± 0.21	−1.71± 0.21	−1.33
LG04a_002459	06 42 31	−50 46 42	15.9	19.15	1.15	4.57	−1.65± 0.10	−1.41± 0.10	−154.86
LG04a_002466	06 43 17	−50 46 33	20.0	18.80	0.89	4.33	−1.78± 0.10	−1.57± 0.10	−2.50
LG04a_002474	06 41 48	−50 46 32	15.7	19.36	0.93	6.66	−0.98± 0.17	−0.58± 0.17	−1.30
LG04a_002478	06 43 42	−50 46 23	23.0	18.79	0.98	4.39	−1.76± 0.17	−1.55± 0.17	−146.32
LG04a_002481	06 42 57	−50 46 25	18.1	18.21	1.07	5.19	−1.62± 0.15	−1.37± 0.15	−45.95
LG04a_002491	06 43 13	−50 46 18	19.7	19.57	0.80	4.92	−1.47± 0.10	−1.19± 0.10	−71.87
LG04a_002498	06 41 47	−50 46 18	16.1	18.08	1.05	5.18	−1.64± 0.10	−1.40± 0.10	−141.60
LG04a_002501	06 43 40	−50 46 09	22.9	20.13	0.92	2.30	−2.18± 0.25	−2.06± 0.25	−61.31
LG04a_002521	06 41 04	−50 46 04	19.4	19.23	0.82	4.31	−1.72± 0.11	−1.49± 0.11	−3.05
LG04a_002523	06 43 48	−50 45 55	24.1	19.50	0.86	3.79	−1.83± 0.10	−1.63± 0.10	−1.48
LG04a_002537	06 43 08	−50 45 53	19.5	19.44	0.90	3.58	−1.90± 0.11	−1.72± 0.11	−1.92
LG04a_002565	06 41 51	−50 45 34	17.0	18.69	1.07	5.06	−1.58± 0.11	−1.32± 0.11	−1.32
LG04a_002568	06 42 39	−50 45 30	17.7	17.81	1.08	4.40	−1.93± 0.08	−1.75± 0.08	−73.52
LG04a_002576	06 41 21	−50 45 28	18.7	18.42	1.12	5.56	−1.47± 0.10	−1.19± 0.10	−155.35
LG04a_002595	06 42 24	−50 45 17	17.4	19.65	1.06	4.03	−1.73± 0.10	−1.51± 0.10	−121.31
LG04a_002607	06 42 46	−50 45 10	18.5	19.57	1.08	5.11	−1.42± 0.12	−1.12± 0.12	−109.01
LG04a_002611	06 42 08	−50 45 11	17.3	20.15	0.89	2.66	−2.06± 0.34	−1.92± 0.34	−2.94
LG04a_002621	06 43 28	−50 44 59	22.4	19.11	0.88	5.52	−1.37± 0.11	−1.06± 0.11	−132.82
LG04a_002630	06 43 27	−50 44 49	22.4	18.48	1.10	5.20	−1.57± 0.13	−1.31± 0.13	−92.85
LG04a_002639	06 42 54	−50 44 44	19.5	18.54	0.97	4.48	−1.78± 0.10	−1.57± 0.10	−124.98
LG04a_002651	06 42 51	−50 44 36	19.5	20.09	0.78	4.90	−1.39± 0.11	−1.09± 0.11	−46.61
LG04a_002660	06 43 35	−50 44 12	23.7	19.85	0.99	4.58	−1.53± 0.13	−1.26± 0.13	−188.04
LG04a_002661	06 43 09	−50 44 13	21.2	19.36	0.79	2.99	−2.10± 0.09	−1.96± 0.09	−89.06
LG04a_002696	06 42 05	−50 43 51	19.1	19.06	1.08	5.55	−1.37± 0.14	−1.06± 0.14	−173.77
LG04a_002708	06 41 50	−50 43 44	19.6	19.84	1.01	4.96	−1.42± 0.15	−1.12± 0.15	−110.23
LG04a_002724	06 43 07	−50 43 32	21.8	17.97	1.43	5.51	−1.56± 0.10	−1.30± 0.10	−172.42
LG04a_002734	06 40 58	−50 43 28	23.5	18.67	1.23	3.18	−2.15± 0.10	−2.03± 0.10	−140.27
LG04a_002735	06 43 35	−50 43 20	24.5	18.27	1.17	4.09	−1.94± 0.10	−1.77± 0.10	−110.50
LG04a_002738	06 40 58	−50 43 26	23.6	19.47	0.93	5.32	−1.37± 0.11	−1.06± 0.11	−183.80
LG04a_002753	06 42 34	−50 43 14	20.3	19.65	0.87	5.25	−1.36± 0.13	−1.05± 0.13	−127.28
LG04a_002761	06 42 35	−50 43 08	20.4	18.26	1.28	3.46	−2.14± 0.08	−2.01± 0.08	−184.85
LG04a_002792	06 41 22	−50 42 46	22.5	20.05	0.90	3.01	−1.97± 0.15	−1.81± 0.15	−3.87
LG04a_002800	06 41 40	−50 42 41	21.5	19.17	1.02	2.40	−2.31± 0.10	−2.22± 0.10	−1.31
LG04a_002882	06 43 21	−50 41 32	24.9	19.07	1.02	4.58	−1.66± 0.14	−1.42± 0.14	−92.44
LG04a_002917	06 41 55	−50 41 16	22.9	18.31	1.10	5.83	−1.41± 0.12	−1.11± 0.12	−115.29
LG04a_002926	06 42 11	−50 41 05	22.9	18.10	1.16	5.31	−1.60± 0.11	−1.35± 0.11	−148.70
LG04a_002966	06 40 49	−50 40 34	28.3	17.75	1.40	5.34	−1.65± 0.10	−1.41± 0.10	−90.18
LG04a_003000	06 41 49	−50 40 00	24.9	18.49	1.21	4.40	−1.81± 0.10	−1.61± 0.10	−125.74
LG04a_003026	06 41 13	−50 39 35	27.6	19.79	0.76	3.36	−1.91± 0.17	−1.73± 0.17	−78.07
LG04a_003065	06 41 19	−50 39 07	27.8	19.54	0.78	5.39	−1.33± 0.12	−1.02± 0.12	−101.37
LG04a_003087	06 41 22	−50 38 52	28.0	18.18	1.12	5.29	−1.59± 0.10	−1.34± 0.10	−99.03
LG04a_003114	06 41 38	−50 38 30	27.5	18.30	1.23	5.81	−1.42± 0.10	−1.12± 0.10	−91.91
LG04a_003201	06 40 59	−50 37 25	31.7	19.40	1.08	3.60	−1.90± 0.10	−1.72± 0.10	−139.48
LG04a_003219	06 41 20	−50 37 07	30.5	18.44	1.10	3.04	−2.23± 0.08	−2.13± 0.08	−1.40

Continued on next page

Table 2.A – *Carina stars, continued*

Star[7]	α (J2000)	δ	r [′]	V	B−V	Σ W [Å]	[Fe/H] R97,ZW	[Fe/H] R97,CG	log p
LG04a_003232	06 40 48	−50 37 00	33.3	19.92	1.05	5.69	−1.18± 0.12	−0.83± 0.12	−141.60
LG04a_003239	06 41 02	−50 36 56	32.1	19.18	1.15	4.98	−1.52± 0.17	−1.25± 0.17	−114.18
LG04a_003304	06 41 14	−50 35 56	32.6	19.46	0.82	4.08	−1.75± 0.13	−1.53± 0.13	−1.74
LG04a_003355	06 40 57	−50 35 08	35.1	18.03	1.21	4.89	−1.74± 0.12	−1.52± 0.12	−106.69
LG04a_003423	06 40 57	−50 34 02	36.6	19.10	0.88	6.11	−1.19± 0.13	−0.84± 0.13	−122.37
LG04a_003432	06 40 53	−50 33 58	37.1	18.81	1.12	10.40	0.07± 0.40	0.71± 0.40	−141.44
LG04a_003435	06 41 20	−50 33 52	35.1	17.93	1.03	4.92	−1.75± 0.12	−1.53± 0.12	−171.27
LG04a_003486	06 40 56	−50 32 54	38.3	18.41	0.94	5.43	−1.51± 0.10	−1.24± 0.10	−49.42
LG04a_003767	06 42 57	−50 59 41	14.9	20.22	0.97	4.94	−1.36± 0.11	−1.05± 0.11	−127.54
LG04a_003774	06 42 01	−50 59 30	5.3	19.93	0.69	3.87	−1.73± 0.18	−1.51± 0.18	−1.59
LG04a_003786	06 41 16	−50 59 03	3.4	18.20	1.04	4.82	−1.73± 0.11	−1.51± 0.11	−95.07
LG04a_003805	06 41 39	−50 58 30	1.0	20.01	0.89	6.28	−0.99± 0.35	−0.59± 0.35	−1.30
LG04a_003808	06 42 44	−50 58 21	11.9	19.23	0.97	4.79	−1.57± 0.12	−1.31± 0.12	−1.65
LG04a_003811	06 41 33	−50 58 22	0.7	19.53	0.86	2.87	−2.10± 0.17	−1.97± 0.17	−1.28
LG04a_003829	06 41 55	−50 57 43	3.1	18.53	1.09	4.70	−1.72± 0.13	−1.49± 0.13	−1.31
LG04a_003830	06 40 57	−50 57 44	7.0	18.56	1.10	2.55	−2.36± 0.12	−2.29± 0.12	−1.34
LG04a_003844	06 41 12	−50 57 26	4.5	18.29	1.10	4.22	−1.90± 0.11	−1.72± 0.11	−1.31
LG04a_003850	06 42 16	−50 57 13	6.6	19.95	0.91	1.65	−2.40± 0.16	−2.34± 0.16	−1.32
LG04a_003860	06 41 04	−50 57 05	6.3	17.94	1.21	5.68	−1.51± 0.11	−1.24± 0.11	−2.60
LG04a_003870	06 41 38	−50 56 44	1.7	17.81	1.20	4.94	−1.76± 0.12	−1.55± 0.12	−181.90
LG04a_003902	06 41 07	−50 55 50	6.7	20.05	0.82	4.18	−1.62± 0.33	−1.37± 0.33	−1.29
LG04a_003925	06 43 16	−50 55 04	16.5	18.26	1.13	4.66	−1.77± 0.12	−1.56± 0.12	−56.27
LG04a_003926	06 43 12	−50 55 04	15.8	18.45	1.17	3.38	−2.13± 0.10	−2.00± 0.10	−1.29
LG04a_003940	06 42 39	−50 54 29	10.5	18.26	1.31	4.15	−1.93± 0.25	−1.75± 0.25	−107.32
LG04a_003944	06 40 48	−50 54 27	11.0	19.95	0.69	4.42	−1.56± 0.14	−1.30± 0.14	−31.86
LG04a_003952	06 41 00	−50 54 09	9.5	19.18	1.16	3.94	−1.84± 0.14	−1.64± 0.14	−1.31
LG04a_003963	06 42 21	−50 53 46	8.2	18.24	1.05	4.91	−1.70± 0.09	−1.47± 0.09	−1.31
LG04a_003990	06 42 25	−50 53 10	9.0	18.28	1.10	5.37	−1.55± 0.12	−1.29± 0.12	−123.33
LG04a_003991	06 42 27	−50 53 07	9.4	19.61	0.92	6.47	−0.99± 0.16	−0.60± 0.16	−105.50
LG04a_003992	06 41 18	−50 53 08	8.5	18.44	1.18	3.89	−1.97± 0.09	−1.81± 0.09	−1.47
LG04a_003997	06 42 05	−50 53 02	7.2	19.76	0.89	3.94	−1.74± 0.15	−1.52± 0.15	−1.34
LG04a_004020	06 43 05	−50 52 31	14.9	19.16	0.93	5.25	−1.44± 0.10	−1.15± 0.10	−31.92
LG04a_004028	06 40 56	−50 52 22	12.2	19.67	1.04	3.64	−1.85± 0.29	−1.65± 0.29	−64.99
LG04a_004032	06 41 54	−50 52 14	7.8	19.87	0.86	4.04	−1.69± 0.16	−1.46± 0.16	−1.29
LG04a_004064	06 42 12	−50 51 12	9.7	19.98	0.81	3.02	−1.98± 0.28	−1.82± 0.28	−2.21
LG04a_004066	06 41 44	−50 51 12	9.3	19.48	1.02	2.63	−2.19± 0.11	−2.07± 0.11	−2.20
LG04a_004079	06 42 16	−50 50 53	10.3	19.99	0.90	3.44	−1.85± 0.24	−1.66± 0.24	−1.37
LG04a_004096	06 41 07	−50 50 24	13.2	20.11	0.82	3.32	−1.87± 0.31	−1.68± 0.31	−1.28
LG04a_004116	06 42 50	−50 49 44	14.4	19.31	1.01	4.21	−1.73± 0.11	−1.51± 0.11	−18.40
LG04a_004148	06 41 45	−50 48 44	12.7	18.55	1.12	3.14	−2.19± 0.09	−2.07± 0.09	−2.11
LG04a_004157	06 42 25	−50 48 35	13.5	18.50	0.96	6.25	−1.25± 0.18	−0.91± 0.18	−80.04
LG04a_004159	06 42 05	−50 48 32	12.8	19.23	1.10	5.08	−1.48± 0.13	−1.20± 0.13	−158.08
LG04a_004179	06 41 22	−50 47 59	15.2	18.71	1.05	3.43	−2.07± 0.10	−1.93± 0.10	−1.70
LG04a_004181	06 42 32	−50 47 56	14.6	18.72	1.23	4.03	−1.89± 0.09	−1.70± 0.09	−166.34
LG04a_004233	06 42 12	−50 46 23	15.7	19.43	0.98	4.41	−1.65± 0.16	−1.41± 0.16	−40.75
LG04a_004248	06 41 58	−50 46 05	16.1	19.16	0.99	4.75	−1.59± 0.14	−1.34± 0.14	−1.44
LG04a_004264	06 41 50	−50 45 23	17.3	19.23	1.04	4.84	−1.55± 0.12	−1.29± 0.12	−121.70
LG04a_004326	06 42 06	−50 43 34	19.5	18.81	0.92	5.66	−1.37± 0.11	−1.07± 0.11	−144.83
LG04a_004451	06 41 39	−50 38 56	26.8	17.94	1.42	5.69	−1.51± 0.17	−1.24± 0.17	−158.74
LG04a_004542	06 40 48	−50 34 21	37.0	19.16	1.02	4.93	−1.54± 0.13	−1.27± 0.13	−66.85
LG04a_004682	06 42 22	−50 52 00	9.7	19.69	1.09	5.55	−1.26± 0.21	−0.93± 0.21	−2.20
LG04a_004712	06 41 30	−50 49 07	12.9	19.27	0.90	2.51	−2.26± 0.15	−2.16± 0.15	−33.73
LG04a_004875	06 42 00	−50 58 40	4.4	17.84	1.07	4.36	−1.93± 0.08	−1.76± 0.08	−151.74

Continued on next page

Table 2.A – *Carina stars, continued*

Star[7]	α	δ	r	V	B−V	Σ W	[Fe/H]	[Fe/H]	log p
	(J2000)		[′]			[Å]	R97,ZW	R97,CG	
LG04a_004882	06 43 14	−50 57 02	16.6	18.47	1.12	5.23	−1.56± 0.15	−1.30± 0.15	−88.25
LG04a_004892	06 43 16	−50 55 36	16.6	19.46	0.97	3.57	−1.90± 0.10	−1.72± 0.10	−1.41
LG04a_004908	06 42 00	−50 53 28	6.4	18.65	1.23	5.61	−1.42± 0.11	−1.12± 0.11	−131.61
LG04a_004911	06 42 23	−50 53 23	8.7	19.38	0.96	3.51	−1.93± 0.14	−1.76± 0.14	−147.94
LG04a_004934	06 43 09	−50 50 26	16.4	18.23	1.05	4.65	−1.78± 0.10	−1.57± 0.10	−131.85
LG04a_005742	06 41 36	−50 59 36	2.3	18.66	1.05	4.60	−1.72± 0.12	−1.50± 0.12	−109.23
LG04a_005765	06 42 32	−50 59 05	10.2	20.15	0.89	3.09	−1.93± 0.29	−1.76± 0.29	−1.29
LG04a_005801	06 42 30	−50 58 00	9.2	19.43	0.82	2.42	−2.26± 0.26	−2.16± 0.26	−138.29
LG04a_005868	06 42 29	−50 56 29	8.6	18.74	1.05	3.14	−2.15± 0.10	−2.03± 0.10	−1.28
LG04a_006057	06 43 22	−50 50 39	18.1	19.92	0.69	5.50	−1.24± 0.16	−0.90± 0.16	−39.57
LG04a_006162	06 41 39	−50 44 31	18.9	20.20	1.00	5.67	−1.14± 0.11	−0.78± 0.11	−136.43
LG04a_006184	06 43 24	−50 43 25	23.3	18.83	1.06	4.21	−1.81± 0.12	−1.61± 0.12	−73.42
LG04a_006382	06 42 28	−51 00 04	10.2	17.75	1.40	5.23	−1.68± 0.09	−1.45± 0.09	−1.53
LG04a_006422	06 40 52	−50 59 58	7.4	19.49	0.83	3.72	−1.85± 0.15	−1.66± 0.15	−1.30
LG04a_006460	06 41 57	−50 59 44	4.9	20.19	0.97	2.40	−2.14± 1.32	−2.01± 1.32	−1.31
LG04a_006914	06 41 34	−50 57 31	0.9	19.85	0.96	4.63	−1.51± 0.50	−1.24± 0.50	−1.56
LG04a_007126	06 41 36	−50 56 23	2.3	17.90	1.26	6.32	−1.33± 0.11	−1.01± 0.11	−1.35
LG04a_007594	06 42 29	−50 53 57	9.1	20.00	0.94	3.25	−1.91± 0.23	−1.73± 0.23	−1.31
LG04a_007596	06 40 54	−50 53 59	10.6	19.83	0.91	4.86	−1.45± 0.21	−1.16± 0.21	−1.48
LG04a_007801	06 41 40	−50 52 33	7.5	19.16	1.00	3.85	−1.87± 0.11	−1.68± 0.11	−1.47
LG04a_008230	06 41 07	−50 48 57	15.1	20.09	0.85	2.05	−2.26± 0.16	−2.16± 0.16	−1.30
LG04a_008282	06 41 36	−50 48 08	13.9	19.11	0.88	3.90	−1.86± 0.11	−1.67± 0.11	−1.30
LG04a_008337	06 41 35	−50 47 29	15.0	19.49	0.83	3.74	−1.85± 0.13	−1.65± 0.13	−1.30
LG04a_008475	06 43 31	−50 45 33	22.3	19.35	1.14	3.66	−1.89± 0.16	−1.71± 0.16	−156.49
LG04a_008493	06 43 24	−50 45 18	21.7	19.11	0.91	4.01	−1.83± 0.21	−1.63± 0.21	−135.50
LG04a_008559	06 41 42	−50 44 28	18.9	18.56	0.93	5.83	−1.37± 0.11	−1.06± 0.11	−83.87
LG04a_008565	06 43 40	−50 44 19	24.2	20.04	0.83	4.45	−1.54± 0.13	−1.27± 0.13	−16.87
LG04a_008572	06 40 52	−50 44 21	22.9	19.22	1.14	5.46	−1.37± 0.10	−1.06± 0.10	−102.20
LG04a_008670	06 43 22	−50 42 37	23.9	19.42	1.02	7.03	−0.86± 0.19	−0.43± 0.19	−129.29
LG04a_009026	06 41 47	−50 36 30	29.9	20.31	0.84	4.11	−1.59± 0.13	−1.34± 0.13	−55.70
LG04a_009505	06 42 28	−50 59 40	10.0	18.71	1.04	3.77	−1.97± 0.09	−1.80± 0.09	−2.41
LG04a_009711	06 41 34	−50 55 50	3.2	20.29	0.82	2.42	−2.11± 0.39	−1.98± 0.39	−1.79
LG04a_009780	06 40 54	−50 54 44	9.9	18.39	0.97	5.55	−1.48± 0.10	−1.20± 0.10	−150.32
LG04a_009955	06 43 23	−50 50 14	18.4	18.43	1.11	2.09	−2.53± 0.47	−2.49± 0.47	−128.06
LG04a_009965	06 42 58	−50 50 01	15.2	19.63	0.82	3.90	−1.77± 0.15	−1.56± 0.15	−1.74
LG04a_010563	06 40 52	−50 44 16	23.0	19.17	1.10	4.61	−1.63± 0.18	−1.39± 0.18	−91.24
LG04b_000072	06 41 15	−50 59 14	3.7	17.66	1.14	5.81	−1.52± 0.10	−1.25± 0.10	−146.80
LG04b_000091	06 40 08	−50 58 54	15.0	19.85	1.02	4.50	−1.55± 0.18	−1.29± 0.18	−147.23
LG04b_000093	06 41 22	−50 58 53	2.5	19.40	0.93	2.67	−2.19± 0.15	−2.07± 0.15	−1.54
LG04b_000142	06 39 59	−50 58 09	16.8	19.80	0.75	3.12	−1.98± 0.16	−1.82± 0.16	−1.45
LG04b_000287	06 40 44	−50 55 12	11.0	19.28	1.02	4.66	−1.60± 0.11	−1.35± 0.11	−152.27
LG04b_000378	06 40 30	−50 53 10	15.2	18.40	1.00	5.54	−1.48± 0.10	−1.20± 0.10	−86.01
LG04b_000438	06 40 45	−50 51 42	14.4	20.02	0.99	5.07	−1.35± 0.11	−1.04± 0.11	−189.65
LG04b_000442	06 40 23	−50 51 38	17.7	20.02	0.90	4.41	−1.55± 0.10	−1.29± 0.10	−147.25
LG04b_000511	06 41 20	−50 49 47	12.8	19.96	0.81	3.69	−1.78± 0.16	−1.57± 0.16	−1.78
LG04b_000546	06 40 33	−50 48 34	19.7	18.46	1.00	5.24	−1.56± 0.10	−1.30± 0.10	−112.26
LG04b_000582	06 40 09	−50 47 29	24.3	19.48	1.05	4.65	−1.57± 0.10	−1.31± 0.10	−112.91
LG04b_000587	06 40 29	−50 47 13	22.0	18.29	1.05	4.77	−1.73± 0.10	−1.51± 0.10	−154.29
LG04b_000604	06 40 23	−50 46 40	23.3	19.14	1.10	4.28	−1.74± 0.12	−1.52± 0.12	−177.73
LG04b_000617	06 40 22	−50 46 22	23.8	19.29	0.81	5.08	−1.47± 0.12	−1.19± 0.12	−129.91
LG04b_000623	06 40 49	−50 46 09	20.8	20.32	0.92	4.30	−1.54± 0.16	−1.27± 0.16	−7.54
LG04b_000746	06 40 13	−50 41 54	30.5	19.20	0.81	5.18	−1.46± 0.17	−1.17± 0.17	−128.55
LG04b_000747	06 41 23	−50 41 51	23.7	19.61	1.08	4.76	−1.51± 0.11	−1.24± 0.11	−176.45

Continued on next page

Table 2.A – *Carina stars, continued*

Star[7]	α	δ	r	V	B−V	Σ W	[Fe/H]	[Fe/H]	log p
	(J2000)		[′]			[Å]	R97,ZW	R97,CG	
LG04b_000795	06 41 13	−50 40 05	26.9	17.97	1.21	5.24	−1.64± 0.10	−1.40± 0.10	−102.76
LG04b_000812	06 39 51	−50 39 34	36.2	19.97	0.95	5.53	−1.22± 0.12	−0.88± 0.12	−62.59
LG04b_000904	06 40 17	−50 36 53	36.6	18.78	1.02	5.81	−1.33± 0.13	−1.02± 0.13	−82.77
LG04b_001283	06 40 36	−51 00 06	10.1	18.48	0.94	2.11	−2.51± 0.24	−2.47± 0.24	−84.02
LG04b_001327	06 39 00	−50 59 53	26.6	18.63	1.15	4.53	−1.75± 0.12	−1.53± 0.12	−129.19
LG04b_001388	06 39 53	−50 59 39	17.5	19.04	0.86	5.35	−1.43± 0.13	−1.14± 0.13	−63.03
LG04b_001422	06 40 36	−50 59 29	10.1	18.39	1.03	5.17	−1.59± 0.12	−1.34± 0.12	−143.53
LG04b_001434	06 40 34	−50 59 23	10.5	19.31	0.97	5.38	−1.37± 0.12	−1.07± 0.12	−115.35
LG04b_001435	06 39 08	−50 59 20	25.3	19.77	1.01	4.81	−1.47± 0.13	−1.19± 0.13	−173.10
LG04b_001437	06 39 41	−50 59 21	19.5	18.18	1.02	5.34	−1.58± 0.14	−1.32± 0.14	−160.08
LG04b_001448	06 39 59	−50 59 19	16.5	19.46	0.98	5.46	−1.33± 0.11	−1.01± 0.11	−78.04
LG04b_001451	06 39 22	−50 59 17	22.9	19.06	0.95	5.15	−1.49± 0.19	−1.21± 0.19	−88.55
LG04b_001466	06 41 27	−50 59 14	2.1	19.00	1.05	4.55	−1.68± 0.17	−1.45± 0.17	−61.99
LG04b_001468	06 39 12	−50 59 11	24.7	20.01	0.80	5.37	−1.26± 0.12	−0.93± 0.12	−134.87
LG04b_001503	06 41 15	−50 59 04	3.6	18.79	0.93	3.14	−2.15± 0.13	−2.02± 0.13	−2.64
LG04b_001511	06 40 26	−50 59 03	11.9	19.90	0.79	5.54	−1.23± 0.17	−0.89± 0.17	−1.28
LG04b_001531	06 38 50	−50 58 53	28.6	19.95	0.76	5.64	−1.19± 0.17	−0.84± 0.17	−17.03
LG04b_001563	06 39 12	−50 58 43	24.9	19.10	0.82	4.51	−1.67± 0.17	−1.44± 0.17	−91.30
LG04b_001577	06 40 54	−50 58 41	7.2	20.04	0.80	2.88	−2.02± 0.39	−1.86± 0.39	−1.43
LG04b_001634	06 39 50	−50 58 21	18.3	19.47	1.06	5.62	−1.28± 0.11	−0.95± 0.11	−85.38
LG04b_001651	06 39 27	−50 58 16	22.5	19.80	0.72	4.88	−1.45± 0.17	−1.16± 0.17	−1.34
LG04b_001676	06 40 24	−50 58 09	12.5	18.86	0.87	4.99	−1.57± 0.25	−1.31± 0.25	−69.94
LG04b_001689	06 40 42	−50 58 03	9.4	20.04	0.99	2.45	−2.15± 1.36	−2.02± 1.36	−148.97
LG04b_001691	06 40 56	−50 58 03	7.1	18.68	1.09	5.38	−1.48± 0.12	−1.20± 0.12	−99.64
LG04b_001754	06 39 04	−50 57 42	26.7	20.16	0.87	5.87	−1.08± 0.14	−0.71± 0.14	−138.48
LG04b_001762	06 41 19	−50 57 42	3.2	19.30	0.83	3.90	−1.83± 0.09	−1.63± 0.09	−89.48
LG04b_001831	06 40 04	−50 57 16	16.4	19.74	0.95	4.56	−1.55± 0.10	−1.29± 0.10	−110.91
LG04b_001856	06 40 01	−50 57 06	17.1	19.80	1.07	3.68	−1.81± 0.17	−1.61± 0.17	−62.44
LG04b_001924	06 39 10	−50 56 42	26.1	19.51	1.05	4.26	−1.68± 0.21	−1.45± 0.21	−1.49
LG04b_001949	06 41 14	−50 56 35	4.9	18.28	1.22	2.33	−2.48± 0.15	−2.43± 0.15	−141.26
LG04b_001989	06 40 44	−50 56 19	10.1	20.23	0.97	4.34	−1.54± 0.64	−1.27± 0.64	−2.00
LG04b_002106	06 39 04	−50 55 37	27.7	19.98	1.04	4.75	−1.46± 0.11	−1.17± 0.11	−75.20
LG04b_002124	06 41 09	−50 55 34	6.6	19.77	1.06	5.21	−1.35± 0.11	−1.04± 0.11	−52.98
LG04b_002153	06 41 27	−50 55 23	4.5	18.61	1.03	5.19	−1.55± 0.21	−1.29± 0.21	−88.10
LG04b_002206	06 40 42	−50 55 04	11.5	19.39	0.86	3.45	−1.95± 0.12	−1.78± 0.12	−2.27
LG04b_002256	06 40 34	−50 54 41	13.1	19.69	0.80	6.40	−1.00± 0.15	−0.61± 0.15	−126.86
LG04b_002298	06 40 46	−50 54 21	11.4	19.92	0.72	3.34	−1.89± 0.14	−1.71± 0.14	−2.32
LG04b_002306	06 41 19	−50 54 16	6.8	19.19	0.93	4.41	−1.69± 0.11	−1.46± 0.11	−135.47
LG04b_002311	06 39 13	−50 54 11	27.2	19.63	0.82	4.81	−1.50± 0.33	−1.22± 0.33	−1.33
LG04b_002333	06 40 46	−50 54 02	11.7	19.50	0.87	5.10	−1.43± 0.20	−1.14± 0.20	−106.65
LG04b_002601	06 40 31	−50 51 16	17.0	19.54	0.82	5.84	−1.20± 0.16	−0.85± 0.16	−122.04
LG04b_002633	06 40 47	−50 50 50	15.2	19.33	0.88	3.24	−2.02± 0.13	−1.87± 0.13	−1.28
LG04b_002637	06 40 35	−50 50 50	16.9	20.09	0.84	5.14	−1.32± 0.11	−1.00± 0.11	−134.59
LG04b_002686	06 40 54	−50 50 23	14.8	19.98	0.75	3.52	−1.83± 0.14	−1.63± 0.14	−65.15
LG04b_002715	06 40 24	−50 50 03	19.2	19.29	0.93	5.08	−1.47± 0.11	−1.19± 0.11	−171.00
LG04b_002772	06 40 15	−50 49 24	21.3	19.56	0.79	5.17	−1.40± 0.11	−1.10± 0.11	−31.45
LG04b_002777	06 40 09	−50 49 21	22.3	19.80	1.05	5.75	−1.18± 0.12	−0.83± 0.12	−117.95
LG04b_002874	06 41 15	−50 47 59	15.7	18.58	1.05	4.67	−1.72± 0.19	−1.49± 0.19	−88.69
LG04b_002892	06 41 13	−50 47 39	16.4	20.31	0.92	4.38	−1.51± 0.14	−1.24± 0.14	−108.73
LG04b_002915	06 40 44	−50 47 23	19.9	19.54	1.02	4.75	−1.53± 0.43	−1.26± 0.43	−172.60
LG04b_002921	06 41 18	−50 47 15	16.5	19.60	1.09	4.88	−1.48± 0.13	−1.20± 0.13	−170.68
LG04b_002935	06 41 14	−50 47 01	17.1	20.24	0.90	5.46	−1.20± 0.15	−0.85± 0.15	−115.15
LG04b_002944	06 40 20	−50 46 55	23.5	19.01	1.04	5.23	−1.47± 0.13	−1.19± 0.13	−135.32

Continued on next page

Table 2.A – *Carina stars, continued*

Star[7]	α (J2000)	δ (J2000)	r [']	V	B−V	Σ W [Å]	[Fe/H] R97,ZW	[Fe/H] R97,CG	$\log p$
LG04b_002950	06 40 54	−50 46 50	19.4	19.62	0.77	5.03	−1.43± 0.10	−1.14± 0.10	−16.63
LG04b_002961	06 40 36	−50 46 45	21.6	19.01	1.04	4.01	−1.85± 0.27	−1.65± 0.27	−79.83
LG04b_003016	06 39 59	−50 46 01	27.4	19.11	0.94	4.83	−1.58± 0.10	−1.32± 0.10	−110.01
LG04b_003027	06 40 46	−50 45 54	21.5	19.44	0.91	5.48	−1.33± 0.17	−1.01± 0.17	−119.97
LG04b_003044	06 40 35	−50 45 37	23.2	19.54	0.76	5.68	−1.25± 0.12	−0.91± 0.12	−81.18
LG04b_003053	06 41 08	−50 45 31	19.8	19.61	0.85	5.70	−1.23± 0.11	−0.89± 0.11	−87.40
LG04b_003066	06 40 20	−50 45 21	25.4	19.85	0.72	5.01	−1.40± 0.12	−1.10± 0.12	−106.05
LG04b_003104	06 40 54	−50 44 31	22.4	19.09	0.84	2.97	−2.15± 0.15	−2.02± 0.15	−1.48
LG04b_003119	06 40 26	−50 44 17	26.0	19.18	0.82	4.74	−1.59± 0.10	−1.34± 0.10	−60.37
LG04b_003120	06 40 18	−50 44 16	26.9	20.08	0.87	5.79	−1.12± 0.13	−0.76± 0.13	−109.35
LG04b_003129	06 40 35	−50 44 11	25.0	20.06	0.89	4.57	−1.50± 0.17	−1.22± 0.17	−143.14
LG04b_003144	06 40 55	−50 44 01	23.1	18.91	0.89	2.17	−2.42± 0.10	−2.36± 0.10	−1.28
LG04b_003150	06 39 53	−50 43 56	30.7	18.28	0.98	4.41	−1.85± 0.09	−1.65± 0.09	−184.08
LG04b_003195	06 40 00	−50 43 13	30.6	19.96	0.96	3.61	−1.80± 0.13	−1.60± 0.13	−168.37
LG04b_003264	06 40 15	−50 42 20	29.8	19.48	0.95	6.06	−1.14± 0.12	−0.78± 0.12	−134.08
LG04b_003277	06 40 09	−50 42 10	30.7	18.88	0.96	5.03	−1.55± 0.12	−1.29± 0.12	−115.58
LG04b_003281	06 40 08	−50 42 07	30.9	19.60	0.81	5.52	−1.29± 0.12	−0.96± 0.12	−31.48
LG04b_003310	06 40 13	−50 41 48	30.6	19.10	0.89	4.73	−1.61± 0.11	−1.36± 0.11	−125.39
LG04b_003369	06 40 54	−50 40 56	27.3	18.50	1.18	5.09	−1.60± 0.10	−1.35± 0.10	−123.69
LG04b_003381	06 40 54	−50 40 47	27.5	19.61	1.10	3.41	−1.93± 0.12	−1.75± 0.12	−51.51
LG04b_003401	06 40 36	−50 40 26	29.8	19.11	0.89	5.55	−1.36± 0.13	−1.05± 0.13	−126.15
LG04b_003407	06 39 54	−50 40 23	34.8	19.88	1.05	5.10	−1.37± 0.13	−1.06± 0.13	−180.79
LG04b_003411	06 40 46	−50 40 20	28.9	19.69	0.90	5.33	−1.33± 0.14	−1.01± 0.14	−114.50
LG04b_003430	06 41 10	−50 40 10	27.0	19.47	0.90	4.98	−1.47± 0.12	−1.19± 0.12	−107.19
LG04b_003436	06 40 25	−50 40 06	31.4	20.07	0.79	3.53	−1.81± 0.16	−1.61± 0.16	−92.12
LG04b_003440	06 40 37	−50 40 03	30.2	19.55	0.85	4.99	−1.46± 0.11	−1.17± 0.11	−126.41
LG04b_003449	06 40 35	−50 40 01	30.5	19.98	0.71	7.12	−0.73± 0.17	−0.28± 0.17	−2.08
LG04b_003506	06 41 11	−50 39 03	28.5	20.21	0.73	5.48	−1.20± 0.11	−0.85± 0.11	−86.27
LG04b_003515	06 40 18	−50 38 54	33.8	20.17	0.79	5.50	−1.20± 0.12	−0.85± 0.12	−17.58
LG04b_003517	06 40 09	−50 38 50	34.9	19.08	1.15	4.61	−1.65± 0.10	−1.41± 0.10	−69.33
LG04b_003523	06 40 06	−50 38 46	35.4	19.42	0.87	5.27	−1.39± 0.10	−1.09± 0.10	−32.71
LG04b_003565	06 40 14	−50 38 14	35.2	19.03	1.00	4.13	−1.80± 0.18	−1.60± 0.18	−92.77
LG04b_003572	06 40 13	−50 38 08	35.4	19.48	0.87	4.81	−1.52± 0.11	−1.25± 0.11	−101.99
LG04b_003632	06 41 26	−50 37 08	30.1	19.57	1.07	5.32	−1.35± 0.17	−1.04± 0.17	−70.85
LG04b_003645	06 41 03	−50 36 57	32.0	19.63	1.04	4.28	−1.66± 0.18	−1.42± 0.18	−150.55
LG04b_003648	06 40 49	−50 36 55	33.3	19.78	1.07	5.71	−1.20± 0.13	−0.85± 0.13	−35.54
LG04b_003660	06 40 10	−50 36 42	37.6	19.99	0.84	4.29	−1.59± 0.10	−1.34± 0.10	−85.06
LG04b_003690	06 40 27	−50 36 21	36.2	20.12	0.97	5.63	−1.16± 0.11	−0.81± 0.11	−96.89
LG04b_003691	06 40 45	−50 36 20	34.4	20.03	0.78	5.17	−1.32± 0.12	−1.00± 0.12	−128.07
LG04b_003692	06 40 42	−50 36 19	34.8	18.79	1.04	4.34	−1.78± 0.12	−1.57± 0.12	−100.22
LG04b_003755	06 40 18	−50 35 26	38.4	19.64	1.07	5.10	−1.41± 0.13	−1.11± 0.13	−60.86
LG04b_003781	06 40 38	−50 35 06	36.9	19.06	1.13	5.89	−1.26± 0.11	−0.93± 0.11	−169.87
LG04b_003903	06 41 24	−50 33 15	35.8	19.50	0.94	5.20	−1.40± 0.19	−1.10± 0.19	−87.91
LG04b_004260	06 40 31	−50 59 15	11.0	17.75	1.05	4.75	−1.83± 0.10	−1.63± 0.10	−1.47
LG04b_004319	06 40 09	−50 57 41	15.4	18.68	1.18	4.53	−1.74± 0.10	−1.52± 0.10	−190.68
LG04b_004346	06 39 26	−50 56 58	23.2	19.39	0.86	4.70	−1.57± 0.11	−1.31± 0.11	−123.96
LG04b_004348	06 40 31	−50 56 56	12.0	19.67	0.77	4.47	−1.59± 0.13	−1.34± 0.13	−1.45
LG04b_004378	06 41 22	−50 56 11	4.0	18.41	1.22	5.77	−1.41± 0.11	−1.11± 0.11	−175.64
LG04b_004421	06 40 35	−50 54 59	12.7	18.84	1.10	4.63	−1.68± 0.33	−1.45± 0.33	−164.15
LG04b_004558	06 41 03	−50 49 50	14.4	18.60	1.11	5.29	−1.52± 0.12	−1.25± 0.12	−150.21
LG04b_004567	06 40 54	−50 49 28	16.0	18.86	1.13	4.46	−1.73± 0.20	−1.51± 0.20	−102.05
LG04b_004628	06 40 35	−50 47 22	21.0	18.80	1.09	5.13	−1.54± 0.10	−1.27± 0.10	−171.65
LG04b_004674	06 41 23	−50 45 16	18.9	18.22	1.18	5.24	−1.60± 0.09	−1.35± 0.09	−140.76

Continued on next page

Table 2.A – *Carina stars, continued*

Star[7]	α	δ	r	V	B−V	Σ W	[Fe/H]	[Fe/H]	log p
	(J2000)		[′]			[Å]	R97,ZW	R97,CG	
LG04b_004737	06 41 26	−50 42 37	22.4	19.98	0.89	5.79	−1.14± 0.12	−0.78± 0.12	−29.22
LG04b_004793	06 40 07	−50 40 00	33.7	19.07	1.02	4.37	−1.72± 0.12	−1.50± 0.12	−120.37
LG04b_004840	06 40 36	−50 37 39	33.5	20.17	0.99	5.53	−1.19± 0.15	−0.84± 0.15	−44.96
LG04b_004879	06 40 35	−50 35 14	36.9	18.82	0.88	5.33	−1.47± 0.11	−1.19± 0.11	−166.43
LG04b_005027	06 39 37	−50 58 03	20.8	19.36	0.79	3.52	−1.93± 0.33	−1.76± 0.33	−131.36
LG04b_005087	06 40 33	−50 49 25	18.8	19.52	1.03	1.81	−2.43± 0.29	−2.37± 0.29	−132.92
LG04b_005131	06 40 36	−50 41 38	28.3	20.26	0.97	5.23	−1.26± 0.12	−0.93± 0.12	−70.40
LG04b_005294	06 40 57	−50 57 19	7.3	19.18	0.81	4.28	−1.73± 0.19	−1.51± 0.19	−1.59
LG04b_005310	06 40 31	−50 50 27	17.8	19.81	0.81	5.53	−1.25± 0.12	−0.91± 0.12	−122.00
LG04b_005359	06 41 25	−50 52 55	8.0	18.48	1.09	5.92	−1.35± 0.15	−1.04± 0.15	−140.34
LG04c_000388	06 39 03	−51 13 33	29.0	17.39	1.22	4.84	−1.86± 0.10	−1.67± 0.10	−177.18
LG04c_000391	06 41 04	−51 13 32	21.1	18.44	0.96	5.09	−1.61± 0.11	−1.36± 0.11	−54.67
LG04c_000429	06 39 02	−51 12 33	28.5	17.57	1.19	4.51	−1.93± 0.20	−1.76± 0.20	−90.58
LG04c_000437	06 39 51	−51 12 06	22.7	18.27	1.41	4.92	−1.69± 0.13	−1.46± 0.13	−165.86
LG04c_000452	06 40 04	−51 11 32	21.0	17.70	1.38	5.93	−1.48± 0.11	−1.20± 0.11	−174.53
LG04c_000455	06 38 45	−51 11 26	30.1	19.46	0.91	3.28	−1.99± 0.20	−1.83± 0.20	−1.64
LG04c_000464	06 39 24	−51 11 13	25.0	18.58	1.11	3.76	−1.99± 0.18	−1.83± 0.18	−153.12
LG04c_000472	06 38 43	−51 11 02	30.2	18.49	1.04	4.21	−1.87± 0.11	−1.68± 0.11	−144.86
LG04c_000489	06 39 38	−51 10 09	22.5	20.28	0.93	5.49	−1.18± 0.12	−0.83± 0.12	−76.53
LG04c_000494	06 40 03	−51 09 58	19.6	18.98	1.08	4.53	−1.69± 0.11	−1.46± 0.11	−115.52
LG04c_000517	06 39 30	−51 09 17	23.0	18.02	1.23	3.62	−2.13± 0.08	−2.00± 0.08	−1.58
LG04c_000518	06 38 47	−51 09 13	28.9	19.26	0.80	4.83	−1.55± 0.12	−1.29± 0.12	−71.25
LG04c_000520	06 39 22	−51 09 14	24.0	18.39	1.23	5.02	−1.64± 0.11	−1.40± 0.11	−188.15
LG04c_000539	06 40 56	−51 08 42	14.7	17.51	1.31	4.70	−1.89± 0.08	−1.70± 0.08	−128.99
LG04c_000544	06 40 17	−51 08 29	17.0	18.36	1.02	5.32	−1.55± 0.11	−1.29± 0.11	−95.57
LG04c_000549	06 39 06	−51 08 14	25.8	20.24	0.83	2.08	−2.23± 0.17	−2.12± 0.17	−18.87
LG04c_000556	06 38 50	−51 08 07	28.1	20.01	0.90	5.72	−1.16± 0.11	−0.80± 0.11	−59.63
LG04c_000603	06 40 28	−51 06 54	14.5	18.25	1.13	5.39	−1.55± 0.10	−1.29± 0.10	−117.31
LG04c_000620	06 40 12	−51 06 09	15.8	19.45	0.97	3.36	−1.97± 0.11	−1.80± 0.11	−1.37
LG04c_000626	06 40 48	−51 06 03	12.0	17.60	1.43	3.69	−2.18± 0.09	−2.06± 0.09	−2.18
LG04c_000627	06 41 30	−51 06 02	11.1	20.05	0.89	3.35	−1.87± 0.18	−1.68± 0.18	−1.28
LG04c_000642	06 39 20	−51 05 32	23.0	18.18	1.44	4.97	−1.69± 0.09	−1.46± 0.09	−101.94
LG04c_000648	06 39 37	−51 05 24	20.3	18.56	0.93	4.87	−1.66± 0.13	−1.42± 0.13	−175.52
LG04c_000662	06 40 12	−51 05 01	15.0	17.91	1.05	5.28	−1.64± 0.10	−1.40± 0.10	−155.82
LG04c_000682	06 39 31	−51 04 23	21.0	18.19	1.14	5.36	−1.57± 0.13	−1.31± 0.13	−158.90
LG04c_000686	06 40 22	−51 04 23	13.4	17.86	1.20	5.54	−1.57± 0.10	−1.31± 0.10	−161.54
LG04c_000688	06 39 44	−51 04 14	18.9	19.09	0.86	5.88	−1.26± 0.18	−0.93± 0.18	−29.32
LG04c_000696	06 40 41	−51 04 02	10.8	19.37	0.90	1.76	−2.47± 0.42	−2.42± 0.42	−144.10
LG04c_000701	06 39 06	−51 03 55	25.0	18.99	0.89	5.11	−1.51± 0.11	−1.24± 0.11	−54.93
LG04c_000710	06 41 02	−51 03 36	8.4	19.17	0.97	5.14	−1.47± 0.14	−1.19± 0.14	−1.33
LG04c_000717	06 40 14	−51 03 19	14.1	18.87	1.04	2.88	−2.21± 0.11	−2.10± 0.11	−1.67
LG04c_000744	06 38 40	−51 02 25	29.4	19.86	0.88	4.73	−1.48± 0.11	−1.20± 0.11	−99.76
LG04c_000761	06 40 08	−51 01 58	14.7	18.34	1.06	4.08	−1.93± 0.08	−1.76± 0.08	−70.75
LG04c_000814	06 41 23	−51 00 51	4.1	17.49	1.32	4.53	−1.94± 0.10	−1.77± 0.10	−75.67
LG04c_000826	06 40 49	−51 00 33	8.0	18.29	1.04	1.76	−2.65± 0.07	−2.64± 0.07	−1.52
LG04c_000835	06 41 27	−51 00 18	3.2	17.66	1.34	4.94	−1.79± 0.09	−1.58± 0.09	−1.59
LG04c_000836	06 40 16	−51 00 18	13.4	18.07	1.25	3.51	−2.15± 0.10	−2.03± 0.10	−1.37
LG04c_000926	06 39 31	−50 58 10	21.8	18.27	1.13	5.16	−1.62± 0.09	−1.37± 0.09	−139.26
LG04c_002026	06 41 22	−51 18 33	28.5	18.61	0.97	3.88	−1.95± 0.10	−1.78± 0.10	−126.94
LG04c_002082	06 41 32	−51 17 57	28.1	19.23	0.95	4.76	−1.58± 0.27	−1.32± 0.27	−29.53
LG04c_002109	06 41 08	−51 17 45	27.0	19.89	1.01	5.44	−1.26± 0.16	−0.93± 0.16	−85.42
LG04c_002156	06 39 58	−51 17 15	27.5	19.76	1.04	4.90	−1.45± 0.14	−1.16± 0.14	−50.43
LG04c_002264	06 39 50	−51 16 19	27.0	18.97	0.99	3.44	−2.02± 0.10	−1.87± 0.10	−1.28

Continued on next page

Table 2.A – *Carina stars, continued*

Star^7	α	δ	r	V	B−V	Σ W	[Fe/H]	[Fe/H]	log p
	(J2000)		[′]			[Å]	R97,ZW	R97,CG	
LG04c_002285	06 39 42	−51 16 07	27.3	19.29	0.96	7.50	−0.73± 0.33	−0.28± 0.33	−5.45
LG04c_002309	06 41 28	−51 15 51	24.9	19.36	0.87	6.45	−1.04± 0.13	−0.66± 0.13	−12.08
LG04c_002324	06 41 14	−51 15 39	24.2	17.62	1.41	5.09	−1.75± 0.09	−1.53± 0.09	−129.43
LG04c_002347	06 39 14	−51 15 20	29.1	19.83	1.00	5.28	−1.32± 0.15	−1.00± 0.15	−36.13
LG04c_002349	06 41 24	−51 15 21	24.1	19.01	1.12	5.07	−1.52± 0.15	−1.25± 0.15	−155.17
LG04c_002357	06 41 19	−51 15 16	23.8	20.03	0.84	5.71	−1.16± 0.14	−0.80± 0.14	−52.84
LG04c_002388	06 41 13	−51 14 55	23.1	17.65	1.19	5.15	−1.72± 0.10	−1.50± 0.10	−124.41
LG04c_002398	06 39 38	−51 14 44	26.4	19.17	0.88	4.95	−1.53± 0.15	−1.26± 0.15	−55.14
LG04c_002415	06 41 01	−51 14 32	22.4	19.75	1.02	5.14	−1.37± 0.11	−1.07± 0.11	−182.10
LG04c_002435	06 41 14	−51 14 21	22.4	19.90	0.78	0.96	−2.62± 0.33	−2.61± 0.33	−1.40
LG04c_002474	06 40 23	−51 13 50	22.3	20.11	0.84	3.32	−1.87± 0.18	−1.68± 0.18	−1.57
LG04c_002475	06 40 15	−51 13 50	22.7	19.86	1.05	5.77	−1.16± 0.11	−0.81± 0.11	−16.16
LG04c_002510	06 41 06	−51 13 31	21.1	18.72	0.93	5.12	−1.55± 0.11	−1.29± 0.11	−68.53
LG04c_002535	06 41 12	−51 13 16	20.8	17.87	1.25	3.43	−2.21± 0.08	−2.10± 0.08	−2.50
LG04c_002539	06 40 16	−51 13 13	21.9	19.56	0.95	4.61	−1.57± 0.10	−1.31± 0.10	−75.63
LG04c_002559	06 40 15	−51 13 00	21.7	19.99	0.79	1.68	−2.39± 0.17	−2.32± 0.17	−1.78
LG04c_002607	06 39 34	−51 12 32	24.7	19.50	0.90	4.54	−1.60± 0.16	−1.35± 0.16	−97.90
LG04c_002608	06 41 20	−51 12 32	20.0	19.22	0.96	4.98	−1.51± 0.10	−1.24± 0.10	−98.52
LG04c_002613	06 41 33	−51 12 30	20.4	18.16	1.01	5.81	−1.44± 0.14	−1.15± 0.14	−102.45
LG04c_002646	06 40 10	−51 12 11	21.2	19.74	0.98	6.13	−1.07± 0.12	−0.70± 0.12	−59.55
LG04c_002648	06 39 19	−51 12 07	26.2	19.48	1.00	5.24	−1.39± 0.13	−1.09± 0.13	−164.23
LG04c_002671	06 39 25	−51 11 52	25.2	19.90	0.73	5.19	−1.33± 0.12	−1.02± 0.12	−74.46
LG04c_002674	06 39 44	−51 11 51	23.1	19.91	0.97	5.24	−1.32± 0.68	−1.00± 0.68	−119.77
LG04c_002675	06 39 36	−51 11 51	24.0	20.24	0.92	5.83	−1.08± 0.16	−0.71± 0.16	−53.71
LG04c_002702	06 40 04	−51 11 38	21.1	19.02	0.85	5.07	−1.52± 0.11	−1.25± 0.11	−114.30
LG04c_002705	06 41 15	−51 11 37	18.6	19.75	0.79	5.65	−1.22± 0.11	−0.88± 0.11	−18.61
LG04c_002714	06 39 12	−51 11 24	26.5	19.01	0.85	3.31	−2.06± 0.08	−1.91± 0.08	−138.18
LG04c_002734	06 41 05	−51 11 16	18.0	17.92	1.25	5.27	−1.64± 0.16	−1.40± 0.16	−194.25
LG04c_002749	06 39 16	−51 11 07	25.8	19.66	1.08	4.47	−1.59± 0.20	−1.34± 0.20	−130.46
LG04c_002769	06 39 23	−51 10 56	24.8	19.25	0.91	4.83	−1.55± 0.11	−1.29± 0.11	−169.19
LG04c_002771	06 41 18	−51 10 57	17.7	19.97	0.89	5.45	−1.25± 0.13	−0.91± 0.13	−29.68
LG04c_002773	06 40 52	−51 10 55	17.7	19.82	0.79	6.51	−0.95± 0.17	−0.54± 0.17	−7.19
LG04c_002780	06 40 56	−51 10 47	17.4	19.36	0.91	3.81	−1.85± 0.35	−1.65± 0.35	−1.57
LG04c_002783	06 40 33	−51 10 45	18.1	19.97	0.71	1.40	−2.48± 0.12	−2.43± 0.12	−2.31
LG04c_002814	06 38 43	−51 10 18	29.9	18.60	1.05	3.04	−2.21± 0.24	−2.10± 0.24	−28.36
LG04c_002850	06 39 49	−51 09 49	21.0	18.86	1.08	5.39	−1.45± 0.14	−1.16± 0.14	−174.70
LG04c_002854	06 41 16	−51 09 49	16.1	19.37	0.82	4.98	−1.49± 0.13	−1.21± 0.13	−99.38
LG04c_002913	06 40 59	−51 09 22	15.5	19.65	0.93	3.73	−1.82± 0.25	−1.62± 0.25	−1.35
LG04c_002927	06 40 45	−51 09 15	15.8	19.35	0.86	2.19	−2.34± 0.10	−2.26± 0.10	−1.90
LG04c_002933	06 40 49	−51 09 12	15.6	19.92	0.71	4.04	−1.68± 0.21	−1.45± 0.21	−1.31
LG04c_002944	06 39 52	−51 09 08	20.2	19.83	0.90	1.74	−2.40± 0.14	−2.33± 0.14	−1.36
LG04c_002959	06 39 20	−51 08 57	24.1	19.77	0.91	2.37	−2.22± 0.13	−2.11± 0.13	−1.41
LG04c_002996	06 41 31	−51 08 43	15.0	19.63	0.82	2.22	−2.28± 0.20	−2.19± 0.20	−1.33
LG04c_003030	06 40 42	−51 08 25	15.0	20.31	0.98	5.21	−1.26± 0.18	−0.93± 0.18	−227.79
LG04c_003061	06 39 01	−51 08 09	26.5	20.25	0.96	4.68	−1.43± 0.10	−1.14± 0.10	−124.13
LG04c_003064	06 39 17	−51 08 08	24.2	19.36	0.99	5.91	−1.20± 0.13	−0.86± 0.13	−90.68
LG04c_003077	06 39 06	−51 07 58	25.7	19.57	1.03	3.81	−1.81± 0.09	−1.61± 0.09	−90.76
LG04c_003085	06 41 03	−51 07 57	13.6	18.88	1.07	5.92	−1.29± 0.14	−0.96± 0.14	−1.31
LG04c_003092	06 39 22	−51 07 49	23.3	19.71	0.93	3.30	−1.94± 0.20	−1.77± 0.20	−1.32
LG04c_003105	06 40 29	−51 07 45	15.3	19.28	0.97	6.15	−1.15± 0.12	−0.79± 0.12	−114.97
LG04c_003121	06 40 02	−51 07 36	17.9	19.32	0.93	4.58	−1.62± 0.16	−1.37± 0.16	−14.63
LG04c_003131	06 40 23	−51 07 33	15.6	20.09	0.92	2.11	−2.24± 0.27	−2.14± 0.27	−1.57
LG04c_003140	06 40 40	−51 07 29	14.1	19.28	1.15	5.16	−1.45± 0.10	−1.16± 0.10	−125.57

Continued on next page

Table 2.A – *Carina stars, continued*

Star[7]	α	δ	r	V	B−V	Σ W	[Fe/H]	[Fe/H]	log *p*
	(J2000)		[′]			[Å]	R97,ZW	R97,CG	
LG04c_003144	06 41 14	−51 07 26	12.8	19.61	0.77	5.43	−1.31± 0.12	−0.99± 0.12	−51.99
LG04c_003175	06 40 59	−51 07 10	12.7	19.76	0.87	4.23	−1.65± 0.32	−1.41± 0.32	−1.67
LG04c_003195	06 40 59	−51 07 01	12.5	18.49	0.95	6.05	−1.31± 0.18	−0.99± 0.18	−79.19
LG04c_003274	06 39 19	−51 06 32	23.3	17.84	1.32	3.83	−2.10± 0.08	−1.96± 0.08	−1.33
LG04c_003280	06 40 40	−51 06 29	13.1	19.49	0.80	3.82	−1.82± 0.16	−1.62± 0.16	−1.30
LG04c_003300	06 40 24	−51 06 16	14.4	19.99	0.88	2.88	−2.02± 0.17	−1.87± 0.17	−1.32
LG04c_003302	06 38 35	−51 06 11	30.1	18.08	1.26	3.69	−2.10± 0.08	−1.96± 0.08	−140.58
LG04c_003308	06 40 31	−51 06 14	13.6	19.25	0.98	4.11	−1.77± 0.10	−1.56± 0.10	−1.28
LG04c_003323	06 41 17	−51 06 06	11.0	18.68	1.03	5.86	−1.33± 0.11	−1.02± 0.11	−139.86
LG04c_003329	06 41 11	−51 06 03	11.0	19.94	0.82	2.67	−2.10± 0.19	−1.96± 0.19	−1.66
LG04c_003358	06 41 27	−51 05 53	10.8	18.68	1.24	5.62	−1.41± 0.11	−1.11± 0.11	−134.92
LG04c_003374	06 39 32	−51 05 44	21.0	19.78	0.81	4.99	−1.42± 0.11	−1.12± 0.11	−81.39
LG04c_003379	06 40 28	−51 05 45	13.6	20.05	1.04	5.32	−1.27± 0.14	−0.94± 0.14	−100.63
LG04c_003419	06 39 50	−51 05 30	18.3	18.95	1.18	5.18	−1.50± 0.10	−1.22± 0.10	−48.07
LG04c_003473	06 41 04	−51 05 03	9.9	20.30	1.00	5.16	−1.28± 0.21	−0.95± 0.21	−139.26
LG04c_003505	06 40 34	−51 04 53	12.2	19.50	0.91	4.48	−1.62± 0.34	−1.37± 0.34	−1.28
LG04c_003538	06 40 49	−51 04 39	10.6	20.07	0.97	5.87	−1.10± 0.36	−0.73± 0.36	−1.44
LG04c_003585	06 41 15	−51 04 22	8.7	20.08	0.87	1.13	−2.54± 0.16	−2.51± 0.16	−1.46
LG04c_003622	06 40 01	−51 04 06	16.3	19.94	0.93	5.22	−1.32± 0.11	−1.00± 0.11	−65.06
LG04c_003625	06 40 16	−51 04 06	14.1	19.44	0.79	5.04	−1.46± 0.11	−1.17± 0.11	−74.23
LG04c_003631	06 39 41	−51 04 03	19.3	19.87	1.05	6.51	−0.94± 0.13	−0.53± 0.13	−122.55
LG04c_003632	06 38 55	−51 04 00	26.8	20.04	0.86	2.99	−1.98± 0.26	−1.82± 0.26	−1.33
LG04c_003666	06 39 44	−51 03 47	18.8	19.17	0.99	5.62	−1.33± 0.16	−1.01± 0.16	−165.92
LG04c_003672	06 40 38	−51 03 47	11.0	19.67	0.91	2.42	−2.22± 0.37	−2.11± 0.37	−2.63
LG04c_003710	06 41 31	−51 03 30	7.6	20.21	0.91	4.70	−1.43± 0.16	−1.14± 0.16	−1.37
LG04c_003713	06 40 43	−51 03 29	10.2	20.00	0.88	1.94	−2.31± 0.17	−2.22± 0.17	−1.30
LG04c_003824	06 39 15	−51 02 50	23.4	20.28	1.00	5.27	−1.25± 0.12	−0.91± 0.12	−92.39
LG04c_003840	06 39 42	−51 02 45	19.0	20.07	0.75	3.56	−1.80± 0.25	−1.60± 0.25	−1.38
LG04c_003854	06 40 41	−51 02 42	9.9	18.12	1.31	5.72	−1.47± 0.14	−1.19± 0.14	−134.44
LG04c_003873	06 41 04	−51 02 34	7.3	19.75	0.94	7.09	−0.78± 0.25	−0.34± 0.25	−1.31
LG04c_003928	06 40 18	−51 02 17	13.2	18.41	1.25	5.27	−1.56± 0.10	−1.30± 0.10	−108.91
LG04c_003974	06 40 02	−51 02 05	15.6	20.12	0.78	3.63	−1.77± 0.17	−1.56± 0.17	−1.30
LG04c_004002	06 41 30	−51 01 54	5.3	18.83	0.93	1.81	−2.54± 0.23	−2.51± 0.23	−1.46
LG04c_004027	06 40 49	−51 01 47	8.4	19.98	0.84	2.06	−2.27± 0.16	−2.18± 0.16	−1.79
LG04c_004067	06 40 11	−51 01 32	14.2	18.97	1.18	1.34	−2.66± 0.09	−2.66± 0.09	−1.99
LG04c_004068	06 41 01	−51 01 32	6.7	19.10	1.16	1.53	−2.58± 0.21	−2.56± 0.21	−1.35
LG04c_004070	06 39 53	−51 01 31	17.2	19.50	0.87	2.99	−2.07± 0.15	−1.93± 0.15	−1.70
LG04c_004078	06 41 26	−51 01 28	4.8	19.50	0.87	2.51	−2.22± 0.13	−2.11± 0.13	−1.36
LG04c_004110	06 40 31	−51 01 21	10.9	19.00	0.95	4.14	−1.80± 0.36	−1.60± 0.36	−63.30
LG04c_004153	06 40 43	−51 01 06	9.0	18.60	1.10	4.47	−1.77± 0.12	−1.56± 0.12	−1.32
LG04c_004172	06 41 08	−51 01 02	5.6	20.07	0.77	4.97	−1.37± 0.12	−1.07± 0.12	−30.16
LG04c_004189	06 41 18	−51 00 56	4.4	20.08	0.77	4.70	−1.46± 0.16	−1.17± 0.16	−11.83
LG04c_004191	06 40 38	−51 00 56	9.8	19.43	0.98	5.45	−1.33± 0.19	−1.02± 0.19	−1.29
LG04c_004195	06 41 17	−51 00 54	4.5	17.70	1.32	4.43	−1.93± 0.08	−1.76± 0.08	−1.30
LG04c_004227	06 40 42	−51 00 42	9.0	18.17	1.21	2.71	−2.38± 0.10	−2.31± 0.10	−1.68
LG04c_004249	06 40 01	−51 00 36	16.0	19.82	0.86	1.46	−2.49± 0.40	−2.44± 0.40	−1.33
LG04c_004251	06 41 20	−51 00 34	3.9	19.16	0.91	3.58	−1.95± 0.13	−1.78± 0.13	−1.32
LG04c_004271	06 41 21	−51 00 27	3.7	19.51	0.90	3.17	−2.02± 0.13	−1.86± 0.13	−1.89
LG04c_004290	06 40 43	−51 00 23	8.8	19.96	0.90	2.10	−2.27± 0.20	−2.17± 0.20	−1.29
LG04c_004308	06 41 16	−51 00 19	4.1	18.04	1.21	3.21	−2.25± 0.10	−2.15± 0.10	−1.28
LG04c_004315	06 41 23	−51 00 17	3.4	19.40	0.95	4.46	−1.64± 0.17	−1.40± 0.17	−1.28
LG04c_004526	06 40 42	−50 59 19	9.2	19.27	0.95	4.00	−1.80± 0.15	−1.60± 0.15	−135.98
LG04c_004714	06 39 46	−50 58 29	19.1	20.01	0.82	4.78	−1.44± 0.11	−1.15± 0.11	−308.60

Continued on next page

Table 2.A – *Carina stars, continued*

Star[7]	α (J2000)	δ	r [']	V	B−V	ΣW [Å]	[Fe/H] R97,ZW	[Fe/H] R97,CG	$\log p$
LG04c_004783	06 40 12	−50 58 14	14.6	19.08	1.01	2.90	−2.17± 0.11	−2.05± 0.11	−1.33
LG04c_004959	06 40 11	−50 57 24	15.2	19.23	0.88	4.39	−1.69± 0.12	−1.46± 0.12	−47.35
LG04c_005044	06 40 41	−50 56 59	10.2	19.35	0.96	4.65	−1.59± 0.21	−1.34± 0.21	−120.23
LG04c_005054	06 40 08	−50 56 57	16.0	19.02	0.91	3.31	−2.06± 0.13	−1.91± 0.13	−1.85
LG04c_005069	06 41 07	−50 56 52	5.8	19.54	0.76	4.67	−1.55± 0.15	−1.29± 0.15	−1.34
LG04c_005672	06 41 21	−51 20 19	31.0	17.95	1.26	4.99	−1.72± 0.14	−1.50± 0.14	−162.16
LG04c_005738	06 41 14	−51 18 52	28.7	18.74	1.00	3.89	−1.93± 0.12	−1.75± 0.12	−220.26
LG04c_005868	06 41 17	−51 16 09	25.0	18.69	1.09	5.22	−1.53± 0.10	−1.26± 0.10	−98.43
LG04c_005871	06 40 17	−51 16 06	25.3	19.97	0.68	5.98	−1.08± 0.14	−0.71± 0.14	−86.61
LG04c_005905	06 40 28	−51 15 24	24.0	18.91	0.92	5.26	−1.48± 0.11	−1.20± 0.11	−51.61
LG04c_005919	06 41 28	−51 15 04	23.8	18.38	1.24	5.98	−1.35± 0.13	−1.04± 0.13	−102.52
LG04c_005920	06 39 55	−51 15 00	25.2	17.65	1.46	6.24	−1.39± 0.13	−1.09± 0.13	−150.26
LG04c_005939	06 40 03	−51 14 34	24.2	19.06	0.87	5.15	−1.49± 0.13	−1.21± 0.13	−196.04
LG04c_005950	06 40 00	−51 14 28	24.3	18.08	1.46	4.84	−1.75± 0.09	−1.53± 0.09	−158.22
LG04c_005955	06 39 48	−51 14 24	25.1	20.06	0.80	4.33	−1.57± 0.20	−1.31± 0.20	−1.34
LG04c_005958	06 39 33	−51 14 21	26.5	17.92	1.13	5.35	−1.62± 0.10	−1.37± 0.10	−186.48
LG04c_005987	06 39 38	−51 13 47	25.4	18.18	1.36	5.15	−1.63± 0.09	−1.39± 0.09	−179.51
LG04c_005999	06 41 24	−51 13 32	21.5	18.39	1.01	5.65	−1.45± 0.10	−1.16± 0.10	−91.45
LG04c_006015	06 39 37	−51 13 01	24.9	18.97	0.87	4.77	−1.62± 0.19	−1.37± 0.19	−150.71
LG04c_006023	06 40 07	−51 12 48	22.1	18.39	1.34	4.77	−1.72± 0.13	−1.49± 0.13	−101.46
LG04c_006025	06 39 28	−51 12 41	25.5	18.88	0.94	5.30	−1.47± 0.12	−1.19± 0.12	−173.33
LG04c_006042	06 41 22	−51 12 26	19.9	18.67	1.09	3.45	−2.07± 0.09	−1.93± 0.09	−1.31
LG04c_006061	06 41 01	−51 12 05	19.1	18.86	1.08	5.29	−1.48± 0.10	−1.20± 0.10	−45.87
LG04c_006063	06 40 31	−51 12 03	19.8	19.46	0.89	3.41	−1.95± 0.16	−1.78± 0.16	−80.26
LG04c_006066	06 39 37	−51 11 59	24.0	18.69	0.90	4.71	−1.68± 0.15	−1.45± 0.15	−102.88
LG04c_006077	06 41 18	−51 11 51	19.0	19.73	0.81	4.81	−1.48± 0.10	−1.20± 0.10	−23.36
LG04c_006087	06 39 32	−51 11 37	24.3	18.78	1.00	5.33	−1.48± 0.11	−1.20± 0.11	−131.59
LG04c_006089	06 40 03	−51 11 31	21.1	19.13	1.09	5.27	−1.44± 0.12	−1.15± 0.12	−86.03
LG04c_006095	06 39 01	−51 11 23	27.9	19.31	0.87	4.05	−1.78± 0.11	−1.57± 0.11	−109.03
LG04c_006118	06 39 32	−51 10 56	23.8	19.06	0.85	4.48	−1.69± 0.14	−1.46± 0.14	−73.70
LG04c_006140	06 39 54	−51 10 27	20.9	19.02	0.85	4.11	−1.81± 0.17	−1.61± 0.17	−56.29
LG04c_006158	06 40 40	−51 09 48	16.7	18.30	1.03	4.90	−1.69± 0.19	−1.46± 0.19	−59.11
LG04c_006159	06 38 46	−51 09 43	29.3	19.78	0.90	5.50	−1.26± 0.12	−0.93± 0.12	−84.65
LG04c_006160	06 39 01	−51 09 42	27.0	18.26	1.41	5.33	−1.57± 0.11	−1.31± 0.11	−153.81
LG04c_006180	06 39 06	−51 09 13	26.2	19.05	1.06	4.46	−1.70± 0.09	−1.47± 0.09	−158.75
LG04c_006195	06 41 20	−51 09 02	15.1	19.52	1.10	5.59	−1.28± 0.11	−0.95± 0.11	−172.37
LG04c_006240	06 40 15	−51 08 05	16.8	18.89	0.98	5.51	−1.41± 0.10	−1.11± 0.10	−48.19
LG04c_006262	06 39 16	−51 07 26	24.0	19.22	0.94	5.30	−1.42± 0.12	−1.12± 0.12	−52.64
LG04c_006265	06 40 32	−51 07 27	14.7	18.86	0.94	5.13	−1.53± 0.10	−1.26± 0.10	−108.41
LG04c_006270	06 39 11	−51 07 15	24.7	19.55	0.97	4.08	−1.73± 0.09	−1.51± 0.09	−116.57
LG04c_006272	06 40 15	−51 07 16	16.2	19.79	1.05	5.28	−1.33± 0.13	−1.01± 0.13	−100.49
LG04c_006292	06 39 34	−51 06 56	21.2	18.41	1.10	6.23	−1.27± 0.14	−0.94± 0.14	−95.69
LG04c_006303	06 40 27	−51 06 38	14.4	19.70	0.80	5.19	−1.37± 0.13	−1.06± 0.13	−18.39
LG04c_006331	06 39 04	−51 06 06	25.4	19.34	0.88	3.34	−1.99± 0.12	−1.83± 0.12	−105.82
LG04c_006341	06 40 23	−51 05 58	14.3	19.29	1.07	4.73	−1.58± 0.10	−1.32± 0.10	−111.91
LG04c_006343	06 39 03	−51 05 54	25.7	19.28	1.15	1.09	−2.69± 0.14	−2.69± 0.14	−1.31
LG04c_006346	06 41 03	−51 05 55	11.0	19.75	0.96	3.70	−1.81± 0.15	−1.61± 0.15	−1.31
LG04c_006347	06 41 11	−51 05 54	10.8	19.54	0.96	3.66	−1.86± 0.14	−1.67± 0.14	−1.29
LG04c_006352	06 41 21	−51 05 48	10.6	19.45	1.09	2.91	−2.10± 0.15	−1.97± 0.15	−1.53
LG04c_006374	06 40 27	−51 05 28	13.5	19.34	1.06	5.69	−1.28± 0.14	−0.95± 0.14	−113.40
LG04c_006381	06 41 14	−51 05 19	10.0	18.58	1.08	4.06	−1.90± 0.11	−1.72± 0.11	−1.35
LG04c_006386	06 39 34	−51 05 16	20.6	18.99	0.94	4.89	−1.58± 0.10	−1.32± 0.10	−55.69
LG04c_006400	06 40 13	−51 05 03	15.0	19.52	0.88	5.61	−1.27± 0.11	−0.94± 0.11	−120.24

Continued on next page

Table 2.A – *Carina stars, continued*

Star[7]	α	δ	r	V	B−V	Σ W	[Fe/H]	[Fe/H]	log *p*
	(J2000)		[′]			[Å]	R97,ZW	R97,CG	
LG04c_006421	06 40 04	−51 04 47	16.0	18.94	1.07	4.31	−1.76± 0.15	−1.55± 0.15	−1.30
LG04c_006433	06 40 50	−51 04 31	10.4	19.20	1.03	2.83	−2.17± 0.30	−2.05± 0.30	−1.66
LG04c_006476	06 40 28	−51 03 43	12.3	19.90	1.03	2.53	−2.15± 0.26	−2.02± 0.26	−1.33
LG04c_006477	06 41 22	−51 03 43	7.8	17.71	1.37	4.99	−1.76± 0.10	−1.55± 0.10	−1.32
LG04c_006479	06 41 00	−51 03 43	8.7	18.37	1.19	4.36	−1.85± 0.10	−1.65± 0.10	−1.28
LG04c_006516	06 40 00	−51 02 58	16.1	18.86	0.94	6.01	−1.26± 0.14	−0.93± 0.14	−52.71
LG04c_006519	06 40 26	−51 02 55	12.1	19.71	0.95	2.55	−2.17± 0.59	−2.05± 0.59	−1.48
LG04c_006552	06 40 58	−51 02 27	7.8	17.63	1.26	5.41	−1.65± 0.09	−1.41± 0.09	−1.28
LG04c_006557	06 41 04	−51 02 19	7.1	19.10	0.92	5.37	−1.42± 0.12	−1.12± 0.12	−124.92
LG04c_006562	06 41 08	−51 02 12	6.5	19.59	0.90	3.26	−1.97± 0.15	−1.81± 0.15	−1.30
LG04c_006563	06 40 11	−51 02 14	14.3	18.90	1.00	5.93	−1.28± 0.34	−0.95± 0.34	−65.16
LG04c_006573	06 40 58	−51 02 00	7.4	17.87	1.26	5.17	−1.68± 0.10	−1.45± 0.10	−1.28
LG04c_006575	06 40 40	−51 01 59	9.8	17.94	1.23	5.02	−1.72± 0.09	−1.49± 0.09	−1.30
LG04c_006577	06 41 19	−51 01 58	5.6	19.27	0.88	5.97	−1.20± 0.22	−0.86± 0.22	−162.30
LG04c_006593	06 40 31	−51 01 45	11.0	18.44	1.00	5.01	−1.63± 0.11	−1.39± 0.11	−11.96
LG04c_006594	06 41 10	−51 01 45	5.9	17.91	1.16	4.13	−1.99± 0.09	−1.83± 0.09	−1.37
LG04c_006599	06 40 34	−51 01 42	10.6	19.03	0.98	1.30	−2.66± 0.39	−2.66± 0.39	−1.49
LG04c_006600	06 40 51	−51 01 39	8.1	18.75	1.14	4.84	−1.63± 0.11	−1.39± 0.11	−180.92
LG04c_006601	06 40 46	−51 01 39	8.7	17.61	1.32	5.07	−1.76± 0.10	−1.54± 0.10	−1.36
LG04c_006613	06 41 10	−51 01 29	5.7	18.90	0.95	4.25	−1.79± 0.13	−1.58± 0.13	−1.30
LG04c_006621	06 41 15	−51 01 16	5.0	17.94	1.16	1.32	−2.84± 0.08	−2.88± 0.08	−1.33
LG04c_006625	06 41 11	−51 01 14	5.4	18.72	1.22	3.87	−1.93± 0.21	−1.76± 0.21	−1.28
LG04c_006633	06 39 06	−51 01 05	25.2	18.39	1.05	4.85	−1.69± 0.09	−1.46± 0.09	−142.79
LG04c_006634	06 39 33	−51 01 06	20.6	19.02	1.01	5.49	−1.39± 0.34	−1.09± 0.34	−161.71
LG04c_006641	06 40 43	−51 01 05	9.1	18.50	1.13	4.63	−1.74± 0.09	−1.52± 0.09	−1.32
LG04c_006654	06 40 41	−51 00 52	9.3	19.18	0.84	3.99	−1.82± 0.12	−1.62± 0.12	−101.13
LG04c_006656	06 38 47	−51 00 47	28.5	18.39	0.95	4.72	−1.73± 0.12	−1.51± 0.12	−134.52
LG04c_006665	06 39 58	−51 00 43	16.4	17.40	1.65	5.10	−1.78± 0.09	−1.57± 0.09	−160.62
LG04c_006673	06 39 55	−51 00 35	16.9	17.91	1.04	3.12	−2.30± 0.16	−2.21± 0.16	−87.78
LG04c_006760	06 38 50	−50 59 18	28.4	18.51	1.14	4.89	−1.66± 0.10	−1.42± 0.10	−122.25
LG04c_006770	06 41 15	−50 59 14	3.6	19.28	1.14	4.42	−1.67± 0.16	−1.44± 0.16	−88.28
LG04c_006788	06 40 22	−50 59 02	12.5	19.03	1.02	4.71	−1.63± 0.13	−1.38± 0.13	−1.83
LG04c_006811	06 39 14	−50 58 45	24.5	18.71	0.90	5.32	−1.50± 0.12	−1.22± 0.12	−97.65
LG04c_006876	06 39 47	−50 57 44	19.2	18.34	0.96	1.53	−2.71± 0.21	−2.72± 0.21	−1.37
LG04c_006878	06 40 46	−50 57 43	8.9	18.92	0.98	4.48	−1.72± 0.13	−1.49± 0.13	−91.44
LG04c_007012	06 38 59	−50 55 27	28.6	18.54	0.99	4.67	−1.72± 0.18	−1.50± 0.18	−74.33
LG04c_007039	06 41 00	−50 55 07	8.5	19.56	0.94	5.46	−1.31± 0.20	−0.99± 0.20	−1.45
LG04c_007244	06 40 36	−51 06 53	13.8	17.53	1.54	4.23	−2.02± 0.08	−1.87± 0.08	−119.51
LG04c_007254	06 41 01	−51 05 48	11.0	18.82	1.06	5.15	−1.53± 0.10	−1.26± 0.10	−57.88
LG04c_007260	06 41 05	−51 05 26	10.3	17.54	1.37	5.16	−1.74± 0.10	−1.52± 0.10	−1.39
LG04c_007283	06 41 07	−51 02 39	7.1	19.68	0.82	6.06	−1.11± 0.25	−0.74± 0.25	−1.28
LG04c_007441	06 39 07	−51 12 18	27.7	18.22	1.35	5.13	−1.63± 0.18	−1.39± 0.18	−49.92
LG04d_000332	06 41 44	−51 19 19	30.7	19.86	1.00	5.08	−1.37± 0.11	−1.07± 0.11	−69.65
LG04d_000367	06 42 59	−51 18 26	36.0	18.97	0.96	5.36	−1.44± 0.14	−1.15± 0.14	−78.76
LG04d_000475	06 41 00	−51 16 15	24.8	18.16	1.00	5.51	−1.53± 0.10	−1.26± 0.10	−108.49
LG04d_000479	06 42 50	−51 16 09	32.0	18.27	1.06	5.35	−1.56± 0.10	−1.30± 0.10	−124.74
LG04d_000505	06 43 07	−51 15 23	32.9	17.92	1.13	5.22	−1.66± 0.11	−1.42± 0.11	−147.50
LG04d_000592	06 42 51	−51 13 47	29.0	19.27	1.06	5.06	−1.48± 0.10	−1.20± 0.10	−128.58
LG04d_000620	06 43 07	−51 13 11	30.2	19.01	1.13	5.20	−1.48± 0.14	−1.20± 0.14	−109.09
LG04d_000636	06 41 22	−51 12 57	20.6	19.66	1.10	4.53	−1.58± 0.14	−1.32± 0.14	−116.24
LG04d_000656	06 42 20	−51 12 13	23.5	18.99	1.07	4.09	−1.82± 0.24	−1.62± 0.24	−157.92
LG04d_000676	06 41 57	−51 11 48	20.9	19.13	1.00	4.82	−1.58± 0.10	−1.32± 0.10	−131.69
LG04d_000677	06 42 23	−51 11 47	23.2	19.22	0.94	5.09	−1.48± 0.13	−1.20± 0.13	−147.75

Continued on next page

Table 2.A – *Carina stars, continued*

Star[7]	α	δ	r	V	B−V	Σ W	[Fe/H]	[Fe/H]	log p
	(J2000)		[′]			[Å]	R97,ZW	R97,CG	
LG04d_000705	06 41 34	−51 11 17	18.8	19.59	0.90	5.23	−1.37± 0.17	−1.07± 0.17	−54.35
LG04d_000812	06 41 34	−51 09 01	15.5	18.68	0.89	3.20	−2.15± 0.22	−2.02± 0.22	−58.60
LG04d_000815	06 42 22	−51 08 58	19.4	17.88	1.37	5.24	−1.66± 0.13	−1.42± 0.13	−192.72
LG04d_000823	06 42 36	−51 08 51	20.9	19.89	0.96	4.45	−1.56± 0.12	−1.30± 0.12	−68.50
LG04d_000827	06 42 25	−51 08 50	19.6	17.84	1.38	4.87	−1.78± 0.14	−1.57± 0.14	−105.43
LG04d_000832	06 43 06	−51 08 43	24.8	18.29	1.04	4.88	−1.70± 0.09	−1.47± 0.09	−90.86
LG04d_000883	06 41 51	−51 07 57	15.1	19.25	1.00	4.25	−1.73± 0.11	−1.51± 0.11	−2.06
LG04d_000888	06 42 06	−51 07 49	16.2	18.52	1.00	4.94	−1.64± 0.10	−1.40± 0.10	−65.29
LG04d_000895	06 41 47	−51 07 42	14.4	19.53	0.76	6.09	−1.12± 0.22	−0.76± 0.22	−58.70
LG04d_000938	06 41 45	−51 06 59	13.3	17.59	1.33	5.29	−1.69± 0.19	−1.46± 0.19	−184.09
LG04d_000959	06 41 39	−51 06 27	12.2	19.97	0.95	3.61	−1.80± 0.19	−1.60± 0.19	−1.33
LG04d_000967	06 41 07	−51 06 20	11.4	17.27	1.16	4.83	−1.89± 0.09	−1.70± 0.09	−120.43
LG04d_000972	06 41 40	−51 06 13	11.9	18.79	0.90	3.41	−2.06± 0.11	−1.92± 0.11	−27.03
LG04d_000997	06 41 34	−51 05 42	10.8	20.02	0.93	3.13	−1.94± 0.19	−1.77± 0.19	−1.32
LG04d_001054	06 42 06	−51 04 43	12.1	19.05	1.12	4.22	−1.77± 0.11	−1.56± 0.11	−158.94
LG04d_001056	06 42 35	−51 04 37	15.7	18.74	1.01	5.78	−1.35± 0.11	−1.04± 0.11	−61.17
LG04d_001065	06 43 08	−51 04 21	20.4	19.00	0.86	5.29	−1.46± 0.11	−1.17± 0.11	−160.32
LG04d_001089	06 42 00	−51 04 01	10.5	19.15	1.08	5.37	−1.41± 0.11	−1.11± 0.11	−65.51
LG04d_001093	06 41 49	−51 03 58	9.4	19.09	1.03	4.71	−1.62± 0.11	−1.37± 0.11	−178.73
LG04d_001107	06 42 01	−51 03 44	10.3	17.79	1.39	5.69	−1.54± 0.10	−1.27± 0.10	−1.28
LG04d_001127	06 42 36	−51 03 25	14.6	17.75	1.14	5.53	−1.59± 0.09	−1.34± 0.09	−76.01
LG04d_001163	06 42 56	−51 02 52	17.1	18.36	1.10	4.71	−1.74± 0.10	−1.52± 0.10	−1.31
LG04d_001219	06 42 00	−51 01 53	7.8	17.63	1.49	4.18	−2.02± 0.08	−1.87± 0.08	−1.58
LG04d_001234	06 43 29	−51 01 36	21.6	19.24	0.80	4.31	−1.72± 0.12	−1.49± 0.12	−31.71
LG04d_001239	06 42 17	−51 01 36	9.8	19.83	1.01	2.94	−2.03± 0.26	−1.88± 0.26	−1.82
LG04d_001240	06 42 11	−51 01 36	9.0	19.55	0.77	3.84	−1.80± 0.17	−1.60± 0.17	−1.58
LG04d_001308	06 41 37	−51 00 38	3.8	17.99	1.26	4.81	−1.77± 0.09	−1.56± 0.09	−1.32
LG04d_001470	06 42 27	−50 58 37	9.0	20.11	0.67	4.44	−1.53± 0.19	−1.26± 0.19	−2.35
LG04d_001485	06 43 24	−50 58 27	18.8	18.40	0.95	5.35	−1.54± 0.15	−1.27± 0.15	−25.08
LG04d_001570	06 41 57	−50 57 32	3.4	19.03	1.11	5.59	−1.36± 0.17	−1.05± 0.17	−108.90
LG04d_001724	06 41 43	−50 55 50	2.9	17.98	1.04	4.78	−1.78± 0.16	−1.57± 0.16	−214.99
LG04d_001762	06 43 03	−50 55 20	14.4	18.73	0.92	5.63	−1.40± 0.10	−1.10± 0.10	−74.08
LG04d_001808	06 42 35	−50 54 40	9.9	20.13	1.01	5.36	−1.25± 0.11	−0.91± 0.11	−19.90
LG04d_002352	06 42 26	−51 19 30	34.1	19.32	1.07	1.12	−2.67± 0.32	−2.67± 0.32	−126.26
LG04d_002444	06 42 14	−51 18 23	31.5	19.15	0.83	5.29	−1.43± 0.13	−1.14± 0.13	−4.43
LG04d_002447	06 41 35	−51 18 22	28.8	19.19	0.98	5.13	−1.47± 0.12	−1.19± 0.12	−3.43
LG04d_002461	06 42 11	−51 18 06	30.8	19.85	0.94	5.83	−1.15± 0.19	−0.79± 0.19	−31.72
LG04d_002522	06 41 39	−51 17 20	27.6	19.26	1.01	2.78	−2.18± 0.14	−2.06± 0.14	−1.63
LG04d_002529	06 43 00	−51 17 12	34.4	19.44	1.06	6.59	−0.99± 0.15	−0.59± 0.15	−83.44
LG04d_002562	06 42 37	−51 16 49	31.4	19.29	1.07	5.48	−1.35± 0.12	−1.04± 0.12	−86.68
LG04d_002637	06 42 26	−51 16 06	29.4	20.12	0.86	6.19	−0.99± 0.14	−0.60± 0.14	−44.04
LG04d_002639	06 41 21	−51 16 06	25.0	19.72	0.73	5.50	−1.27± 0.27	−0.94± 0.27	−32.81
LG04d_002642	06 42 40	−51 16 02	30.7	19.40	0.90	4.48	−1.63± 0.17	−1.39± 0.17	−7.86
LG04d_002663	06 42 37	−51 15 48	30.1	18.43	0.98	4.86	−1.68± 0.16	−1.45± 0.16	−31.82
LG04d_002676	06 41 43	−51 15 45	25.6	19.31	0.80	4.75	−1.57± 0.13	−1.31± 0.13	−75.97
LG04d_002760	06 41 53	−51 14 52	25.0	19.49	0.88	4.28	−1.68± 0.12	−1.45± 0.12	−162.53
LG04d_002805	06 42 03	−51 14 22	25.0	18.80	1.16	5.21	−1.51± 0.21	−1.24± 0.21	−70.36
LG04d_002862	06 42 25	−51 13 41	26.1	18.92	0.95	5.89	−1.29± 0.10	−0.96± 0.10	−171.46
LG04d_002926	06 42 10	−51 12 47	23.4	19.94	0.90	4.69	−1.48± 0.12	−1.20± 0.12	−146.82
LG04d_002928	06 42 12	−51 12 43	23.5	18.82	0.87	4.67	−1.67± 0.10	−1.44± 0.10	−99.40
LG04d_002931	06 41 47	−51 12 42	21.5	18.66	1.14	2.44	−2.38± 0.08	−2.31± 0.08	−1.30
LG04d_002949	06 42 32	−51 12 32	25.2	19.70	0.83	4.11	−1.70± 0.20	−1.47± 0.20	−1.89
LG04d_002972	06 42 39	−51 12 17	25.7	18.74	1.25	5.78	−1.35± 0.11	−1.04± 0.11	−74.72

Continued on next page

Table 2.A – *Carina stars, continued*

Star[7]	α	δ	r	V	B−V	Σ W	[Fe/H]	[Fe/H]	log p
	(J2000)		[′]			[Å]	R97,ZW	R97,CG	
LG04d_003089	06 42 45	−51 10 41	24.3	19.06	0.92	4.06	−1.82± 0.11	−1.62± 0.11	−109.70
LG04d_003092	06 42 10	−51 10 36	20.4	18.65	0.91	5.00	−1.60± 0.10	−1.35± 0.10	−175.47
LG04d_003138	06 42 12	−51 09 58	19.7	19.71	0.73	4.98	−1.43± 0.13	−1.14± 0.13	−112.99
LG04d_003251	06 43 21	−51 08 51	27.0	19.41	0.78	4.88	−1.51± 0.16	−1.24± 0.16	−125.79
LG04d_003275	06 42 55	−51 08 33	23.1	19.16	1.02	5.02	−1.51± 0.10	−1.24± 0.10	−3.31
LG04d_003299	06 42 40	−51 08 21	20.9	18.28	1.00	5.63	−1.47± 0.10	−1.19± 0.10	−118.36
LG04d_003342	06 42 40	−51 07 55	20.2	19.71	0.79	3.01	−2.03± 0.32	−1.88± 0.32	−1.65
LG04d_003357	06 42 07	−51 07 49	16.4	19.07	1.01	5.28	−1.45± 0.14	−1.16± 0.14	−70.09
LG04d_003362	06 42 27	−51 07 44	18.5	19.66	0.87	3.65	−1.85± 0.08	−1.65± 0.08	−70.52
LG04d_003375	06 42 07	−51 07 37	16.0	19.51	0.96	3.25	−1.99± 0.16	−1.83± 0.16	−1.47
LG04d_003426	06 41 51	−51 07 05	13.9	19.62	0.74	4.49	−1.59± 0.13	−1.34± 0.13	−76.60
LG04d_003428	06 42 31	−51 07 02	18.0	19.16	0.93	4.03	−1.81± 0.12	−1.61± 0.12	−64.36
LG04d_003459	06 41 59	−51 06 48	14.2	19.13	1.07	3.86	−1.87± 0.12	−1.68± 0.12	−1.34
LG04d_003471	06 42 21	−51 06 41	16.3	20.22	1.01	3.95	−1.66± 0.09	−1.42± 0.09	−26.12
LG04d_003496	06 41 53	−51 06 32	13.2	19.77	0.87	5.58	−1.24± 0.12	−0.90± 0.12	−19.86
LG04d_003527	06 41 51	−51 06 19	12.8	19.22	0.87	4.82	−1.56± 0.12	−1.30± 0.12	−82.97
LG04d_003539	06 41 34	−51 06 14	11.6	18.54	0.96	4.96	−1.63± 0.14	−1.39± 0.14	−119.77
LG04d_003625	06 41 41	−51 05 39	11.2	19.29	1.06	3.77	−1.87± 0.18	−1.68± 0.18	−1.33
LG04d_003626	06 41 50	−51 05 39	11.8	19.47	0.88	5.33	−1.37± 0.11	−1.06± 0.11	−107.60
LG04d_003634	06 41 59	−51 05 35	12.5	19.48	1.10	5.02	−1.46± 0.12	−1.17± 0.12	−98.80
LG04d_003644	06 41 46	−51 05 33	11.4	20.17	1.00	7.12	−0.70± 0.29	−0.24± 0.29	−10.06
LG04d_003688	06 41 23	−51 05 14	9.9	19.42	0.79	5.64	−1.28± 0.26	−0.95± 0.26	−20.46
LG04d_003702	06 41 44	−51 05 07	10.6	20.01	0.76	4.94	−1.39± 0.12	−1.09± 0.12	−17.55
LG04d_003711	06 42 47	−51 04 59	17.8	19.11	0.94	3.55	−1.97± 0.11	−1.80± 0.11	−35.62
LG04d_003819	06 43 01	−51 04 12	19.3	19.71	0.76	4.50	−1.58± 0.13	−1.32± 0.13	−82.39
LG04d_003823	06 43 13	−51 04 10	21.0	19.51	0.76	5.73	−1.24± 0.21	−0.90± 0.21	−26.27
LG04d_003859	06 42 21	−51 04 00	13.0	19.68	0.92	2.52	−2.19± 0.24	−2.07± 0.24	−1.30
LG04d_003890	06 42 21	−51 03 51	12.9	18.72	1.09	5.52	−1.43± 0.11	−1.14± 0.11	−150.17
LG04d_003893	06 41 48	−51 03 51	9.1	19.79	0.93	3.10	−1.99± 0.12	−1.83± 0.12	−1.91
LG04d_003955	06 42 20	−51 03 32	12.4	18.36	1.18	4.79	−1.72± 0.11	−1.49± 0.11	−144.50
LG04d_003981	06 42 20	−51 03 24	12.3	20.13	0.89	3.07	−1.94± 0.18	−1.77± 0.18	−1.35
LG04d_004005	06 42 54	−51 03 11	17.2	19.65	0.99	5.09	−1.41± 0.20	−1.11± 0.20	−1.79
LG04d_004013	06 42 16	−51 03 11	11.4	20.06	0.95	2.20	−2.22± 0.21	−2.11± 0.21	−1.94
LG04d_004016	06 42 29	−51 03 09	13.2	19.25	0.86	5.21	−1.44± 0.15	−1.15± 0.15	−123.14
LG04d_004028	06 42 18	−51 03 04	11.6	19.91	0.88	3.88	−1.73± 0.17	−1.51± 0.17	−1.29
LG04d_004046	06 41 52	−51 02 59	8.3	19.49	1.01	4.25	−1.69± 0.18	−1.46± 0.18	−1.60
LG04d_004090	06 43 06	−51 02 38	18.5	19.86	0.78	4.47	−1.56± 0.11	−1.30± 0.11	−48.84
LG04d_004094	06 42 10	−51 02 41	10.1	19.67	0.86	3.72	−1.82± 0.14	−1.62± 0.14	−1.28
LG04d_004119	06 40 52	−51 02 33	8.4	19.44	0.78	4.94	−1.49± 0.11	−1.21± 0.11	−115.60
LG04d_004201	06 42 09	−51 02 05	9.3	19.57	0.76	3.67	−1.85± 0.08	−1.66± 0.08	−66.26
LG04d_004287	06 41 53	−51 01 31	6.5	19.59	1.00	1.80	−2.42± 0.34	−2.36± 0.34	−1.28
LG04d_004311	06 41 54	−51 01 23	6.4	19.48	0.84	3.72	−1.85± 0.12	−1.66± 0.12	−1.35
LG04d_004325	06 43 19	−51 01 13	19.6	19.79	0.89	4.08	−1.69± 0.34	−1.46± 0.34	−2.37
LG04d_004357	06 43 17	−51 01 01	19.2	18.69	0.91	4.56	−1.73± 0.10	−1.51± 0.10	−39.34
LG04d_004398	06 42 17	−51 00 53	9.1	20.03	1.00	4.13	−1.63± 0.20	−1.39± 0.20	−1.69
LG04d_004514	06 42 48	−51 00 22	13.7	19.82	0.99	5.85	−1.15± 0.13	−0.79± 0.13	−72.12
LG04d_004528	06 42 16	−51 00 19	8.5	19.52	0.96	2.84	−2.11± 0.12	−1.98± 0.12	−1.46
LG04d_004565	06 41 56	−51 00 10	5.2	19.01	1.08	2.94	−2.17± 0.14	−2.05± 0.14	−1.30
LG04d_004684	06 42 20	−50 59 42	8.6	19.97	1.04	5.63	−1.19± 0.12	−0.84± 0.12	−149.49
LG04d_004712	06 42 52	−50 59 34	14.0	20.09	0.90	3.76	−1.74± 0.16	−1.52± 0.16	−1.33
LG04d_004946	06 41 57	−50 58 44	3.9	19.00	0.93	4.49	−1.70± 0.10	−1.47± 0.10	−114.19
LG04d_005032	06 43 54	−50 58 19	24.0	19.51	0.98	2.48	−2.23± 0.51	−2.12± 0.51	−1.58
LG04d_005162	06 42 48	−50 57 59	12.4	19.91	1.04	5.19	−1.33± 0.13	−1.02± 0.13	−36.11

Continued on next page

Table 2.A – *Carina stars, continued*

Star[7]	α	δ	r	V	B−V	Σ W	[Fe/H]	[Fe/H]	log p
	(J2000)		[′]			[Å]	R97,ZW	R97,CG	
LG04d_005211	06 42 28	−50 57 48	8.9	18.89	0.91	4.31	−1.77± 0.10	−1.56± 0.10	−1.34
LG04d_005218	06 42 05	−50 57 48	4.9	18.22	1.26	3.32	−2.19± 0.14	−2.07± 0.14	−1.28
LG04d_005313	06 42 01	−50 57 27	4.0	19.67	0.77	2.98	−2.05± 0.14	−1.90± 0.14	−1.29
LG04d_005317	06 42 17	−50 57 25	6.9	19.68	0.78	3.90	−1.76± 0.16	−1.55± 0.16	−1.29
LG04d_005810	06 41 42	−50 55 28	3.4	18.78	0.89	5.30	−1.49± 0.12	−1.21± 0.12	−108.72
LG04d_005813	06 43 42	−50 55 19	21.0	18.65	0.98	5.67	−1.40± 0.11	−1.10± 0.11	−128.63
LG04d_005869	06 42 14	−50 55 12	6.4	19.68	1.00	2.33	−2.24± 0.16	−2.14± 0.16	−1.83
LG04d_006048	06 41 54	−51 21 45	34.7	18.84	1.20	4.87	−1.61± 0.49	−1.36± 0.49	−98.26
LG04d_006106	06 42 57	−51 19 10	36.7	19.21	0.93	5.10	−1.48± 0.14	−1.20± 0.14	−117.99
LG04d_006151	06 41 46	−51 17 15	27.9	19.04	0.97	4.76	−1.61± 0.10	−1.36± 0.10	−76.75
LG04d_006192	06 42 31	−51 15 46	29.5	19.74	1.00	5.15	−1.37± 0.12	−1.07± 0.12	−18.17
LG04d_006198	06 42 32	−51 15 29	29.1	18.65	1.24	5.30	−1.51± 0.10	−1.24± 0.10	−194.57
LG04d_006199	06 42 36	−51 15 27	29.5	19.30	0.98	5.07	−1.47± 0.10	−1.19± 0.10	−124.63
LG04d_006210	06 43 01	−51 14 48	31.4	19.90	0.90	4.71	−1.48± 0.16	−1.20± 0.16	−56.35
LG04d_006211	06 42 33	−51 14 48	28.3	19.15	1.08	4.76	−1.59± 0.13	−1.34± 0.13	−120.61
LG04d_006261	06 42 50	−51 13 02	27.9	18.82	1.13	3.02	−2.18± 0.13	−2.06± 0.13	−1.30
LG04d_006264	06 42 05	−51 13 00	23.2	18.86	1.02	5.23	−1.50± 0.14	−1.22± 0.14	−66.46
LG04d_006306	06 42 53	−51 11 27	26.3	18.19	1.14	5.20	−1.62± 0.13	−1.37± 0.13	−77.55
LG04d_006349	06 41 26	−51 10 17	17.0	19.35	0.98	3.90	−1.82± 0.09	−1.62± 0.09	−46.36
LG04d_006370	06 42 21	−51 09 31	20.0	18.57	0.99	5.05	−1.60± 0.10	−1.35± 0.10	−117.29
LG04d_006371	06 41 07	−51 09 33	15.7	19.45	0.85	3.47	−1.93± 0.21	−1.76± 0.21	−84.73
LG04d_006377	06 42 18	−51 09 18	19.4	19.41	0.82	4.96	−1.49± 0.12	−1.21± 0.12	−154.96
LG04d_006433	06 42 38	−51 07 15	19.3	19.90	1.02	3.73	−1.78± 0.17	−1.57± 0.17	−1.28
LG04d_006434	06 42 17	−51 07 16	16.7	19.17	1.08	4.74	−1.59± 0.20	−1.34± 0.20	−96.51
LG04d_006454	06 43 07	−51 06 14	22.1	18.83	0.91	4.99	−1.58± 0.16	−1.32± 0.16	−120.32
LG04d_006469	06 42 33	−51 05 50	16.8	18.45	0.95	5.00	−1.63± 0.12	−1.39± 0.12	−112.47
LG04d_006485	06 42 06	−51 05 31	13.2	18.67	1.23	3.05	−2.19± 0.10	−2.08± 0.10	−140.27
LG04d_006517	06 42 02	−51 04 22	11.2	17.87	1.14	4.82	−1.79± 0.09	−1.58± 0.09	−1.28
LG04d_006544	06 42 28	−51 03 47	13.8	19.13	0.97	4.37	−1.72± 0.10	−1.49± 0.10	−100.47
LG04d_006554	06 42 13	−51 03 26	11.3	18.81	0.96	5.21	−1.51± 0.11	−1.24± 0.11	−50.59
LG04d_006568	06 43 24	−51 03 04	21.9	19.42	0.91	3.60	−1.90± 0.07	−1.72± 0.07	−53.62
LG04d_006637	06 42 01	−51 01 29	7.4	18.35	1.20	5.25	−1.58± 0.37	−1.32± 0.37	−177.87
LG04d_006644	06 41 46	−51 01 23	5.6	17.88	1.31	3.56	−2.16± 0.08	−2.04± 0.08	−1.60
LG04d_006677	06 41 45	−51 00 50	4.6	19.43	0.80	2.82	−2.14± 0.12	−2.01± 0.12	−1.35
LG04d_006686	06 42 46	−51 00 38	13.6	20.03	0.85	1.47	−2.45± 0.38	−2.39± 0.38	−1.60
LG04d_006687	06 43 11	−51 00 34	17.9	19.83	0.86	2.59	−2.14± 0.17	−2.01± 0.17	−5.26
LG04d_006694	06 42 23	−51 00 32	9.8	19.89	0.79	3.95	−1.72± 0.23	−1.49± 0.23	−1.35
LG04d_006744	06 43 31	−50 59 43	20.7	18.11	1.06	5.06	−1.67± 0.15	−1.44± 0.15	−154.61
LG04d_006791	06 43 55	−50 58 57	24.5	18.46	1.22	3.38	−2.13± 0.09	−2.00± 0.09	−1.30
LG04d_006824	06 43 23	−50 58 29	18.8	19.09	0.96	5.13	−1.49± 0.15	−1.21± 0.15	−63.88
LG04d_006889	06 42 14	−50 57 38	6.3	18.34	0.99	5.25	−1.58± 0.11	−1.32± 0.11	−122.32
LG04d_007195	06 42 08	−51 21 02	34.7	17.82	1.28	3.99	−2.05± 0.13	−1.90± 0.13	−150.62
LG04d_007222	06 42 34	−51 15 54	29.9	18.90	1.14	5.93	−1.28± 0.12	−0.95± 0.12	−106.24
LG04d_007229	06 41 28	−51 13 19	21.3	18.41	0.98	4.84	−1.69± 0.16	−1.46± 0.16	−136.85
LG04d_007274	06 41 31	−51 07 58	13.9	19.79	0.76	5.20	−1.35± 0.12	−1.04± 0.12	−106.20
LG04d_007318	06 41 46	−51 02 01	6.4	19.78	1.02	4.22	−1.65± 0.12	−1.41± 0.12	−1.52
LG04d_007330	06 41 33	−51 00 48	3.9	19.66	1.03	4.18	−1.68± 0.15	−1.45± 0.15	−1.42
car1_t005	06 42 31	−50 51 45	10.8	19.49	0.94	2.68	−2.17± 0.32	−2.05± 0.32	−1.32
car1_t007	06 42 30	−50 56 33	8.9	18.77	1.01	4.91	−1.61± 0.35	−1.36± 0.35	−1.39
car1_t015	06 41 50	−50 56 35	2.6	18.62	1.00	4.41	−1.79± 0.12	−1.58± 0.12	−1.35
car1_t016	06 42 17	−50 56 26	6.8	18.64	1.02	5.30	−1.51± 0.12	−1.24± 0.12	−1.28
car1_t023	06 41 37	−50 54 59	4.2	18.71	1.00	4.81	−1.65± 0.13	−1.41± 0.13	−1.36
car1_t024	06 41 41	−50 54 46	4.4	18.59	1.02	2.40	−2.40± 0.51	−2.34± 0.51	−1.97

Continued on next page

Table 2.A – *Carina stars, continued*

Star[7]	α	δ	r	V	B−V	Σ W	[Fe/H]	[Fe/H]	log p
	(J2000)		[′]			[Å]	R97,ZW	R97,CG	
car1_t026	06 42 19	−50 54 28	7.5	18.82	0.99	3.81	−1.93± 0.22	−1.76± 0.22	−1.49
car1_t027	06 42 02	−50 53 19	6.7	19.05	0.99	2.28	−2.36± 0.11	−2.29± 0.11	−1.39
car1_t028	06 42 01	−50 53 18	6.7	19.06	0.96	3.76	−1.91± 0.25	−1.73± 0.25	−1.30
car1_t029	06 41 45	−50 52 49	7.0	18.94	0.99	2.93	−2.19± 0.12	−2.07± 0.12	−1.37
car1_t036	06 42 19	−50 50 25	11.0	19.01	0.99	2.06	−2.44± 0.26	−2.38± 0.26	−2.17
car1_t043	06 42 00	−50 47 23	14.3	19.50	0.91	3.28	−1.98± 0.34	−1.82± 0.34	−1.57
car1_t044	06 42 18	−50 56 56	6.8	18.67	1.01	4.88	−1.63± 0.12	−1.39± 0.12	−1.36
car1_t045	06 41 46	−50 56 54	1.8	19.29	0.92	4.28	−1.72± 0.20	−1.49± 0.20	−1.31
car1_t046	06 42 13	−50 56 44	6.0	18.31	1.05	4.31	−1.87± 0.16	−1.68± 0.16	−1.29
car1_t049	06 42 00	−50 55 31	4.5	19.36	0.89	1.71	−2.49± 0.28	−2.44± 0.28	−1.69
car1_t050	06 42 09	−50 55 14	5.8	19.13	0.91	2.72	−2.22± 0.16	−2.11± 0.16	−1.32
car1_t059	06 41 58	−50 48 58	12.2	18.45	1.05	4.02	−1.93± 0.16	−1.76± 0.16	−1.39
car1_t061	06 42 09	−50 48 42	12.6	19.37	0.94	5.30	−1.39± 0.22	−1.09± 0.22	−1.35
car1_t064	06 41 58	−50 46 41	15.3	18.48	1.03	2.78	−2.31± 0.28	−2.22± 0.28	−1.30
car1_t067	06 41 46	−50 51 01	9.5	18.19	1.10	3.61	−2.10± 0.09	−1.97± 0.09	−1.40
car1_t070	06 41 29	−50 56 46	2.4	19.02	0.93	5.28	−1.46± 0.14	−1.17± 0.14	−2.15
car1_t076	06 40 58	−50 53 35	10.4	17.84	1.16	5.19	−1.68± 0.10	−1.45± 0.10	−1.29
car1_t078	06 41 19	−50 53 12	8.3	18.10	1.12	4.24	−1.93± 0.10	−1.75± 0.10	−1.35
car1_t084	06 40 45	−50 51 02	15.1	19.16	0.92	4.16	−1.77± 0.36	−1.56± 0.36	−1.49
car1_t087	06 41 11	−50 55 53	6.1	18.02	1.12	5.09	−1.68± 0.14	−1.45± 0.14	−1.78
car1_t089	06 41 17	−50 55 08	6.0	19.37	0.88	3.76	−1.86± 0.23	−1.67± 0.23	−1.35
car1_t093	06 41 12	−50 51 52	10.7	19.29	0.91	3.64	−1.91± 0.36	−1.73± 0.36	−1.83
car1_t100	06 41 03	−50 50 48	13.2	18.93	1.01	3.09	−2.14± 0.11	−2.01± 0.11	−1.51
car1_t101	06 40 35	−50 56 36	11.5	19.44	0.88	2.54	−2.22± 2.04	−2.11± 2.04	−2.15
car1_t102	06 40 35	−50 54 08	13.4	18.23	1.11	4.70	−1.76± 0.10	−1.55± 0.10	−1.29
car1_t107	06 40 38	−50 53 20	13.7	19.10	0.96	5.69	−1.32± 0.28	−1.00± 0.28	−1.31
car1_t113	06 40 31	−50 59 03	11.0	19.10	0.97	4.14	−1.79± 0.64	−1.58± 0.64	−1.76
car1_t117	06 41 09	−51 04 39	9.3	19.13	0.97	4.87	−1.56± 0.15	−1.30± 0.15	−1.53
car1_t122	06 40 54	−51 02 53	8.6	19.46	0.92	4.58	−1.59± 0.70	−1.34± 0.70	−1.81
car1_t132	06 41 28	−51 00 35	3.6	18.67	1.03	4.67	−1.70± 0.12	−1.47± 0.12	−1.65
car1_t136	06 41 17	−51 00 17	3.9	18.97	0.96	3.95	−1.87± 0.12	−1.68± 0.12	−1.41
car1_t137	06 41 30	−50 59 58	2.7	19.20	0.90	3.21	−2.06± 0.19	−1.91± 0.19	−1.37
car1_t140	06 41 05	−50 59 12	5.2	19.38	0.96	4.87	−1.52± 0.21	−1.25± 0.21	−1.57
car1_t141	06 40 57	−50 58 38	6.7	18.13	1.13	5.31	−1.59± 0.11	−1.34± 0.11	−1.44
car1_t150	06 41 29	−51 05 22	10.2	18.67	1.05	4.25	−1.83± 0.11	−1.63± 0.11	−1.29
car1_t151	06 41 15	−51 04 15	8.6	19.43	0.92	2.42	−2.26± 0.50	−2.16± 0.50	−1.32
car1_t153	06 40 58	−51 02 41	8.0	18.99	0.95	4.84	−1.59± 0.17	−1.34± 0.17	−1.35
car1_t154	06 40 59	−51 02 27	7.6	18.18	1.08	4.78	−1.75± 0.15	−1.53± 0.15	−1.40
car1_t155	06 41 25	−51 01 39	5.0	18.72	0.99	4.25	−1.82± 0.14	−1.62± 0.14	−1.73
car1_t156	06 41 05	−51 01 36	6.3	17.68	1.22	5.70	−1.55± 0.10	−1.29± 0.10	−1.33
car1_t158	06 41 13	−50 59 44	4.2	19.24	0.91	4.23	−1.74± 0.17	−1.52± 0.17	−1.53
car1_t162	06 41 31	−50 58 22	0.9	19.23	0.91	4.71	−1.59± 0.15	−1.34± 0.15	−1.33
car1_t163	06 41 18	−50 58 08	3.1	19.38	0.88	2.87	−2.13± 1.45	−2.00± 1.45	−1.31
car1_t164	06 41 04	−51 03 40	8.4	19.07	0.94	3.38	−2.02± 0.13	−1.87± 0.13	−1.43
car1_t165	06 41 12	−51 03 12	7.4	19.36	0.91	4.43	−1.66± 0.39	−1.42± 0.39	−1.74
car1_t167	06 41 07	−51 02 10	6.6	18.93	0.93	1.98	−2.48± 0.16	−2.43± 0.16	−146.72
car1_t169	06 41 23	−50 58 11	2.4	18.76	0.98	5.18	−1.53± 0.14	−1.26± 0.14	−1.36
car1_t174	06 41 59	−51 06 40	14.0	19.13	0.98	1.52	−2.58± 0.15	−2.56± 0.15	−1.29
car1_t180	06 42 05	−51 02 59	9.8	18.81	1.02	3.45	−2.05± 0.15	−1.90± 0.15	−1.36
car1_t181	06 41 54	−51 02 46	8.3	18.46	1.06	4.68	−1.73± 0.12	−1.51± 0.12	−1.30
car1_t182	06 42 16	−51 02 00	10.1	18.73	0.99	3.20	−2.14± 0.11	−2.01± 0.11	−3.36
car1_t187	06 42 06	−51 00 30	7.1	18.32	1.08	4.49	−1.81± 0.11	−1.61± 0.11	−1.29
car1_t189	06 41 49	−50 59 42	3.7	19.35	0.86	1.88	−2.44± 0.17	−2.38± 0.17	−1.84

Continued on next page

Table 2.A – *Carina stars, continued*

Star[7]	α	δ	r	V	B−V	Σ W	[Fe/H]	[Fe/H]	log p
	(J2000)		[′]			[Å]	R97,ZW	R97,CG	
car1_t190	06 42 03	−50 58 59	5.2	18.28	1.11	4.97	−1.67± 0.10	−1.44± 0.10	−1.28
car1_t192	06 41 54	−50 57 57	3.0	18.35	1.05	3.68	−2.06± 0.17	−1.91± 0.17	−1.35
car1_t194	06 41 43	−51 05 30	11.0	19.25	0.96	3.02	−2.10± 0.18	−1.97± 0.18	−1.96
car1_t196	06 41 52	−51 03 36	9.1	18.69	0.99	4.24	−1.83± 0.13	−1.63± 0.13	−1.38
car1_t198	06 41 45	−51 03 31	8.4	18.40	1.09	4.98	−1.65± 0.11	−1.41± 0.11	−1.72
car1_t199	06 42 03	−51 03 30	10.1	19.47	0.88	3.30	−1.98± 0.19	−1.82± 0.19	−1.45
car1_t200	06 41 50	−51 01 31	6.1	19.32	0.91	0.98	−2.71± 0.52	−2.72± 0.52	−1.36
car1_t202	06 42 09	−51 00 48	7.8	18.59	1.05	4.74	−1.69± 0.14	−1.46± 0.14	−1.56
car1_t204	06 42 06	−51 00 19	6.9	19.10	0.98	4.28	−1.75± 0.15	−1.53± 0.15	−1.30
car1_t213	06 41 54	−50 58 11	3.1	17.92	1.14	2.77	−2.40± 0.08	−2.34± 0.08	−1.53
car1_t314	06 42 24	−50 54 03	8.4	18.75	1.14	2.34	−2.40± 0.43	−2.33± 0.43	−1.62

---

[7] The nomenclature is such that LG04a–d designates the EIS-fields targeting Carina (P. Lynam [EIS-team] 2003, private communication) followed by the number in the respective input catalog. Stars labeled as car1_t are numbered according to our own input catalogues (M. Odenkirchen 2003, private communication).

Chapter 3

High-resolution abundance studies in Carina

> “*Nous ne saurons jamais étudier par aucun moyen la composition chimique des étoiles…*”
> — Auguste Comte, *Cours de philosophie positive*

Abstract

We have obtained high-resolution spectroscopy of ten red giants in the Carina dwarf spheroidal (dSph) galaxy with the UVES spectrograph at the ESO Very Large Telescope in order to study the detailed chemical evolution of this Galactic satellite. Here we present the abundances of five chemical elements, comprising iron and the α-elements Mg, Si, Ca and Ti. By comparison of the derived iron abundances with metallicities based on the well established calcium triplet (CaT) calibration we show that the empirical CaT technique yields a good agreement with the high-resolution data for [Fe/H] $\gtrsim -2$ dex, but tends to deviate from the results of the high-resolution study at lower metallicities. With [Fe/H]~ -1.7 dex the mean metallicity of our targets is fully consistent with the peak metallicity of Carina as derived from low-resolution spectroscopy and previous photometric studies. We detect two metal poor stars in our sample with iron abundances between -2.7 and -2.5 dex. These stars are found to have enhanced, halo-like [α/Fe] ratios. Overall, the Carina red giants exhibit a depletion in the [α/Fe] abundance ratios with respect to the Galactic halo at a given metallicity, a result which is in compliance with the characteristic low star formation rates of dSphs and which underscores previous suggestions that dSph galaxies may in fact not have been the major contributor to the build-up of the Galactic halo. Furthermore, at a given [Fe/H], there is a large scatter of ~ 0.3 dex present in the [α/Fe] ratios. One of our targets is depleted in nearly all of the α-elements by ~ 0.5 dex. Since its moderately low metallicity of -1.5 dex indicates that SNe Ia already considerably contributed to the enrichment in Fe, this star may have been significantly affected by an environment with a negligible amount of type II SNe. Our derived chemical element ratios are consistent with the episodic star formation in Carina, but the overall large scatter in the abundance ratios impedes the quantification Carina’s star formation history in detail. By comparison with extant chemical evolutionary models, we show that the overall α-element ratios are reasonably well matched by predictions that assume a low star formation efficiency and moderate galactic wind rates, although such models provide at most an upper limit to our observed abundance trends.

3.1 Introduction

Low- to medium resolution spectroscopic studies are well suited to derive spectroscopic metallicities and thus to analyze the dSphs' overall metal content. Hence in Chapter 2 this procedure allowed us to investigate the true, spectroscopic mean metallicity and metallicity spread of Carina, to derive its metallicity distribution function, to investigate to which extent age and metallicity do indeed conspire, to search for possible spatial gradients, and to explore the galaxy's evolutionary history taking into account its chemical enrichment by applying some simple models of chemical evolution. However, since the evolution of chemical elements is intimately linked to the star formation (SF) history of galaxies, deriving individual element abundance ratios in stars is invaluable for imposing strong constraints on the modes of SF in these systems.

An important example of such abundance ratios is [α/Fe], which can be efficiently used as a "chemical clock" (Matteucci 2003). The α-elements (O, Mg, Si, Ca, Ti) form in quickly evolving high-mass stars, which end their lives in core-collapse supernovae (SNe) of Type II, whereas Fe is synthesized both in SNe II, but predominantly in SNe Ia explosions on much longer time-scales. Hence, the [α/Fe]-ratio mirrors the evolutionary history of a stellar population and its SF time-scales due to the different formation sites of Fe and the α-elements and the resulting relative delay in their injection into the ISM. Stars in dSphs have lower [α/Fe] abundance ratios on average than the (low-metallicity) Galactic halo stars of the same metallicity (Shetrone, Côté & Sargent 2001; Shetrone et al. 2003 [hereafter S03]; Tolstoy et al. 2003 [hereafter T03]; Venn et al. 2004). This is generally interpreted as evidence of a low star formation rate in dSphs compared to the Galactic halo (Matteucci 2003) and will sensitively depend on the SF history and the initial mass function of the galaxy, and also on the time scales for mixing the SNe ejecta back into the interstellar medium (ISM).

Other important tracers of SF comprise the *r*- and *s*-process elements. In this context, the formation of the *r*-process (*r*apid neutron capture) elements such as Nd and Eu is assumed to occur in quickly evolving SNe II[1] (e.g., Woosley et al. 1994; Thielemann et al. 2001; Koch & Edvardsson 2001). The *s*-process (*s*low neutron capture, producing, e.g., Ba and La) is, on the other hand, believed to originate in low-mass AGB stars (Busso et al. 1999) or He-burning in massive stars (Prantzos et al. 1990). Consequently, *r*-to-*s* process element ratios can be employed as important indicators of the evolutionary histories, both for Galactic components (Travaglio et al. 1999; Quian & Wasserburg 2001) and dSphs (S03; T03; Matteucci 2003; Lanfranchi et al. 2006a). In a galaxy with episodic SF, such as evidenced in the Galactic dSph satellite Carina (see Sections 2.1, 2.4 ff.), the relative interplay between *r*- and *s*-process enrichment can provide a particularly useful insight into the processes governing the onset and cessation of SF. In this context, an increase in, e.g., [Ba/Eu] is indicative of an *s*-process enrichment and/or a decrease in *r*-process contributing SNe II. While one should expect to see mainly *r*-process patterns during SF episodes, a hiatus of about 3 Gyr between the SF episodes (as suggested, e.g., by Hurley-Keller et al. 1998) would provide a sufficient time interval for AGB stars to contribute a certain fraction of *s*-process enrichment (see discussions in S03; Venn et al. 2004).

From their analysis of five red giants in Carina S03 and T03 report on the imprints of SF bursts and intermitted SF in Carina's abundance patterns. In this vein, each SF burst can be expected to be accompanied by a rapid increase in [α/Fe] (Gilmore & Wyse 1991), followed by a smoother decline in this ratio, which is caused by the continuous production of Fe in SNe Ia. This

---

[1] One should note that alternative sites with sufficient high neutron densities for the *r*-process cannot be ruled out at present. Among these are, e.g., neutron star-neutron star mergers (Rosswog et al. 2000).

was then claimed to be also reflected in variations of the heavy-element patterns, such as some $[s/r]$ abundance ratios, vs. metallicity. However, as S03 note, the interpretation of these elements' trends in term of a distinct SF burst pattern should be taken with caution. Some pure-r-process abundances like [Eu/H] exhibit flat to declining trends with metallicity, contrary to expected rise due to a larger r-process injection by SNe II into the ISM during the burst. This may point to a sensitivity of the Eu production to the possible mass range of the r-process contributing SNe II progenitors and thus a strong dependence on the IMF (S03).

The purely illustrative scenarios brought forth by S03 and T03, based on abundance ratios in five of Carina's red giants, suggest an ancient epoch of SF (around 13 Gyr ago), a subsequent quiescent phase of some 3 Gyr and another SF burst approximately 7–11 Gyr ago. This is, however, not fully compatible with Carina's detailed SF history from CMD modeling (e.g., Smecker-Hane et al. 1994; Mighell et al. 1997; Hurley-Keller et al. 1998; Monelli et al. 2003; Rizzi et al. 2003) and thus merits further investigation.

The full sampling of chemical elements with [Fe/H] (as an approximate proxy for age) requires a large data set, covering a wide range of metallicities, thus sampling all SF episodes and quiescent periods in Carina's history, and yielding a high accuracy in order to trace even small abundance variations. By analysing the abundance patterns in ten red giants in Carina as derived from high-resolution spectra obtained with the UVES spectrograph at ESO's Very Large Telescope, we can pursue the issues addressed above to a high level of accuracy. In this current study we will concentrate on deriving iron and α-element abundances in Carina, whereas an analysis of the heavy element abundance ratios will be left for future work (Koch et al., in preparation).

Apart from their implications for the chemical evolutionary history of dSphs, these elements are of particular interest for assessing the validity of the calibration of the calcium triplet reduced width onto the global metallicity (see Sect. 2.3). The widely used empirical calibrations (Armandroff & Da Costa 1991; Rutledge et al. 1997a,b) are all based on the metallicity scales of Galactic globular clusters (e.g., Zinn & West 1984; Carretta & Gratton 1997; Kraft & Ivans 2003). Although this strictly would imply an unbiassed applicability only to old and metal-poor systems, Cole et al. (2004) have demonstrated that the calibration can be extended to younger ages of ∼2.5 Gyr without loss of accuracy, while extrapolation to ages $\lesssim$1 Gyr may still yield reliable results (see also Cole et al. 2005). Hence, individual metallicities in those dSph galaxies with mean metallicities comparable to those of the calibration clusters, which covered the range of $-2.0 <$ [Fe/H] < -0.6 dex, and which may exhibit a wide range in ages (such as Leo II, see Chapter 4), can also be expected to be accurately measured and calibrated from the CaT. Still it remains unsolved, whether and to what extent the extrapolation of the calibrations towards the metal poor and metal rich tails of the metallicity distributions introduces any bias or significant deviations from the "true" stellar metallicity as established from high-resolution spectroscopy. In addition, the CaT method requires a [Ca/Fe] ratio, which is similar to that found in the Galactic globular clusters and halo and thus of the order $\sim +0.3$ dex (Carney 1996; McWilliam 1997; Pritzl et al. 2005). However, this is not an *a priori* known quantity. Despite recent evidence that [Ca/Fe] is similarly enhanced in dSphs as the Galactic halo (Shetrone et al. 2001, S03; Bosler 2004), this ratio will strongly depend on the evolutionary history of the stellar systems in question (see discussion in Sect. 2.3.3). In particular in the light of Carina's extended and episodic star formation history, which gives rise to a progressively larger contribution of the iron-producing SNe Ia, the calcium abundances may tend to have lower values as was also found in the five Carina giants analyzed by S03. Hence, measuring $[\alpha/\mathrm{Fe}]$ in this galaxy will aid in elucidating the validity and accuracy of traditional CaT metallicity measurements in the dSphs.

3.2 Data and reduction

In the course of the same ESO Large Programme, which was extensively described in Section 2.2, a number of high-resolution spectra of red giants in Carina were obtained in order to study the detailed chemical composition of this particular galaxy. To allow us to perform highly accurate abundance studies at a high signal-to-noise ratio within a reasonable integration time, only bright giants below the tip of the RGB were selected from the CMD, reaching V-band magnitudes slightly above 18 mag (see Table 3.1). Moreover, some of the targets were taken to coincide with the medium-resolution observations around the CaT region, hence enabling us to compare the stellar metallicities derived via the CaT calibration with the "true" iron abundance from these high resolution measurements.

3.2.1 Data acquisition

In parallel with the observing runs in December 2003, during which medium-resolution spectroscopy of red giants in Carina was obtained (see Table 2.2), we used the high-resolution spectrograph UVES (Ultraviolet and Visual Echelle Spectrograph) at the ESO/VLT in multi-object mode. Using UVES in combination with the FLAMES fibre facility permits one to feed nine fibres to the UVES instrument, where we dedicated one fibre per setup to observing blank sky. This configuration will facilitate the later sky subtraction.

The FLAMES/UVES fibre mode has been designed to work on the red arm of the spectrograph. Our observations used the standard setup with a central wavelength of 580 nm, which gives a total spectral range of 470–680 nm. With an aperture on the sky of $1''$ and our chosen CCD binning of 1×1 the instrument provides a resolving power of $\sim$47000.

3.2.2 Data reduction

The data were reduced using the standard UVES pipeline (Modigliani 2004[2]), which operates within the MIDAS environment[3]. The respective standard steps comprise bias subtraction and division by a master slit flat field. Definition of the spectral orders is obtained by means of processing odd- and even-numbered fibre flat field frames, combined with a first guess order position table from Th-Ar wavelength-calibration lamp. In the next step, the wavelength solution is determined via calibration exposures from this Th-Ar lamp, followed by extraction of the target (and sky) spectra using an optimal extraction algorithm. The final extracted, wavelength-calibrated spectra with merged orders are then sky subtracted using the dedicated sky spectrum. Finally, the individual exposures are shifted to the heliocentric standard of rest and coadded, weighted by the spectrum's individual S/N. Typical S/N ratios of the final spectra achieved in this way lie at $\sim$20 pixel^{-1}.

3.2.3 Membership estimates

Membership of the targets was assessed by means of their radial velocities. For this purpose, we generated a template spectrum from a linelist comprising 101 strong absorption features with equivalent widths representative of typical red giant spectra. Cross-correlation of the observations

---

[2] This document is available online via `http://www.eso.org/projects/dfs/dfs-shared/web/vlt/vlt-instrument-pipelines.html`.

[3] The European Southern Observatory Munich Image Data Analysis System (ESO-MIDAS) is developed and maintained by the European Southern Observatory.

Star	α	δ	V	B−V	V−K	J−K	v_r	$\Delta\ v_r$	S/N
LG04b_004260	06 40 30	−50 59 15	17.75	0.99	3.17	0.96	215.6	0.9	18
LG04c_006477	06 41 21	−51 03 43	17.71	1.31	2.71	0.57	219.5	0.7	17
LG04a_000377	06 41 59	−50 51 13	17.78	1.30	3.23	1.00	219.5	0.8	18
LG04a_001556	06 42 17	−50 55 55	17.82	1.25	3.10	1.01	223.1	0.9	19
LG04a_000057[a]	06 41 46	−50 58 55	17.67	1.34	3.05	0.88	223.3	1.0	11
LG04a_001826	06 40 58	−50 53 35	17.76	1.29	2.88	0.63	224.8	0.9	18
LG04c_000777	06 41 04	−51 01 35	17.55	1.31	3.02	0.67	225.1	0.9	20
LG04b_000569[a]	06 41 08	−50 47 49	17.67	1.17	3.26	0.87	226.2	1.3	10
LG04a_002181	06 41 39	−50 49 58	17.62	1.36	2.88	0.63	230.6	0.7	21
LG04d_006628	06 41 37	−51 01 43	17.95	1.28	2.90	0.78	231.1	1.0	23
LG04c_000951	06 39 55	−50 57 36	17.79	1.19	2.72	0.56	233.2	1.1	15
LG04c_000626	06 40 47	−51 06 03	17.60	1.37	3.10	0.73	237.6	0.9	16

[a] Carbon stars

Table 3.1: Stars targeted with UVES. Only the confirmed radial velocity members are listed. The given colours are dereddened values, where B−V is in the Johnson-Cousins system, whereas the infrared colours are in the photometric system of the Telescopio Carlos-Sánchez (TCS), needed to apply the temperature calibrations of Alonso et al. (1999b; 2001).

against this template using IRAF's *fxcor*-task finally yielded accurate radial velocities with a median uncertainty of $0.9\,\mathrm{km\,s^{-1}}$.

For 11 of our targets medium-resolution spectra of the CaT region are also available. For these stars the velocity measurements from the UVES spectra are remarkably consistent with the velocities derived from the CaT (see Chapter 2.4) to within their uncertainties, and we find a median offset between both estimates of $0.5\,\mathrm{km\,s^{-1}}$.

Out of the 30 targets, 12 stars clearly peak at Carina's systemic velocity around a mean of $225\,\mathrm{km\,s^{-1}}$ with a dispersion of $6.4\,\mathrm{km\,s^{-1}}$. This is in good agreement with Carina's radial velocity distribution (Chapter 2.4; Mateo 1998; Majewski et al. 2005; Wilkinson et al. 2006a). The remaining 18 targets have radial velocities that deviate by more than $120\,\mathrm{km\,s^{-1}}$ from this mean, corresponding to $20\,\sigma$. Their membership with this galaxy can be ruled out unambiguously, and they were not considered in any of the subsequent studies. Owing to the presence of the strong C_2 Swan bands at $\lambda\lambda\,5165,\ 5635\,\text{Å}$ in the spectra of the two radial velocity members LG04a_000057 and LG04b_000569, we could identify these as carbon stars. Although tabulated in Table 3.1 for completeness, these spectra were omitted from the present abundance analyses.

3.3 Abundance analysis

For the abundance determinations, we employed the common technique of an EW analysis. For this purpose, we applied the revised 2002 version of the stellar abundance code MOOG (Sneden 1973), in particular using its *abfind* driver.

The accurate derivation of stellar abundance ratios sensitively relies on the choice of proper atomic data, in particular the oscillator strengths. Concern about using the common solar gf-values for the analysis of our late-type red giant target stars prompted us to perform a differential abundance analysis relative to Arcturus (α Boo), a bright K1.5 disk giant of only moderate metal-deficiency and with atmospheric parameters very similar to those expected for the Carina stars of our sample (e.g., Peterson et al. 1993; Friel et al. 2003).

3.3.1 Equivalent widths and gf-values

In order to identify suitable transitions for our abundance determinations, we compiled a linelist from various literature sources. Essentially, we exploited the compilations from the bulge giant and thick disk star studies of McWilliam et al. (1995) and Prochaska et al. (2000), from which we assembled a number of absorption features for a number of chemical elements (see references in these works for the sources of the respective atomic data). We chose the lines with the least amount of stellar and telluric contamination, which thus appear reasonably unblended.

The EWs of these lines were measured using IRAF's *splot*-task assuming a single Gaussian line profile. By repeatedly re-measuring a set of lines, we could estimate the typical uncertainty in the EWs from the scatter in these measurements. As a result, our *splot*-widths are accurate to approximately the 5% level (a few mÅ). An additional method of quantifying the errors on our EWs is provided by Cayrel (1988), who assumes a line profile simply affected by S/N and the number of pixels per resolution element. From this, he analytically derived the expression

$$\sigma_{EW} = \sqrt{3}\,\pi^{1/4}\,\sqrt{\sigma_G\,\delta x}\ \ \mathrm{RMS}_c, \tag{3.1}$$

where σ_G denotes the Gaussian width of the line, δx is the instrumental pixel scale and RMS_c estimates the relative RMS of the continuum around the line. Based on our spectral quality and the IRAF measurements, this formalism yields comparable error estimates.

The oscillator strengths used in the majority of abundance studies are nowadays based on laboratory measurements, such as the the O'Brian values (O'Brian et al. 1991), Hannover measurements (Bard & Kock 1994) or the Oxford gf-values (Blackwell et al. 1995), all of which are, amongst others, employed in the work of McWilliam et al. (1995) and Prochaska et al. (2000). Still, as Prochaska et al. (2000) note, even with such maximally accurate laboratory measurements at hand, the gf-values impose a major error source in red giant abundance studies, particularly when referencing one's abundances to the solar meteoritic (Anders & Grevesse 1989) or to the updated empirical (Grevesse & Sauval 1999; Asplund et al. 2005) solar abundance reference frame. Therefore we have chosen to conduct our analysis differentially with respect to the well-studied red giant Arcturus, thus minimizing the uncertainties associated with solar and laboratory gf-values. Furthermore, since Arcturus exhibits atmospheric properties similar to the stars of our own study, such an analysis aids the reduction of systematic errors, such as a priori unknown deficiencies in the model atmospheres or the influence of weak, unknown blends, which might scale with metallicity (e.g., Fulbright et al. 2006). Hence, we measured the EWs of the lines in Arcturus from the high-quality spectral atlas of Hinkle et al. (2000). Adopting the well established atmospheric parameters of α Boo ($T_{\rm eff} = 4290$ K, $\log g = 1.55$, $\xi = 1.67\,\mathrm{km\,s^{-1}}$, $[m/\mathrm{H}] = -0.5$) from Fulbright et al. (2006) and our measured EWs, we derived the gf-values on a line-by-line basis such as to reproduce each element's abundance from Peterson et al. (1993) and Fulbright et al. (2006). The full linelist with the respective atomic data determined in this way is given in the Appendix to this Chapter, together with the respective EW measurements for each star.

3.3.2 Model Atmospheres and stellar parameters

Throughout our analyses we interpolated the model atmospheres from the updated grid of R. L. Kurucz's[4] one-dimensional 72-layer plane-parallel line-blanketed models with the convective overshoot option switched off and assuming that local thermodynamic equilibrium (LTE) holds for all

---

[4] These atmosphere grids can be downloaded from `http://cfaku5.cfa.harvard.edu/grids.html`

species. Moreover, our model calculations incorporated the new opacity distribution functions, ODFNEW, provided by F. Castelli[5] (Castelli & Kurucz 2003) for the Carina stars, and the respective α-element enhanced models, AODFNEW, for Arcturus. The latter is rendered necessary, since it is known that Arcturus exhibits a considerable enhancement in these elements (Peterson et al. 1993; Fulbright et al. 2006).

The initial estimates for the stellar parameters required in the atmosphere calculations are largely obtained from the targets' photometry. Hence, stellar effective temperatures were derived using dereddened colours from the EIS photometry, complemented by infrared colours, which were drawn from the Point Source Catalogue of 2MASS (Cutri 2003). For Carina, we use a reddening of $\mathrm{E\,(B-V)} = 0.06$ (Mighell 1997), which is also consistent with the value found from the maps of Schlegel et al. (1998). To correct each of the infrared colours, the respective reddening relations from Cardelli et al. (1989) were applied. Finally, photometric effective temperatures were calibrated using the empirical relations derived by Alonso et al. (1999b, 2001), which are based on the infrared flux method (IRFM; e.g., Blackwell et al. 1990). In essence, the IRFM determines $\mathrm{T_{eff}}$ by a comparison of the ratio betweeen the bolometric flux and a monochromatic flux in the infrared continuum, obtained for a set of well defined standard stars, with the expected ratio computed from theoretical stellar atmosphere models.

Since the Alonso calibrations of B−V and V−K require colours in the Johnson-Cousins (JC) system, we employed the photometric transformations described in Chapter 2.2.1 in order to convert the input B and V magnitudes from the photometric system of the ESO Imaging Survey to the standard JC system. The 2MASS K-band magnitude, on the other hand, was transformed to the Bessel & Brett (1988) homogenized system, using the equations provided by the Explanatory Supplement to the 2MASS All Sky Data Release (Cutri 2003). Since this transformation includes two steps of calibrations, i.e., from the 2MASS to the CIT system and from CIT to the Bessel & Brett (1998) system, ethe transformation errors from both calibrations have to be incorporated to yield the final photometric uncertainty of the colours to be used (see also Sivarani et al. 2004). The Alonso-calibration via the J−K-colour, however, requires infrared magnitudes in the photometric system of the Telescopio Carlos-Sánchez (TCS, Alonso et al. 1994), which again requires two separate calibrations. Hence we transformed the 2MASS colours into the CIT system (Cutri 2003) and then derived TCS colours from the CIT system using the equations provided by Alonso et al. (1996), again accounting for transformation errors in the final photometric accuracies. Table 3.1 lists the photometric properties of all target stars, with radial velocities that are consistent with membership of Carina. The empirical temperature calibrations themselves are provided as polynomials of the kind $\theta = P(\text{colour, [Fe/H]})$, where $\theta = 5040/\mathrm{T_{eff}}$. All of our targets lie within the colour-metallicity space spanned by

$$\begin{array}{lclcl}
+0.2 \leq [Fe/H] \leq -0.5 & \Longleftrightarrow & 0.7 \leq (B-V) \leq 1.90 & \Longleftrightarrow & 2.00 \leq (V-K) \leq 4.90 \\
-0.5 \leq [Fe/H] \leq -1.5 & \Longleftrightarrow & 0.7 \leq (B-V) \leq 1.80 & \Longleftrightarrow & 2.00 \leq (V-K) \leq 4.60 \\
-1.5 \leq [Fe/H] \leq -2.5 & \Longleftrightarrow & 0.7 \leq (B-V) \leq 1.35 & \Longleftrightarrow & 2.00 \leq (V-K) \leq 3.40 \\
-2.5 \leq [Fe/H] \leq -3.0 & \Longleftrightarrow & 0.7 \leq (B-V) \leq 1.00 & \Longleftrightarrow & 2.00 \leq (V-K) \leq 2.80
\end{array}$$

so that the following calibration equations from Alonso et al. (1999b, 2001) apply:

$$\begin{aligned}
\theta &= 0.6177 + 0.4354\,(B-V) - 4.025 \cdot 10^{-3}\,(B-V)^2 + 5.204 \cdot 10^{-2}\,(B-V)[Fe/H] \\
&\quad - 0.1127\,[Fe/H] - 1.385 \cdot 10^{-2}\,[Fe/H]^2, \qquad (3.2) \\
\theta &= 0.3770 + 0.3660\,(V-K) - 3.170 \cdot 10^{-2}(V-K)^2 - 3.074 \cdot 10^{-3}\,(V-K)[Fe/H] \\
&\quad - 2.765 \cdot 10{-}3\,[Fe/H] - 2.973 \cdot 10^{-3}\,[Fe/H]^2. \qquad (3.3)
\end{aligned}$$

---

[5] See `http://wwwuser.oat.ts.astro.it/castelli`.

As initial guesses for the metallicity to be used in these calibrations and the model atmospheres we adopted the value derived from our CaT study (Chapter 2.4) for the six overlapping member stars. Otherwise Carina's mean metallicity of -1.7 dex was assumed for the remaining four red giants for which no other metallicity measurement was available.

In practice, we adopted the $\mathrm{T_{eff}}$ (V−K) value as the final stellar photometric temperature, since the large wavelength baseline of this colour index makes this temperature the least susceptible to the underlying photometric uncertainties, yielding the most accurate results. The temperatures obtained from the B−V colours are systematically cooler than their respective V−K counterparts by ∼70 K on average. Although Alonso et al. (1999b) note potential divergences of the estalished calibrations towards lower temperatures, the reason for such differences remain yet unknown (see also Wylie et al. 2006). The formal errors on the thus calibrated effective temperature, based on the full photometric uncertainties, amount to 70 K on average.[6]

The stellar surface gravities, $\log g$, were initially determined using the canonical relationship

$$\log \frac{g}{g_\odot} = \log \frac{M}{M_\odot} + 4 \log \frac{\mathrm{T_{eff}}}{\mathrm{T_{eff,\odot}}} - 0.4\,(M_{\mathrm{bol},\odot} - M_V - \mathrm{B.C.}), \tag{3.4}$$

where we adopted $\mathrm{T_{eff,\odot}} = 5777\,\mathrm{K}$, $M_{\mathrm{bol},\odot} = 4.74$ and $\log g_\odot = 4.44$ and a distance of Carina of 94 kpc (Mighell 1997). Moreover, the photometric temperature as derived above was used in this relation, and the stellar mass was taken as $0.8\,M_\odot$, in correspondence to the typical main sequence turn-off mass (e.g., Johnson et al. 2006). Finally, the bolometric correction (B.C.) was obtained by interpolation of the respective Kurucz-atmosphere grids.

Adopting this set of values as the input parameters, the final spectroscopic parameters were determined from a subset of the clean Fe I lines listed in Table 3.A in the Appendix, the equivalent widths, W_λ, of which obey $-5.4 \lesssim \log_{10}(W_\lambda/\lambda) \lesssim -4.5$, corresponding to a range of ∼20 to 160 mÅ at 5000Å. The lower limit of this selection prevents weak lines being spuriously detected, thus artificially raising the mean iron abundance near the cut-off. Moreover, the strongest, saturated lines were pruned from the list, since they do not lie on the linear part of the curve of growth and are predominantly formed in the highest layers, where the atmosphere models become progressively unreliable (McWilliam et al. 1995; Johnson 2002). Consequently, the atmospheric parameters were then measured by iteratively modifying the models to satisfy three constraints:

As the first step in our abundance loop, we determined the microturbulent velocity ξ. To fix its value, abundances from the neutral iron lines were iteratively calculated, demanding that there is no trend of abundance with the reduced width W_λ/λ. In essence, such trends are caused by the fact that the adopted microturbulent has a significant effect on the abundances derived from lines with larger EWs, i.e., those particularly affected by saturation. The respective scatter about the zero slope from a least-squares fit was then taken as a measure of the uncertainty on the microturbulence parameter. In this way, we conservatively obtain typical accuracies of $0.1\,\mathrm{km\,s^{-1}}$ on ξ.

In the second step, spectroscopic effective temperatures were set from excitation equilibrium, i.e., the abundance of the Fe I lines is required to be independent of the excitation potential (EP). Based on the range of $\mathrm{T_{eff}}$ that produces acceptable fits of the abundance versus EP plot, we estimate the typical errors on the spectroscopic temperature as ±100 K, thus being slightly larger than the photometry based errors. Generally, our spectroscopic $\mathrm{T_{eff}}$-values are systematically

---

[6] In principle, the availability of J−K colours from 2MASS would also allow us to establish a $\mathrm{T_{eff}}$-value. However, we refrain from using this indicator, since the J−K colour is not as sensitive to temperature changes as is V−K (e.g., Fulbright et al. 2006). Moreover, the internal uncertainty of the colour-$\mathrm{T_{eff}}$-relation increases fivefold, when applying the J−K-calibration (Alonso et al. 1999b).

higher than the photometric estimates, and we note an offset of +250 K on average for our standard atmospheres, representing an error of ∼6% at our temperature regime. For some of the targets (e.g., LG04b_004260), this discrepancy can be as high as 500 K. Although a systematic offset of ∼250 K may raise some concern, differences between the spectroscopic temperature scales do not come as a surprise. First of all, the photometric errors on the input infrared colours are rather high, where the median uncertainty of our targets from 2MASS amounts to 0.1 mag in V−K. Consequently, a reddening uncertainty of 0.1 mag reflects in a $T_{\rm eff}$-variation of ±100K. It turns out that an average decrease of 0.4 mag in V−K (up to 0.71 mag for the most deviating stars), be it due to photometric or reddening uncertainties, would be required to reconcile the spectroscopic temperatures. However, this would correspond to an unreasonably large increase of Carina's distance modulus of 0.45–0.8 mag (reflecting a distance shift of ∼18–30 kpc). Secondly, it is unlikely that inconsistencies arise due to stars with different characteristics than our giants used in the original calibrations: All the prescriptions of Alonso et al. (1999a,b) were based on metal poor giants, comparable to the Carina stars in question. Nevertheless, according to Alonso et al. (1999b) the calibrations from the IRFM commence to diverge below 4500 K. In this vein, one should keep in mind that all common calibrated colour-temperature relationships necessarily rely on model atmospheres at some stage. Hence, for want of measurements of bolometric luminosities of metal poor giants, the IRFM has to rely on the conversion of an observed IR flux into a total flux by means of atmospheric models (Alonso et al. 1999a). As a result, effective temperatures from IRFM measurements may vary at the 1% level each with respect to many effects, among these are (1) the use of standard Kurucz versus MARCS (Bell et al. 1976; Mégessier 1994) models; (2) the proper incorporation of convection, which governs the layers where the flux emerges (Castelli et al. 1997); or (3) the correct treatment of photometric zeropoints as well as the use of the newest available opacities, in particular for H^- in the atmosphere models (Blackwell et al. 1991). In summary, the model dependence of both the photometric IRFM $T_{\rm eff}$ and our spectroscopic estimates will inevitably lead to systematic differences as long as a non-identical set of models was used. Such a failure of coincidence underscores the inability of any model to simultaneously predict the correct emerging flux, as measured, and the width and shape of observed absorption features (see also the discussion in Johnson 2002). Additionally, inconsistent spectroscopic $T_{\rm eff}$-values could occur due to errors in the gf-values, which may correlate with EP (Johnson 2002). However, this has been shown to be neither the case for laboratory oscillator strengths (e.g., Blackwell et al. 1995), nor should it place a problem in our differential line-by-line analysis. At the expense of not reproducing the correct bolometric flux or the stellar colours, we stick to our spectroscopic estimates to define the atmospheric $T_{\rm eff}$, since it does not introduce any trend of abundances with the EP. In this way, one circumvents any potential bias of the derived abundances, since the metal poor stars that we expect in Carina from our low-resolution studies (Chapter 2.4), exhibit less detectable lines with higher EP (Johnson 2002). Finally, Johnson et al. (2006) have shown that the use of a photometric $T_{\rm eff}$ yielded highly distinct non-standard abundance ratios for their sample of old red giants in LMC clusters, again strengthening our confidence in the use of the spectroscopic values for our analysis.

Finally, the appropriate surface gravity for each star was constrained from ionization equilibrium, thus requiring that the iron abundance from the Fe II lines, which are sensitive to $\log g$, match the abundance from the Fe I lines. These abundances were repeatedly computed for both species with $\log g$ varying in small steps until the results from both ionization stages agreed reasonably well. By thus demanding that both stages did not deviate by more than 0.1 dex we could effectively constrain our gravity estimate to within an accuracy of ±0.2 dex. As for the case of $T_{\rm eff}$, the spectroscopically determined gravities are systematically also higher than the purely photometrically determined values. On the one hand, this can be due to a mild degeneracy of the entire parameter set, where a fraction of the offset can be explained by discrepancies in the adopted temperature. Since an increase in $T_{\rm eff}$ decreases the difference between log ε(Fe I) and log ε(Fe II), one inevitably derives an increased stellar gravity. Due to this covariance, this change in $\log g$ entails a slight change in the slope of the EP plot, which again reflects in another rise in effective temperature (e.g., Fulbright et al. 2006). Likewise, the model's microturbulence has a mutual influence on $\log g$, though to a lesser extent. On the other hand, while matching log ε(Fe I) and log ε(Fe II) to gain ionization equilibrium itself can be done precisely, one should keep in mind that there is only a small number of stronger and well determined Fe II transitions available in our spectra and the literature. On average, we have only ~7 Fe II lines at hand, which will not only lead to larger standard errors on the derived [Fe II/H] values, but also frustrate accurate gravity estimates. Lastly, it has been suggested that the effects of non-LTE (NLTE) can significantly alter spectroscopically derived surface gravities (Thévenin & Idiart 1999; Allende Prieto et al. 1999). In the framework of NLTE, ultraviolet radiation from deeper layers tends to depopulate Fe I levels, whereas the relevant levels of the ionized stage are left rather unaffected. Hence, neglect of NLTE effects leads to an underestimate of log ε(Fe I) and, in turn, too low surface gravities. From her study of metal poor field giants Johnson (2002) found that requiring an LTE Fe I abundance lower by 0.2 dex than Fe II, which is the typically expected order of magnitude of NLTE corrections (Thévenin & Idiart 1999), to define $\log g$ increased the $\log g$ value from ionization balance by 0.4 dex. However, since for our data the use of the photometric $\log g$ value would render the Fe I abundances *lower* by ~0.3 dex compared to Fe II and for want of available detailed NLTE models, we will in the following adopt our spectroscopic gravity in the model atmospheres. Moreover, as we will show in the next Section, even a larger variation of $\log g$ has an only marginal effect on the abundances, in particular in the light of the fact that we rely primarily on the neutral iron lines to assign the stellar [Fe/H].

The entire parameter determination for ξ, $T_{\rm eff}$ and $\log g$ was successively iterated upon simultaneous convergence, where we adopted the Fe I abundance from the last iteration as the input metallicity for the subsequent atmosphere calculation. Nevertheless, we found that our abundances are very stable with regard to the "metallicity" of the model atmosphere. We note that changing the input [Fe/H] by 0.2 dex did not significantly affect the derived abundance (see also Section 3.3.3). The final atmospheric parameters for each star derived in this way are tabulated in Table 3.2.

Star	$T_{\rm eff}$	$\sigma\,T_{\rm eff}$	$T_{\rm eff}$	ξ	log g	[Fe/H]	[M/H]
	Photometric		Spectroscopic	[km/s]	cgs	(CaT)	
LG04b_004260	4091	62	4594	1.52	1.53	−1.63	−1.50
LG04c_006477	4397	80	4600	1.54	1.49	−1.55	−1.42
LG04a_000377	4060	60	4511	1.74	1.39	−1.45	−1.50
LG04a_001556	4134	64	4570	1.75	1.68	−1.41	−1.30
LG04a_001826	4271	73	4384	1.74	0.84	...	−1.46
LG04c_000777	4183	67	4205	1.25	0.85	...	−1.38
LG04a_002181	4279	73	4317	1.66	1.26	−1.39	−1.39
LG04d_006628	4260	72	4717	1.40	2.02	...	−1.81
LG04c_000951	4387	80	4395	1.66	0.90	...	−2.74
LG04c_000626	4130	64	4420	1.70	1.80	−2.06	−2.57

Table 3.2: Model atmospheric, spectroscopic and photometric parameters of the Carina targets.

With this final optimized parameter set, the abundance from the ionized state Fe II deviates by no more than 0.04 dex from the Fe I abundance, with an average deviation of ~0.01–0.02 dex.

3.3.3 Errors on abundances

In order to evaluate the systematic effects of the uncertainties in the atmospheric parameters on the measurements of the elemental abundances, we performed the commonly used standard abundance error analysis (e.g., Edvardsson et al. 1993; Prochaska et al. 2000; Koch & Edvardsson 2002). In this vein, abundance ratios were obtained for ten different model atmospheres for two stars (LG04c_000777 and LG04d_006628). The two stars were chosen to have significantly different stellar atmospheres in terms of their parameters, in particular such as to cover a broad range in $T_{\rm eff}$. Moreover, they are representative of the whole magnitude range that our observations cover. In each of the models, the stellar parameters were separately varied around their typical random $1\,\sigma$-uncertainty as estimated in the previous section. Tables 3.3 and 3.4 specify the differences of the element ratios for each of these models, i.e., for $T_{\rm eff} \pm 100\,{\rm K}$, $\xi \pm 0.1\,{\rm km\,s^{-1}}$, $\log g \pm 0.2$ dex and $[M/{\rm H}] \pm 0.2$ dex, from the values obtained from the standard atmospheres.

The α-elements are important electron donors in the atmospheres of red giants. These metals supply a significant portion of free electrons, which sustain the formation of H^- – the dominant source of the continuum opacity in these stars. However, it cannot be presumed a priori that the Carina stars also exhibit any kind of enhancement in these elements unless their abundances are accurately determined in the course of the present analysis. Nonetheless, measurements in seven dSphs of the Local Group, also comprising five stars in Carina, indicate that these galaxies are in fact enhanced in a number of α-elements (Shetrone et al. 2001, S03; Venn et al. 2004; Geisler et al. 2005). Hence, we also derived abundances under the assumption of an α-enhancement of +0.4 dex in the atmospheres, where we calculated models with the stellar default parameters, but using the α-enhanced opacity distributions, AODFNEW (see e.g., Fulbright et al. 2006). The respective deviation of each elements' abundance ratio derived with this atmosphere from the standard atmosphere's value is given in Tables 3.3,4 in the column labeled "α". An estimate of the influence of measurement errors in the EWs is also given in the Tables. Here, ΔEW corresponds to the mean error in the abundances obtained from each individual line weighted by the square root of the number of absorption features, N, used in the derivation of ε (e.g., Carretta 2006). This value of the statistical errors accounts in principle for the abundances' line-to-line scatter and input atomic parameters. However, for those elements with $N \gtrsim 5$, which is the case for our Ca-, Ti I- and Fe-lines, the total abundance error is generally dominated by the uncertainties in the atmospheric parameters (Prochaska et al. 2000). The major error source in terms of

Ion	$\Delta\,T_{\rm eff}$		$\Delta\log g$		$\Delta\,\xi$		$\Delta\,[M/{\rm H}]$		α	ΔEW	σ_{tot}
	+100 K	−100 K	+0.2	−0.2	+0.1	−0.1	+0.2	−0.2			
Mg I	−0.039	+0.028	−0.018	+0.017	+0.049	−0.051	−0.012	+0.011	−0.036	0.046	0.11
Si I	−0.132	+0.138	+0.032	−0.033	+0.069	−0.065	+0.025	−0.023	+0.010	0.027	0.22
Ca I	+0.023	−0.054	−0.025	+0.023	+0.021	−0.021	−0.035	+0.027	−0.037	0.030	0.10
Ti I	+0.094	−0.125	−0.006	+0.011	+0.033	−0.030	−0.034	+0.029	−0.035	0.017	0.17
Ti II	−0.130	+0.113	+0.056	−0.059	+0.019	−0.015	+0.041	−0.045	+0.056	0.056	0.22
Fe I	+0.116	−0.081	−0.002	+0.003	−0.075	+0.075	+0.005	−0.001	+0.040	0.014	0.18
Fe II	−0.112	+0.162	+0.065	−0.070	−0.053	+0.058	+0.070	−0.062	+0.125	0.057	0.29

Table 3.3: Error analysis for LG04c_000777 ($T_{\rm eff}/\log g/\xi/[M/{\rm H}]$ = 4205/0.85/1.25/−1.38).

Ion	$\Delta\,T_{\rm eff}$		$\Delta\log g$		$\Delta\,\xi$		$\Delta\,[M/{\rm H}]$		α	ΔEW	σ_{tot}
	+100 K	−100 K	+0.2	−0.2	+0.1	−0.1	+0.2	−0.2			
Mg I	−0.040	+0.054	−0.011	+0.023	+0.010	−0.003	+0.006	−0.006	+0.012	+0.127	0.15
Si I	−0.110	+0.114	+0.029	−0.027	+0.040	−0.043	+0.016	−0.026	+0.032	+0.036	0.18
Ca I	−0.044	+0.039	−0.001	+0.003	+0.020	−0.020	+0.006	−0.009	+0.001	+0.023	0.07
Ti I	+0.022	−0.041	−0.005	−0.003	+0.024	−0.025	−0.001	+0.005	−0.015	+0.018	0.06
Ti II	−0.115	+0.136	+0.096	−0.082	0	0	+0.056	−0.064	+0.092	+0.050	0.26
Fe I	+0.140	−0.134	−0.019	+0.017	−0.040	+0.043	−0.016	+0.026	−0.022	+0.011	0.21
Fe II	0	+0.051	+0.084	−0.067	−0.023	+0.021	+0.034	−0.034	+0.063	+0.025	0.15

Table 3.4: Error analysis for LG04d_006628 ($T_{\rm eff}$/log g/ξ/[M/H] = 4717/2.02/1.40/−1.81).

atmospheric parameters is in this case the temperature sensitivity. In the opposite case, there is a progressively larger contribution of EW errors due to enhanced noise, unresolved blends or uncertainties in the continuum placement. Interestingly, neglect of any α-enhancement does not significantly alter any of the derived abundance ratios and has only a major effect on the ionized species, such as Ti II and Fe II, where the enhancement tends to overestimate the abundances by ~0.1 dex. The total uncertainty of each elemental abundance ratio is finally obtained by adding in quadrature the individual contributions. As a result, the average error on our derived [Fe/H] amounts to ~0.2 dex and ranges from ~0.1 to ~0.25 dex for the other elements.

One should keep in mind, however, that the model parameters are not independent but rather intricately correlated in several ways (McWilliam et al. 1995). This leads to covariances of the parameters' uncertainties, which can be particularly significant for the case of $T_{\rm eff}$ and log g, e.g., caused by the explicit temperature-gravity dependence. Hence, a change in $T_{\rm eff}$ can introduce a slope in the abundance vs. EW relation, which is used to fix ξ. It is also possible that a different temperature upsets the balance between both Fe ionization stages, which determines the surface gravity. By means of Monte Carlo modeling techniques, Johnson (2002) and Johnson et al. (2006) have elaborated to which extent the different parameters correlate on the RGB. In fact, the $T_{\rm eff}$-log g covariance dominates most of the other parameter combinations. If we also recompute our abundances (for the case of LG04d_006628) with a $T_{\rm eff}$ that is 100 K cooler and use the corresponding log g (~0.25 dex smaller) and ξ (~0.03 km s^{-1} larger) that re-adjust the respective imbalances, the resulting abundances experience another change by $\lesssim$0.03 dex. However, the demanded equilibria would not be reached as well as if the the correct parameter set had been used (e.g., Bensby et al. 2005). Johnson (2002) has efficiently demonstrated that the [Mg/Fe] abundance ratio tightly correlates with $T_{\rm eff}$. This is to be explained by the reactions of Mg and Fe to the changes in temperature and the correlated gravity changes and should, though to a lesser extent, hold for most abundance ratios [X/Fe]. However, their observed slope was also predicted and reproduced by a set of Monte Carlo simulations and thus is not of great concern. For our data the observed Pearson's r statistics[7] for [Mg/Fe] vs. $T_{\rm eff}$ amounts to 0.05, which could be shown to be compatible with no significant correlation by means of Monte Carlo simulations. Hence, we continue by only assuming the uncorrelated contributions in our random error analysis, which is also justified by our conservatively large choice of uncertainties in the parameters and the number of lines available.

Finally, it should be noted that none of our abundances has been corrected for NLTE effects.

---

[7] The coefficient r is a measure of the correlation of two quantities and averages to zero in case of no correlation, whereas $|r|$=1 for tightly correlated values.

But since our results will be compared with similar LTE analyses in the following (e.g., S03; Venn et al. 2004), this source of uncertainty will be minimized on the whole. Furthermore, this neglect is justified by the lack of any significant correlation of $\varepsilon(\mathrm{Fe\,I}) - \varepsilon(\mathrm{Fe\,II})$ (and likewise for both Ti-species) with temperature or metallicity, which one would expect if departures from LTE were a major concern in our analysis (e.g., Bosler 2004; Carretta 2006).

3.4 Results

Table 3.5 shows the final abundance ratios [X/Fe] ([Fe/H] for the iron lines themselves) for the chemical elements X, which were derived as described above. These ratios are given w.r.t. the mean abundance of the neutral iron lines, $\varepsilon(\mathrm{Fe\,I})$. Also tabulated are the number of lines, N, used to determine the mean abundance ratio for each element and standard deviation of each measured ε from these lines.

	LG04a_002181			LG04b_004260			LG04c_006477			LG04a_000377		
Element	[X/Fe]	σ	N	[X/Fe]	σ	N	[X/Fe]	σ	N	[X/Fe]	σ	N
Mg I	0.15	0.03	2	−0.23	0.13	2	0.15	0.18	2	0.10	0.19	2
Si I	0.16	0.10	7	−0.08	0.13	3	−0.36	0.14	4	0.02	0.09	3
Ca I	0.26	0.04	17	0.16	0.07	14	0.23	0.08	14	0.19	0.04	14
Ti I	−0.02	0.04	34	−0.07	0.06	18	0.14	0.07	20	0.17	0.06	26
Ti II	0.07	0.11	6	0.09	0.07	5	0.11	0.05	5	−0.11	0.07	5
Fe I/H	−1.39	0.22	97	−1.51	0.16	96	−1.42	0.16	97	−1.50	0.16	91
Fe II/H	−1.40	0.18	97	−1.50	0.13	96	−1.39	0.12	97	−1.51	0.12	91

	LG04a_001556			LG04a_001826			LG04c_000777			LG04d_006628		
Element	[X/Fe]	σ	N	[X/Fe]	σ	N	[X/Fe]	σ	N	[X/Fe]	σ	N
Mg I	−0.14	0.10	2	−0.78	...	1	−0.18	0.20	2	−0.01	...	1
Si I	0.08	0.17	3	−0.02	0.28	3	0.11	0.24	3	0.19	...	1
Ca I	0.16	0.07	13	0.04	0.05	14	0.32	0.06	17	0.18	0.10	9
Ti I	−0.08	0.05	31	−0.60	0.08	16	−0.12	0.06	30	−0.14	0.08	12
Ti II	−0.08	0.13	6	−0.46	0.11	5	0.12	0.15	5	0.23	0.17	4
Fe I/H	−1.27	0.14	98	−1.51	0.16	81	−1.36	0.12	90	−1.80	0.15	88
Fe II/H	−1.31	0.14	98	−1.47	0.14	81	−1.36	0.19	90	−1.81	0.12	88

	LG04c_000951			LG04c_00626		
Element	[X/Fe]	σ	N	[X/Fe]	σ	N
Mg I	0.31	0.08	2	0.41	...	1
Si I	...	...	...	0.94	0.13	3
Ca I	0.71	0.05	5	0.24	0.11	5
Ti I	0.27	0.14	9	0.16	0.05	9
Ti II	0.02	0.12	3	0.50	0.08	3
Fe I/H	−2.73	0.16	68	−2.54	0.15	80
Fe II/H	−2.73	0.12	68	−2.58	0.11	80

Table 3.5: Abundance results for the analysed Carina red giants. Also listed is the 1 σ standard deviation about the mean abundance and the number of absorption lines employed to derive these values.

3.4.1 Iron

The distribution of the Fe abundances of the red giants in Carina obtained from the high resolution spectra is in good agreement with both the values measured from the low resolution CaT measurements (see Chapter 2.4) and overall metallicity estimates from photometric and spectroscopic studies (Smecker-Hane 1999; Rizzi et al. 2003; Monelli et al. 2003 – see references in Chapter 2.4.2). Accordingly, the mean iron abundance of the present sample is found to be -1.70 dex with a a standard deviation of 0.51 dex, which is in excellent agreement with the mean of -1.72 (CG-scale) and a full width of $\sim$0.90 dex from our CaT studies. Also S03 find a mean of -1.64 with a scatter of 0.2 dex from their high resolution analysis of five red giants. From this point of view, our targets can be considered as Carina members representing the typical metallicity range in this particular dSph. Fig. 3.1 displays the MDF from the CaT measurements, supplemented with the high resolution data points from this Chapter.

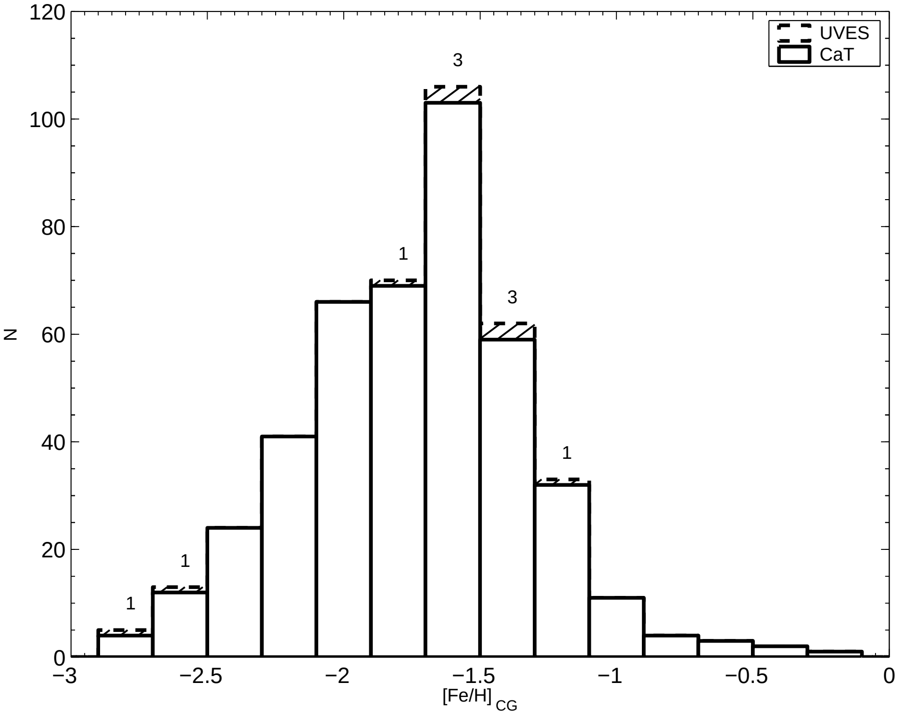

Figure 3.1: Carina's MDF as in Fig. 2.10 (solid histogram), complemented with the iron abundances derived in this Chapter (hatched histogram). The numbers above the bars indicate the numbers of targets added to the respective bin. For the six targets, where both CaT and high-resolution estimates are available, the accurate UVES values superseded those from the calcium calibration from Chapter 2.4.

There are some mildly metal rich targets, which reach metallicities of -1.27 dex. Furthermore, we detect two metal poor stars with [Fe/H]< -2.5 dex, which contribute to the metal poor tail of Carina's MDF. These metallicities lie 1.5–2 σ below the peak of the MDF. Nevertheless, this small number of metal poor objects is not sufficient to resolve the G-dwarf problem addressed in Chapter 2.7.

The six stars that were observed both in low- and high resolution mode enable us to efficiently assess the accuracy of the calibration of the CaT onto of iron, in particular since these targets cover a broad range of abundances. Fig. 3.2 shows a comparison of the estimates from both methods. Reassuringly, these measurements agree well in the more metal rich regime. An error-weighted least-squares fit to the full sample yields the linear relation

$$[M/\mathrm{H}] = (1.84 \pm 0.29)\,[\mathrm{Fe/H}]_{\mathrm{CG}} \; + \; (1.31 \pm 0.46),$$

whereas exclusion of the most metal poor, deviating star yields

$$[M/\mathrm{H}] = (0.58 \pm 0.82)\,[\mathrm{Fe/H}]_{\mathrm{CG}} \; + \; (0.82 \pm 1.22),$$

As the dashed line in Fig. 3.2 implies, all of the five metal richer red giants show a consistency between their CaT metallicity and the high resolution iron abundance to within the uncertainties, not deviating by more than $0.8\,\sigma$ from unity. This range of metallicities was well sampled by the Galactic globular clusters in the calibrations of R97 and significant discrepancies are not to be expected. On the other hand, the most metal poor object we found (with an iron abundance of -2.74 dex) deviates by 0.51 dex ($3.2\,\sigma$) from the CaT value.

This deviation points to a general shortcoming of the method to devise global metallicities based on the CaT in red giants. Since the globular clusters in the sample of R97 "only" comprised a metallicity range from -0.64 down to -2.02 dex (CG scale), measurements of stars beyond these limits necessarily rely on an extrapolation of the calibrations. Moreover, the clusters employed for our calibrations span a range from -2.0 to -1.12 dex (see Table 2.1).

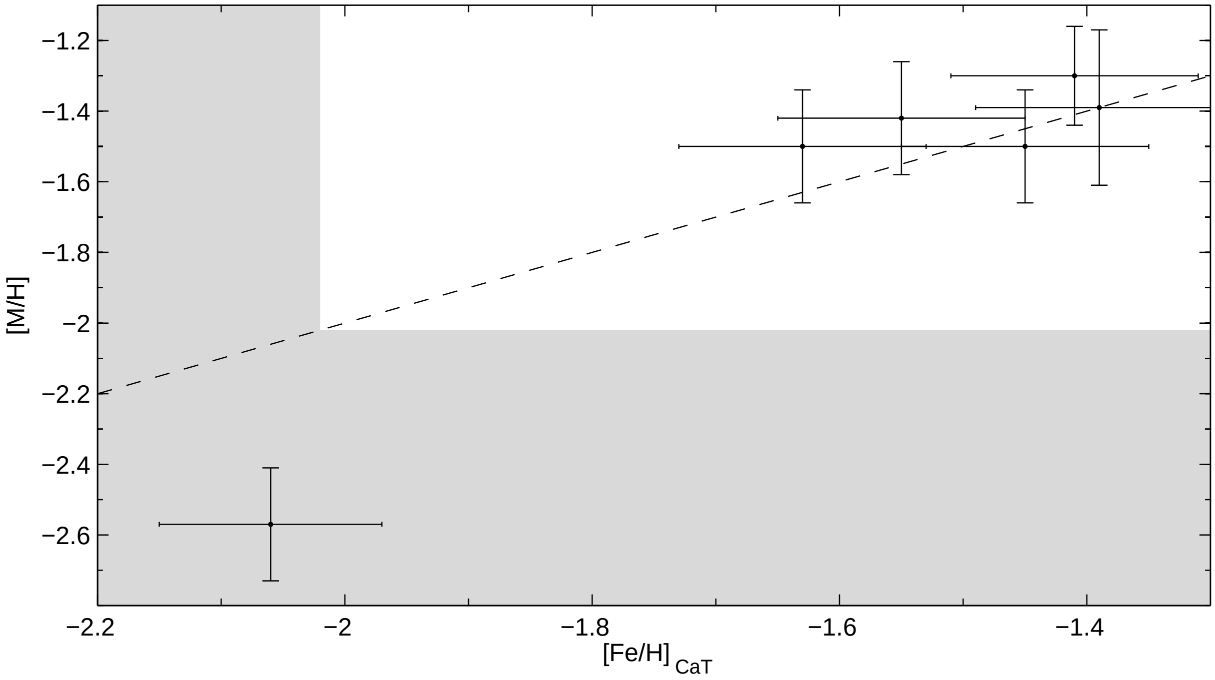

Figure 3.2: Comparison of the metallicities from medium (CaT) and high-resolution analyses. Shown are the six of our target stars, for which CaT widths could be measured in Chapter 2. The horizontal errorbars are formal measurements errors, not accounting for the calibration uncertainties discussed in Sections 2.3.3 and 2.3.4. The $1\,\sigma$-errorbars on [M/H] are those deduced in Section 3.3.3. The grey-shaded area illustrates the range, where the CaT calibrations have to be extrapolated due to the lack of very metal poor calibrating clusters in R97a,b.

Although Cole et al. (2004) have demonstrated from a sample of young open clusters that the CaT technique is generally applicable for a broad age range of 2.5–13 Gyr and over a metallicity range spanning $-2 <$[Fe/H]< -0.2, the MDFs' metal poor tails remain unsatisfactorily sampled in high resolution studies. The question of whether the metal poor extensions of the MDFs of dwarf galaxies based on the CaT, which are reported throughout the literature (e.g., Smecker-Hane et al. 1999; Tolstoy et al. 2001; Bosler 2004; Pont et al. 2004; Tolstoy et al. 2004; Cole et al. 2004, 2005; Koch et al. 2006), are then reliable estimates has to await more and highly accurate data in this regime. Nonetheless, the CaT is well suited to the identification of metal poor stars, albeit their exact [Fe/H] may be not sampled, which then can be used in follow-up high-resolution studies.

A useful test of the calibrations' reliability towards the metal poor tail would then consist of synthesizing the spectral range around the CaT for our target stars, using atmospheres based on their derived stellar parameters and the instrumental resolution of our (UVES-) observations. By reapplying the EW code and the empirical calibrations from Chapters 2.3.1, 2.3.2 one could assess to what extent the iron abundance from the high resolution spectra and the metallicity from the synthesized CaT agree. This procedure is unfortunately not possible given the current state of the art of atmospheric modeling: The broadening of the three extremely strong Ca lines is caused by a number of various, in parts poorly understood mechanisms. Moreover, the wings of these lines are formed in the deep layers of the stellar atmospheres, whereas their cores originate in the highest parts of the photospheres up to the chromospheres. Hence, modeling the CaT remains insecure and cannot be employed to shed light on the empirical metallicity calibration (see also Bosler 2004).

3.4.2 Alpha Elements – Mg, Si, Ca, Ti

While iron is synthesized both in SNe II and SNe Ia, the even-Z elements (O, Mg, Si, Ca, Ti) are predicted to be produced during the nucleosynthetic shell-burning in high-mass stars with negligible lifetimes, which end their lives in SNe II explosions. This picture comprises those elements formed by α-capture (like O, Mg, Si), as well as the heavy even-Z elements Ca and Ti (e.g., McWilliam 1997).

A simple prediction for the formation of the Galactic halo is that an initial burst of SF produced large amounts of α-elements on short time scales leading to an enhancement of the [α/Fe] ratio. At these early epochs, the long-lived SNe Ia had not yet time to significantly pollute the initial SNe II abundance pattern. Once SNe Ia start to contribute (after ∼1 Gyr), the iron abundance will increase, leading to a decline in the [α/Fe] abundance ratio. The exact pattern of the transitions in [α/Fe] with metallicity (taken as a proxy for time) are strongly dependent on the SF history of a stellar system, its initial mass function (IMF) and the timescales for mixing the SNe products in the interstellar medium (Matteucci 2003; S03; Venn et al. 2004).

The metal poor stars of the Galactic halos evidently populate a plateau of [α/Fe]$\sim$0.4 dex (see review by McWilliam 1997). However, from the analyses of 36 red giants in seven dwarf galaxies in comparison with stars in the Galaxy, S03 found only little evidence to connect these stellar populations to those in the Milky Way. In fact, stars in dSphs have been shown to be well separated from Galactic disk and in particular halo stars in terms of lower [α/Fe] ratios (S03; T03; Venn et al. 2004; see also Fig. 2). Consequently, it was argued that a low SF rate of the order of $\sim 10^{-4}\,\mathrm{M}_{\odot}\mathrm{yr}^{-1}$), such as those typical for dSphs (Ikuta & Arimoto 2002; Matteucci 2003; Lanfranchi & Matteucci 2004; Hensler et al. 2004; Font et el. 2006), are well able to produce abundances that are significantly less enhanced compared to the Galactic halo (Gibson

1998; S03; T03). Hence, the α-elements have often been considered as an important testbench for Searle & Zinn's (1978) hypothesis of the origin of the Galactic halo from satellite accretion events (Gilmore & Wyse 1998). Despite the characteristic low [α/Fe] in most stars of the dSphs, their wide abundance range from approximately -0.3 to 0.3 dex and the fact that some stars also exhibit higher, Galactic [α/Fe] values suggest that using these elements as a unequivocal test for chemical imprints of accretion events should be taken with caution (Venn et al. 2004). Moreover, the α-elements hold an important clue to elucidating the evolutionary histories of each individual dwarf galaxy (e.g., S03; T03). We will turn to discussing the implications of our derived [α/Fe] ratios for Carina's chemical evolution in Section 3.5.

Figs. 3.3 and 3.4 display the derived abundances for each α-element separately as well as a combination of the individual elements, in the sense that [α/Fe]=[(Mg+Ca+Ti)/3 Fe] (e.g., Table 1 in Venn et al. 2004), which is a common average to reduce the scatter in the trends of individual elements vs. metallicity (Lambert 1987). These figures also include a vast compilation of Galactic thin and thick disk stars as well as a large number of halo field stars[8]. The separation into these Galactic components is purely based on kinematic information, where present. In addition, stars on retrograde orbits and those with a high-velocity Toomre component, i.e., $\sqrt{U^2+W^2} > 340\,\mathrm{km\,s^{-1}}$, are distinguished. In order to place Carina onto a reference frame of LG abundances, also the currently available abundance ratios of seven dSphs are shown (Dra, Sex, UMi from Shetrone et al. 2001; Scl, For, Leo I, Car from S03; UMi from Sadakane et al. 2004 and Scl from Geisler et al. 2005). Note that five red giants in Carina were also included in the study of S03. However, none of their targets coincides with our present sample (cf. Tables 2.4, 3.1).

When comparing such copious data sets from various sources as done by Venn et al. (2004), Pritzl et al. (2005) and as shown in Figs. 3.3, 3.4, one has to keep in mind that each analysis uses a variety of spectral lines, presumably differing oscillator strengths and different model atmosphere techniques. The combination of such data will then reflect a larger spread in the abundance ratios of the order of 0.1–0.2 dex (Venn et al. 2004), a value comparable to the abundance offsets found by S03 by using different stellar atmospheres and atomic data. In the light of our quoted measurement uncertainties, we did not attempt to homogenize the data shown in Figs. 3.3, 3.4. and we do not expect such potential inconsistencies to alter any of the conclusions drawn in the following.

Since the Mg triplet lines at ∼5180Å are strongly saturated in the majority of our spectra, their EWs cannot be reliably employed to determine accurate Mg abundances. Hence, we have to rely on two different absorption features on average in our spectral range. As Venn et al. (2004) note, the scatter in [Mg/Fe] is much larger than in either [Ca/Fe] or [Ti/Fe], which is also reflected by our data points. Ignoring the strongly discrepant target at [Fe/H]=-1.51 with [Mg/Fe]=-0.78, which we will discuss separately below, we find an average <[Mg/Fe]> of 0.06 ± 0.22 dex (-0.02 ± 0.16 for [Fe/H] > -2). The two most metal poor stars in our sample exhibit enhanced Mg abundances of 0.4 dex and thus partially overlap with those of the Galactic halo and in particular the stars on retrograde orbits. From this point of view, this retrograde component is likely to originate from satellite accretion events (Venn et al. 2004). This view is, on the other hand, not sustainable in the light of the Mg (and other α-element, as we will show below) depletion of the more metal rich stars w.r.t. the Galactic components.

Si is often considered as a prototypical α-element. Its production site is identified with SNe II

---

[8] The stellar abundances for these illustrations are tabulated in Venn et al. (2004), who in turn assembled the data from various literature sources. See their paper for references.

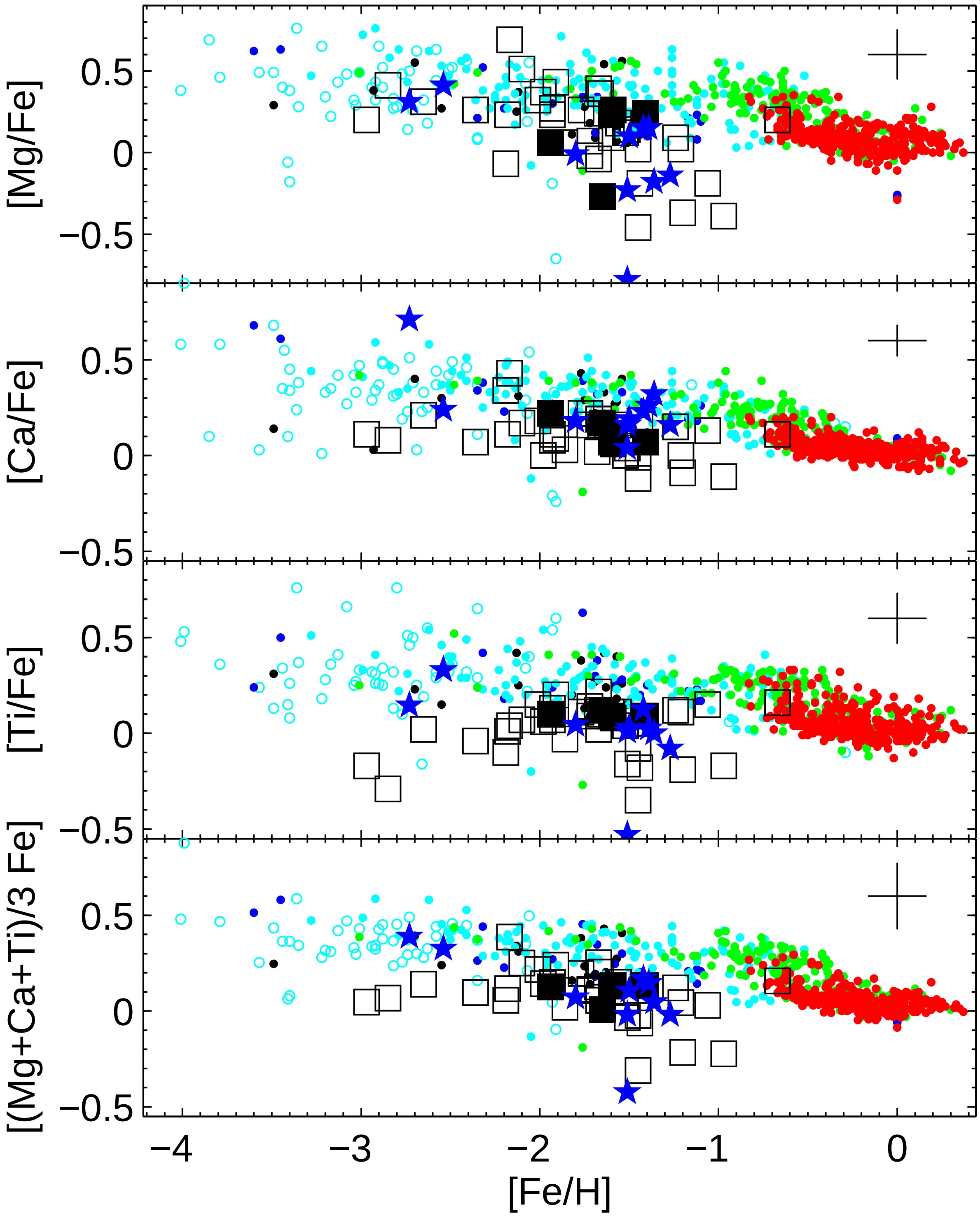

Figure 3.3: Abundance ratios for the α-elements: Our measurements for the ten Carina red giants are shown as filled blue stars. Filled black squares are the Carina stars from S03 and the open squares are data for seven other dSphs (Shetrone et al. 2001, S03; Sadakane et al. 2004; Geisler et al. 2005). The other data points are field stars, where the colour coding illustrates the kinematical separation into Galactic components and is shown in analogy to Venn et al. (2004); halo (cyan), thick disk (green), thin disk (red), retrograde orbits (black) and those with a high-velocity Toomre component (blue). For stars shown as open cyan symbols, there is no existing velocity information. The errorbars in the upper right corner display typical conservative estimates as derived in Section 3.3.3.

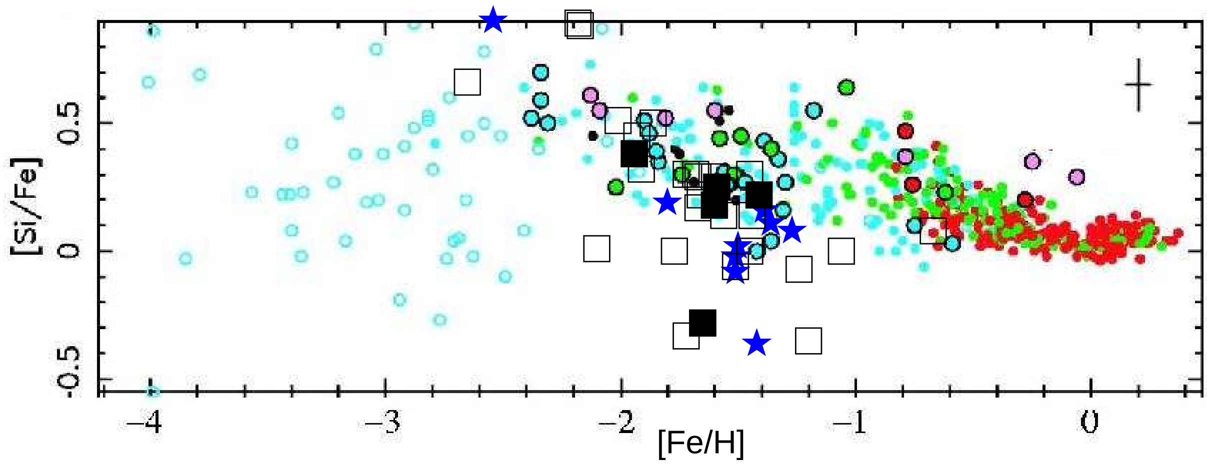

Figure 3.4: Same as Fig. 3.4, but for silicon abundances. Due to the lack of Si information in Venn et al. (2004), this figure was taken from Pritzl et al. (2005) and additionally displays a sample of globular clusters (filled large circles). [Reproduced with kind permission by B. J. Pritzl.]

of moderate masses around 20 M$_\odot$ (Woosley & Weaver 1995). On average, we could determine its abundance from three lines. For the most metal poor star no information could be extracted, since no measurable line was detected in its spectrum. In the secondmost metal poor star, there is a strong indication of a significant enrichment, as found in most metal-poor stellar abundance studies (McWilliam 1997; Prochaska et al. 2000; Venn et al. 2004 and references therein). As Fig. 3.4 implies, an enhancement of ∼0.9 dex is not atypical for metal poor giants in dSphs and is also found in UMi (Shetrone et al. 2001). Our stars show a lower average [Si/Fe] compared to the Shetrone samples, where our mean value is $<$[Si/Fe]$>$ = 0.01±0.16 dex (for [Fe/H] > -2). It is worth noticing, however, that there is a large scatter in [Si/Fe], both in the Galactic halo and all dSph samples considered here, including our own data. Owing to this scatter, parts of the dSph stars' abundances may well be considered to be consistent with the halo component. In this context, the low value of −0.4 reached by one of our stars is also broadly consistent with the range covered in LG dSphs.

Ca is, similar to Si, predominately produced in the intermediate mass SNe II (Woosley & Weaver 1995). Thus, an enhancement in metal-poor field stars is not surprising and well established (as reviewed by McWilliam 1997). While the most metal poor stars of the Shetrone et al. (2001) and S03 samples in Sex and Dra are clearly depleted w.r.t. the Galactic components (at [Ca/Fe]∼0.1), our most metal poor Carina giant is significantly enhanced in Ca (by 0.7 dex). However, already the second most metal poor star (0.2 dex more metal rich) has a [Ca/Fe] that is only slightly larger than the average we find from the rest of our sample: $<$[Ca/Fe]$>$ = 0.19±0.08 dex. While the majority of our targets with [Fe/H]> -2 tend to follow the trend of the other dSphs' Ca abundances and also are compliant with S03's measurements, one should note that three or four of the more metal rich giants appear to overlap with the Galactic thick disk and/or halo component. All in all, our Ca abundances in Carina can be considered as compatible with those in Galactic globular clusters, at least with those used to infer our Ca triplet based metallicities in Chapter 2.4 (see also Table 2.1). Hence, the use of a *Galactic* reference system to calibrate the *dSphs'* metallicities is not to be expected to introduce a significant bias of our measurements.

Although it is still unclear if the nucleosynthesis of Ti proceeds in analogy to the other

α-elements (e.g., Timmes et al. 1995; Woosley & Weaver 1995), it is traditionally included in the group of these elements, due to its similarly enhanced abundances in metal poor stars (Gratton & Sneden 1991). From this point of view, one might expect Ti to exhibit different trends from Si or Ca abundance trends (Prochaska et al. 2000). However, with the exception of the strongly depleted LG04a_001826, Ti in Carina tends to follow the other α-elements' overall trends: its average abundance is $<$[Ti/Fe]$> = 0.07 \pm 0.12$ dex (0.02 ± 0.06 for [Fe/H] > -2), which is significantly lower than the Galactic abundance ratios. In fact, the two most metal poor stars of our sample show an enhanced [Ti/Fe] of $\sim$0.24 dex, which is consistent with the Galactic halo, but at odds with the two comparably metal poor red giants from Shetrone et al. (2001) and S03. The latter stars in the Sex and Dra dSphs are deficient in [Ti/Fe] by ~ -0.23 dex. Still, the majority of our targets is consistent with both the Carina data and most of the other dSphs' abundances of Shetrone et al. (2001) and S03.

The abundances from both ionization stages of Ti provide a useful check for the stellar gravities, since these were derived independently of the Ti ionization equilibrium (e.g., McWilliam et al. 1995). The mean $\varepsilon(\mathrm{Ti\,I}) - \varepsilon(\mathrm{Ti\,II})$ for our Carina members is 0.08 ± 0.13 dex, arguing in favour of our average choice of $\log g$. If we conversely demanded ionization equilibrium for the Ti lines to establish a $\log g$, our spectroscopic surface gravities would have had to be lower by 0.13 dex on average, which is well within our estimate of the uncertainty on this atmospheric parameter (see Section 3.3.2). Moreover, the fact that our data does not exhibit any significant trend of $\varepsilon(\mathrm{Ti\,I})$ or $\varepsilon(\mathrm{Ti\,II})$ with $\mathrm{T_{eff}}$ supports our view that we can, for the moment, neglect NLTE effects in our analyses (Luck & Bond 1985; cf. Johnson 2002).

3.4.3 The α-depleted case of LG04a_001826

We now turn to the question of whether our target LG04a_001826, which shows a considerable depletion in almost all of the α-element ratios, i.e., in [Mg/Fe], [Si/Fe] and [Ti/Fe], can provide further insight into general galactic evolution or should be rather considered as an outlier.

A possible class of metal poor stars, in which heavy elements, in particular Mg, are significantly depleted are λ Boo stars (Venn & Lambert 1990). However, these Population I stars are typically of a spectral type earlier than F4 and thus hotter than our target stars in question. Moreover, they are predominantly found in the Milky Way, although recent observations have detected a large number of these stars in the LMC (e.g., Paunzen et al. 2005). Nevertheless, nothing is presently known about the presence of λ Boo type stars in dSphs and we refrain from further pursuing such conjectures.

One possible realistic interpretation of a selective depletion of the α-elements can be the occurrence of deep mixing. In this vein, processed material from the inside regions of a star can be transported into the upper atmosphere. Nucleosynthetic burning processes O, N and Ne to Na, whereas Mg is converted into Al in deep layers of red giants. Hence, typical deep mixing patterns predict that an atmospheric depletion in O coincides with an enhancement of Na (Langer et al. 1993), while any observed Mg depletion is accompanied by an enhanced Al abundance (Langer & Hoffmann 1995). However, such (anti-) correlations are primarily detected in globular clusters of the Galaxy (Pritzl et al. 2005 and references therein) and of dSphs (Letarte et al. 2006), but they are neither observed in Galactic field stars (Gratton et al. 2004) nor in dSph stars (S03; Venn et al. 2004). Unfortunately, in none of our spectra could Al be detected, since all suitable transitions in our spectral range produce lines that are too weak. On the other hand, preliminary evidence suggests that LG04a_001826 shows a considerable enhancement in sodium w.r.t. the other stars in our sample. From this point of view, we cannot exclude the possibility that its abundance patterns are in fact influenced by deep mixing. Detailed measurements of O and Na abundances will aid in elucidating this scenario and are underway.

Generally speaking, the α-elements are synthesized in core-collapse SNe II. Nevertheless, one has to keep in mind that different elements originate in different stages of these endphases in the lives of massive stars. Oxygen and magnesium are produced mainly during the hydrostatic (carbon- and ensuing neon-) burning phases. Thus their yields are in the first place a function of the progenitor's mass and are heavily affected by the thickness of the burning shells, the treatment of rotation and convection and the mass cut between the proto-neutron star and the SN ejecta (Thielemann et al. 1996; Argast et al. 2002). Hence, due to a larger range of possible realizations of these factors, a larger scatter in the resulting element ratios such as [O/Fe] and [Mg/Fe] is to be expected (Argast et al. 2002; Venn et al. 2004). Depending on the exact mass of the SN II progenitor, also a low value of [Mg/Fe] is not unusual (see Fig. 1 in Argast et al. 2002). Moreover, this is also observed in a low number of metal poor bulge-stars (McWilliam et al. 1995) and in mildly metal-poor halo stars (e.g., Carney et al. 1997), though to a lesser extent. Although SNe models (like those of Argast et al. 2000, 2002) predict the occurrence of such depleted stars at lower, halo-like metallicities due to the mixing of the SN ejecta into a gas reservoir of $\sim 10^4 \mathrm{M}_\odot$, comparable variations at a higher [Fe/H] as in the case of LG04a_001826 (-1.5 dex) can be explained analogously and give reasonable estimates, in particular in the light of the uncertainties associated with the modeling of Mg and Fe yields. Alternatively, one could assume that this star exhibits a normal average elemental abundance of Mg, but shows indication of a deviating Fe abundance for a typical star with this [Mg/H]. In this vein, its low [Mg/H] would be representative of a halo-like star of [Fe/H]~ -2.6 dex. Thus, in order to realize its comparatively low [Mg/Fe], LG04a_001826 had to originate from SNe Ia pre-enriched material (Gilmore & Wyse 1998), which could be subject to a significantly higher iron yield and/or which is diluted less than the characteristic halo ISM, producing a [Fe/H] higher by ~ 1.1 dex than expected from its α-yield.

The other α-elements Si, Ca and Ti originate in the explosive burning during the outburst itself and hence are exclusively dependent on the explosion energy, which covers only a small range. Hence, their abundance ratios can be expected to show a much lesser scatter, which is in fact in agreement with the observations (Venn et al. 2004; see also Figs. 3.3 and 3.4). In this vein, one should note that the otherwise depleted star in our sample exhibits a rather average [Ca/Fe] abundance ratio. The fact that it then also deviates in [Si/Fe] may support suggestions that Si contains a non-negligible admixture of material originating in hydrostatic burning (Thielemann et al. 1996; Argast et al. 2000). The intermediate-mass α-element Ti has also a contribution from complete Si burning with an alpha-rich freezeout (Thielemann et al. 1996 and references therein). Small differences between Ca, Si and Ti are naturally to be expected. Finally, the production of Ti is not yet fully understood (Woosley 1986; Woosley & Weaver 1995) and Galactic evolution models often fail to reproduce the observed abundance patterns (e.g., Timmes et al. 1995). A detailed interpretation of this star's abundance ratios in terms of the yields for each individual α-element, however, has to rely on finetuned nucleosynthetic modeling and is presently hampered by the lack of an accurate understanding of the exact SN II explosion mechanism (e.g., see discussions in Woosley & Weaver 1995; Timmes et al. 1995; McWilliam et al. 1995; Thielemann et al. 1996; Argast et al. 2000, 2002).

All in all, the presence of a strongly α-element depleted object may suggest that we can see here the influence of *single* SN events. Contrary to a homogeneous, close to uniform [α/Fe] pattern resulting from well mixed, IMF-averaged SNe, this star is likely to reflect the imprint of stochastic inhomogeneous chemical evolution, where the progenitor interacted with its immediate surroundings and a complete mixing has not yet occurred. Hence, instead of overinterpreting this star's abundance pattern in terms of Carina's SF history we rather attribute it to statistical fluctuations due to incomplete ISM mixing processes. It is then also possible to assign the strong Ca enhancement of the most metal poor star in our sample to such scatter, which becomes progressively dominant in metal-poor stars of [Fe/H]$\lesssim -3$ dex (e.g., Argast et al. 2000).

3.5 Implications for Carina's chemical evolution

Apart from the two most metal poor stars in our sample and the strongly depleted red giant LG04a_001826, the majority of our targets have slightly enhanced α-abundance ratios: we thus find a mean [α/Fe] of 0.07 ± 0.07 dex. In this context, our data confirm the earlier important finding that the α-elements in dSph stars are significantly depleted w.r.t. Galactic halo stars of the same metallicity (Shetrone et al. 2001; S03; T03; Venn et al. 2004). The metal poor (halo) stars at the plateau in [α/Fe] versus [Fe/H] are typically identified with old ages (e.g., T03). Since the two most metal poor stars in Carina coincide with the halo abundances, we can interpret their enhancement in terms of an early halo evolution. These stars should be expected to be old[9] and have formed at an early epoch, when SNe Ia have not yet started to contribute, but when an initial starburst has already polluted the pristine material with a significant amount of the α-elements ejected in short-lived SNe II. On the other hand, those stars with higher metallicities between ~ -1.8 and -1.3 dex comply with the stars analyzed in other dSph galaxies, although they populate, with the exception of the extremely α-depleted object, the higher end of the dSphs' [α/Fe] abundances. These progressively lower values of [α/Fe] are characteristic of the slow chemical evolution and low SF rates in dwarf galaxies (Matteucci 2003). Differences between individual galaxies' abundance ratios are, however, to be expected, since these chemical tracers sensitively depend on the details of each galaxy's environment, SF history, IMF etc. Overall, these stars' abundance ratios are also in good agreement with the values found in the five stars studied by S03.

It has been proposed that Carina's episodic SF history, i.e., its bursty and quiescent phases are reflected in the [α/Fe]-abundance ratios (S03, T03). In this context, S03 suggested that the considerable rise in [α/Fe] – after the typical decline due to the permanent feedback from SNe Ia – seen in their data at [Fe/H]~ -1.65 indicates that the respective stars may be related to either Carina's second star burst around 7 Gyr ago or to an intermediate SF event well before this burst. Both interpretations are compatible with Carina's proposed SF histories and the time intervals of each SF episode and hiatus (Smecker-Hane et al. 1996; Hurley-Keller et al. 1998; Rizzi et al. 2003) and also appear to be strengthened by comparable variations in a number of heavy element abundance ratios, although fully resolving and quantifying the SF history clearly requires further investigation.

It is then tempting to interpret the [α/Fe] pattern of the full data set (Fig. 3.5; in particular bottom left panel) in terms of Carina's SF bursts. In this vein, there may be an indication of a rise in [α/Fe] between -1.65 and -1.6 dex as already noted by S03. After a decline in SF, this ratio tends to rise again towards a maximum in [α/Fe] at around [Fe/H]$=-1.4$ dex, before leveling off again. Accordingly, these patterns could be assigned to an increase in SF activity, perhaps associated with separate SF bursts 7 and 3 Gyr ago (Hurley-Keller et al. 1998). However, in the light of the measurement uncertainties (Fig. 3.5, bottom right) we refrain from such an

---

[9] Unfortunately, these targets lie redwards of the most metal metal poor isochrones and cannot be reliably age-dated.

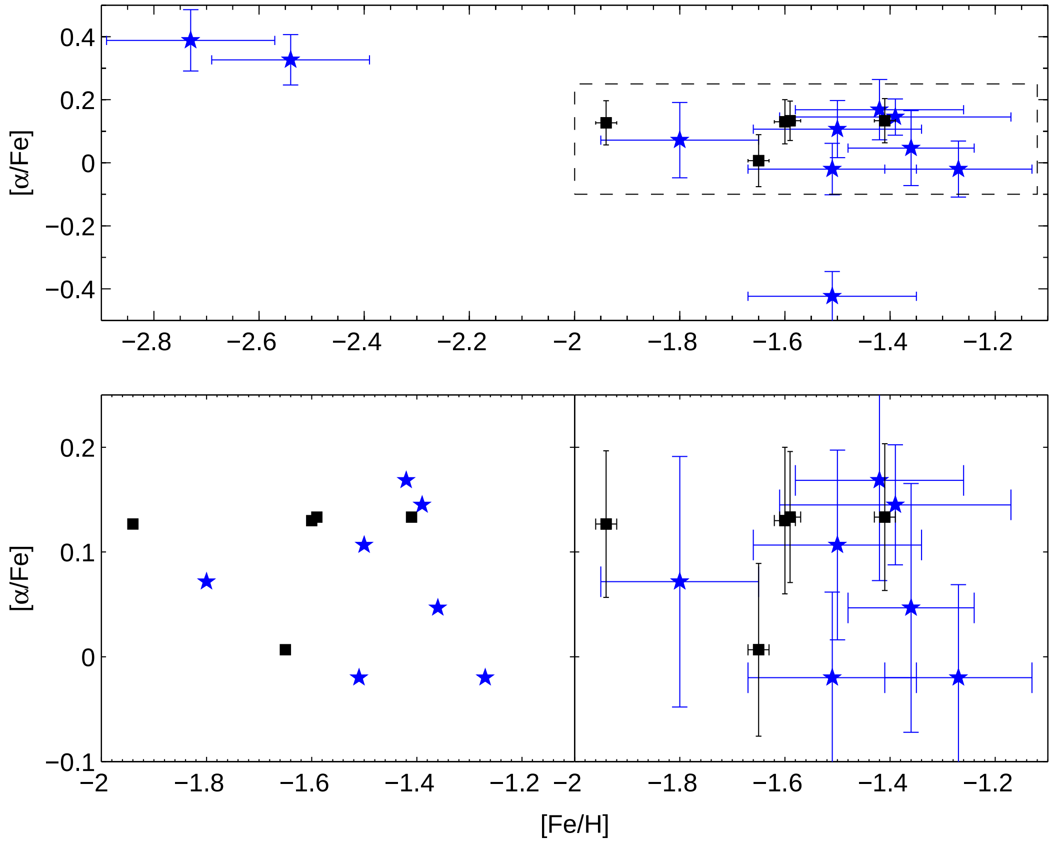

Figure 3.5: Our measured [α/Fe] (blue stars) shown together with the data from S03 (black squares). The bottom panels are blow-ups of the region enclosed by the dashed quadrangle in the top panel. In the bottom left panel errorbars were omitted for clarity.

overinterpretation of our results and reconstructing Carina's detailed SF history. We rather note that the bulk of our targets (disregarding the most metal poor and strongly α-depleted one for the moment) are rather uniform in their abundances, albeit that the presumably intrinsic and overall large scatter in [α/Fe] increases towards higher metallicities. These uniformly low [α/Fe]-ratios over a wider range of metallicities may point to the fact that Carina's SF was in fact dominated by blowout (e.g., Mac Low & Ferrara 1999; see also Chapter 2.7.)

Finally, it is also instructive to compare our [α/Fe]-data with the model predictions from Lanfranchi et al. (2006b, hereafter LMC06), which are an extension of the models presented in LM04. As outlined in detail in Section 2.7.3, this set of models was tailored in terms of best-fit SF and wind efficiencies, such as to reproduce the total mass, present-day gas mass and the few elemental abundances available at that time of a number of dSphs. In addition to the aforementioned observables used in LM04, LMC06 also incorporated the MDF of Carina from Koch et al. (2006, see Sect. 2.4) to update their choice of model parameters. In this context, a marginally higher SF efficiency (of 0.15 Gyr^{-1}) and a slightly lower wind efficiency of 5 (times the SF rate) has been adopted to better match the observations. Furthermore, contrary to the models described in LM04, which assumed Carina's SF history according to Hernandez, Gilmore, & Valls-Gabaud (2000) therefore neglecting the prominent red clump and substantial old population as

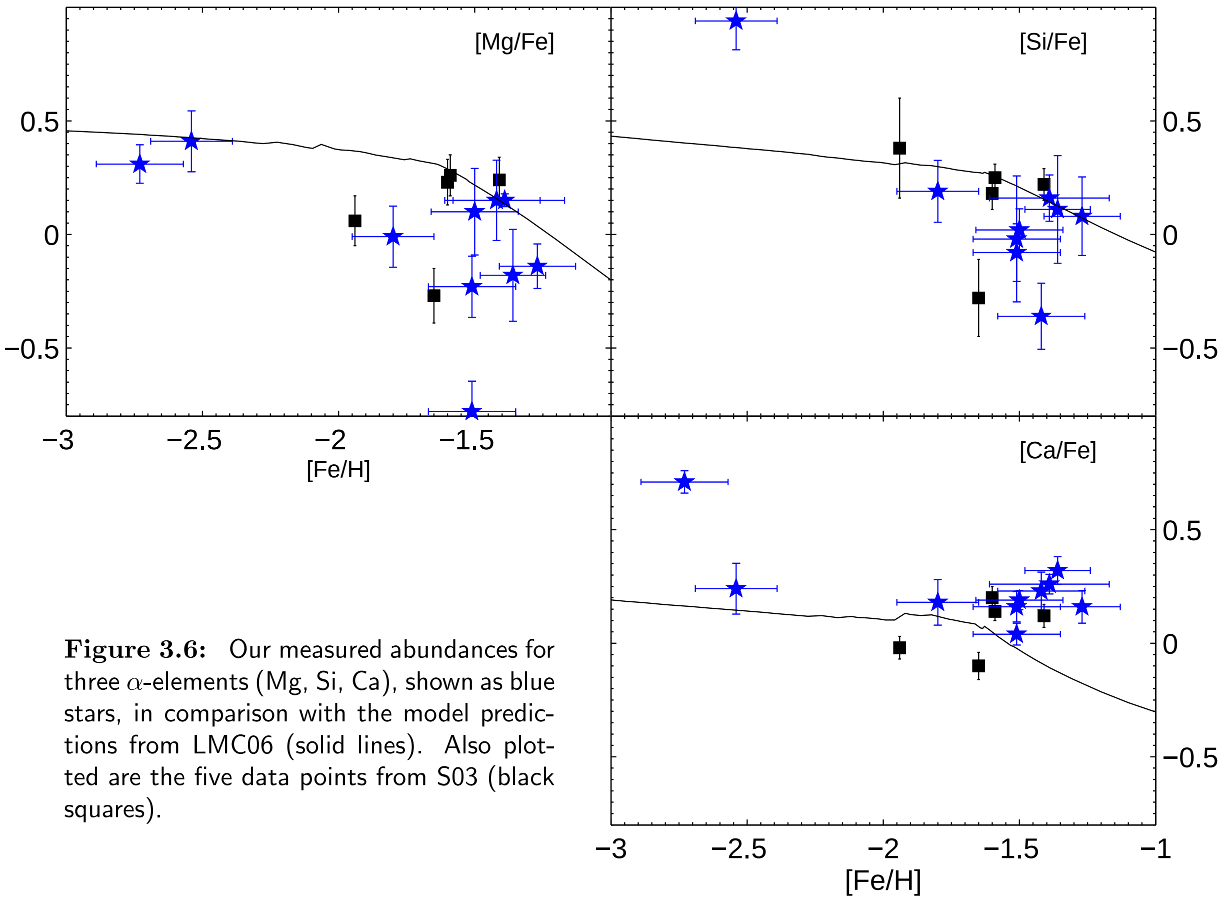

Figure 3.6: Our measured abundances for three α-elements (Mg, Si, Ca), shown as blue stars, in comparison with the model predictions from LMC06 (solid lines). Also plotted are the five data points from S03 (black squares).

witnessed by the populous horizontal branch (e.g., Smecker-Hane et al. 1994; Monelli et al. 2003), the LMC06 models adopt the SF history from Rizzi et al. (2003). In the latter, SF occurs episodically with an initial active period at an early epoch, while the majority of stars is formed ∼3–7 Gyr ago.

Fig 3.6 shows our observed data points for three α-elements together with the targets from S03, thus representing the entire currently available high resolution abundance data for Carina, in comparison with the aforementioned model predictions from LMC06.

For all the elements shown there is a sudden decrease in the predicted [α/Fe] at [Fe/H]~ -1.6, which is a consequence of the combination of the onset of galactic winds and the regular injection of Fe into the ISM via SNe Ia events. Once the winds set in, the available amount of gas for SF is reduced, resulting in a decline of the overall SF. Consequently, the formation of new stars almost ceases and, in turn, the occurrence of SNe II and the related production and injection of the α-elements is halted as well. Since, on the other hand, Fe is continuously produced and injected into the ISM by the slowly evolving SNe Ia for several Gyr, disregarding the cessation of SF, the start of efficient winds leads to the sudden decrease seen in the predicted [α/Fe] abundance ratios.

With the exception of Ca, for which the majority of our stars lies significantly above the models, the observed element ratios tend to lie below the predictions at any given metallicity. This may in part be attributed to the large scatter in [α/Fe] for basically all metallicities, which also has been reported to exist in previous observational studies (see Venn et al. 2004). At present, the models appear to provide at best an upper limit to the observations and thus reproduce the more chemically enhanced stars fairly well. Nevertheless, it is remarkable that the [Mg/Fe] and in particular the [Si/Fe] abundances of the more metal rich stars are also reproduced rather well by the models[10]. The overall impression to glean from this figure is, however, that, although being well able to predict certain patterns in chemical abundance ratios, there is a need for models of chemical evolution to steadily improve the parameters governing the SF processes. In essence, matching the full sample of available α-elemental data appears to require an earlier turnoff from the plateau in [α/Fe] at lower metallicities (again with the exception of Ca). These low abundances at higher metallicities could well be achieved through adopting a less intense wind and/or an onset of these winds at earlier epochs. More intense winds, on the other hand, would provide lower values for *all* [α/Fe] ratios, once the wind developed, due to the correspondingly decreased SF rate (G. A. Lanfranchi, private comm.). Finally, this may well be attributed to the difficulties in assuming a proper SF history for the models and will depend both on the number, duration and epoch of the assigned SF episodes. Similarly, an overall lower SF efficiency would be able to retain the lower [α/Fe]-values. Since these parameters, in turn, affect the shape of Carina's MDF (as they have been adjusted to match the latter) it is clear that ideally the MDF, the full set of observed abundance ratios and a fully sampled SF history have to be simultaneously taken into account to reliably devise the evolutionary history of Carina.

Acknowledgments The data used in Chapter 3 are based on the same collaboration within the ESO Large Programme as described in Chaper 2. I am grateful to Andy McWilliam for providing his versions of the atmosphere interpolators and photometric gravity codes and many helpful comments. I would also like to thank F.-K. Thielemann for helpful discussions about α-element production and Gustavo Lanfranchi for sending me his model data.

---

[10] One should keep in mind that the original model parameters were optimized to fit the abundance patterns as observed by S03 so that their element ratios, as they are, are fit fairly well.

Appendix 3.A: Linelist

Table 3.A: Linelist

Ion	Wavelength [Å]	EP [eV]	log gf	Equivalent Width [mÅ]										
				Arcturus	4260^a	6477^a	377^a	1556^a	1826^a	777^a	2181^a	6628^a	951^a	626^a
Mg I	5528.418	4.35	−0.481	256.0	101	145	148	126	88	147	156	99	68	102
Mg I	5711.091	4.33	−1.660	153.0	50	60	57	70	11	65	86	...	...	23
Si I	5665.560	4.90	−1.970	63.0	...	7	...	10	...	...	23	...	...	7
Si I	5690.433	4.93	−1.953	62.0	...	...	9	...	...	19	24	...	...	...
Si I	5948.548	5.08	−1.298	88.0	14	7	28	56	...	23	36	...	...	...
Si I	6125.026	5.61	−1.445	43.0	7	...	...	13	18	...	4	...	...	...
Si I	6145.020	5.62	−1.528	38.8	...	...	8	...	...	...	12	...	...	...
Si I	6155.130	5.62	−0.828	76.0	...	12	...	...	9	...	25	15	...	...
Si I	6237.328	5.61	−1.050	64.0	13	14	...	...	13	40	41	...	...	19
Si I	6721.844	5.86	−1.016	49.0	...	...	...	...	...	...	...	...	...	6
Ca I	5260.390	2.52	−2.099	74.5	7.0	...	...	14.0	...	...	17.0	...	5.0	...
Ca I	5261.708	2.52	−0.626	150.0	62.0	61.0	68.0	85.0	74.0	95.0	100.0	38.0	38.0	20.0
Ca I	5349.469	2.71	−0.716	133.0	64.0	84.0	49.0	90.0	64.0	96.0	83.0	67.0	...	42.0
Ca I	5512.989	2.93	−0.666	122.2	36.0	39.0	53.0	59.0	50.0	56.0	54.0	...	20.0	...
Ca I	5581.970	2.52	−0.820	144.0	52.0	52.0	61.0	118.0	56.0	91.0	98.0	41.0	17.0	15.0
Ca I	5590.126	2.52	−0.891	140.2	37.0	71.0	81.0	86.0	63.0	96.0	101.0	44.0	31.0	29.0
Ca I	5857.459	2.93	0.140	173.7	74.0	72.0	94.0	108.0	96.0	126.0	99.0	48.0	60.0	39.0
Ca I	5867.572	2.93	−1.819	61.0	...	...	23.0	...	...	100.0	12.0	...	...	...
Ca I	6102.727	1.88	−0.910	202.7	101.0	103.0	101.0	137.0	106.0	150.0	149.5	61.0	75.0	48.0
Ca I	6162.180	1.90	−0.195	288.0	156.0	175.0	170.0	187.0	154.0	202.6	198.0	120.0	103.0	86.0
Ca I	6166.440	2.52	−1.149	132.2	27.0	42.0	51.0	55.0	43.0	75.0	65.0	...	...	...
Ca I	6169.044	2.52	−0.907	145.7	60.0	67.0	59.0	76.0	44.0	89.0	80.0	...	...	...
Ca I	6169.564	2.52	−0.738	155.7	81.0	66.0	77.0	95.0	61.0	104.0	99.0	17.0	26.0	...
Ca I	6439.083	2.53	−0.030	211.0	...	147.0	126.0	...	132.0	168.0	156.0	93.0	88.0	45.0
Ca I	6455.605	2.52	−1.540	113.3	...	42.0	46.0	55.0	...	55.0	51.0	...	...	...
Ca I	6471.668	2.52	−0.875	151.0	79.0	59.0	90.0	90.0	65.0	109.0	102.0	29.0	...	...
Ca I	6493.788	2.52	−0.410	181.8	90.0	...	...	...	...	...	...	...	...	...
Ca I	6499.650	2.52	−1.016	143.3	60.0	59.0	80.0	84.0	63.0	62.0	91.0	22.0	...	...
Ca I	6717.690	2.71	−0.054	191.0	90.0	91.0	96.0	95.0	76.0	106.0	111.0	...	...	...
Ti I	4778.258	2.24	−0.510	79.2	...	...	...	8	...	...	...	...	...	...
Ti I	4820.414	1.50	−0.055	146.7	51	44	58	41	40	69	71	...	16	...
Ti I	4840.884	0.90	−0.633	160.5	62	...	73	71	42	102	92	19	22	32
Ti I	4913.622	1.87	−0.016	127.1	13	...	43	51	29	55	62	...	...	...
Ti I	4997.100	0.00	−1.722	174.3	54	69	...	78	51	76	88	22	...	32

Continued on next page

Table 3.3 – *Linelist, continued*

Ion	Wavelength [Å]	EP [eV]	log gf	Equivalent Width [mÅ]										
				Arcturus	4260 ^{a}	6477 ^{a}	377 ^{a}	1556 ^{a}	1826 ^{a}	777 ^{a}	2181 ^{a}	6628 ^{a}	951 ^{a}	626 ^{a}
Ti I	4999.510	0.83	0.140	239.3	98	120	133	123	122	141	166	69	60	83
Ti I	5001.010	2.00	−0.052	119.1	...	...	25	22	...	36	...	...	...	...
Ti I	5009.655	0.02	−1.900	163.7	48	44	61	68	26	77	87	...	...	12
Ti I	5016.168	0.85	−0.510	176.3	55	70	80	62	41	83	97	30	30	46
Ti I	5039.964	0.02	−1.170	215.0	94	114	114	103	79	138	151	60	26	70
Ti I	5043.588	0.84	−1.797	114.5	36	...	34	43	...	...	52	...	14	...
Ti I	5062.110	2.16	−0.460	90.0	...	...	...	...	...	30	...	...	...	...
Ti I	5064.650	0.05	−0.985	232.6	94	98	125	117	86	124	146	58	32	64
Ti I	5071.491	1.46	−0.783	120.8	23	...	12	53	...	36	44	...	...	...
Ti I	5113.447	1.44	−0.607	131.0	...	...	23	28	...	57	62	...	...	...
Ti I	5145.460	1.46	−0.670	127.5	...	45	...	...	27	51	58	24	8	...
Ti I	5147.482	0.00	−1.876	170.5	48	77	81	70	50	97	100	16	...	26
Ti I	5152.190	0.02	−1.912	166.8	...	...	...	96	...	...	...	15	...	...
Ti I	5192.978	0.02	−1.035	236.0	91	137	152	117	93	143	168	90	49	79
Ti I	5219.700	0.02	−1.980	165.5	31	47	78	72	42	95	85	...	...	...
Ti I	5223.630	2.09	−0.690	83.7	11	...	...	15	...	...	10	...	...	...
Ti I	5282.402	1.05	−1.850	100.6	...	...	...	...	13	40	32	...	...	...
Ti I	5295.780	1.07	−1.757	104.4	10	...	24	...	...	...	34	...	...	...
Ti I	5471.205	1.44	−1.580	86.5	...	19	...	...	...	10	30	...	...	...
Ti I	5474.230	1.46	−1.525	88.7	...	...	...	16	...	...	...	...	...	...
Ti I	5490.150	1.46	−1.113	110.9	...	45	43	29	...	48	37	...	...	...
Ti I	5503.900	2.58	−0.316	69.9	...	...	22	...	...	42	23	...	...	...
Ti I	5689.490	2.30	−0.613	76.2	...	...	...	...	...	33	15	...	...	...
Ti I	5866.461	1.07	−0.635	171.3	54	70	90	98	44	100	102	30	...	...
Ti I	5922.123	1.05	−1.437	130.8	...	31	26	46	...	68	47	...	...	...
Ti I	5937.814	1.07	−2.030	95.4	...	...	...	8	...	27	40	...	...	...
Ti I	5965.830	1.88	−0.353	124.6	...	...	32	10	...	...	22	...	...	...
Ti I	5978.540	1.87	−0.670	108.5	...	27	29	26	...	34	38	...	...	...
Ti I	6064.630	1.05	−1.970	102.1	...	...	24	24	...	39	...	...	...	...
Ti I	6126.220	1.07	−1.439	131.8	...	...	42	47	27	62	60	...	...	...
Ti I	6336.100	1.44	−1.840	77.2	...	10	...	...	...	...	7	...	...	...
Ti I	6554.238	1.44	−1.262	115.0	...	...	...	17	...	46	44	...	...	...
Ti I	6556.077	1.46	−0.943	132.4	...	11	37	33	...	49	50	7	...	...
Ti I	6599.130	0.90	−2.052	115.7	...	21	...	...	...	...	19	...	...	...
Ti I	6743.127	0.90	−1.705	139.4	22	18	39	33	...	48	47	...	...	...
Ti II	4798.530	1.08	−2.608	108.1	...	72	...	57	...	...	68	32	...	40
Ti II	4865.618	1.12	−2.592	107.4	60	...	53	64	43	56	63	...	...	...

Continued on next page

Table 3.3 – *Linelist, continued*

Ion	Wavelength [Å]	EP [eV]	log gf	Equivalent Width [mÅ]										
				Arcturus	4260[a]	6477[a]	377[a]	1556[a]	1826[a]	777[a]	2181[a]	6628[a]	951[a]	626[a]
Ti II	5005.171	1.57	−2.840	67.3	37	25	25	30	14	34	41	...	...	14
Ti II	5226.545	1.57	−0.993	159.9	116	126	109	100	95	122	112	109	68	...
Ti II	5336.780	1.58	−1.680	125.4	80	89	93	106	78	94	113	63	52	60
Ti II	5418.770	1.58	−2.264	97.9	54	64	57	78	61	85	74	60	13	...
Fe I	4802.887	3.69	−1.680	89.8	38.8	35.0	79.3	20.5	37.5	39.6	43.5	21.5	...	3.5
Fe I	4839.544	3.27	−1.952	102.4	34.0	42.1	69.8	44.6	60.2	54.3	59.5	30.5	29.3	38.1
Fe I	4871.325	2.85	−0.472	246.9	91.8	102.5	120.8	126.6	114.5	125.6	141.1	82.7	74.5	116.2
Fe I	4903.316	2.88	−0.720	206.6	88.9	107.7	109.9	107.9	95.6	97.0	112.4	71.7	36.1	70.2
Fe I	4918.998	2.85	−0.462	250.5	136.1	127.2	142.9	137.5	141.2	151.0	142.4	95.0	74.2	98.4
Fe I	4938.820	2.88	−1.312	158.1	86.0	53.2	83.2	108.8	107.8	93.3	108.1	49.5	32.4	55.5
Fe I	4939.694	0.86	−3.344	207.6	117.7	82.7	134.1	122.1	127.5	149.1	136.0	77.7	53.8	83.3
Fe I	4962.576	4.18	−1.472	70.9	37.9	43.9	...	30.1	30.4	37.7	38.5	...	...	15.9
Fe I	5001.870	3.88	−0.355	140.5	86.6	96.7	95.3	97.3	109.5	85.7	113.0	74.3	56.2	65.6
Fe I	5006.120	2.82	−0.802	207.8	141.3	116.3	128.0	148.4	125.8	123.1	154.8	104.4	64.4	75.8
Fe I	5028.130	3.57	−1.602	102.1	50.0	55.5	75.9	69.3	80.5	78.0	68.8	28.1	4.8	18.5
Fe I	5044.210	2.85	−1.809	135.3	59.7	78.2	77.1	76.7	72.0	81.6	104.3	43.7	...	16.8
Fe I	5048.440	3.94	−1.520	84.1	...	35.6	40.2	36.5	52.0	43.8	56.6	16.1	...	...
Fe I	5068.770	2.94	−1.331	154.8	87.1	98.0	86.6	75.1	111.3	...	115.2	59.7	59.5	57.5
Fe I	5074.753	3.55	−0.790	140.8	71.2	75.3	67.5	58.0	82.0	84.9	95.3	55.0	14.1	42.2
Fe I	5079.230	2.20	−1.980	175.0	94.9	107.3	...	134.9	...	133.0	...	79.9	36.6	74.5
Fe I	5127.360	0.92	−3.390	201.6	146.3	140.9	150.5	177.2	161.4	140.1	188.3	115.6	93.5	102.9
Fe I	5131.476	2.22	−2.745	132.7	72.3	97.3	129.3	95.5	114.5	120.0	137.4	74.8	35.3	51.1
Fe I	5141.746	3.23	−0.860	161.3	86.4	87.9	103.8	105.8	115.0	...	106.4	63.9	43.2	50.9
Fe I	5145.102	2.20	−2.396	151.6	30.9	65.2	51.2	52.2	60.2	...	89.5	25.4	...	...
Fe I	5150.852	0.99	−3.067	226.7	110.6	120.2	136.5	128.7	123.8	146.0	171.9	114.5	83.9	94.2
Fe I	5151.920	1.01	−2.921	242.8	113.0	125.8	200.9	155.0	166.4	151.0	...	87.1	94.2	98.9
Fe I	5162.281	4.18	0.252	156.9	60.2	100.4	98.1	102.7	119.4	82.5	96.8	57.2	31.6	31.9
Fe I	5191.465	3.03	−0.451	224.3	84.7	114.6	120.8	139.4	135.9	136.1	163.9	81.0	41.8	79.2
Fe I	5192.353	3.00	−0.401	236.3	107.4	121.6	143.3	129.9	141.6	133.6	176.9	82.4	53.4	96.4
Fe I	5198.710	2.22	−1.665	202.0	101.2	108.1	112.7	136.1	111.7	103.9	136.8	76.6	51.8	89.2
Fe I	5215.188	3.27	−0.980	152.9	81.3	84.9	112.8	122.0	108.0	99.0	108.9	69.0	49.1	62.5
Fe I	5216.280	1.61	−2.240	229.3	130.9	153.7	148.1	152.0	153.0	164.8	174.5	120.2	98.6	102.3
Fe I	5217.390	3.21	−1.147	147.8	86.7	98.4	96.1	115.0	103.2	100.5	113.5	48.9	28.8	51.5
Fe I	5225.520	0.11	−4.409	211.9	121.7	128.9	141.5	143.8	141.3	146.4	171.6	84.8	67.8	93.3
Fe I	5232.952	2.94	−0.196	290.3	144.9	108.5	162.3	165.0	155.2	146.5	168.3	136.8	73.7	100.0
Fe I	5242.490	3.62	−1.147	121.4	43.2	84.8	50.0	95.8	84.2	85.0	79.7	42.2	13.4	30.3
Fe I	5247.050	0.09	−4.656	193.9	107.1	130.1	133.2	121.0	116.7	129.2	152.0	87.2	61.7	99.8

Continued on next page

Table 3.3 – *Linelist, continued*

Ion	Wavelength [Å]	EP [eV]	log gf	Equivalent Width [mÅ]										
				Arcturus	4260[a]	6477[a]	377[a]	1556[a]	1826[a]	777[a]	2181[a]	6628[a]	951[a]	626[a]
Fe I	5250.217	0.12	−4.600	194.4	121.1	124.7	133.3	128.3	140.5	152.8	180.0	88.6	75.1	112.4
Fe I	5281.798	3.04	−0.760	190.0	87.9	109.1	110.4	112.8	113.3	123.5	138.8	78.1	46.5	67.9
Fe I	5288.533	3.69	−1.812	86.4	36.1	54.1	...	51.1	53.5	38.2	54.2	...	...	15.6
Fe I	5302.307	3.28	−0.968	153.6	80.3	120.8	104.6	132.6	125.9	111.5	127.8	97.5	32.4	59.5
Fe I	5307.369	1.61	−2.900	172.4	96.9	123.0	121.3	130.0	128.8	132.3	139.2	90.4	49.6	81.4
Fe I	5324.191	3.21	−0.213	227.3	120.8	133.5	130.6	143.3	166.1	155.5	161.5	104.4	73.1	81.0
Fe I	5326.145	3.57	−2.221	74.6	...	13.9	...	...	16.7	31.9	32.0	...	...	...
Fe I	5339.937	3.27	−0.872	161.1	104.7	123.3	113.3	121.5	113.0	128.5	136.3	69.3	57.7	93.8
Fe I	5369.974	4.37	0.200	141.3	78.3	77.6	82.1	95.1	102.2	93.1	103.3	62.4	34.0	55.1
Fe I	5379.570	3.68	−1.664	95.5	44.0	36.6	49.6	41.6	54.3	62.9	54.5	...	...	23.6
Fe I	5389.486	4.42	−0.490	104.9	30.4	49.6	62.9	54.2	71.8	50.9	67.5	11.3	...	19.5
Fe I	5393.176	3.24	−0.795	169.1	87.7	123.1	119.3	115.7	126.2	143.6	154.4	98.5	59.1	63.3
Fe I	5424.080	4.32	0.540	168.6	90.3	95.6	107.6	112.0	120.9	111.0	126.7	80.9	34.6	58.5
Fe I	5491.835	4.19	−2.218	31.3	71.3	...	...	...	36.6	...	...	32.6	...	...
Fe I	5569.631	3.42	−0.590	169.8	93.2	109.1	109.4	131.9	119.7	115.7	130.8	83.5	46.8	60.4
Fe I	5576.099	3.43	−1.010	144.0	84.2	106.6	95.0	119.1	122.3	86.7	116.4	66.9	33.1	65.9
Fe I	5615.658	3.33	−0.155	220.6	150.8	143.1	243.7	149.8	...	159.3	183.6	118.8	71.4	85.8
Fe I	5618.642	4.21	−1.515	68.4	23.5	...	41.1	62.0	...	47.1	37.5	...	...	...
Fe I	5662.520	4.18	−0.777	107.7	54.1	69.9	70.9	65.5	77.1	73.2	87.8	37.6	...	15.7
Fe I	5705.468	4.30	−1.585	58.4	...	14.9	...	16.3	...	...	29.4	...	...	...
Fe I	5753.120	4.26	−1.078	88.3	50.0	42.3	...	103.6	92.0	...	58.6	...	13.3	14.3
Fe I	5909.978	3.21	−2.430	91.8	29.0	11.6	44.6	46.9	51.9	52.1	39.0	6.4	15.1	...
Fe I	5916.250	2.45	−2.964	116.7	63.1	52.8	86.0	84.4	74.9	80.5	89.7	32.5	29.3	22.9
Fe I	5956.706	0.86	−4.415	158.2	84.1	92.1	114.4	112.2	110.9	112.1	138.0	52.2	27.6	46.1
Fe I	6027.059	4.08	−1.210	94.7	50.8	34.5	46.9	56.9	50.2	75.8	43.4	16.7	...	...
Fe I	6065.480	2.61	−1.453	192.4	101.8	112.8	141.1	152.5	147.9	160.9	160.4	91.4	34.5	47.8
Fe I	6082.720	2.22	−3.585	103.4	31.1	45.5	54.6	65.5	49.2	76.3	67.8	15.1	12.0	59.4
Fe I	6136.624	2.45	−1.415	215.9	137.2	127.9	173.7	160.2	170.2	144.1	161.7	109.1	60.2	58.5
Fe I	6137.000	2.20	−2.940	138.1	102.8	52.8	71.4	97.6	124.1	81.7	93.4	40.0	19.5	25.8
Fe I	6137.702	2.59	−1.241	215.4	111.7	144.2	168.2	157.6	155.0	143.9	152.7	96.8	62.6	61.8
Fe I	6151.620	2.18	−3.335	119.2	69.0	78.0	79.8	87.7	80.9	80.1	85.3	41.0	...	14.9
Fe I	6173.340	2.22	−2.945	136.7	76.2	88.1	81.3	112.7	103.5	111.1	121.3	48.3	19.9	48.3
Fe I	6180.209	2.73	−2.616	116.8	71.4	53.4	74.4	83.7	78.9	90.8	76.3	19.4	...	31.0
Fe I	6191.571	2.43	−1.273	236.9	135.9	133.8	146.6	165.0	...	195.4	165.2	95.8	57.9	87.4
Fe I	6213.437	2.22	−2.545	158.5	105.0	132.8	121.0	131.7	148.7	121.4	135.5	73.9	38.3	35.6
Fe I	6219.287	2.20	−2.263	177.5	116.5	125.0	114.8	139.3	141.1	137.2	142.2	77.2	37.5	56.1
Fe I	6229.232	2.83	−2.955	93.0	54.3	33.5	...	67.1	59.2	53.2	54.8	...	...	...

Continued on next page

Table 3.3 – *Linelist, continued*

Ion	Wavelength [Å]	EP [eV]	log gf	Equivalent Width [mÅ]										
				Arcturus	4260[a]	6477[a]	377[a]	1556[a]	1826[a]	777[a]	2181[a]	6628[a]	951[a]	626[a]
Fe I	6230.730	2.56	−0.568	339.8	173.9	167.1	188.5	195.2	172.4	183.2	169.4	94.8	60.4	44.0
Fe I	6232.640	3.65	−1.215	124.2	70.4	68.3	47.3	95.0	65.5	79.2	60.4	...	...	...
Fe I	6240.653	2.22	−3.430	112.4	50.4	56.0	47.0	88.8	75.3	67.2	85.1	21.7	...	32.5
Fe I	6246.320	3.60	−0.886	145.0	82.4	89.7	94.0	116.1	99.5	100.4	121.6	54.2	...	40.1
Fe I	6252.565	2.40	−1.680	200.2	114.2	125.3	134.9	170.2	143.6	154.6	169.0	98.2	96.4	59.6
Fe I	6254.253	2.28	−2.200	174.9	82.2	110.1	105.7	148.3	128.5	...	132.7	85.2	59.9	45.8
Fe I	6265.141	2.18	−2.335	175.5	95.4	...	102.8	132.4	127.4	135.0	157.2	66.0	62.3	46.0
Fe I	6270.231	2.86	−2.695	104.8	43.3	47.6	82.3	69.2	68.6	92.0	67.4	25.9	...	16.2
Fe I	6271.283	3.33	−2.835	61.9	...	15.8	16.5	27.9	13.3	...	20.6	10.8	...	...
Fe I	6301.508	3.65	−0.858	143.3	116.9	76.2	91.6	104.8	109.6	89.8	119.4	68.0	36.0	...
Fe I	6322.690	2.59	−2.386	140.9	63.9	85.2	92.7	101.8	102.2	97.5	91.6	56.9	34.5	...
Fe I	6335.337	2.20	−2.125	188.7	126.1	114.4	112.4	136.3	128.2	148.4	141.3	83.7	63.1	37.7
Fe I	6336.830	3.69	−0.936	136.5	67.0	75.7	102.3	99.2	96.7	98.3	107.1	52.8	...	29.8
Fe I	6344.150	2.43	−2.780	131.6	45.0	65.5	80.3	92.8	92.3	98.7	118.0	47.6	26.7	21.4
Fe I	6355.035	2.84	−1.835	152.1	61.7	75.1	65.2	91.1	92.3	115.6	93.0	35.6	...	...
Fe I	6358.690	0.86	−3.878	198.3	130.4	143.8	138.6	142.1	132.3	...	139.4	58.3	...	...
Fe I	6380.750	4.19	−1.335	82.3	41.4	19.5	30.6	26.7	34.1	...	29.9	...	...	...
Fe I	6393.612	2.43	−1.545	211.7	121.0	128.9	156.3	151.3	164.0	140.8	168.4	106.4	66.4	54.2
Fe I	6421.360	2.28	−1.724	213.8	121.6	131.8	159.7	154.6	150.3	167.4	172.7	107.0	76.0	68.6
Fe I	6430.850	2.18	−1.836	216.5	131.0	121.9	145.3	158.3	166.7	155.9	181.5	115.1	86.4	75.8
Fe I	6475.632	2.56	−2.841	120.1	79.5	76.4	...	109.0	83.1	102.3	87.3	37.4	...	22.1
Fe I	6481.878	2.28	−2.926	136.4	67.0	80.7	87.8	96.3	110.9	115.6	115.1	40.5	...	...
Fe I	6498.950	0.96	−4.547	152.3	97.8	71.2	94.0	110.2	116.3	127.0	123.5	48.5	...	29.4
Fe I	6518.373	2.83	−2.565	114.9	45.8	51.1	68.7	76.0	70.1	62.6	81.5	24.1	12.4	28.6
Fe I	6574.224	0.99	−4.914	129.7	86.2	76.5	67.7	82.0	88.4	113.2	101.1	33.2	...	28.1
Fe I	6581.214	1.48	−4.777	97.7	21.3	36.9	40.8	41.1	57.4	75.1	62.8	...	...	...
Fe I	6609.119	2.56	−2.606	133.5	68.2	85.5	69.4	89.0	96.8	97.0	92.5	36.0	30.2	40.9
Fe I	6677.997	2.69	−1.370	200.5	142.1	106.2	135.3	152.0	162.9	161.3	168.4	88.7	49.9	64.6
Fe I	6739.524	1.56	−5.034	76.8	29.6	21.8	19.2	50.4	38.5	44.0	43.1	...	...	...
Fe I	6750.150	2.42	−2.568	147.6	96.2	103.9	100.1	138.8	129.7	106.4	100.4	46.4	21.6	...
Fe II	4923.930	2.89	−1.432	149.1	125.3	135.2	129.9	149.7	157.8	115.1	143.3	99.3	91.5	93.0
Fe II	4993.352	2.81	−3.387	61.5	...	...	...	25.0	48.0	55.0	23.8	37.9	13.3	9.7
Fe II	5234.630	3.22	−2.260	88.8	70.3	62.2	75.3	81.7	77.5	54.6	54.1	37.9	27.5	25.1
Fe II	5264.810	3.23	−3.163	47.8	...	35.5	42.5	17.8	56.0	...	24.6	31.9	6.6	20.1
Fe II	5425.259	3.20	−3.272	44.3	...	35.0	42.7	42.0	66.5	...	46.1	15.0	...	...
Fe II	6247.562	3.89	−2.449	41.2	28.9	54.4	39.1	40.3	58.5	...	54.5	23.8	...	12.3
Fe II	6456.391	3.90	−2.205	50.6	60.0	66.2	...	65.6	68.5	51.4	57.0	35.2	16.8	...

[a] For the sake of readability, only the catalogue-numbers are given here, omitting the prefixes "LG04[abcd]_" (cf. Table 3.1)

Chapter 4

Complexity on Small Scales II: Metallicities and Ages in the Leo II Dwarf Spheroidal Galaxy

“ *O, Sir, you are old.*
Nature in you stands on the very verge
Of her confine: you should be ruled and led
By some discretion, that discerns your state
Better than you yourself.”
— William Shakespeare, *King Lear*

Abstract

We present metallicities and ages for 52 red giants in the remote Galactic dwarf spheroidal (dSph) galaxy Leo II. These stars cover the entire surface area of Leo II and are radial velocity members. We obtained medium-resolution multi-fiber spectroscopy with the FLAMES multi-object spectrograph as part of a Large Programme with the Very Large Telescope at the European Southern Observatory, Chile. The metallicities were determined based on the well-established near-infrared Ca II triplet technique. The resulting metallicity distribution is asymmetric and peaks at [Fe/H] $= -1.74$ dex on the Carretta & Gratton scale. The full range in metallicities extends from -2.4 to -1.08 dex. As in other dSph galaxies, no extremely metal-poor red giants were found. We compare Leo II's observed metallicity distribution with simple chemical evolution models and with model predictions for several other Galactic dSphs from the literature. Leo II clearly exhibits a G-dwarf problem, and its evolution appears to have been affected by galactic winds. We use our inferred metallicities as an input parameter for isochrone fits to Sloan Digital Sky Survey photometry of our target stars and derive approximate ages. The resulting age-metallicity distribution covers the full age range from 2 to about 15 Gyr on our adopted isochrone scale. During the first ~ 7 Gyr relative to the oldest stars the metallicity of Leo II appears to have remained almost constant, centering on the mean metallicity of this galaxy. The almost constant metallicity at higher ages and a slight drop by about 0.3 dex thereafter may be indicative of rejuvenation by low metallicity gas. Overall, the age-metallicity relation appears to support the formation of Leo II from pre-enriched gas. Evidence for enrichment is seen during the recent 2 to 4 Gyr. Star formation appears to have increased in Leo II approximately 9 Gyr ago and to have continued at a higher rate until 2 Gyr ago. This trend supports earlier derived photometric findings of Leo II as a galaxy with a prominent old population and dominant intermediate-age populations. We do not see a significant indication of a radial metallicity gradient nor age gradient in our data.

4.1 Introduction

More than 75% of *all* Milky Way companions are found within 150 kpc; only three additional dSphs believed to be Galactic satellites are found at larger distances. Leo II, the dSph studied in the current paper, is one of the latter.

Leo II was discovered by Harrington & Wilson (1950). A number of mainly photometric studies were conducted in the subsequent decades. Earlier studies based on resolved color-magnitude diagrams (CMDs) placed Leo II at a distance of ~ 230 kpc (e.g., Demers & Harris 1983; Bellazzini, Gennari, & Ferraro 2005), ~ 215 kpc (Demers & Irwin 1993; Lee 1995), and ~ 205 kpc (Mighell & Rich 1996). These studies used different values for the (low) amount of Galactic foreground reddening, different mean metallicities, and different methods to derive the distance of Leo II, e.g., the apparent luminosity of the horizontal branch or of the tip of the red giant branch (TRGB). In the current study, we adopt the TRGB distance of 233 ± 15 kpc obtained by Bellazzini et al. (2005), which excludes the contribution of luminous asymptotic giant branch (AGB) stars and also shows consistency with the horizontal branch (HB) locus. If this distance is representative of Leo II's distance from the Milky Way during most of its existence, it should have been little affected by tidal stripping and other environmental effects exerted by the Galaxy.

Leo II is a dSph galaxy with prominent old and intermediate-age populations. The presence of old populations was first established by Swope (1967), who reported the detection of a red HB and of RR Lyrae variables. Deeper CCD exposures by Demers & Irwin (1993) revealed the existence of a less well populated blue HB. The most comprehensive variability study is that of Siegel & Majewski (2000), which presents 148 RR Lyrae stars and four anomalous Cepheids. The RR Lyrae stars indicate a dominant metallicity of -1.9 dex with a metal-poor tail out to -2.3 dex. The presence of intermediate-age populations was first inferred from the detection of luminous carbon stars in Leo II (Aaronson, Olszewski, & Hodge 1983; Aaronson & Mould 1985, Azzopardi et al. 1985). Five out of the seven C stars and C star candidates probably belong to an intermediate-age population judging from their position above the TRGB, although the colors and luminosities of these stars suggest that they may be 3–4 Gyr older than the C stars detected in Leo I (see Lee 1995 for details). Moreover, a number of luminous AGB stars and a red clump were detected in Leo II, which demonstrate the presence of an intermediate-age population beyond any doubt (Lee 1995; Mighell & Rich 1996). Hence the stellar age tracers show that Leo II experienced an extended star formation (SF) history.

The SF history of Leo II was quantified using deep Hubble Space Telescope (HST) imaging extending below the old main-sequence turnoff of this galaxy and theoretical isochrones. Mighell & Rich (1996) found a mean age of 9 ± 1 Gyr with SF lasting for more than 7 Gyr. They conclude that about half of the stars in Leo II formed between 8 and 12 Gyr ago. The oldest stars in Leo II are as old as the oldest Galactic globular clusters, a common feature for all Galactic dSphs and other nearby galaxies (Grebel & Gallagher 2004). Hernandez, Gilmore, & Valls-Gabaud (2000) suggest that the peak SF activity occurred ~ 8 Gyr ago and that SF ended ~ 6 Gyr ago. They excised the HB populations from their CMD analysis, and their SF history does not reproduce the old populations of Leo II. Dolphin's (2002) CMD-fitting algorithm reveals an extended SF history starting some 15 Gyr ago and extending until 2 to 4 Gyr ago, although very little activity occurred within that age bin. The main SF activity takes place in the 8 to 15 Gyr bin according to Dolphin (2002). All three photometric analyses agree in finding an extended SF history for Leo II that lasted many Gyr, and that the main SF activity occurred at relatively high ages of 8 Gyr or more.

In a recent, shallower ground-based study Bellazzini et al. (2005) discuss the detection of red giant branch bumps in Leo II. The luminosity of the main bump indicates that the majority of the stars in Leo II is ~ 4 Gyr younger than regular Galactic globular clusters of comparable low metallicity to the dominant stellar population in Leo II. They also demonstrate that the red HB and red clump stars in Leo II are more centrally concentrated than the ancient HB population, akin to the population gradients found in many dSphs (e.g., Stetson, Hesser, & Smecker-Hane 1998; Hurley-Keller, Mateo, & Grebel 1999; Da Costa et al. 2000; Harbeck et al. 2001).

Interestingly, in all three deep HST CMD studies the isochrone fits require a relatively high metallicity of ~ -1.6 dex or even ~ -1.1 dex. Indeed, when comparing isochrones for old populations to globular clusters with metallicity determinations on the traditionally used Zinn & West (1984) scale, the isochrones favor too high a metallicity for metal-poor populations (Grebel 1997, 1999). As discussed by Dolphin (2002), this can be in part circumvented by using the Carretta & Gratton (1997) scale for globular clusters instead (see also discussion in Bellazzini et al. 2005). Nevertheless, the age-metallicity degeneracy that plagues purely photometric derivations of SF histories from resolved stellar populations remains.

The age-metallicity degeneracy can be resolved through spectroscopic metallicities. The first spectroscopic metallicity determination for Leo II was carried out by Suntzeff et al. (1986), who measured three red giants in this galaxy and found [Fe/H] ~ -1.9 dex. Their metallicity scale corresponds to the Zinn & West (1984) scale. More recently, Bosler et al. (2004) spectrometered 41 red giants in Leo II and found a mean metallicity of -1.57 dex with a spread ranging from $-1.26 >$ [Fe/H] > -2.32 on the Carretta & Gratton (1997) scale. In the current Chapter, we present spectroscopic metallicity and age measurements for 52 red giants in order to glean detailed information about the evolutionary and enrichment history of this remote Galactic satellite.

4.2 Observations and reduction

Our observations of Leo II were taken as part of the European Southern Observatory (ESO) Large Programme 171.B-0520(A) (principal investigator: G.F. Gilmore; see Koch et al. 2006a, 2006b; Wyse et al. 2006; Wilkinson et al. 2006b for more information), which aims at elucidating the kinematic and chemical characteristics of Galactic dSphs. Five fields in Leo II were observed with the FLAMES spectrograph (Pasquini et al. 2002) at ESO's Very Large Telescope (VLT). FLAMES was used with the GIRAFFE multi-object spectrograph in low-resolution mode ($R \sim 6500$). The GIRAFFE spectrograph was fed by the MEDUSA fiber system, which provides up to 132 fibers per exposure. In the same Large Programme, we also analyzed the metallicities of the Carina dSph, which is described in detail in Chapter 2 and Koch et al. (2006a). We refer the reader to Chaper 2 for details on observing strategy, data reduction, and calibration techniques, which will be briefly summarized in the following. Both for Carina and for Leo II the L8 grating was used, centered on the near-infrared Ca II triplet (CaT) and covering a wavelength range of 820.6 nm to 940 nm.

4.2.1 Target selection and acquisition

The wide field of view of the FLAMES instrument has a diameter of $25'$. In principle, this enables one to cover stars in the entire projected area of the Leo II dSph with one single pointing, since its nominal tidal radius is $8\overset{'}{.}7$ (Irwin & Hatzidimitriou 1995). However, in order to account for crowding, varying stellar density, and fiber collisions, and also in order to optimize the sampling out to large radii near and beyond the tidal radius, we observed five different (overlapping) fields in several fiber configurations (see Table 4.1).

Date	Field (Configuration)	α	δ	Total Exposure Time
		(J2000.0)		[s]
2003 Feb 21	Center	11 13 23.9	22 14 33	1436
2003 Feb 22	Center			18000
2003 Mar 04	Center_2	11 13 32.8	22 06 30	18000
2003 Mar 05	Offset	11 12 42.6	22 02 21	14400
2004 Feb 21	2 (a)	11 13 36.2	22 11 08	10800
2004 Feb 22	2 (a)			3600
2004 Feb 23	2 (a)			10800
2004 Feb 24	2 (b)			10020
2004 Feb 26	4 (a)	11 12 45.9	21 58 35	18300
2004 Feb 27	4 (b)			15166
2004 Feb 28	4 (b)			14700

Table 4.1: Observation log and field centers in Leo II

Our target stars were selected using photometry and astrometry obtained by the Cambridge Astronomical Survey Unit (CASU) at the 2.5 m Isaac Newton Telescope (INT) on La Palma, Spain. From these data we selected red giant candidates covering the luminosity range from the TRGB region ($V \sim 18.5$) down to 2.5 mag below the TRGB ($V \sim 21$). As the CMD in Fig. 4.1 shows we furthermore aimed at covering the full width of the red giant branch (RGB) to ensure that also potential extremely metal-poor and metal-rich red giants were included and in order to minimize any bias with regard to age or metallicity. In total, we selected and observed 195 red giant candidates.

For the purpose of age determinations once metallicities have been measured, it is desirable to obtain as accurate a set of photometry as possible in a suitable set of filters. Since the INT filter system used in the CASU[1] parallels the SDSS system (Karaali et al. 2005; Jordi, Grebel, & Ammon 2006) and since Leo II is also covered by the fifth data release (DR5) of the Sloan Digital Sky Survey[2] (SDSS; e.g., Stoughton et al. 2002; Adelman-McCarthy et al. 2006), we matched the CASU photometry of our targets with the (less deep) SDSS photometry. SDSS photometry is obtained by driftscan techniques, is very well calibrated, and offers a highly homogeneous data set. Moreover, the theoretical isochrones of the Padova group have been transformed into the SDSS photometric system (Girardi et al. 2004), facilitating age estimates via isochrone fitting. We determined the following transformation relations for the conversion of CASU to SDSS photometry:

$$
\begin{aligned}
g\prime &= g + 0.127 \times (g - r) - \quad 0.814 && (4.1)\\
i\prime &= i + 0.114 \times (r - i) - \quad 0.385 && (4.2)\\
&(1700 \text{ stars}, \sigma = \quad 0.15).
\end{aligned}
$$

Here the standard SDSS photometric system is denoted by the letters g, r, and i as is the usual notation, while the CASU magnitudes are given by g' and i'.

As mentioned already, the spectroscopic observations were carried out using the same strategy and instrumental setups as described in Section 2.2. The location of our fields and the dates of observation are listed in Table 4.1. Although we aimed at exposing each configuration for 6 hrs to reach nominal signal-to-noise (S/N) ratios of at least 20, which would enable us to derive highly

---

[1] see `http://www.ast.cam.ac.uk/~wfcsur/`.

[2] The data from the SDSS DR5 are publicly available under `http://www.sdss.org/dr5/`.

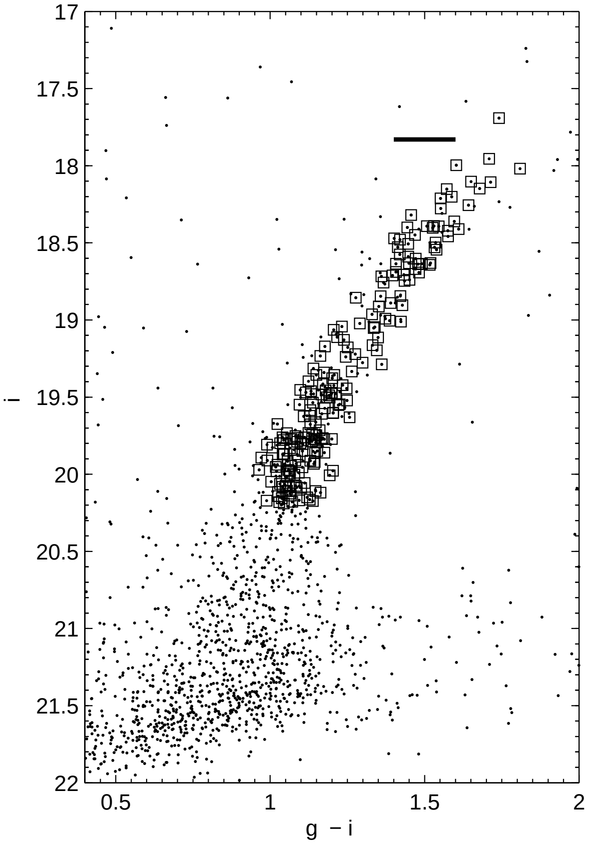

Figure 4.1: The color-magnitude diagram of the upper red giant branch of Leo II. Stars for which we obtained spectra are marked by open squares. The g and i photometry shown is in the SDSS photometric system and was transformed into this system from INT/CASU g and i magnitudes. Also indicated by the black solid line is the location of the TRGB according to Bellazzini et al. (2005).

accurate EWs at our spectral resolution of ~ 6500, a large fraction of our nights was hampered by sky conditions with a seeing as bad as $2''$. Therefore, the median S/N actually achieved after processing the spectra was only $15\,\mathrm{pixel}^{-1}$. Altogether 197 targets were observed, whose individual positions are shown in Fig. 4.2.

4.2.2 Data reduction

Details of the reduction process are given in Section 2.2. In essence, we used version 1.09 of the FLAMES data reduction system, girbldrs, and the associated pipeline version 1.05 (Blecha et al. 2000). After standard bias correction and flatfielding, the spectra were extracted by summing the pixels along a slit of 1 pixel width. The final rebinning to the linear wavelength regime was done using Th-Ar calibration spectra taken during daytime.

Sky subtraction was facilitated by the allocation of about 20 fibers configuration to blank sky. By subtracting the average sky spectrum from the science exposures using IRAF's *skytweak*, we obtained an accuracy of the final sky-subtracted spectra of the order of 2%, taken as the 1σ-dispersion of the medians of the sky-subtracted spectra in any exposure divided by the median

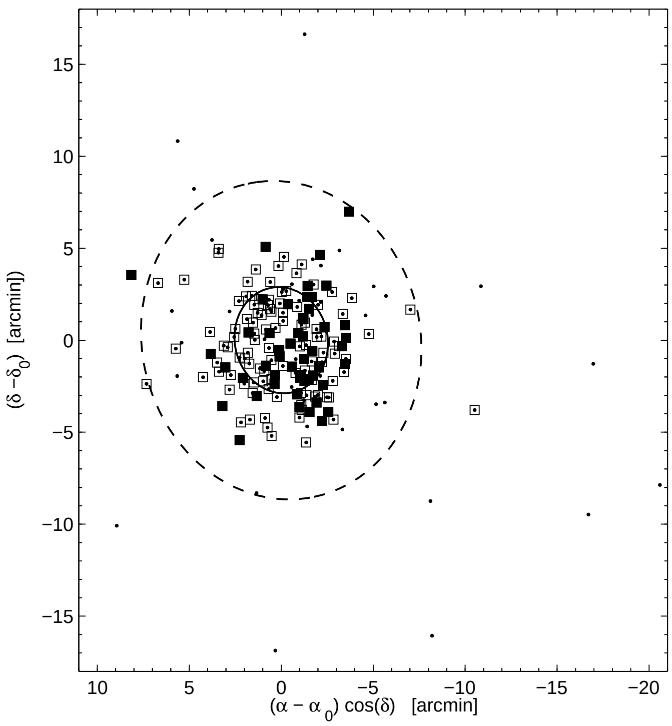

Figure 4.2: Location of our 197 targets (shown as small dots) in a right ascension versus declination plot after subtracting the central coordinates α_0 and δ_0 of Leo II. Open squares mark radial velocity members. Stars indicated by filled squares have sufficient signal to noise to permit us to derive their metallicities. The dashed line shows Leo II's nominal tidal radius (8$'$.9.)

sky.

Our data set was then completed by co-adding the dispersion-corrected and sky-subtracted science frames, weighted by the exposures' individual S/N, and subsequent rectification of the continuum. Fig. 4.3 shows representative spectra across our magnitude range for which reliable EWs could be determined.

4.2.3 Membership estimates

In order to separate Leo II's RGB stars from Galactic foreground stars, we determined the individual radial velocities of each target star by means of cross-correlation of the CaT region against synthetic template spectra. This method will be laid out in detail in a forthcoming paper focusing on the dynamical aspects of Leo II (Kleyna et al. 2006, in prep.).

At a systemic velocity of $(76 \pm 1.3)\,\mathrm{km\,s^{-1}}$ (Vogt et al. 1995), Leo II's velocity distribution is inevitably embedded in the peak of the velocity distribution of Galactic foreground stars along this line of sight. However, owing to our selection of target stars whose colors and luminosities are consistent with membership in Leo II and due to the much lower Galactic field star density, Leo II's velocity peak clearly stands out against the Galactic contribution (see the histogram in Fig. 4.4). By application of the Besançon synthetic Galaxy model (Robin et all. 2003) we estimate that the Galactic interloper fraction, subject to our color-criteria, in the radial velocity interval of interest does not exceed 10%. Rejecting 23 apparent radial velocity non-members that deviate

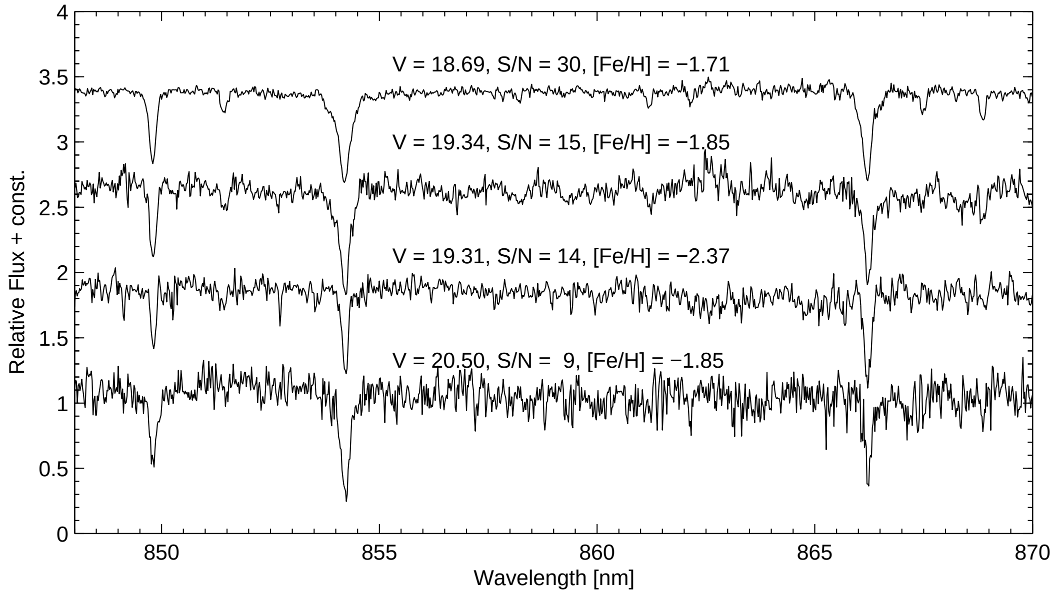

Figure 4.3: Sample spectra showing some of the more metal-poor stars covering a range of different magnitudes and signal-to-noise ratios.

more than $5\,\sigma$ from our observed velocity peak at $\sim$79 km s^{-1}, we approach the mean heliocentric velocity and line-of-sight velocity dispersion by performing an iterative error-weighted maximum-likelihood fit assuming a Gaussian velocity distribution.

The resulting mean of (79.2 ± 0.6) km s^{-1} and velocity dispersion of (6.8 ± 0.7) km s^{-1} are in very good agreement with Vogt et al. (1995). These authors found a a central velocity dispersion of (6.7 ± 1.1) km s^{-1} based on 31 high-resolution spectra of stars within the core radius. Depending on the criteria for defining membership we end up with 166 radial velocity members if we adopt a 3σ-cut in the velocity distribution, whereas a more conservative cut at $\pm 2\sigma$ leaves 155 apparent member stars. Given the low likelihood of interlopers in our sample, we will apply the 3σ-cut in the following.

4.3 Metallicity calibration

The infrared lines of the singly ionized calcium ion at 8498, 8542, and 8662 Å are among the strongest absorption features in the spectra of RGB stars. Their EWs can thus be accurately determined and reach values of typically a few Ångströms. As was nicely demonstrated in the pioneering works of Armandroff & Zinn (1988); Armandroff & Da Costa (1991) and Rutledge et al. (1997a,b), the CaT can be employed to measure the metallicity of red giants in old and metal-poor populations. Subsequently, the CaT method was extended to and calibrated for the entire range of metallicities of $-2 <$ [Fe/H] < -0.2 and for ages covering $2.5 <$ age [Gyr] < 13 by Cole et al. (2004). This fundamental work permits us to apply the CaT method to populations that also contain stars of intermediate ages, such as Carina or Leo II.

The EWs of the CaT lines were measured using a modified version of Da Costa's EWPROG code kindly made available by A. A. Cole (see also Cole et al. 2004). Each of the lines was fit by a Gaussian plus a Lorentzian component in the line bandpasses (and associated continuum) as

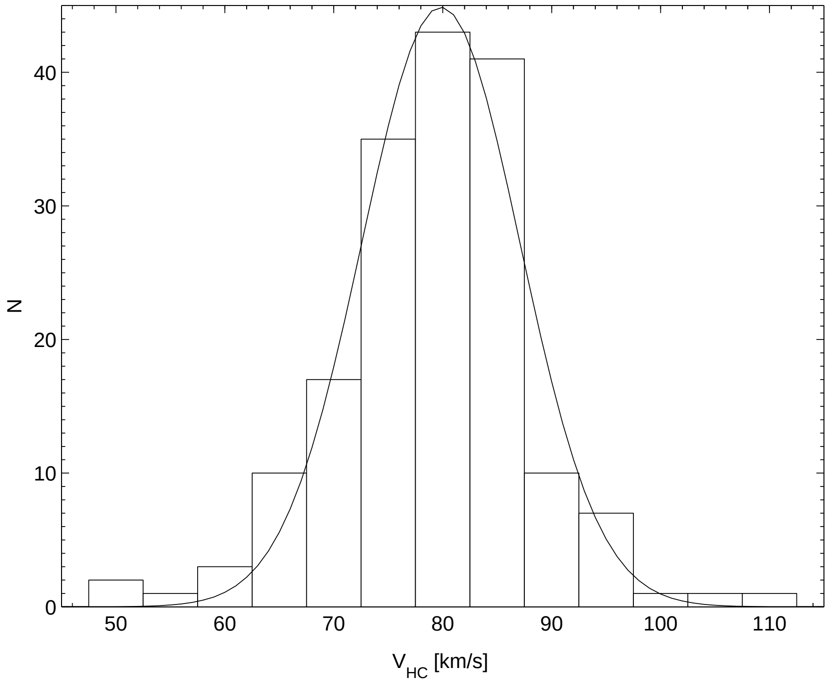

Figure 4.4: Radial velocity histogram of our target stars, most of which are red giants in Leo II. The solid line is the best-fit Gaussian to this distribution.

defined in Armandroff & Zinn (1988). The final EW was then obtained by summing up the flux in the theoretical profile across the bandpass. The corresponding uncertainties were determined from the residuals of the fit.

In order to obtain a self-consistent analysis of the Leo II data, we rederived the relation between line strengths and metallicity. We follow the original prescription of Rutledge et al. (1997a, hereafter R97a) in defining the Ca line strength as the weighted sum of the three CaT lines:

$$\Sigma W = 0.5\, W_{8498} + W_{8542} + 0.6\, W_{8662} \tag{4.3}$$

However, owing to the generally low S/N of our Leo II spectra, we were able to measure EWs of all the three CaT lines for only 20 radial velocity members (down to a S/N of approximately 10), while we could reliably fit the two stronger lines at $\lambda\lambda\, 8542,\, 8662$ in a further 32 stars (down to S/N $\sim$ 6). In order to place the linestrengths derived from these spectra on the same scale as the ones with better data quality, we established a linear relationship between the linestrength ΣW and the strength using only the two stronger lines from the 72 high S/N spectra (with S/N ratios of about 60–80) of our calibration clusters (for details on our calibration clusters, we refer to Sect. 2.2, 2.3 and Paper I.) We find the linear relation

$$\Sigma W = 1.13\, (W_{8542} + 0.6\, W_{8662}) + 0.04, \tag{4.4}$$

with associated uncertainties of 0.02 on each of its coefficients.

The power of the CaT calibration lies in the introduction of a *reduced* width, W', which reduces the strong effects of stellar gravity on the Ca line strengths to first order (and the far lesser influence of effective temperature). This calibration applies within a given cluster, for which

V_{HB} is the apparent magnitude of the Horizontal Branch. The reduced width is defined in the high-resolution work of R97a as

$$W' = \Sigma W + \beta\,(V - V_{HB}), \tag{4.5}$$

where V denotes the stellar magnitude. Based on our observed high S/N spectra of the calibration clusters, we find the slope in this relation to be $\beta = -0.55 \pm 0.01$Å mag^{-1}, which is somewhat shallower than the canonical value of −0.64. For the HB level V_{HB} of Leo II, we adopted the value of 22.17±0.14 mag (Siegel & Majewski 2000), which refers to the HB locus based on the analysis of a sample of RR Lyrae stars.

4.3.1 Uncertainties affecting the metallicity measurements

There are various metallicity scales to be found in the literature (e.g., ZW, CG, Kraft & Ivans 2003). The CG scale and the Kraft & Ivans scale are based on high resolution data, but there is no physical reason to give preference to any of them. Traditionally the ZW has been the most widely used scale, but more recent calibrations of the CaT method have mainly used the reference metallicity scale of CG as introduced by Rutledge et al. (1997b). In our current study, we adopt this scale as well. The final calibration of the reduced width onto metallicity is then obtained via the linear relation

$$[Fe/H]_{CG} = -2.85 + 0.43\,W', \tag{4.6}$$

as established from our four calibration clusters.

The median formal uncertainty that we achieve in this way is 0.13 dex, accounting for errors in the calibrations and measurement errors in the EWs. However, there are numerous additional potential sources of uncertainty, which may affect the accuracy of our calibration of Ca onto iron. Among these are the [Ca/Fe] ratios for the stars in dSphs, which, for the sake of the method, have to be assumed to be comparable to the abundance ratios in Galactic globular clusters. On the other hand, high-resolution spectroscopic data of red giants in dSphs and dwarf irregulars found generally lower [α/Fe] ratios than in Galactic populations of the same [Fe/H] (e.g., Hill et al. 2000; Shetrone, Côté, & Sargent 2001; Fulbright 2002; Shetrone et al. 2003; Tolstoy et al. 2003; Geisler et al. 2005; Pritzl et al. 2005). However, our own high-dispersion analysis of stars in the Carina dSph galaxy (see Chapter 3) and the comparison with CaT measurements of the same stars from Paper I (see Sect. 2.4) shows generally good agreement in the derived metallicities albeit with some scatter.

In this context it is worth noting that the recent high-dispersion analyses by Bosler (2004; hereafter B04) have allowed these authors to establish a calibration of CaT line strength directly onto [Ca/H], yielding a median [Ca/H] ratio of −1.65 dex with stars covering the regime of ∼ −2.6 to ∼ −0.6 dex. Under the simplifying assumption that all these stars share an average metal content of [Fe/H]∼ −1.9 dex, B04 estimate Leo II's global [Ca/Fe] ratio to be of the order of ∼ +0.3 dex, in concordance with old Galactic globular clusters and field stars. This apparently indicates that the calibration of the CaT onto metallicity, which assumes a [Ca/Fe] as in Galactic globular clusters, can safely be applied to the Leo II dSph without introducing any bias due to a significantly deviant Ca abundance ratio.

Other potential error sources also include the *a priori* unknown variations of the HB level with both age and metallicity, which may introduce uncertainties of the order of ±0.05 dex (Da Costa & Hatzidimitriou 1998; Cole et al. 2004), which is below the precision of the abundance measurements themselves. These effects are discussed in detail in Sect. 2.3.

Hence, in the light of the comparatively low S/N of our spectra, we conclude that the formal measurement errors on the CaT EWs are the major contributors to the quoted uncertainty, which will effectively lead to a broadening of the derived MDF.

4.3.2 Comparison with other spectroscopic measurements for individual stars

Of the 74 red giants from the study of B04, which were observed with the Low-Resolution Spectrograph (LRIS) at the Keck 10-meter telescope, 32 coincide with our targets. Fifteen of these had sufficient S/N in our data to allow us to determine metallicities[3]. These common CaT measurements can be employed for a cross check of the accuracy of the method and to validate the respective measurements. Fig. 4.5 shows the comparison of the reduced width from both data sets.

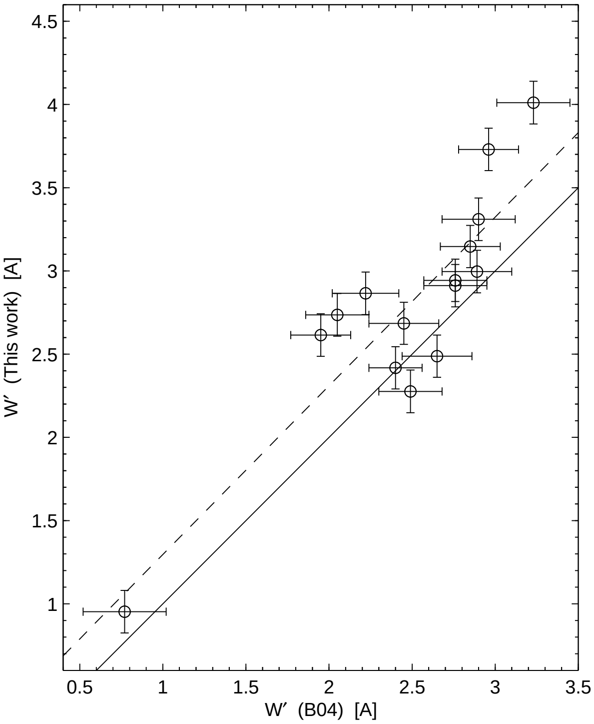

Figure 4.5: The reduced width of the CaT as measured in this work versus the data from B04. The solid and dashed lines are unity and the best-fit relation, respectively. Errorbars indicate formal 1σ uncertainties.

A linear error-weighted least-squares fit to the sample yields the relation

$$W'_{\mathrm{This\,work}} = (1.01 \pm 0.12)\, W'_{\mathrm{B04}} + (0.28 \pm 0.30). \tag{4.7}$$

The fact that this is not a one-to-one relation is to be expected, since B04 relied on the definition of W' in terms of a slope β from the literature (R97a), whereas we obtained different estimates of W' by using our own internal calibration. Moreover, B04 measured EWs of the CaT lines by fitting a single Gaussian, whereas we used an additional Lorentzian profile to yield a better fit in

---

[3] Note that both spectrographs achieve comparable resolutions – 1.55Å in the case of LRIS and 1.31Å for our GIRAFFE data.

the line wings (see also Cole et al. 2004). Generally, our analysis yields reduced widths that are larger by ∼ 0.2 Å.

As it turns out, there is a large scatter around the slope of unity and the majority of the reduced EWs of the stars do not coincide within their errorbars, which indicates that the formal measurement uncertainties underestimate the true underlying accuracy of the EW determinations. Hence we take the χ^2 discrepancy between both data sets as a measure of the deviation and rescale our formal errors on W' such as to reach a reduced χ^2 of unity. In this vein, the final median abundance error we obtain reaches 0.17 dex, which is a reasonable uncertainty considering the relatively low S/N of our data (we note that, with a median value of 23, B04 achieved S/N ratios slightly higher than ours).

4.4 Leo II's metallicity distribution function and chemical evolution models

4.4.1 The metallicity distribution function

Our measured values for [Fe/H] are tabulated in the Appendix. Fig. 4.6 shows the final metallicity distribution (MDF) for these 52 Leo II red giants on the scale of CG.

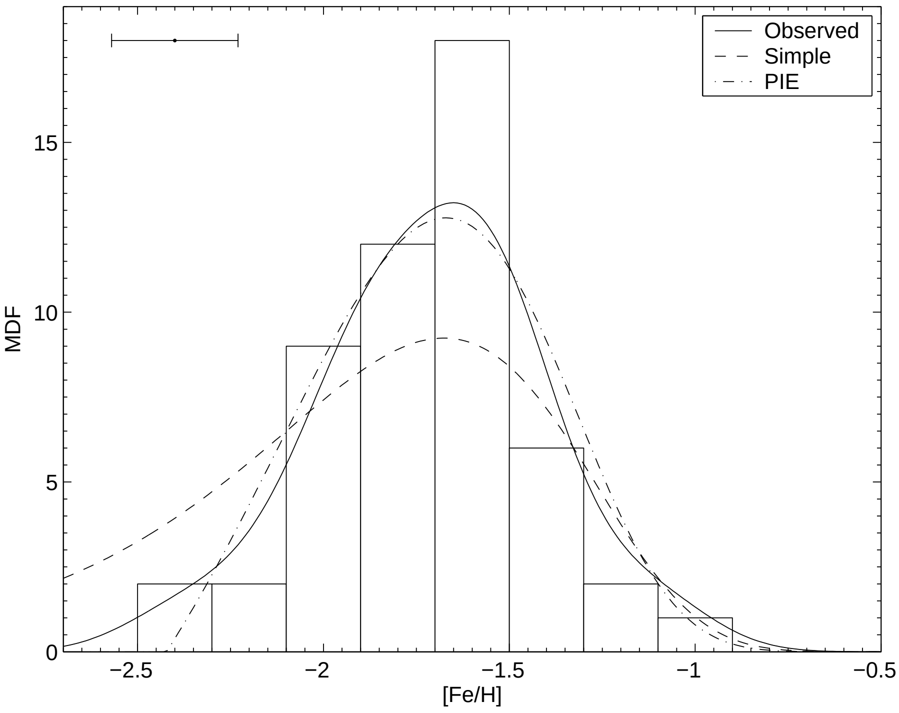

Figure 4.6: Metallicity distribution function on the scale of CG for the 52 Leo II member stars for which we were able to measure metallicities. Overplotted as a solid line is the MDF convolved with observational uncertainties, also indicated in the top left corner by a representative 1σ errorbar. Additionally shown are two best-fit chemical models: The dashed curve refers to a modified simple model ("Simple"), whereas the dash-dotted line is the best-fit prediction from a model with prompt initial enrichment ("PIE"). All models were scaled to the same number of stars.

This MDF is peaked at an error-weighted mean metallicity of (-1.74 ± 0.02) dex and exhibits a full range in [Fe/H] of -2.4 to -1.08 dex. Note the apparent lack of more metal-poor stars. The observed dispersion of the MDF amounts to ca. 0.29 dex, but accounting for the measurement uncertainties by subtracting these in quadrature, Leo II's internal metallicity dispersion is estimated to be 0.23 dex. These values are in reasonable agreement with the estimates of Bosler et al. (2004), who derived a mean metallicity of -1.57 dex on the CG scale based on CaT spectra of 41 red giants.

All in all, our spectroscopic metallicities span about 1.3 dex in [Fe/H]. As Fig. 4.7 implies, there is no apparent trend of metallicity and location in the CMD seen in our data: both metal-rich and metal-poor giants are found at the same location on the RGB.

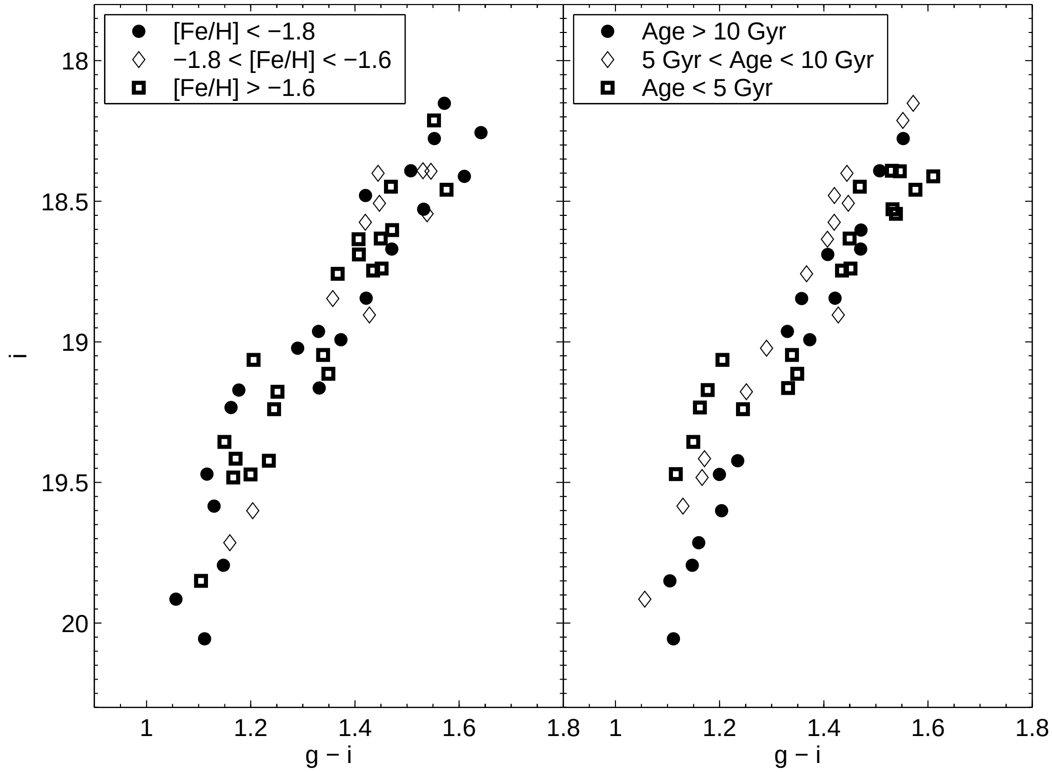

Figure 4.7: Color-magnitude diagrams showing the targeted red giants in Leo II. In the left panel, the different symbols indicate three different metallicity ranges. In the right panel, the symbols show three different age ranges.

This indicates that there is a comparably broad range of ages present in Leo II. In fact, Bosler et al. (2004) have demonstrated that Leo II's RGB stars may span ages between 2 and 13 Gyrs. We will address the question of an age-metallicity relation in our data in Section 5. The range of metallicities and the mean metallicity measured by us are also in excellent agreement with fiducial-based photometric metallicity estimates on the CG scale by Bellazzini et al. (2005). These authors find a mean metallicity of -1.74 with a dispersion of 0.3 dex. The full range of metallicities that they derive from globular cluster fiducials is $-2.4 < \mathrm{[Fe/H]} < -1.2$, also on the CG scale. This also agrees well with the estimates from Mighell & Rich's (1996) HST photometry (mean metallicity -1.6).

The overall shape of the MDF is highly asymmetric. At the metal-poor end it shows a noticeable number of metal-poor stars and exhibits a sharp drop below -2 dex, while at the metal-rich end it shows a smooth, but rapid, fall-off. A sharp drop-off of an MDF towards higher metallicities is generally attributed to a sudden cessation of SF, possibly caused by a strong mass loss (e.g., through winds). Although we see a metal-rich fall-off in our MDF, it is not as distinct in our data as, e.g., in the MDF of Bosler et al. (2004).

In order to gain an insight into basic aspects of Leo II's chemical evolution, we follow long-standing practice of considering variants of a simple chemical evolution model (e.g., Pagel 1997, p. 218), which provides us a viable method to derive some gross evolutionary properties from the MDF.

4.4.2 Simple chemical evolution models with outflows

In the simple model the mean metallicity of long-lived stars, determined at a time close to gas exhaustion of a galaxy, can be assumed to be representative of the *true* nucleosynthetic yield p, provided that all metals are retained in the system. Since this is generally an unphysical approach in dSphs, where gas outflows are possible (e.g., Hensler, Theis, & Gallagher 2004), the mean metallicity should rather be interpreted in terms of the "effective yield", which accounts for the loss of metals (Hartwick 1976). Outflows, which are proportional to the SF rate by a factor c tend to reduce the mean metallicity below the true yield by the same factor; hence, $p_{\mathrm{eff}} \sim p/c$. As a result, the standard model for gas-poor dwarf galaxies explains the observed low-metallicity peak of our MDF – low as compared to, e.g., the G-dwarf MDF in the solar neighborhood (Nordström et al. 2004) – with the occurrence of strong outflows, presumably via supernovae of type II.

Thus we performed an error weighted least-squares fit of a modified simple model, which is solely parameterized by p_{eff}, to our metallicity data. As the resulting best-fit model in Fig. 4.6 implies, there is an excess of metal-poor stars predicted that is not observed, analogous to the "G dwarf problem" in the solar neighborhood. This simple closed-box fit is characterized by an effective yield of $p_{\mathrm{eff}} \sim 0.021\,Z_{\odot}$. However, the deviation from the observed MDF becomes significant above the $2\,\sigma$-level only in the metal-poor regime below -2.5 dex.

The canonical remedy against this overprediction is to adopt a certain amount of non-zero initial metallicity, which is nowadays interpreted as originating from pregalactic Population III stars. This approach is often referred to as prompt initial enrichment (PIE, Truran & Cameron 1971; Tinsley 1975). In this context, Leo II is represented by an invariant effective yield of $p_{\mathrm{eff}} \sim 0.02\,Z_{\odot}$ and an initial metal enrichment of $Z_0 \sim 0.004\,Z_{\odot}$, as determined from a least-squares fit. Assuming such a pre-enrichment leads to a cessation of the MDF around -2.5 dex and to an improved representation of the observed metal-poor tail. Such a pre-enrichment is a reasonable estimate, considering the typical metallicities of the intergalactic medium at higher redshifts (corresponding to lookback times of about 12 Gyr). These may exhibit values of less than around -2 dex (e.g., Schaye & Aguirre 2005). Both simple models are well able to retain the metal-rich part of the MDF. The fact that the drop towards metallicities above the peak value in our data is not as distinct as observed, e.g., by Bosler et al. (2004) and B04 may be due to stochastic fluctuations in our data, where the respective part of the MDF is smeared out by observational errors. Neither of the simple models predicts such a cut-off.

4.4.3 Comparison with more sophisticated chemical evolution models for other dSphs

We now turn to the question whether more information can be extracted from the observed MDF when comparing it to more sophisticated models, which preferably incorporate the effects of outflows and infalling gas. A number of such models were calculated for dSph galaxies (e.g., Ikuta & Arimoto 2002; Lanfranchi & Matteucci 2003, 2004; Hensler et al. 2004; Font et al. 2006). Carigi, Hernandez, & Gilmore (2002) calculated chemical evolution models of Leo II based on the SF history derived by Hernandez et al. (2000), which do not account for the old population in this galaxy (see also Dolphin 2002). Carigi et al. (2002) do not provide model predictions for Leo II's stellar MDF in the literature, yet for our current work, we need theoretical MDFs to compare to.

For convenience, we therefore chose to overplot the models by Lanfranchi & Matteucci (2004, hereafter LM04) on our data. Although these authors did *not* model the evolution of Leo II itself, we can derive some basic properties of this galaxy by comparing our observed MDF with the published theoretical MDFs for other dSphs. The modeled MDFs comprise the dSphs Carina, Draco, Sagittarius, Sextans, Sculptor and Ursa Minor (Fig. 4.8). Each of the dSphs is characterized by its SF rate and a wind efficiency, the latter being the proportionality constant between gas mass and SF rate. These parameters were optimized by LM04 to fit extant observational data such as the $[\alpha/\mathrm{Fe}]$ ratio, total mass, and total gas mass.

As Fig. 4.8 implies, all the shown MDFs are rather similar, with the exception of Sgr. This is particularly interesting considering the wide range of absolute magnitudes covered by these galaxies (Mateo 1998). In this context, the mean abundances are comparatively similar and individual differences are basically reflected in the distributions' details, as we will discuss below. In terms of the location of its peak metallicity Leo II's observed MDF resembles the model MDFs of the dSphs Car, Scl, and UMi. However, the probabilities for the same underlying population derived from a Kolmogorov-Smirnov (K-S) test are 13% for UMi and Leo II, 29% for Car and Leo II, and zero for all other dwarfs shown in Fig. 4.8. In this simplified sense, Leo II and Car are the two most similar dSphs of the entire set.

In contrast to Leo II, which shows an extended SF history from early times on that seems to have peaked around 9 Gyr (e.g., Mighell & Rich 1996; Dolphin 2002; Bosler et al. 2004), the dSph UMi is essentially a purely old galaxy (Carrera et al. 2002; Wyse et al. 2002) and hence not a good comparison object for Leo II, even though the ancient SF lasted several Gyr (see Ikuta & Arimoto 2002; Grebel & Gallagher 2004). The Car dSph, on the other hand, has experienced ancient and intermediate-age SF, but in contrast to Leo II this activity occurred in well-separated episodes (e.g., Smecker-Hane et al. 1994; Hurley-Keller et al. 1998). In fact, it is the only dSph known to exhibit such clearly episodic SF. The bulk of the stars in Car seems to have formed some 7 Gyr ago (Hurley-Keller et al. 1998). In terms of the age range covered by the SF in Car and Leo II, these two dSphs are similar. However, they show considerable differences in the details of their evolutionary histories (see, e.g., Grebel 1999, 2000; van den Bergh 1999, 2000).

The overall low mean metallicities of dSphs (Grebel et al. 2003, Table 1) are most easily explained by a low SF rate according to the models of LM04, which would then leave a reservoir of gas at the final epoch of SF. The fact that there is an observed termination of the SF is then indicative of an efficient gas removal, e.g., via stripping by the Galaxy (Ikuta & Arimoto 2002). It nonetheless remains difficult to explain the *present-day* gas deficiency in dSphs (e.g., Gallagher et al. 2003), which cannot be caused by pure ram pressure stripping in a smooth intergalactic medium (Grebel et al. 2003).

In order to gain insight in the processes governing the shape of the MDF and the related

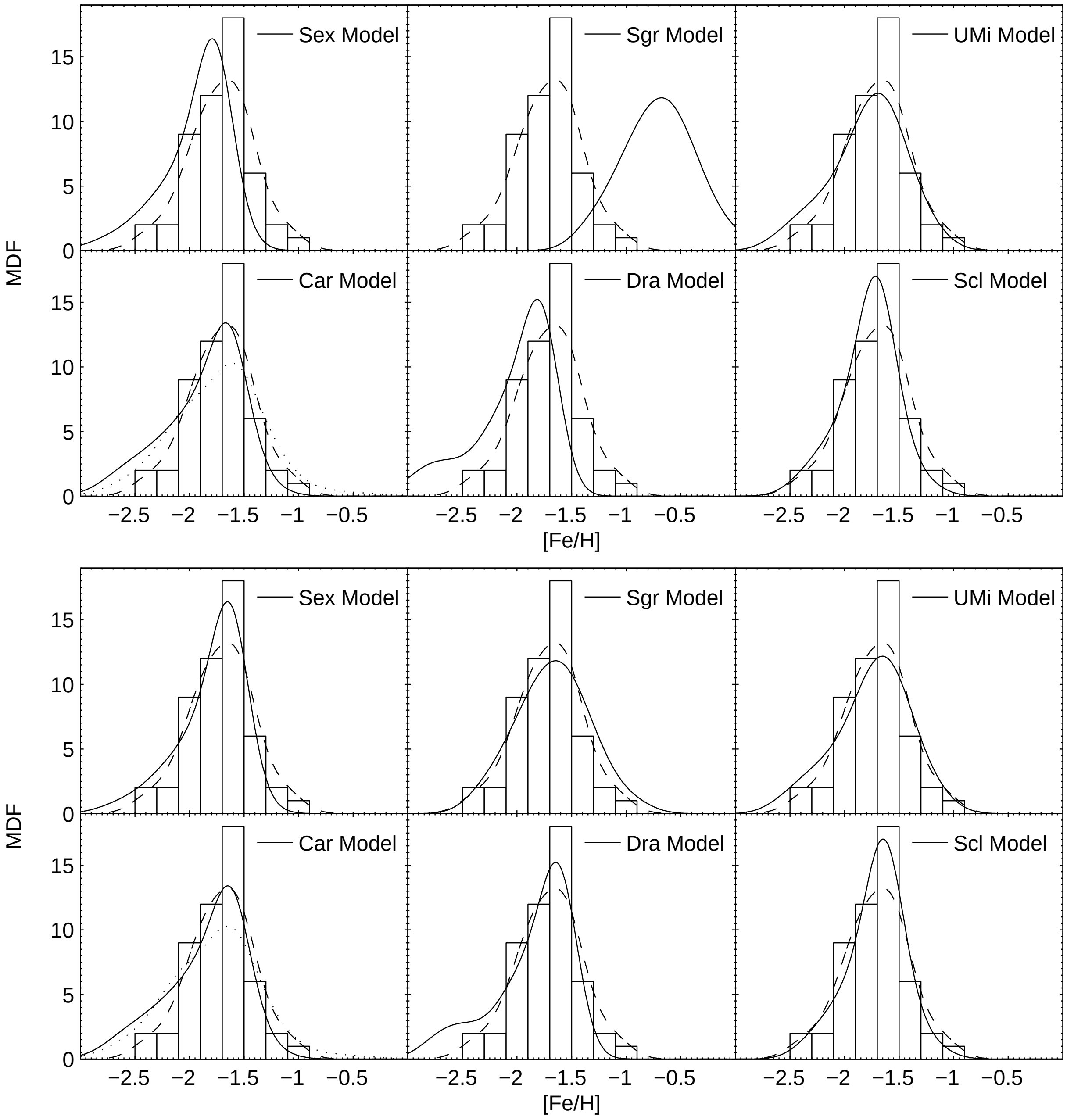

Figure 4.8: Observed MDF versus different models: The histogram and dashed curve show the observed MDF of Leo II (convolved with measurement errors). The solid lines in each panel are the predictions for six dSphs from the models of LM04, also convolved with the observational errors from the present study. The lower left panel also superimposes the observed MDF of Carina from Sect. 2.4 (dotted line). All distributions were normalized to the same number of stars. In the bottom panel all models were shifted such in metallicity that the location of their peaks coincide with the peak of the observed MDF of Leo II.

evolutionary parameters, we shifted all LM04 models to the same peak metallicity as measured in Leo II (Fig. 4.8, bottom panel). Thus one assumes the identical effective nucleosynthetic yield and similar SF efficiencies for all the modeled systems. The majority of the models, except for the predictions for Sgr and UMi, tend to produce a steep decline of the MDFs towards the metal-rich tail. This is caused by an intense wind, which effectively drives out the metals and thus prevents any further substantial enrichment or subsequent SF. For the cases of Scl, Sgr, and UMi, the drop in the MDF is not that sudden and approximates the observations of Leo II fairly well. The respective galactic wind efficiencies are 13 (times the SF rate) for Scl, 9 for Sgr, and 10 for UMi. The LM04 models tend to overestimate the number of metal-poor stars, leading to the well known G-dwarf problem (Sect. 4.1). This is most pronounced in the comparison of the models for Car and Dra with Leo II's MDF (Fig. 4.8, bottom panel), while the Scl and Sgr model MDFs resemble Leo II's metal-poor tail more closely. The latter coincidence is remarkable, as LM04 did not include any pre-enrichment in their models. In the context of the intense galactic winds it is worth noticing that the gas masses of these galaxies predicted by the LM04-models (of the order of $3\times10^{-4}\,\mathrm{M_{tot}}$) are lower than the upper limits placed by observations (Mateo 1998; Grebel et al. 2003), but still well consistent with the overall gas deficiency in dSph galaxies.

Overall, as one might expect none of the dSphs models gives a perfect representation of Leo II's MDF since LM04's models were not made to fit its MDF. The K-S probabilities are below the 5% level with the exception of Scl (45%), UMi (34%), and Sgr(25%). Scl is a predominantly old galaxy with subpopulations distinct in metallicity and possibly in age and kinematics (Grebel, Roberts, & van de Rydt 1994; Grebel 1996; Hurley-Keller et al. 1999; Majewski et al. 1999; Harbeck et al. 2001; Tolstoy et al. 2004). Likewise, UMi is an ancient galaxy, but in spite of its extended early SF it does not seem to show metallicity gradients (e.g., Carrera et al. 2002). Sgr formed stars over a very long period of time. Intermediate-age populations dominate (mean age of 8±1.5 Gyr; Bellazzini et al. 2006), but low-level SF may still have occurred until 0.5 to 1 Gyr ago (Bellazzini, Ferraro, & Buonanno 1999). In fact, SF may have occurred with a variable rate leading to multiple peaks (Layden & Sarajedini 2000). The massive Sgr is an exceptional case among the dSphs considered here since its evolution has been strongly affected by its continuing disruption by the Milky Way (Ibata et al. 1994; Majewski et al. 2003). No two dSphs share the same SF history or enrichment history, and in addition external effects such as ram pressure or tidal stripping or the early Galactic UV radiation field may have affected their evolution (Grebel 1997, van den Bergh 1994). Hence it may not be surprising that Leo II's MDF is not well matched by models calculated for other dSphs. If Leo II's distance of $\sim$230 kpc is representative of the distance that it had during most of its existence, then external effects may have played less of a role than for the closer dSphs. For instance, Siegel & Majewski (2005) report on only a marginal stellar component beyond the King (1962) tidal radius, which cannot be distinguished from statistical fluctuations. It is clear that the detailed understanding of Leo II's MDF and evolution will require detailed modeling adapted to the special properties of this galaxy. However, based on the comparison with the LM04 models, we may speculate that also Leo II has been affected by winds, albeit at a modest level.

4.5 Stellar Ages

4.5.1 Obtaining age estimates

In order to gain a deeper insight into the detailed SF history of Leo II we need to couple our spectroscopic abundances with age estimates. We can derive ages for all stars with metallicity estimates through isochrone fitting. For each of these stars we fit its location in the CMD using ($g - i$, g)-isochrones of that star's individual metallicity. For this purpose, we employed a set of Padova isochrones (Girardi et al. 2004) in the SDSS photometric system. These were interpolated to yield an estimate of each red giant's age.

A few of our targets lie outside of the applicable isochrone grid. On the one hand this may be due to problems arising from the color transformations of theoretical isochrone models to the observational plane and the resulting failure to simultaneously and perfectly reproduce all features of a stellar system and in particular the RGB (e.g., Vandenberg et al. 2000; Gallart, Zoccali & Aparicio 2005). In the light our data, this happens when our targets either turn out to be brighter than the respective theoretical tip of the RGB, or when they lie redwards of the oldest available isochrone. The latter may be caused by statistical fluctuations of the metallicity estimates, where the respective measurement error associates the RGB star with an isochrone not necessarily corresponding to its true metallicity. In these cases, the isochrone fit can only yield a lower limit for the "true" stellar age. Hence, we were able to derive ages for 33 targets and lower limits for 18 stars. For one star, T_21, no reliable age could be established, since its red color places it far outside the applicable isochrone grid. In 14 cases, the location of the targets above the theoretical tip RGB coupled with their CaT metallicity makes them likely bright AGB star candidates. Seven of these stars could also be re-identified in the infrared point source catalog of 2MASS (Cutri et al. 2003). All of the 2MASS stars have metallicities consistent with the peak value of our MDF. Three of these stars are apparently younger than 5 Gyr. The uncertainty of each stellar age was finally obtained by means of Monte Carlo simulations, in which each target was varied around its uncertainty in metallicity and its photometric error and then re-fit by the appropriate isochrones. The resulting variation of the thus derived new ages around the original value was then taken as a representative number of our measurement uncertainty.

4.5.2 Age-metallicity relation

Fig. 4.9 shows a plot of the age-metallicity relation (AMR) obtained from our CaT metallicities and successive isochrone fits. The first thing to note is that our data cover a wide range in ages, ranging from 2 to 15 Gyr. The AMR is essentially flat for ages above $\sim$ 5 Gyr. For the main population we find ages between 5 and 11.5 Gyr with an indication of a peak around (9 ± 2) Gyr. Approximately ten stars are older than this limit (note, however, that the limits of the applied isochrone grids extend beyond the ages of the oldest globular clusters and of the current WMAP estimate of the age of the Universe). Given the small sample and the uncertainties of our data, the inferred distribution of the stellar populations is in good agreement with the SF histories derived from deep CMDs (Mighell & Rich 1996) and underscore the widely extended SF history of Leo II already from early epochs on.

The majority of the most metal-rich stars above ~ -1.5 dex is identified with a number of objects younger than 5 Gyr. Such a seemingly sudden jump in the AMR caused by this populous group of young stars had not been detected in Leo II before (see, e.g., Bosler et al. 2004). Provided the ages of this component are real and not an artifact caused by an overestimate of their metallicity, by Galactic interlopers, or by problems with the isochrones and the photometry, this points to the presence of a younger population in Leo II. As summarized in the Introduction, earlier photometric studies suggested that the main star formation occurred longer ago, peaking at 8 or 9 Gyr (e.g., Mighell & Rich 1998; Dolphin 2002). Our age estimates for the metal-rich population are consistent with the youngest photometric ages proposed by Dolphin (2002). If star formation in Leo II did indeed last until about 2 Gyr ago, then this dSph resembles other

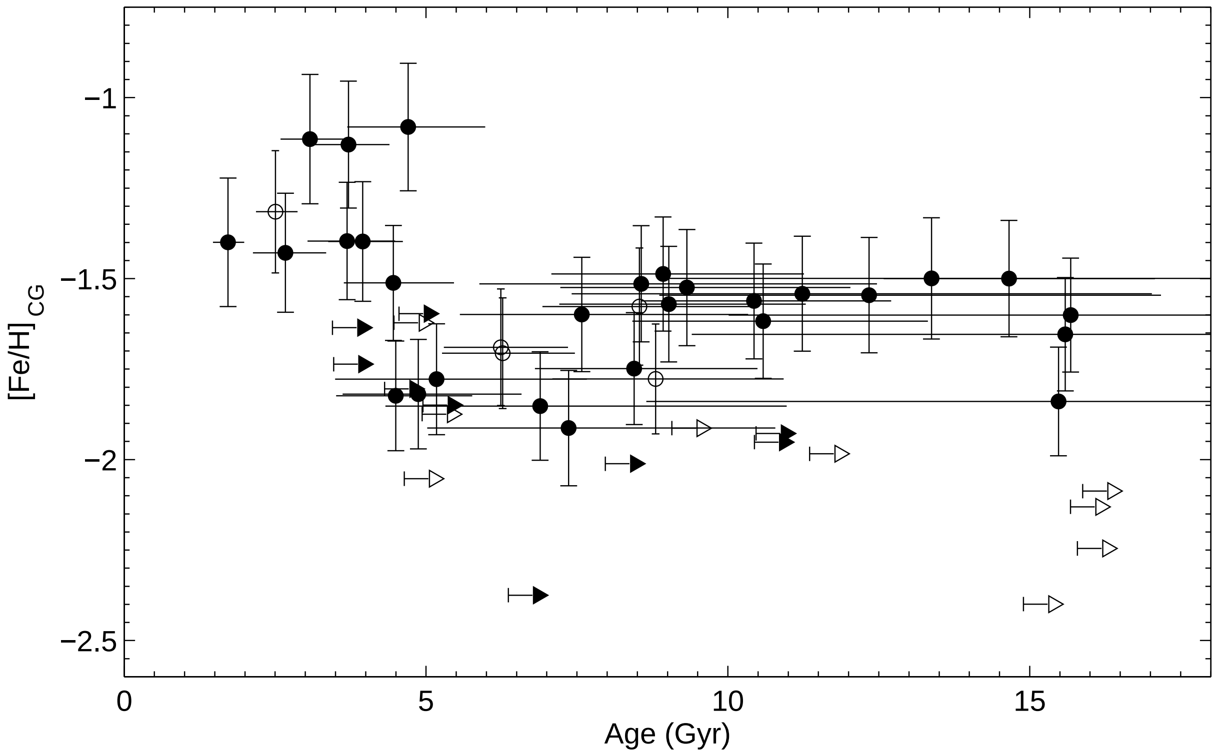

Figure 4.9: The age-metallicity relation inferred from our CaT data and isochrone fits to the SDSS photometry. The arrows indicate lower limits where no reliable age could be determined. The open symbols denote targets that lie above the theoretical tip of the RGB of their respective metallicity. See text for details.

distant dSph companions of the Milky Way, in particular Leo I, the most remote Galactic dSph satellite (Gallart et al. 1999; Held et al. 2000; Bosler et al. 2004). Furthermore, we note that stars more metal-poor than ~ -2 dex are practically found across the full age range from 5 to 15 Gyr, although the age estimates for these objects provide mostly a lower boundary.

It is clear that age derivations in Leo II have to be taken with care. Bellazzini et al. (2005) report the detection of a secondary bump in the RGB luminosity function at $M_V \simeq -0.5$ mag ($i \simeq 20.4$ mag), which may either be attributed to the RGB bump of a potential secondary stellar population or to the AGB clump (Gallart 1998; Lee et al. 2003), from which it is indistinguishable in practice. Although the latter feature occurs at fainter magnitudes than our target stars (cf. Fig. 4.1), its presence indicates that our RGB sample may contain a non-negligible admixture of stars belonging to the AGB, or coming from the RGB of a secondary population.

Taking our AMR at face value, our ages indicate that Leo II experienced star formation continuously until about 2 Gyr ago. Our AMR suggests an increase in the star formation rate for ages younger than 11 Gyr. However, it would also appear that Leo II did not undergo significant enrichment during the first seven or so Gyr after the Big Bang. If this was indeed the case, it would indicate that either freshly synthesized metals must have been lost (e.g., through galactic winds) or that Leo II was constantly rejuvenated by infall of low-metallicity gas. In this vein, a constant mean metallicity can be retained if metal-poor gas flows in at a same rate as the SF rate (e.g., Larson 1972; Lynden-Bell 1975). From 7 to approximately 4 Gyr ago, the metallicity may have been slightly lower than the mean. These stars then seem to have formed from more metal-poor material than the bulk of Leo II's population. If the more metal-rich stars are indeed younger than 5 Gyr, then this appears to have been a period in which either metals were retained more efficiently and used in subsequent star formation, or in which gas accretion did not play a major role. Overall, the AMR seems to have remained almost flat in metallicity over many Gyr before experiencing more enrichment at more recent times. The lack of extremely metal-poor stars, which has also been observed in all the other dSphs with available CaT spectroscopy so far, is very noticeable in Leo II as well. More data are needed to define the AMR more completely.

4.5.3 Radial or spatial trends

Many of the Local Group dSphs exhibit radial population gradients (Harbeck et al. 2001), which broadly resemble each other in the sense that the more metal-poor (and/or older) stellar populations are more extended compared to the more metal-rich and younger populations, which tend to be more centrally concentrated. This general trend has also been detected in Leo II, where Bellazzini et al. (2005) have shown that the predominant red clump stars are in fact significantly more concentrated than the old blue HB and RR Lyrae stars. Based on the deep CMDs of Mighell & Rich (1996), who associated the numerous red clump stars with the dominant intermediate-age population of an age of ∼9 Gyr as opposed to the older (>10 Gyr) HB population, the radial population gradient is primarily a reflection of an age gradient (Bellazzini et al. 2005). In Fig. 4.10 (top panel) we plot our CaT based metallicities versus elliptical radius, adopting an ellipticity of 0.13 (Irwin & Hatzidimitriou 1995).

In this representation, there is only a weak gradient recognizable. An error-weighted least-squares fit yields a slope of (0.042 ± 0.010) dex arcmin^{-1}, corresponding to a change of ∼0.2 dex across the face of the galaxy, which is of the order of the measurement uncertainties. The cumulative number distributions in Fig. 4.10 do not exhibit a distinct spatial separation of the metal-rich and metal-poor populations when subdividing our the data at the median value of −1.65 dex. Although there is a weak indication of an excess of metal-rich stars at about 4–5′, we cannot exclude the possibility that both populations have the same spatial distribution. A K-S test shows a probability of 76% ($1.2\,\sigma$) for this possibility. This result underscores the suggestion by Bellazzini et al. (2005) that, despite the presence of metallicity variations, the main driver of a population gradient in Leo II seems to be the age.

On the other hand, in terms of an age gradient, stars younger and older than 11.5 Gyr exhibit the same spatial distribution with a K-S probability of 86%. Also when confining the data to only those stars of the age peak around 9 Gyr, the probability of a same radial distribution is comparably high, but may be hampered by the sparse sampling of older stars. In fact we cannot exclude the hypothesis that the populations of different ages are equally distributed, although the probability for this is at the $1.5\,\sigma$-level. Considering the uncertainties associated with RGB age dating and with the small number statistics of our study, a better way of investigating the presence of any age gradients is by using stars that are secure age tracers such as HB stars, red clump stars, and stars along the vertical red clump (see, e.g., Grebel 1997; Stetson et al. 1998; Harbeck et al. 2001).

4.6 Summary and Discussion

After Leo I, Leo II is the most remote dSph companion of the Milky Way. Its prevailing intermediate-age stellar population as well as its significant population of old stars make it an

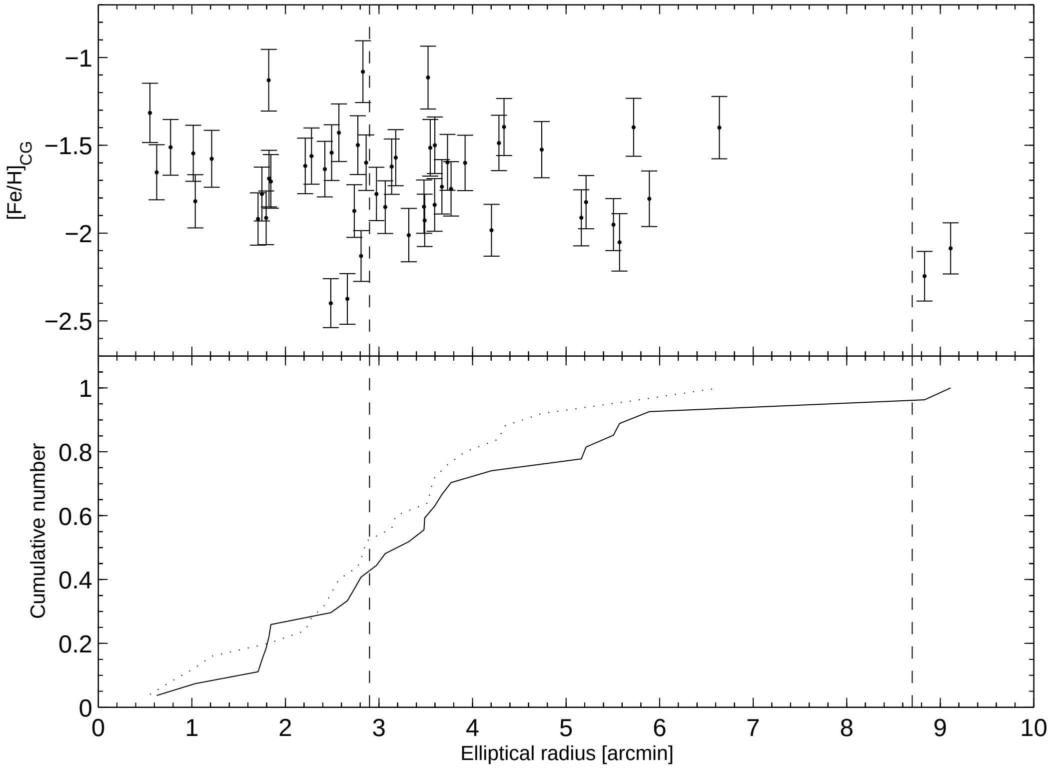

Figure 4.10: Top panel: Metallicity versus distance from the center of the galaxy. The bottom panel shows the cumulative number fraction, separately for the metal-poor ([Fe/H]< -1.65, solid line) and metal-rich ([Fe/H]≥ -1.65, dotted line) targets. The dashed vertical lines represent the location of Leo II's core and nominal tidal radius, respectively. There is only a weak indication of a radial metallicity gradient.

ideal testbench to study star formation that extended over many billions of years. Existing photometric and spectroscopic data as well as our own results suggest that SF activity may have ceased only 2 Gyr ago (Dolphin 2002; Bosler et al. 2004). In the framework of a VLT Large Programme tailored to investigate kinematical and chemical evolutionary aspects of Galactic dSphs we have determined CaT metallicities for 52 red giants in this system, thereby doubling the largest previously published data sets (Bosler et al. 2004; B04). Our targets cover the entire area of the galaxy, thus allowing us to efficiently trace potential spatial metallicity variations.

By employing the well-established CaT technique we showed that Leo II's MDF peaks at -1.74 dex (CG scale), in agreement with previous spectroscopic and photometric estimates (e.g., Bellazzini et al. 2005 and references therein). We infer a range of metallicities of ~ 1.3 dex. We emphasize that Leo II does not contain any extremely metal-poor stars of comparably low metallicities as found in the Galactic halo field stars. The lowest metallicities inferred in our study are similar to those of metal-poor Galactic globular clusters. A similar lack of extremely metal-poor stars has also been observed in other Galactic dSphs (e.g., Shetrone et al. 2001; Pont et al. 2004; Bosler et al. 2004; Tolstoy et al. 2004; Koch et al. 2006a,b). While this might still be blamed on small number statistics, these studies all tried to cover the full color range of the RGB to ensure that stars of very low or very high metallicities would not be missed.

Fitting a modified simple model to the MDF of Leo II reveals a pronounced G dwarf problem, giving further support to early star formation from pre-enriched gas. This model as well as prescriptions adopting prompt initial enrichment may be too simplistic and do not adequately reproduce the drop of the MDF towards higher metallicities. For want of more sophisticated chemical evolution models of the Leo II dSph itself, we compared the observed MDF to the model predictions for other Galactic dSphs from LM04. These models include the effects of supernovae of type Ia and II and galactic winds. None of these models really fits Leo II's MDF well, which may not be surprising given that each Galactic dSph has experienced its own unique evolutionary history (e.g., Grebel 1997, 1999). LM04's model for the Carina dSph approximates the MDF of Leo II best, and although Car experienced strongly episodic star formation its age range is comparable to that of Leo II.

The range in [Fe/H] covered by our MDF, combined with the fact that there is no obvious trend of metallicity with the color of the red giants indicate that there is a broad range of ages present in Leo II, a fact already known from earlier photometric CMD analyses. By means of isochrone fitting using our spectroscopic metallicities as an additional constraint, we could show that the ages span the full range from 2 to 15 Gyr. There is a considerable fraction of "younger" and more metal-rich stars with ages of a few Gyr in our data, but one cannot exclude the possibility that these may in fact be AGB contaminants.

Our AMR suggests continuous star formation across our entire age range. The metallicity remained fairly constant for most of the active periods of Leo II, indicating early star formation from pre-enriched gas and possibly continued rejuvenation by little-enriched gas until some 5 Gyr ago. However, we caution that this qualitative interpretation is subject to the many uncertainties affecting the derivation of ages.

There appears to be no radial population gradient from the spectroscopic point of view, at least not in metallicity and at best weakly indicated in our inferred age distribution. Bellazzini et al. (2005) show that Leo II follows the common trend of containing more centrally concentrated intermediate-age populations as compared to the old component. In the case of Leo II the main driver of the population gradient appears to be age, since we have demonstrated that the AMR shows little evidence for metallicity variations (i.e., enrichment) across most of the age range.

Acknowledgments The results presented in the preceeding Chapter have been accepted for publication in the AJ as *Koch et al.* (astro-ph/0609700) and are based on a collaboration with Eva K. Grebel, Jan Kleyna, Mark Wilkinson, Gerry Gilmore, Daniel Harbeck, Rosemary F.G. Wyse and Wyn Evans.

Appendix 4.A

Radial velocity members in Leo II

Table 4.A: Derived properties of stars in Leo II. Only those stars, for which metallicities could be determined are listed. W' and r denote the reduced CaT width and the elliptical radius. [Fe/H] and the respective uncertainty are given following eq. 4.5.

Star	α (J2000)	δ (J2000)	r [′]	V	g−i	W' [Å]	[Fe/H]$_{\rm CG}$	Age [Gyr]
T_11	11 13 12.2	22 16 09	8.83	20.72	1.11	1.42	-2.25 ± 0.14	15.8^{+6}_{-5}
T_13	11 13 35.8	22 09 35	1.84	18.69	1.74	2.69	-1.71 ± 0.15	6.3^{+1}_{-1}
T_16	11 13 13.9	22 08 50	3.32	19.06	1.57	1.97	-2.01 ± 0.15	8.0^{+2}_{-1}
T_19	11 13 23.0	22 09 23	1.21	19.08	1.55	2.99	-1.58 ± 0.16	8.5^{+2}_{-2}
T_21	11 13 22.7	22 08 09	1.71	19.19	1.64	2.19	-1.92 ± 0.15	...
T_22	11 13 24.5	22 06 13	3.49	19.17	1.55	2.17	-1.93 ± 0.15	10.5^{+2}_{-2}
T_25	11 13 21.9	22 12 07	3.67	19.25	1.53	2.62	-1.74 ± 0.15	3.5^{+3}_{-2}
T_26	11 13 20.8	22 08 35	1.82	19.23	1.44	2.73	-1.69 ± 0.16	6.2^{+1}_{-1}
T_28	11 13 23.4	22 07 17	2.42	19.27	1.55	2.86	-1.64 ± 0.16	3.4^{+3}_{-1}
T_30	11 13 25.9	22 08 59	0.55	19.26	1.47	3.61	-1.32 ± 0.17	2.5^{+0}_{-0}
T_33	11 13 18.5	22 04 47	5.51	19.27	1.51	2.11	-1.95 ± 0.15	10.4^{+2}_{-2}
T_37	11 13 13.2	22 07 53	3.77	19.33	1.42	2.59	-1.75 ± 0.15	8.4^{+2}_{-2}
T_38	11 13 41.3	22 07 41	3.48	19.34	1.61	2.35	-1.85 ± 0.15	4.9^{+1}_{-1}
T_39	11 13 25.7	22 06 38	2.97	19.32	1.45	2.52	-1.78 ± 0.15	8.8^{+2}_{-2}
T_40	11 13 19.3	22 07 42	2.66	19.30	1.42	1.12	-2.37 ± 0.14	6.4^{+1}_{-1}
T_43	11 13 31.8	22 14 14	5.89	19.39	1.53	2.46	-1.80 ± 0.16	4.3^{+1}_{-1}
T_44	11 13 33.9	22 06 08	3.73	19.38	1.58	2.95	-1.60 ± 0.16	4.6^{+1}_{-1}
T_46	11 13 37.1	22 07 07	3.14	19.41	1.54	2.89	-1.62 ± 0.16	4.5^{+2}_{-1}
T_48	11 13 29.7	22 06 47	2.77	19.43	1.47	3.18	-1.50 ± 0.17	13.4^{+7}_{-4}
T_49	11 13 12.9	22 09 18	3.53	19.45	1.45	4.08	-1.11 ± 0.18	3.1^{+1}_{-0}
T_50	11 13 23.9	22 05 33	4.28	19.43	1.41	3.21	-1.49 ± 0.16	8.9^{+2}_{-2}
T_57	11 13 26.5	22 11 08	2.28	19.50	1.41	3.03	-1.56 ± 0.16	10.4^{+2}_{-2}
T_61	11 13 23.0	22 10 23	1.82	19.56	1.43	4.05	-1.13 ± 0.18	3.7^{+1}_{-1}
T_63	11 13 13.1	22 09 59	3.60	19.54	1.47	2.38	-1.84 ± 0.15	15.5^{+12}_{-7}
T_65	11 13 20.9	22 11 31	3.18	19.54	1.37	3.01	-1.57 ± 0.16	9.0^{+2}_{-2}
T_66	11 13 19.0	22 13 48	5.72	19.57	1.45	3.42	-1.40 ± 0.17	4.0^{+1}_{-1}
T_68	11 13 29.6	22 07 16	2.21	19.62	1.36	2.90	-1.62 ± 0.16	10.6^{+3}_{-2}
T_70	11 13 20.6	22 07 15	2.81	19.69	1.37	1.69	-2.13 ± 0.14	15.7^{+1}_{-1}
T_73	11 13 25.6	22 07 44	1.75	19.71	1.43	2.52	-1.78 ± 0.15	5.2^{+2}_{-2}
T_75	11 14 03.4	22 12 43	9.11	19.69	1.42	1.80	-2.09 ± 0.15	15.9^{+2}_{-2}
T_77	11 13 17.5	22 12 08	4.20	19.72	1.33	2.04	-1.98 ± 0.15	11.4^{+3}_{-2}
T_80	11 13 30.9	22 09 33	0.77	19.73	1.21	3.15	-1.51 ± 0.16	4.5^{+1}_{-1}
T_82	11 13 31.7	22 07 47	1.79	19.75	1.29	2.20	-1.91 ± 0.15	9.1^{+3}_{-2}
T_89	11 13 19.8	22 05 47	4.34	19.82	1.34	3.42	-1.40 ± 0.16	3.7^{+1}_{-1}

Continued on next page

Table 4.A – *Leo II stars, continued*

Star	α (J2000)	δ (J2000)	r [′]	V	g−i	W' [Å]	[Fe/H]$_{\rm CG}$	Age [Gyr]
T_92	11 13 22.7	22 06 58	2.83	19.87	1.35	4.16	−1.08 ± 0.18	4.7^{+1}_{-1}
T_93	11 13 41.9	22 05 35	5.22	19.83	1.18	2.41	−1.82 ± 0.15	4.5^{+1}_{-1}
T_95	11 13 21.5	22 05 16	4.74	19.87	1.25	3.12	−1.52 ± 0.16	9.3^{+3}_{-2}
T_97	11 13 23.6	22 07 07	2.57	19.93	1.24	3.34	−1.43 ± 0.16	2.7^{+1}_{-1}
T_98	11 13 22.0	22 04 29	5.57	19.89	1.16	1.88	−2.05 ± 0.16	4.6^{+1}_{-1}
T_99	11 13 32.5	22 11 23	2.74	19.94	1.33	2.30	−1.87 ± 0.15	4.9^{+3}_{-2}
T_109	11 13 24.1	22 09 34	1.04	20.05	1.12	2.43	−1.82 ± 0.15	4.9^{+2}_{-1}
T_110	11 13 37.9	22 03 44	6.64	20.02	1.15	3.41	−1.40 ± 0.18	1.7^{+0}_{-0}
T_113	11 13 28.5	22 08 17	1.02	20.10	1.20	3.07	−1.55 ± 0.16	12.3^{+5}_{-3}
T_115	11 13 18.3	22 06 45	3.60	20.10	1.23	3.18	−1.50 ± 0.16	14.7^{+2}_{-2}
T_116	11 13 21.7	22 07 02	2.86	20.07	1.17	2.94	−1.60 ± 0.16	7.6^{+3}_{-2}
T_135	11 13 25.6	22 12 13	3.55	20.16	1.17	3.14	−1.51 ± 0.16	8.6^{+4}_{-3}
T_146	11 13 17.1	22 05 16	5.16	20.24	1.13	2.20	−1.91 ± 0.16	7.4^{+3}_{-2}
T_155	11 13 28.6	22 08 38	0.62	20.30	1.20	2.81	−1.65 ± 0.16	15.6^{+10}_{-6}
T_171	11 13 44.7	22 08 25	3.92	20.38	1.16	2.94	−1.60 ± 0.16	15.7^{+9}_{-6}
T_194	11 13 21.6	22 10 53	2.49	20.45	1.15	1.06	−2.40 ± 0.14	14.9^{+3}_{-4}
T_203	11 13 22.0	22 11 32	3.07	20.50	1.06	2.35	−1.85 ± 0.15	6.9^{+4}_{-3}
T_205	11 13 18.0	22 09 53	2.49	20.50	1.10	3.08	−1.54 ± 0.16	11.2^{+6}_{-4}

Chapter 5

Stellar kinematics and metallicities in the Leo I dwarf spheroidal galaxy – (wide field) implications for galactic evolution

> “**Leo:** *A metric unit of acceleration representing an acceleration of 1 decametre per second per second.”*
> — H. G. Jerrard & D. B McNeill,
> *A Dictionary of Scientific Units (1980).*

Abstract

We present low-resolution spectroscopy of 120 red giants in the Galactic satellite dwarf spheroidal (dSph) Leo I, obtained with the GeminiN-GMOS and Keck-DEIMOS spectrographs. We find stars with velocities suggesting their membership with Leo I out to 1.3 King tidal radii. By measuring accurate radial velocities we find a mean systemic velocity of 284.2 $\mathrm{km\,s^{-1}}$ with a global velocity dispersion of 9.9 $\mathrm{km\,s^{-1}}$. The dispersion profile is consistent with being flat out to the last data. We show that a marginally-significant rise in the radial dispersion profile at a radius of $3'$ is not associated with any localized kinematical substructure. Given its large distance from the Galaxy, tides are not likely to have affected the velocity dispersion, a statement we support from a quantitative kinematical analysis, as we observationally reject the occurrence of any significant apparent rotational signal. Mass determinations adopting both isotropic stellar velocity dispersions and more general models yield a M/L ratio of 24, which is consistent with the presence of a significant dark halo with a mass of about $3 \times 10^7\,M_\odot$, in which the luminous component is embedded. This suggests that Leo I exhibits dark matter properties similar to those of other dSphs in the Local Group. Our data allowed us also to determine metallicities for 58 of the targets. We find mildly metal poor mean of -1.31 dex and a full spread covering 1 dex. In contrast to the majority of dSphs, Leo I appears to show no radial gradient in its metallicities, which points a negligible role of external influences in this galaxy's evolution.

5.1 Introduction

Leo I is the most remote dwarf spheroidal (dSph) galaxy generally believed to be associated with the Milky Way (MW) subsystem in the Local Group (see Table 1 in Grebel, Gallagher, & Harbeck

2003). Due to its remarkably high radial velocity of about 287 km s^{-1} (Zaritsky et al. 1989; Mateo et al. 1998b) and its large distance of ~ 254 kpc (Bellazzini et al. 2004), Leo I is a crucial tracer for determining the total mass of the Galaxy (e.g., Kochanek 1996). The question of whether Leo I is actually bound to the Galaxy remains open (e.g., Byrd et al. 1994). A quantitative assessment of the possible role of Galactic tides in the internal (dynamical, star-formation history, etc.) evolution of the Galactic satellite dSphs is of considerable importance, for its implications for the evolution of small galaxies, and for the distribution of dark matter on small scales. In particular, Leo I is of great interest here, given its very large Galactocentric distance, as it is the least-likely dSph to be affected by tides. From detailed kinematical modeling of the velocity dispersion profile of 35 stars within the core region of Leo I, Mateo et al. (1998b, hereinafter M98) concluded that this dSph contains a significant amount of dark matter. Consequently, similarities in Leo I's dynamics with those of more nearby dwarfs would strengthen our confidence that Galactic tides are not a major effect in determinations of the dark matter distribution both of Leo I itself and the other dSphs.

As discussed in the Introduction (Sect. 1.2), dSphs are characterized by high central stellar radial velocity dispersions of order 10 km s^{-1}, low luminosities and large core sizes of the order of a few hundred pc. These characteristics suggest that these galaxies are dominated by dark matter at all radii (Mateo et al. 1997; Wilkinson et al. 2004, 2006a), provided they are in a state of dynamical equilibrium. The latter assumption, however, is supported by the fact that the dSph are not highly disrupted down our lines of sight (e.g., Odenkirchen et al. 2001; Mackey & Gilmore 2003; Klessen et al. 2003). This has to be carefully tested, especially in the outermost parts of the dSph, where Galactic tides might become significant. Moreover, the inferred high mass-to-light ratios (M/L), obtained under the assumption of dynamical equilibrium, are as large as $500\,(M/L)_\odot$ or more, argue in favour of a dark matter dominance, making dSphs the smallest observable objects available to study the properties of dark matter halos. Available measurements suggest that the dark matter in dSphs has some common properties, including a minimum halo mass scale of $\sim 4 \times 10^7$ M$_\odot$, a small range in central (dark) mass densities, and a minimum length (core radius) scale of order 100 pc (Wilkinson et al. 2006a). If established, these are the first characteristic properties of dark matter.

The spatial distribution of dark matter on small scales is an additional test of the nature of dark matter. Numerical simulations of dark matter halos in which it is assumed that there is no physical process except gravity acting remain limited in spatial resolution, but in general are characterized by a central density cusp $\rho(r) \propto r^{-a}$ with a=1–1.5 (e.g., Navarro, Frenk & White 1995, hereafter NFW; Ghighna et al. 2000). It is far from clear that these expectations are consistent with observations of galaxies significantly more massive than the dSphs (de Blok et al. 2001; Spekkens et al. 2005), which are better accounted for by flat density cores. The available data on dSph kinematics appear to be consistent with cored halos as well (Łokas 2002; Read & Gilmore 2005; Wilkinson et al. 2006a). In the Ursa Minor dSph a central, constant-density core has been detected (Kleyna et al. 2003), and also in the Fornax dSph a core may be more likely than a cusped distribution, although these inferences are still subject to large uncertainties (Strigari et al. 2006; Goerdt et al. 2006). It has been suggested that the cusp/core distinction could be the first indications of the properties of the physical particles which make up CDM (Read & Gilmore 2005), though it is essential that one allows for dynamical evolution associated with the astrophysical evolution of the dSph progenitors (Grebel et al. 2003).

According to another scenario, the large observed velocity dispersions may be explained if dSphs are unbound tidal remnants that underwent tidal disruption while orbiting the Milky Way (Kuhn 1993; Kroupa 1997; Klessen & Kroupa 1998; Klessen & Zhao 2002; Fleck & Kuhn 2003;

Majewski et al. 2005), and all happen to be aligned to mimic a bound system. In this case the dSphs are predicted to exhibit a large depth extent and elongation along the line of sight (Klessen & Kroupa 1998; Klessen & Zhao 2002). However, in two of the closest Milky Way companions, the Draco dSph (Klessen et al. 2003) and the Fornax dwarf (Mackey & Gilmore 2003) no evidence supporting these effects has been found. Other arguments against dSphs being unbound tidal remnants without dark matter include that they all experienced extended star formation histories with considerable enrichment and that they follow a metallicity-luminosity relation (see Grebel et al. 2003 for details).

It is sometimes suggested that high-frequency “distorted” photometric structure is indicative of tidal damage, but no available numerical simulations support this view: rather, if tides are important, they produce smooth systematic distortions in the outer parts of a system. Furthermore, the occurrence of stars beyond a certain cut off-radius may point to a failure of one-component models, assigning the stellar system a nominal tidal radius, rather than this “extratidal” material actually indicating tidal disruption (see discussion in Section 1.2). One test for the occurrence and influence of tides, applicable in some circumstances, is the detection of apparent rotation associated with such a distortion. We will consider that in the following analysis of Leo I.

Based on its projected position on the sky, Leo I was suggested to be part of a Galactic Fornax-Leo-Sculptor Stream (Lynden-Bell 1982; Majewski 1994), i.e., that it lies along a Galactic polar great plane together with these other dSph galaxies. However, despite the lack of proper motion and orbital measurements for Leo I, the radial velocity and kinematical data to hand apparently rule out a physical association of Leo I with such a physical group (Lynden-Bell & Lynden-Bell 1995; Piatek et al. 2002, 2006).

Apart from its stellar kinematics, Leo I is interesting in terms of its star formation history (SFH). The dSphs of the Local Group exhibit a variety of SFHs, where no two dwarfs are alike (Grebel 1997; Mateo 1998). In spite of this diversity, all nearby galaxies studied in sufficient detail have been shown to share a common epoch of ancient star formation, although the fraction of old populations with ages > 10 Gyr varies from galaxy to galaxy (Grebel 2000; Grebel & Gallagher 2004). Indeed Leo I has a prominent old stellar population (Held et al. 2000), but more striking is the prevalence of intermediate-age populations – about 87% of its stars formed between 1 and 7 Gyr ago (Gallart et al. 1999a). The details of the SFH of Leo I were derived photometrically, but particularly in galaxies with mixed populations the age-metallicity degeneracy cannot be broken without spectroscopy. Our current inferences of the chemical evolutionary histories of nearby dwarf galaxies are still mainly based on photometry, while detailed and numerous spectroscopy of as many stars as possible is invaluable for helping to securely constrain the SFHs or to quantify age-metallicity relations. It is also essential to study the chemical evolution of dSphs in order to understand their complex SFHs in terms of regulating processes such as the inflow or accretion as well as the outflow of gas (Carigi et al. 2002; Dong et al. 2003; Lanfranchi & Matteucci 2004; Hensler, Theis, & Gallagher 2004; Robertson et al. 2005; Font et al. 2006).

In this Chapter we present a kinematic and abundance study of the distant Galactic dSph Leo I. In addition to a detailed dynamical analysis, appropriate to the size of the available data set, we have measured the average metallicity and the spread and shape of Leo I’s metallicity distribution function (MDF), which provide valuable insights on any possible environmental dependence of the processes governing the evolution of dSphs.

5.2 Data

5.2.1 Target selection

Targets were selected from photometry obtained within the framework of the Cambridge Astronomical Survey Unit (CASU) at the 2.5 m Isaac Newton Telescope (INT) on La Palma, Spain[1]. From this, we selected red giants so as to cover magnitudes from the tip of the red giant branch (RGB) at $I \sim 18$ mag (Bellazzini et al. 2004) down to ~1.6 mag below the RGB tip, going as faint as $I \lesssim 19.6$. At our faintest observed magnitudes, our spectra reach signal-to-noise (S/N) ratios of ~5, which is sufficient to enable accurate radial velocity measurements at our low resolution.

5.2.2 Observations

One part of our observations was carried out in queue mode with the Gemini Multiobject Spectrograph GMOS at the 8-meter Gemini North telescope, Hawaii, over four nights between December 2004 and January 2005. These data were obtained under photometric conditions and a clear sky. The camera consists of three adjacent 2048×4068 CCDs, which are separated by gaps with a width of ~37 pixel each. We used $0\farcs5$ wide multiobject slits and the R400+G5305 grating set in two modes, with central wavelengths of 8550 Å and 8600 Å, providing a spectral coverage of 1800 Å. This dithering enabled us to efficiently interpolate the spectra across the CCDs' gaps during the later coaddition process. The CCDs were binned by 2×4 during readout and the resulting spectra have a nominal resolution of 2200. In total, we targeted 68 red giants spread over three different fields in the western half of the galaxy (see Fig. 5.1, Table 5.1).

Field	α	δ	Date	Instrument	Exposure time
	(J2000)				[s]
Field 1	10 09 01	+12 22 47	2004 12 11	GMOS	3×1800
			2004 12 12	GMOS	3×1800
Field 2	10 08 59	+12 16 00	2004 12 12	GMOS	3×1800
			2004 12 15	GMOS	3×1800
Field 3	10 08 39	+12 19 43	2005 01 06	GMOS	2×1800
#1	10 09 14	+12 18 00	2005 02 06	DEIMOS	7200
#2	10 07 40	+12 17 00	2005 02 07	DEIMOS	9000
#3	10 08 05	+12 18 00	2005 02 08	DEIMOS	5400

Table 5.1: Observation log

Each of the three fields was exposed for three hours in total, where we split up the exposures into 3×1800 s per setup (i.e., each of the two wavelength modes) to facilitate sky subtraction and cosmic ray removal. Due to bad weather, the central pointing (Field 3, see Table 5.1) was exposed for only 3600 s in total.

The other part of our data was obtained with the DEep Imaging Multi-Object Spectrograph (DEIMOS) at the 10-meter Keck II telescope. Leo I was observed on the DEIMOS multislit spectrograph on the Keck II telescope on February 6 to February 8 2005. Conditions were mediocre, with high humidity and poor seeing, but approximately six hours of Leo I observations were obtained, consisting of five slit masks concentrated on the dSph's periphery. Slits were $0.7''$ in size, and resolution was about 0.3 Å per pixel.

---

[1] see `http://www.ast.cam.ac.uk/~wfcsur/`.

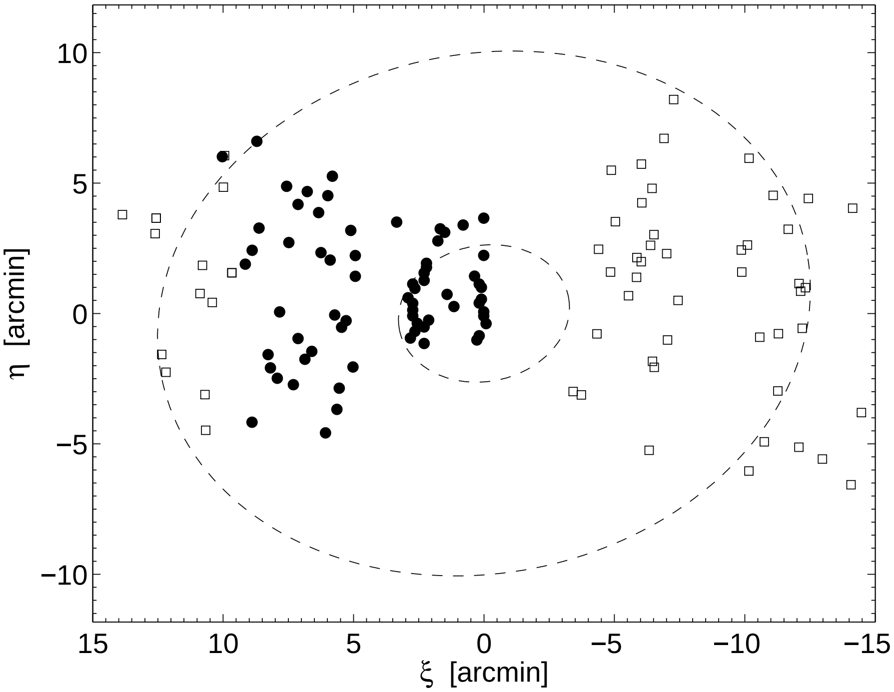

Figure 5.1: Location of our targets centered on the Leo I dSph at (α, δ) = (10:08:28, +12:18:18). Red giants observed with GMOS are shown as filled circles, DEIMOS targets are depicted as open squares. Overlaid ellipses designate respectively Leo I's core and nominal tidal radius at 3.′3, 12.′6, respectively. The system's ellipticity and position angle are assumed to be 0.21 and 79°.

5.2.3 Data Reduction

GMOS data

The GMOS data were reduced using the standard GMOS reduction package in IRAF, starting with the bias frames taken as part of the day-time calibration process. Spectroscopic flat-field exposures were obtained adjacent to each set of science exposures, from which we could model and remove the spectral signature and spatial profile of the illumination pattern. Through dividing by the remaining normalized flat-field frame, we ensured a complete removal of any residual sensitivity variation. Since the CuAr wavelength calibration frames were taken up to four days before and/or after the science spectra, during which time the telescope flexure may significantly change, we had to rely on the skylines of each individual science exposure to obtain an accurate wavelength solution. Hence, we chose a number of strong and isolated, unblended night-sky OH-emission lines around the CaT region from the atlas of Osterbrock et al. (1996, 1997). Fitting the respective lines with a low- order polynomial yielded a RMS uncertainty in the wavelength calibration of the order of 0.05 Å, corresponding to $\sim 2\,\mathrm{km\,s^{-1}}$ at our region of interest[2]. A crucial step in the analysis of CaT absorption features consists of the accurate subtraction of

---

[2] Using the entire spectral region at hand, covering ca. 1800 Å, yielded highly inaccurate results in the wavelength solution, as too large a range of distortions were being fitted with too few lines, resulting in offsets between individual exposures of the order of $\sim 50 - 100\,\mathrm{km\,s^{-1}}$. However, when concentrating on the narrow window (∼500Å) around the CaT, in which we are primarily interested, we circumvent any distortions towards the edges of the spectra and could thus obtain a highly improved accuracy.

the prominent skylines in the near-infrared spectral region. While the centers of the first two of the Ca triplet lines are unaffected by adjacent skylines at Leo I's systemic velocity, the third Ca absorption line coincides with the dominant OH-band at ∼8670 Å. These undesired contaminants are efficiently removed by the software by fitting a low order polynomial to the background and subtracting this fit column by column from the science spectra. Moreover, the accuracy of our sky subtracted spectra (after coaddition) was improved by the fact that we obtained spectra with the slit centred both at the centre and offset towards the right and left hand side of the stellar seeing disk, yielding a better coverage of the average sky background. Finally, the extracted spectra were shifted towards the local standard of rest barycenter and median-combined using a standard σ-clipping algorithm. The average S/N ratio achieved throughout our reductions is ∼28, with a minimum of 5.3 at $\mathrm{I} = 19.6$.

DEIMOS data

The data were reduced with the DEEP DEIMOS pipeline. For some masks, it was necessary to modify the code to properly extract the flat-lamp traces. After extracting the spectra, custom code was used to convert the DEEP output to ordinary one-dimensional FITS image spectra.

5.2.4 Radial Velocities

Radial velocities were derived from our final reduced set of spectra by cross-correlating the three strong Ca lines at $\lambda\lambda 8498, 8542, 8662$ against a synthetic template spectrum of the CaT region using IRAF's cross-correlation package FXCOR. The template was synthesized using representative equivalent widths of the CaT in red giants. The final velocity difference between object spectrum and the rest-frame template was then determined from a parabolic fit to the strongest correlation peak.

5.2.5 Velocity errors

The formal velocity errors returned from the cross-correlation in IRAF have a median value of $1.7\,\mathrm{km\,s^{-1}}$. However, we have found in past studies that the FXCOR estimates are generally too optimistic (see e.g., M98; Kleyna et al. 2002). Since we have only single epoch data at hand, lacking the possibility to compare the velocity stability over a longer time period, we cannot estimate the true uncertainties through the discrepancies of measurements taken at different times (Vogt el al. 1995, M98). For the GMOS data, we rather follow the prescription of Kleyna et al. (2002) and combine the data of the brightest stars (with $I \leq 19\,\mathrm{mag}$) into two final sets of spectra, the first comprising those individual spectra with a central wavelength of 8550 Å and the second being those centered at 8600 Å. Each of these sets was separately cross-correlated against the template. We use the discrepancy between the two resultant velocities as an estimate of the true measurement error. Hence, we rescaled the Tonry-Davis R-based errors (Tonry & Davis 1979) returned by FXCOR to obtain the expected reduced χ^2 discrepancy of unity. We found that we had to apply a scale factor of 2.7 to yield an accurate estimate of our velocity errors. In order to check whether our wavelength calibration, which is based on only a narrow spectral window around the CaT has introduced any bias, we also determined radial velocities by cross-correlating each of the three Ca lines separately against the same template. In this case, the mean deviation of the resultant velocities did not exceed $1.8\,\mathrm{km\,s^{-1}}$. These uncertainties were added in quadrature to the formal measurement errors (according to the above Tonry-Davis R

scaling) to yield the final velocity error, which we list in the Appendix. The final GMOS data set contained 68 stars with a median velocity error of 5.0 km s^{-1}.

For the DEIMOS data, the nominal IRAF velocity errors were also rescaled by a common factor. The rescaling was performed by computing separate velocities for lines 1+2 and line 3 of the CaT, and then requiring the difference between the two velocities divided by the quadrature sum of the rescaled nominal errors to obey the expected χ^2 statistics. The final DEIMOS member list includes 27 member velocities with per pixel $S/N > 10$, and a median velocity error of 2.7 km s^{-1}.

5.3 Radial Velocity Distributions

To determine an overall mean velocity and a global dispersion for Leo I, a prerequisite for an assessment of the targets' membership, we used the maximization method described in Kleyna et al. (2002) and Walker et al. (2006a). In this approach, the probability that an observed distribution of velocities v_i and corresponding measurement errors σ_i is drawn from a Gaussian distribution with mean $\langle v\rangle$ and dispersion σ is given by

$$p\left(\{v_i,\sigma_i\}|(\langle v\rangle\,,\sigma)\,\right)\;\propto\Pi_{i=1}^{N}\frac{1}{\sqrt{2\pi(\sigma^2\,+\,\sigma_i^2)}}\,\exp\left\{-\frac{(v_i\,-\,\langle v\rangle)^2}{2\,(\sigma^2\,+\,\sigma_i^2)}\right\} \tag{5.1}$$

It is mathematically more convenient to calculate the natural logarithm of this expression, and maximizing $\ln p$ is equivalent to maximizing p itself. Rejecting stars deviating more by than 3σ as likely non-members, we iterated until convergence. The respective uncertainties in the mean and dispersion were then calculated from the covariance matrix (Walker et al. 2006a). This procedure yielded a mean systemic velocity of Leo I of (284.2± 1.0) km s^{-1} and a dispersion of 9.9 ±1.5 km s^{-1} from the combined GMOS plus DEIMOS sample, (284.6±1.5, 9.9±2.1) km s^{-1} for the GMOS data alone and (283.8±1.5, 9.9±2.1) km s^{-1} as derived from the DEIMOS targets only. This compares to a value of 287.0 ± 1.9 km s^{-1} as found by M98 and their respective dispersion of 8.8 ± 1.3 km s^{-1} for stars in the innermost $3\farcm5$. The mean velocities and global dispersions are tabulated in Table 5.2 separately for the different fields and Fig. 5.2 shows the resulting histograms.

If we take the 3σ-cut as a membership criterion, 5 of the 68 GMOS targets and 5 of the red giants from the DEIMOS sample have to be rejected as foreground contamination, where 4 out of the 5 stars in each sample have velocities below 200 km s^{-1}. In order to generate the final sample for determining the dispersion profile of Leo I we combined both of our GMOS and

Field	$\langle v\rangle$ [km s^{-1}]	σ [km s^{-1}]
GMOS, Field 1	284.0 ± 2.6	7.4 ± 3.4
GMOS, Field 2	283.6 ± 2.8	8.8 ± 3.8
GMOS, Field 3	284.2 ± 2.3	12.5 ± 3.6
GMOS, all	284.6 ± 1.5	9.9 ± 2.1
DEIMOS, all	283.8 ± 1.5	9.9 ± 2.1
GMOS + DEIMOS	284.2 ± 1.0	9.9 ± 1.5
GMOS + DEIMOS + M98	287.0 ± 0.9	9.8 ± 1.3

Table 5.2: Mean velocities and dispersions for different fields.

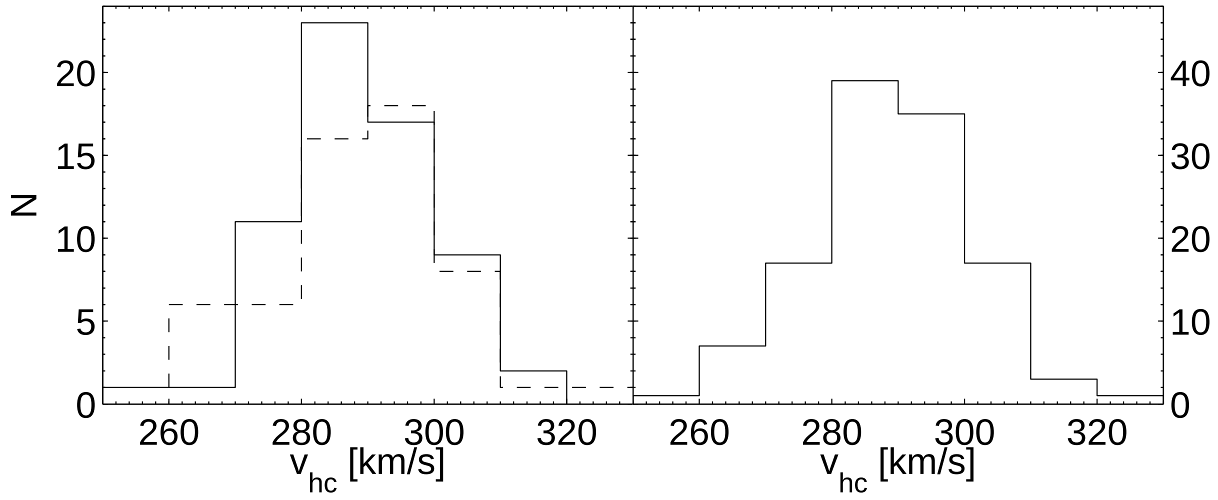

Figure 5.2: Radial velocity histograms of the GMOS data (solid line in the left panel), DEIMOS stars (dashed line, left panel) and combined GMOS plus DEIMOS set (right panel). All targets with velocities larger than 200 km s^{-1} are shown. Within this range, two targets (at 251 and 324 km s^{-1}, respectively) fall outside a $\pm 3\sigma$-cut.

DEIMOS sets by shifting them to a common median velocity. This procedure is justified by the lack of any significant radial gradient in the velocities from DEIMOS, which is found to be (-0.04 ± 0.18) km s^{-1} arcmin^{-1} so that such a shift does not introduce any artificial velocity gradient or a falsification of the dispersion profiles. At the end of this procedure, we found that our median velocity from the GMOS plus DEIMOS set differed from that of M98 by -2.8 km s^{-1}, a difference significant only at the $p = 0.31$ level (note that our sample has no stars in common with the M98 sample, which would allow for a direct comparison of the velocities). These values are finally listed in the Appendix to this Chapter.

5.4 Kinematic tests for tidal damage and apparent rotation

Those dSph galaxies studied so far show no significant contribution from angular momentum to the systems' dynamical structure: dSphs obtain their size and shape from anisotropic random pressure. This is, incidentally, an argument against an evolutionary transformation from dwarf irregular to dSph galaxies via ram pressure stripping (e.g., van den Bergh 1999; Grebel et al. 2003). More fundamentally, apparent rotation (generally visible in projection) is a characteristic signature of tidal disturbance. In this context, apparent rotation of the stellar component of a dSph is a test of possible tidal 'heating' of the stellar orbits in the course of the galaxy's orbit within the external tidal field of the Milky Way. N-body simulations, e.g., of Oh et al. (1995) have shown that the velocity dispersion of a tidally-limited system is sustained at the actual virial equilibrium value. On the other hand, these simulations suggest that any strong dynamical effects on a dSph from the tidal field of the Galaxy can invoke streaming motions in the outskirts of the dwarf, which will lead to a systematic change in the mean velocity along its major axis, thus mimicking apparent rotation (Piatek & Pryor 1995; Oh et al. 1995; Johnston et al. 1995; M98). A more detailed analysis of tidal effects on dSph galaxies is provided by Read et al. (2006b).

It has frequently been suggested in the literature that the detection of member stars well beyond the formal tidal-limit radius of dSphs, canonically defined via single-component King model representation of the observed surface brightness profiles, is evidence for physical tides. A large number of dSphs have been claimed to show hints of extratidal stars and thus tidal disruption (Irwin & Hatzidimitriou 1995; Martínez-Delgado et al. 2001; Palma et al. 2003; Muñoz et al. 2005, 2006). What these papers show, in fact, is that the presumed parametric fit to the measured surface brightness (and/or direct star counts) is inappropriate at large radii. The physical reason for this inappropriateness is not provided by the historical label in the King model however. Given that there is no astrophysical basis to the application of a King model to a galaxy, there is no basis for an astrophysical interpretation of the corresponding labels as physical processes. Evidence that a specific dSph is being affected by tides sufficiently strongly that its kinematics are affected can be provided only from a kinematic analysis. A test for apparent outer rotation is such a test.

With its present-day Galactocentric distance of (254±19) kpc and its high systemic velocity, Leo I is not expected to be affected by tides. M98 concluded from their kinematical data that the core of this galaxy has not been significantly heated by tides. Sohn et al. (2006) report a large population of photometrical and radial velocity member red giant stars out to nearly two nominal tidal radii, which they interpret as evidence of tidal disruption. We note that also our sample comprises nine red giants outside r_{tid}, whose velocities suggest membership. We emphasise that these statements tell us that the outer parts of Leo I are not well-fit by a single King model. They tell us nothing about the dynamics of Leo I.

In order to assess whether there is any significant indication of rotation in the Leo I velocities, which may help to elucidate the role of tides, we calculated the difference in mean velocity on either side of bisecting lines passing through each of the targets, assuming that each such line is a potential rotation axis. The axis yielding the maximum mean velocity difference is then taken as the "rotation axis", with the associated velocity difference being an estimate of the amplitude of the rotation. Fig. 5.3 shows the resulting velocity differences for our data set. Due to the confinement of our GMOS fields to the western half of Leo I, we cannot perform any test for rotation in this subsample alone. However, based on only the 56 candidate members from DEIMOS, we find a maximum velocity difference of 1.2 km s^{-1}. Nevertheless, the spatial distribution of these stars does not allow one to unambiguously determine a potential rotation axis (see top panel of Fig. 5.3).

In the case of the combined GMOS and DEIMOS sample, the amplitude of the potential rotation reaches a value of 5.2 km s^{-1} (middle panel of Fig. 5.3). When also the 35 stars from M98 are added, the mean velocity difference changes to 3.0 km s^{-1} (bottom panel of Fig. 5.3). It is worth noticing that in both of the latter cases the axis of the maximum rotation signal occurs at a position angle (78°, 80°) which coincides with Leo I's position angle of $(79 \pm 3)^\circ$ (Irwin & Hatzidimitriou 1995).

In order to test the significance of these results, we constructed 10^4 random samples of radial velocities at the observed spatial positions. The velocities were taken from a normal distribution with the same mean and standard deviation as in our observations, additionally allowing for a variation around the measurement uncertainty. By means of this Monte Carlo simulation we find that the significance of the rotation in the DEIMOS sample is consistent with zero, whereas the amplitudes of the combined GMOS plus DEIMOS data sets and the full data including M98's stars amount to a significance of 86.7% (1.5 σ) and 20% (0.3 σ), respectively. Thus the rotational signature we detected appears not to be statistically significant in either case. Consequently, we have no evidence of any kinematical effect due to Galactic tides operating on Leo I.

Another cause of apparent rotation is relative transverse motion. Unfortunately, there is no

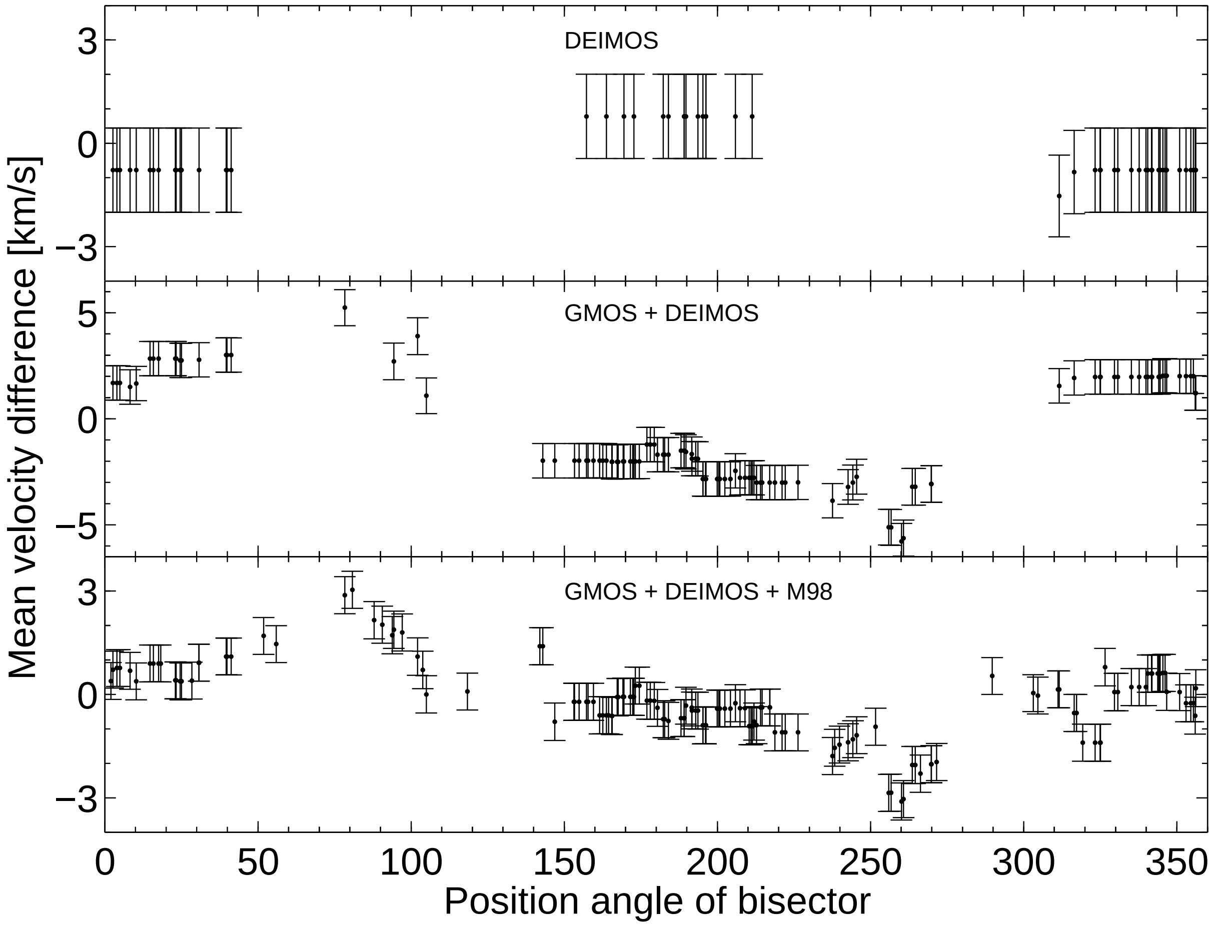

Figure 5.3: Tests for rotation in different subsamples of our data (as labeled): shown is the mean velocity difference with respect to rotation around axes at the respective position angles. A rotation signal around the minor axis (at PA∼ $79°$) is distinguishable, but its significance is marginal.

estimate of Leo I's proper motion available in the literature at present. Hence, we cannot rule out the possibility that the amount of observed rotation is entirely due to the relative motion between the Sun and the dSph, $v_{rel}(l, b)$, in the Galactocentric rest frame. A non-rotating object will appear to rotate as seen in the heliocentric rest frame, provided there is a significant gradient in this relative motion across the dSph (see Walker et al. 2006a). We can attempt the inverse calculation: we tested whether one can constrain Leo I's true proper motion by demanding that this galaxy does not rotate but the entire amplitude of the observed velocity gradient is caused by such projection effects. For this purpose, we calculated the Galactocentric rest frame velocity of each star through the formalism provided in Piatek et al. (2002) and Walker et al. (2006a). This was done for a wide grid of assumed proper motions, corresponding to transverse velocities from -500 to $+500\,\mathrm{km\,s^{-1}}$ in both μ_l and μ_b. Regrettably, the full range of input (μ_l, μ_b) was able to reproduce the observed apparent rotation amplitude adequately (see Fig. 5.4, left panel), so no deductions are possible. We then re-ran the same formalism by adopting a toy distance of 50 kpc to Leo I and secondly assumed its line-of-sight velocity as zero. In both cases the parameter space of possible proper motions increased even more, as the middle and right panels of Fig. 5.4 imply. In consequence, we can neither unequivocally exclude the possibility that Leo I's observed,

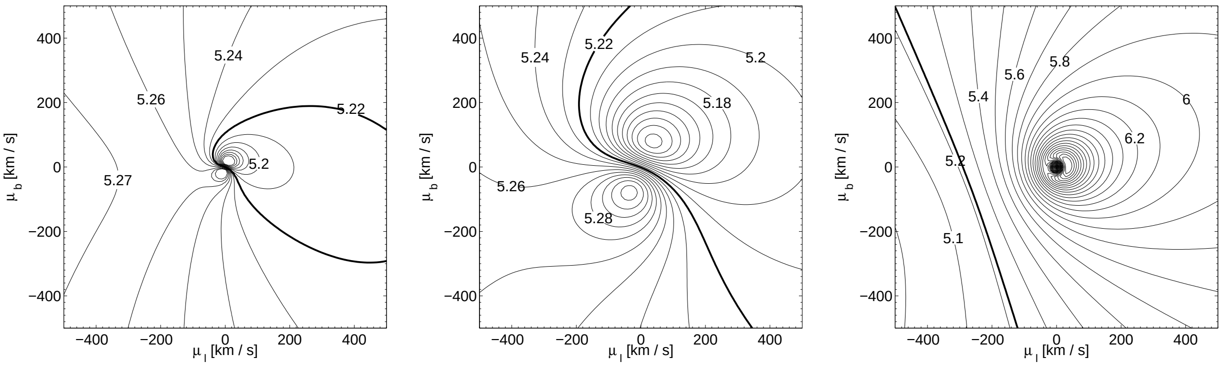

Figure 5.4: Contours of same velocity gradient that were derived under the assumption of a grid of proper motions. The left panel refers to Leo I's real distance and observed systemic velocity, whereas the middle panel adopts a fake distance of 50 kpc and the right panel was derived by assuming a radial velocity of zero. The thick line is the observed value from the GMOS+DEIMOS data (the arguments do not change after inclusion of the M98 data set). A few contours are labeled to illustrate the covered range of apparent rotational amplitudes.

though insignificant, velocity gradient is purely caused by the aforementioned projection effects and/or primarily driven by its large distance or systemic velocity, nor can we conclusively restrict its proper motion to a reasonable estimate.

5.5 Velocity Dispersion Profile

From their sample of 35 stars, M98 reported *central* velocity dispersions ranging from $(8.6\pm1.2)\,\mathrm{km\,s^{-1}}$ to $(9.2\pm1.6)\,\mathrm{km\,s^{-1}}$, which were obtained using several model-independent estimators. This is slightly lower than our global estimate from eq. 5.1, but consistent within the uncertainties.

We determined the velocity dispersion profile using the maximum likelihood method outlined in Kleyna et al. (2004). The data were binned such as to maintain a constant number of stars per bin, where we chose the binsize such that no fewer than ten stars were included. A Gaussian velocity distribution around the single mean velocity of the entire ensemble is then assumed for each radial bin, convolved with the observational errors. The member velocity distribution centred on the systemic velocity is then combined with an interloper distribution, $P_{int}(v)$, contributing a fraction f_{int} to each bin. This allows the probability distribution of the true dispersion σ in the bin through an extension of eq. 5.1:

$$\begin{aligned} p\left(\{v_i,\sigma_i\}|(\langle v\rangle\,,\sigma)\,\right) \quad &\propto \quad \Pi_i \left[(1-f_{int})\,\frac{1}{\sqrt{2\pi(\sigma^2\,+\,\sigma_i^2)}} \right. \\ &\times \quad \left. \exp\left\{-\frac{(v_i\,-\,\langle v\rangle)}{2\,(\sigma^2\,+\,\sigma_i^2)}\right\} + f_{int}P_{int}(v)\right] \end{aligned} \tag{5.2}$$

We then perform a maximum likelihood fit over σ and f_{int}, marginalise over the interloper fraction and finally find the most likely dispersion from the marginalised distribution.

We take account of the effects of the Galactic foreground interlopers in our data set by assuming various associated distributions $P_{int}(v)$ over the whole range of interest around the systemic velocity of Leo I. Consequently, we tested power-law velocity distributions with varying indices against the uniform case and against each other and found from a Kolmogorov-Smirnov (K-S) test that the resulting dispersion profiles were practically identical at a 100% confidence level. The velocity distribution of the ten non-member stars in our sample itself is best represented by a power-law with an exponent of −0.7 (with a K-S probability of 93%), whereas the K-S probability that these stars' velocities are uniformly distributed is 52%. We emphasise, however, that the resulting dispersion profiles do not change with respect to the adopted parameterisation of the underlying interloper distribution. This is also to be expected, given the low total number of non-members sampled, a consequence of the overall high systemic velocity of Leo I relative to line-of-sight galactic halo stars. We will, for convenience, use the uniform case in the following. Typically, the peak interloper fraction for the outermost bin does not exceed 0.1 and is compatible with zero in the inner bins.

Finally, formal error bounds were determined by numerically integrating the total probability of the data set and finding the corresponding 68 per cent confidence intervals. Fig. 5.5 shows the resulting velocity dispersion profiles as a function of the projected spherical radius for different membership criteria, and separately for the subsamples.

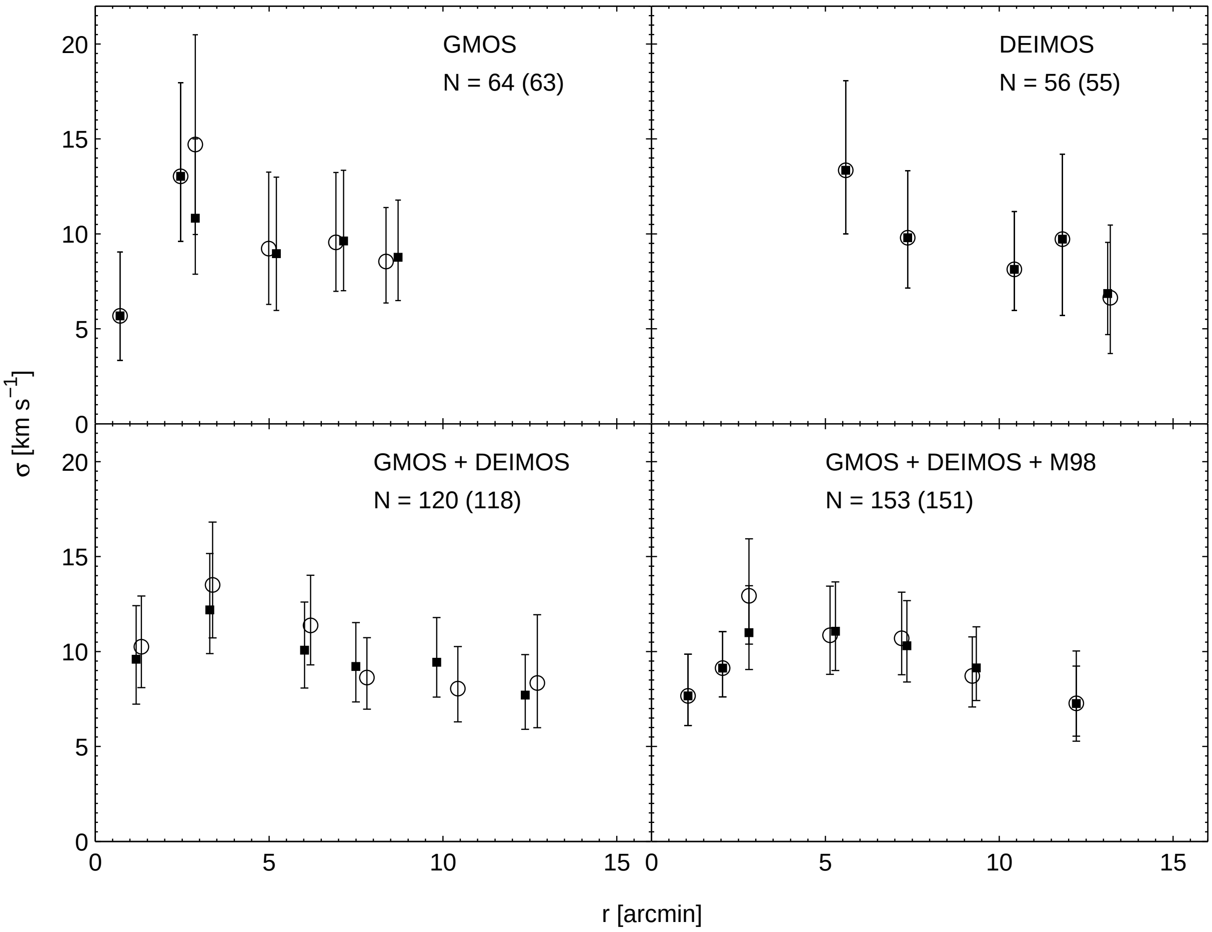

Figure 5.5: Velocity dispersion profile for different subsamples, as labeled, and rejection cuts. The numbers given refer to the sample size. Open circles refer to the full samples, whereas filled squares as well as the numbers in parentheses relate to the data cut at 3σ.

5.5.1 Radial variations

Given the derived uncertainties in the profiles, the dispersion profile of Leo I can be considered to be approximately flat out to the nominal tidal radius for the majority of the data combinations shown. Exclusion of the 3σ-outlier in the last bin leads to only a marginal change. Inclusion of the data from M98 with our own data into the maximum sample decreases the dispersion in the central $3'$ by $\sim 2\,\mathrm{km\,s^{-1}}$, while the associated rebinning of the data introduces a small drop in the dispersion beyond $10'$, illustrating the sensitivity of the binned dispersions to sample binning.

5.5.2 Absence or presence of kinematical substructure

Localized, kinematical structures in Local Group dSphs have been detected, specifically in the form of low local velocity dispersion (cold) spatially clumpy substructure in the UMi dSph (Kleyna et al. 2003; Wilkinson et al. 2004). In Sextans a low velocity dispersion (cold) central core has been found (Kleyna et al. 2004) and independently the presence of an off-centered kinematically distinct subpopulation has been reported (Walker et al. 2006b). Such distinct cold features can be interpreted as the remains of dispersing star clusters, with their central locations arising due to the clusters being dragged towards the inner regions by dynamical friction (Kleyna et al. 2003, 2004; Goerdt et al. 2006). An alternative proposal involves the after effects of a merger between a dSph and an even smaller system (Coleman et al. 2004).

Despite the overall flatness of Leo I's velocity dispersion towards larger radii, the profile does show some radial structure. A noteworthy radial feature is an apparent rise in the dispersion profile at $\sim 3'$ ($\mathrm{r}/\mathrm{r}_t \sim 0.25$). This trend is persistent, regardless of radial binning and the chosen sample, and it is also inherent in the profile observed by Mateo (2005). The major difference between our profile and the one reported in Mateo (2005) is that his dispersion rises continuously out to $10\overset{\prime}{.}5$ after having reached its minimum after the bump. Hence, it cannot be excluded *a priori* that the local dispersion maximum may in fact be localized and physically real.

In order to test whether our data set supports the presence of any underlying localized kinematical substructure, we estimate the position-dependent dispersion using a non-parametric approach. We define the locally weighted, average dispersion as

$$\sigma\,(x,y) \;=\; \frac{\sum_{i=1}^{N} \left\{ (v_i - \langle v \rangle)^2 - \sigma_i^2 \right\} \, K(x, x_i, y, y_i, h)}{\sum_{i=1}^{N} \, K(x, x_i, y, y_i, h)} \tag{5.3}$$

(Walker et al. 2006b, after Nadaraya 1964; Watson 1964). Here, v_i and σ_i are as usual the observed radial velocities and associated uncertainties of the N targets at the location (x_i, y_i). The smoothing kernel K is characterized by its smoothing bandwidth h, which we adopted as variable such as to include a fixed number n of stars within $3h$ at each location (x, y). For convenience in comparing our analyses, we follow the prescription of Walker et al. (2006b) in adopting a bivariate Gaussian kernel; hence $K \propto \exp\left\{ -\frac{1}{2} \frac{(x-x_i)^2 + (y-y_i)^2}{h^2} \right\}$. The number of nearest neighbors n was chosen sufficiently high to yield a statistically significant estimate of each local dispersion measurement, but sufficiently low so that any real spatial information would not be averaged out. Hence we varied n from 5 to 30, corresponding to at most about 25% of the entire sample size.

The significance of any potential substructure in our data was then determined via detailed Monte Carlo modeling. For this purpose, 10^3 random data sets were generated, where the (x, y) coordinates of our targets were preserved, but the observed velocities and error estimates were permuted with respect to their position. In this way, the sample mean and dispersion were retained, whereas any spatial information was dissolved. For each of these random data sets, the spatial dispersion distribution (eq. 5.3) and its maxima and minima were determined. The significance p_{hot} (p_{cold}) of hot (cold) substructures at each spatial point was then defined by the fraction of random data sets with a maximum (minimum) dispersion, which is lower (higher) than the actual observed local dispersion $\sigma(x, y)$ (see Walker et al. 2006b).

We do not find evidence of any localized cold substructure with low radial velocity dispersions in our data (see Fig. 5.6). In both the GMOS + DEIMOS data sets of Leo I and after inclusion of M98 targets, the significance of cold structures, p_{cold}, does not exceed 50% for any choice of the number of neighboring points. The typical value of this significance lies at 30%.

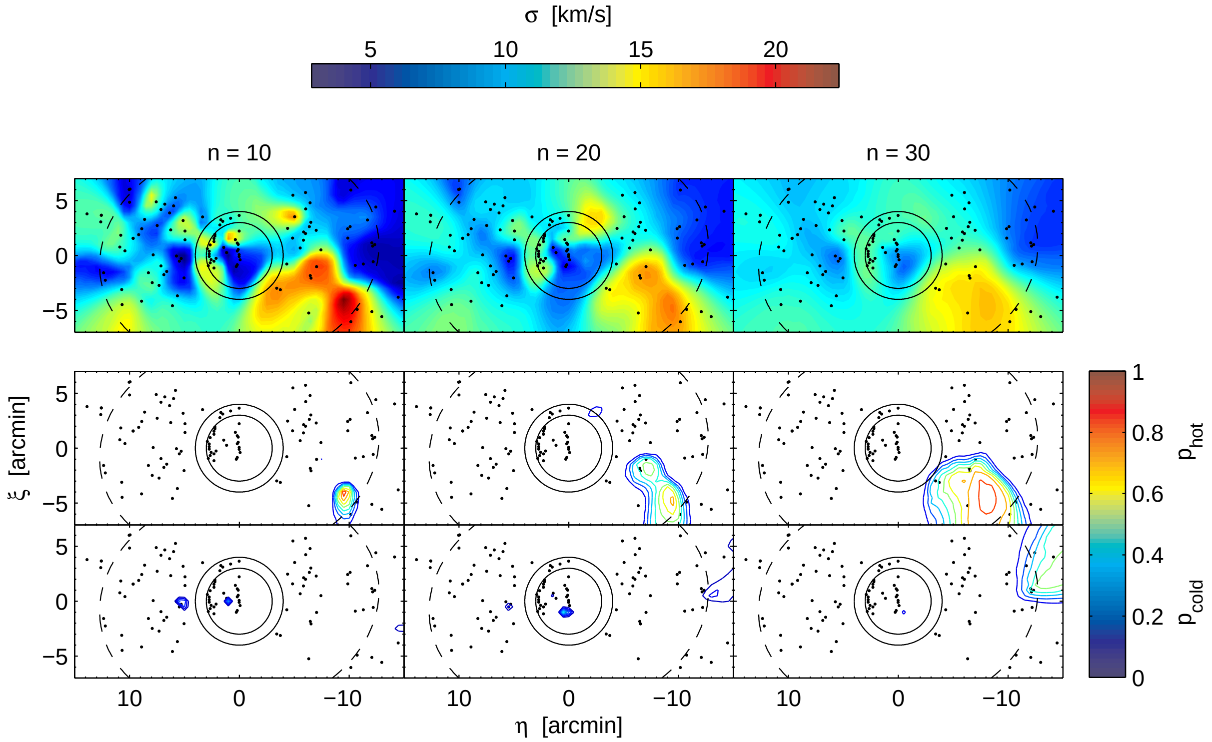

Figure 5.6: Top panel: Radial velocity dispersion estimator according to eq. (5.3), following the method of Walker et al. (2006b). Shown are the data for the combined GMOS + DEIMOS samples (small dots are the target locations), but the results do not alter after inclusion of the M98 sample. The middle and bottom panels display contours of the statistical significances p_{hot} and p_{cold} for the occurrence of any kinematically hot (middle) or cold (bottom) substructure. The individual panels show results for different choices of neighboring points included in the dispersion estimates. Contours are shown in intervals of 0.1. The dashed ellipse circumfers the nominal tidal radius and the two solid lines inscribe the interval of $3'$–$4'$, in which the radial dispersion profile exhibits a bump. See text for details.

On the other hand, the presence of a physically real local maximum in the radial dispersion profile could indicate the presence of a locally *hot* structure at radii of $\sim$3–$4'$. Although the probabilities for an occurrence of hot substructure increase towards the nominal tidal radius, where the data are only sparsely distributed, the formal significances p_{hot} are generally well below the 80% level. Hence, the apparent localized kinematical structure is consistent with statistical fluctuations about a constant dispersion value within a 1σ-level. In particular, there is no significant evidence of any localized structure at the radii in question – at loci between $3'$ and

$4'$, the probability of an occurrence of any dynamically hot substructure is less than 15% for any reasonable choice of n.

We conclude that the apparent rise in the velocity dispersion profile does not exclude the presence of any kinematical substructure, but it is probably not a localized feature.

5.5.3 (Non-) Influence of binaries

The presence of a significant population of binaries in any kinematical data set leads to an inflation of the observed velocity distribution, or, in other words, the true line of sight velocity dispersion of a stellar system is smaller than the observed dispersion, as soon a non-zero binary fraction is considered. Moreover, the high-velocity tail of a binary distribution drives a distribution function away from Gaussian, so that an over-simple determination tends to produce larger errors in the derived velocity dispersion, which in turn may reduce the statistical significance of any real radial gradient in the dispersion profile (see error bars in Fig. 5.7). Fortunately, the effect of binary stars has been shown to be negligible in dSphs in the past. Hargreaves, Gilmore & Annan (1996) could effectively show by using Monte Carlo simulations that the velocity dispersion caused by pure binary orbits is small compared with the generally large observed dispersions in dSphs, provided that the ensemble of orbital parameters in the dSph stars is similar to the distribution in the solar neighbourhood. Likewise, Olszewski et al. (1996) concluded from their simulations that none of the kinematical estimates in the UMi and Draco dSphs significantly changes under the influence of binary stars. This finding was underscored by repeat observations of red giants in the Draco dSph (Kleyna et al 2002). These observed kinematics did not show any evidence that would support an overall binary content larger than 40%. Moreover, the dynamically significant fraction in the Draco sample amounted to less than 5%. In the case of Leo I, Gallart et al. (1999a) argued from their modeled SFH based on deep HST color magnitude diagrams (CMDs) that it is unlikely that the total binary fraction in this galaxy exceeds 60%, again with a far lower dynamically significant number.

In order to explore the importance of binaries for the velocity dispersion profile of Leo I, we added an additional term to eq. 5.2, accounting for a binary star distribution $P_b(v)$, which is then convolved with the observed velocity distribution, in accordance with eq. 1 of Kleyna et al. (2002). The binary probability distribution $P_b(v)$ was adopted from Kleyna et al. (2002) and is based on the velocity measurements of Duquennoy & Mayor (1991) for a sample of solar-type primary stars in the solar neighbourhood. Kleyna et al. (2002) then obtained a realistic distribution by taking into account the giant branch binary evolution through circularization of the orbits. We note that the presence of a non-zero binary fraction does not alter the derived interloper fraction, which is still consistent with zero (less than 5% in the outermost bin).

Fig. 5.7 shows velocity dispersion profiles obtained under the assumption of different binary fractions. The average errorbar on the velocity dispersion measurements increases by 10% for a binary fraction of 0.4 and by 25% for an implausibly large f_b of 0.8. Likewise, the overall decrease of the dispersion profiles is, with less than $0.7\,\mathrm{km\,s^{-1}}$ deviation for 40% binaries, well below the $0.5\,\sigma$ level. An increase of f_b leads to a progressively more pronounced fall off of the underlying dispersion profiles. Nonetheless, the velocity dispersion profile assuming 40% binaries is consistent with that using no binaries at 90% confidence level, as confirmed by a K-S test so that henceforth the effect of binaries on our observed line of sight velocity dispersion profiles is taken to be negligible.

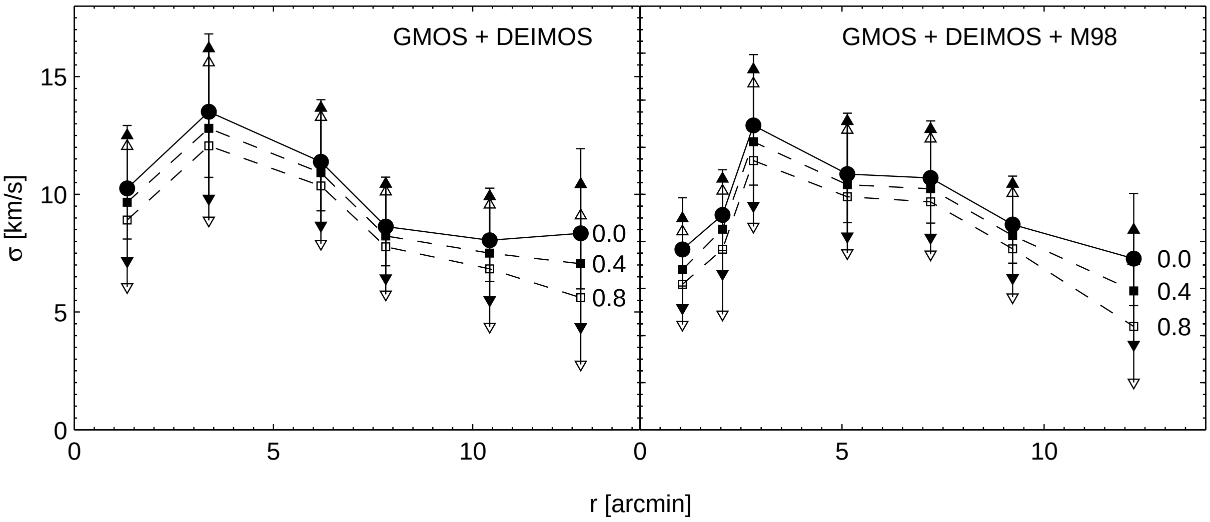

Figure 5.7: Radial velocity dispersion profiles for the subsamples as in Fig. 5.5. From top to bottom each curve was calculated with increased binary fractions f_b (labeled right of the outer bins). The solid curve and filled points refer to the observed profile assuming no binaries. Open (solid) squares and dashed lines are drawn from a maximization assuming an f_b of 0.4 and 0.8, respectively. In order to illustrate the effect of a binary population on the errors on the velocity dispersion, the respective error bounds of the profiles with $f_b > 0$ are displayed as solid (open) triangles.

5.6 Isotropic mass estimates

The simplest possible estimate of the mass profiles of dSphs uses single-component dynamical models, in which it is assumed that the mass distribution follows that of the visible component ("mass follows light", e.g., Richstone & Tremaine 1986). In this context, King models (King 1966) were often used to describe both the surface density and the velocity dispersion profile. However, the parameters describing the visible content of dSphs, i.e., core radius r_c and velocity dispersion profile σ, are in all cases studied in detail inconsistent with the mass-follows-light assumption inherent in this style of analysis (Kormendy & Freeman 2004). In the case here, where the approximately flat observed dispersion profile of Leo I requires that the stars orbit in a (dark matter) halo which extends to radii larger than the nominal tidal radius of the observed light distribution, this historical approach is inappropriate. Where sufficient data exist, two parameter dynamical models for spherical stellar systems (Pryor & Kormendy 1990; Kleyna et al. 2002), additionally accounting for velocity anisotropies and a dark matter component or non-parametric modeling schemes (Wang et al. 2005, Walker et al. 2006a) are progressively being applied to reproduce observed profiles, in particular out to large radii.

Where only limited data exist, sufficient to define a binned dispersion profile but insufficient to support a full dynamical analysis of the distribution function, an intermediate level of analysis is appropriate, and is applied here. We pursued a simple approach to obtain an estimate of the galaxy's mass and density profile by integrating Jeans' equation (Binney & Tremaine 1998, eqs. 4-54 ff.) first under the assumptions of an isotropic velocity distribution and spherical symmetry, and below considering anisotropic distribution functions, using smooth functional fits to represent the light distribution and dispersion profile of Leo I.

In the case of an isotropic velocity distribution, the Jeans equations give rise to the simple mass estimator

$$M(r) = -\frac{r^2}{G\nu}\left(\frac{\mathrm{d}\,(\nu\overline{v_r^2})}{\mathrm{d}\,r}\right), \tag{5.4}$$

where ν and $\overline{v_r^2}$ denote the deprojected, three dimensional light density distribution and radial velocity dispersions, respectively. Both these quantities are obtained via direct deprojection of the observed surface brightness, $I(r)$, and projected dispersion profile $\sigma(r)$ adopting a convenient functional form, which in this case is a Plummer model (Wilkinson et al. 2006a, after Binney & Tremaine 1987). In this case, the surface brightness and associated, deprojected 3D profiles read

$$\begin{aligned} I(r) &= \frac{I_0\,a^4}{(a^2\,+\,r^2)^2}, \\ \nu(r) &= \frac{3\,I_0\,a^4}{4\,(a^2\,+\,r^2)^{5/2}}. \end{aligned} \tag{5.5}$$

The surface brightness profile of Leo I, which we adopted from Irwin & Hatzidimitriou (1995), is well fit by a Plummer model (left panel of Fig 7) with a scale radius a of $4\overset{\prime}{.}6$, which also nicely accounts for objects near the nominal tidal radius at $12\overset{\prime}{.}6$. Since the observed velocity dispersion profile, on the other hand, appears to be consistent with being flat, we fit this component with a Plummer profile with a large scale radius of $74'$ to ensure a flat shape throughout the observed radius (right panels of Fig. 5.8).

However, as Fig. 5.6 indicates, this argument is slightly sensitive to the value of the outer bin, which may give rise to a fall-off in the profile. Hence, we also chose a Plummer profile with a smaller radius ($36'$), which fits the observations best. In either case, the central value of the velocity dispersion σ_0 was determined as $9.8\,\mathrm{km\,s^{-1}}$. These values hold only for the combined GMOS + DEIMOS sample. The inclusion of M98's data leads to a decreased central velocity dispersion and consequently yields a lower central density ρ_0. The resulting density profiles in Fig. 5.9 fall off faster in the case that Leo I has a falling dispersion profile. Either density profile reaches a r^{-1} slope at $\sim 3'$, but under the assumption of a flat velocity dispersion the density converges to the r^{-2}-law (linearly rising mass), whereas it tends to be consistent with a $r^{-2.5\ldots-3}$ behavior towards the nominal tidal radius for the falling dispersion profile.

As discussed above our data suggest a rising feature in our velocity dispersion profile at approximately $3'$. Although it has been shown above that this is not a statistically-significant localized structure, it may be physically real, and so provide useful constraints on the dark-matter mass distribution in Leo I. Consequently, we consider this particular shape by fitting the dispersion profile with an additional asymmetric Gaussian component of the form $\sigma_{bump} \propto 10^{-\alpha\,r} \times \exp\left(-10^{(r-\mu)/p}\right)$ overlaid on the Plummer profiles. The free parameters α, μ and p are then determined in a least-squares sense. Using this best-fit representation in the dynamical calculations results in an unphysical behaviour in the resulting mass profile, i.e., a drop in the cumulative mass and the density profile at the location of the bump (left panels of Fig. 5.9). This is attributed to a too steep rise in the additional component as opposed to the smooth decline towards larger radii. Hence, the associated gradient, which enters the Jeans' equation, overwhelms the gradient of the declining portion in the dispersion and light profiles leading to a negative contribution in the derived mass profile. We note that varying the parameters of the Gaussian peak, retaining consistency with the GMOS + DEIMOS profile, does not remove this inconsistency. Conversely, a comparable fit to the GMOS + DEIMOS + M98 data does not exhibit this unphysical outcome, since for the respective best-fit profile the gradient in the innermost regions does not counteract the gradient of the more gradually declining profile at larger

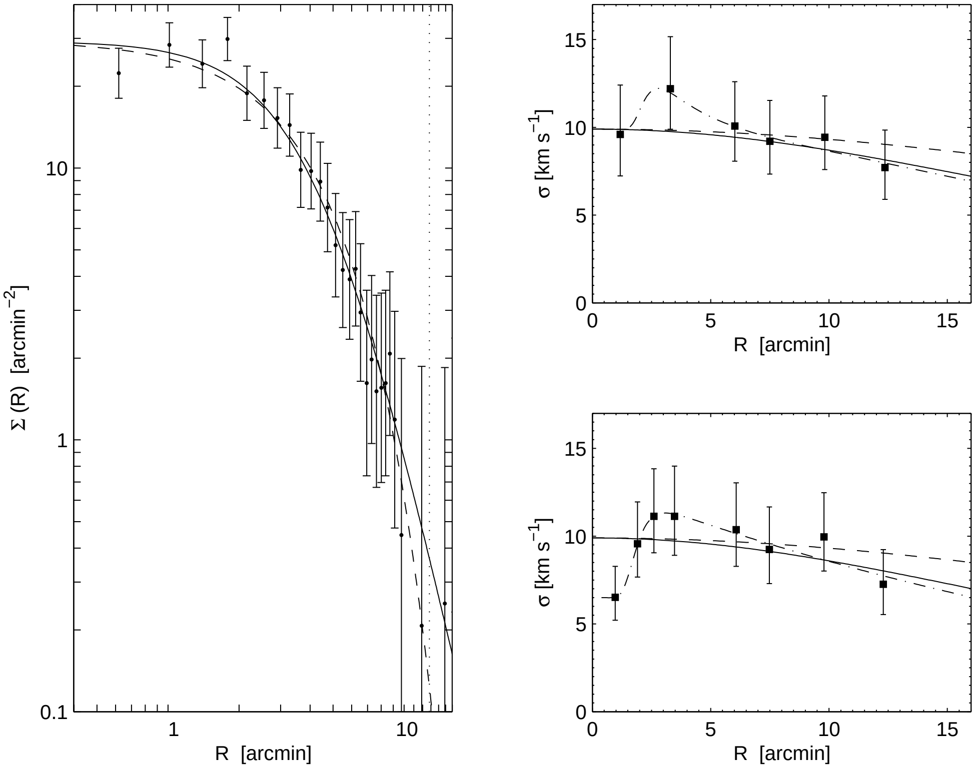

Figure 5.8: Left panel: Surface brightness profile of Leo I from Irwin & Hatzidimitriou (1995) together with the fit of a Plummer law (solid line) and an exponential fit (dashed). The upper right panel shows fits to the dispersion profiles from the GMOS plus DEIMOS sample, and the analogon after inclusion of M98's data is displayed in the lower right panel. Overplotted are fits of Plummer laws with different scale radii such as to reproduce a close-to flat (dashed line) or falling (solid) profile and also to incorporate the bump at $3'$ (dash-dotted).

radii. We conclude that the failure of such a basic functional approach to simultaneously yield a physically expedient representation of all profiles considered suggests that we in fact do not see a real substructure. If, on the other hand, the dispersion profile could be modeled sufficiently well in either case and the radial feature was assumed to reflect a real structure, its particular shape would result in a close to uniform density profile at central radii. This would be indicative of a central core in Leo I. We will explore the plausibility of cored mass profiles in the next Section.

The upper and lower mass- and central density limits were finally derived by determining a profile that reproduced the observed velocity dispersion profile within the measurement uncertainties on either side. An estimate of Leo I's mass thus yields $M_{tot} = (8 \pm 2) \times 10^7\,M_\odot$ enclosed within the King radius of $12\overset{\prime}{.}6$, corresponding to 0.9 kpc at the distance of Leo I. The exact values depend on the choice of the formal representation of the line-of-sight velocity dispersion profile and are detailed in Table 5.3. Similarly, the central density is found to be $\rho_0 = (2.8 \pm 0.8) \times 10^8\,M_\odot$ kpc^{-3}, which is, in the light of the measurement uncertainties, consistent with the value of $(3.4 \pm 0.9) \times 10^8\,M_\odot$ kpc^{-3} obtained by M98 from single-component King fitting. The available dynamical mass estimates for dSphs yield total masses out to the radial limits of the respective kinematic data in the range of 3–8 $\times 10^7\,M_\odot$ (e.g, Mateo 1998, Wilkinson

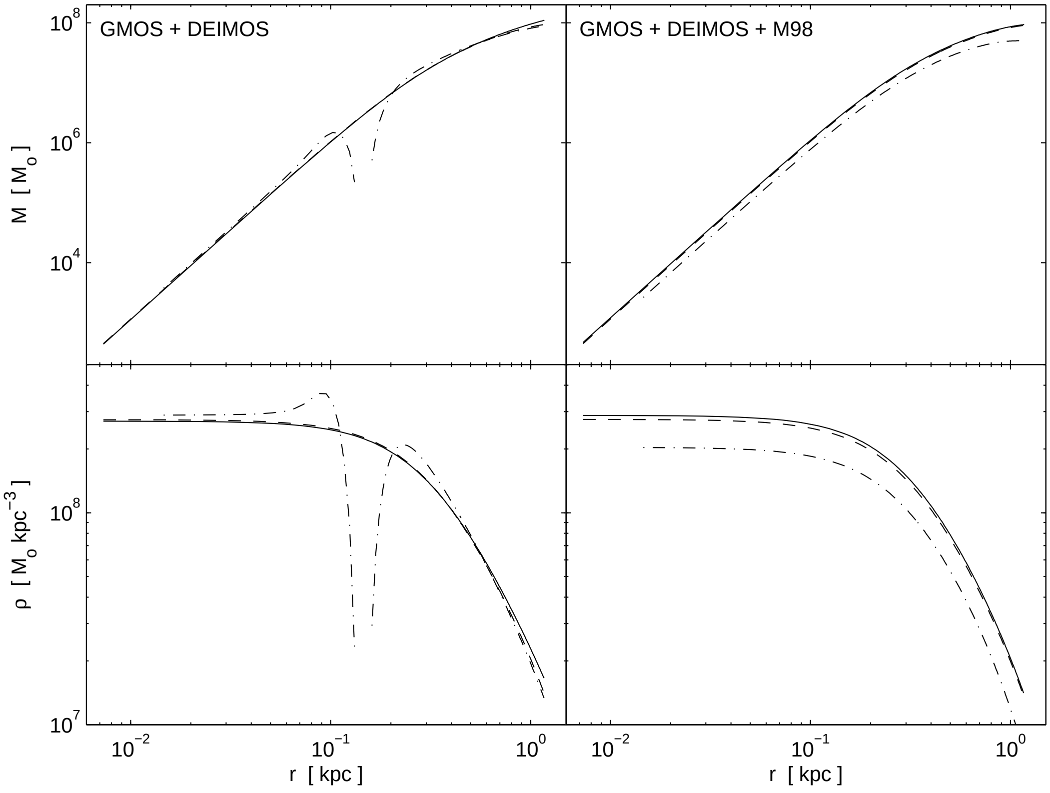

Figure 5.9: Mass (upper panel) and density (lower panel) estimates from Jeans equation, assuming an isotropic velocity distribution. The left panels each refer to the GMOS + DEIMOS sample, whereas the right panels additionally account for the M98 data set. Different line types signify different approaches to fit the observed dispersion profile (see Fig. 5.9). The unphysical drop in the profiles of the left panels is due to the inclusion of an additional peak in the best-fit velocity dispersion profile, which exhibits a steep rising gradient in the inner regions opposed to a slower decline of the underlying Plummer profiles. These counteracting gradients are not as distinct after inclusion of the M98 sample so that the right panels do not display this drop.

et al. 2004; Kleyna et al. 2004; Chapman et al. 2005; Walker et al. 2006a; Wilkinson et al. 2006a). This places Leo I in the upper range of known LG dSph masses. Adopting a total luminosity of $L = (3.4 \pm 1.1) \times 10^6 \, L_\odot$ (Irwin & Hatzidimitriou) we find an isotropic mass-to-light ratio of $(M/L)_{tot} = (24 \pm 6) \, (M/L)_\odot$ (see Table 5.3). This value is three times larger than the central value quoted by M98, who obtained their estimate based on analyses of the galaxy's core region and adopted a higher luminosity of $L = 4.9 \times 10^6 \, L_\odot$. If we adopt this latter value for L, we obtain a $(M/L)_{tot}$ of $17 \, (M/L)_\odot$

In Fig. 5.10 we plot the V-band mass to light ratios versus V-band luminosities of the known Galactic dSphs, including some of the recently discovered systems, like Ursa Major (Willman et al. 2005), plus two of the M 31 companions with published masses. In particular, we adopted mass estimates from Mateo (1998) for Leo II and Sculptor, whereas more recent measurements were used for the other satellites (Côté et al. 1999b for And II; Wilkinson et al. 2004 for UMi and Draco; Kleyna et al. 2006 for Ursa Major; Chapman et al. 2005 for And lX; Wilkinson et al. 2006a for Carina and Sextans, and Wang et al. 2005 for Fornax).

The idea that dSphs may be dominated by dark matter out to large radii raises the intriguing

Dispersion profile	Sample	$M[r < r_{tid}]$ $[10^7\,M_\odot]$	ρ_0 $[10^8\,M_\odot\,kpc^{-3}]$	(M/L_V) $[(M/L_V)_\odot]$
Flat		$8.7^{+1.6}_{-2.6}$	$2.7^{+0.6}_{-0.9}$	26^{+5}_{-8}
Falling	GMOS + DEIMOS	$8.0^{+2.7}_{-2.4}$	$2.8^{+0.9}_{-0.9}$	24^{+7}_{-6}
Peaked		$7.7^{+2.4}_{-1.6}$	$2.9^{+0.9}_{-0.6}$	23^{+7}_{-5}
Flat		$7.9^{+2.4}_{-1.0}$	$2.8^{+0.8}_{-0.4}$	23^{+7}_{-3}
Falling	GMOS + DEIMOS + M98	$7.8^{+2.4}_{-1.0}$	$2.8^{+0.8}_{-0.4}$	23^{+7}_{-3}
Peaked		$4.8^{+2.7}_{-1.8}$	$2.0^{+1.2}_{-0.8}$	14^{+8}_{-6}

Table 5.3: Mass and central density estimates.

question whether all these dwarf galaxies could be enclosed in comparable dark matter halos of similar total mass. In this case, they can be represented by the the simple relation

$$(M/L)_{tot} = (M/L)_* + M_{DM}/L, \tag{5.6}$$

where $(M/L)_*$ is the intrinsic mass-to-light ratio of the stellar component in the galaxy, M_{DM} denotes the mass of the dark matter halo and L is the integrated luminosity in the V-band (M98; Wilkinson et al. 2006a). It is realistic to assume that the (M/L)-ratio of the the luminous component in dSphs is of the order of the mean value observed in low-concentration globular clusters, which are characterised by low values implying no dark matter (Pryor et al. 1989; Moore 1996; Dubath & Grillmair 1997; M98; Baumgardt et al. 2005). We do not correct the observed M/L-ratios for the (small) effects of stellar evolution, accounting for each individual dSph's SFHs. Thus we set $(M/L)_* = 1.5\,(M/L)_\odot$. As the best fit dashed line in Fig. 5.10 implies, the observed dSphs scatter around this expected relation for a population of luminous objects that are embedded in a dark halo with a common mass scale of the order of $3 \times 10^7\,M_\odot$. Considering the generally large scatter in such a (M/L)-M_V-diagram, Leo I fits well into the global picture and apparently is governed by the same uniform dark halo properties. It is hence worth noticing that the narrow range of dSph velocity dispersions of 6–10 km s^{-1}, combined with their rather similar physical length scales, can generally be interpreted in terms of a common mass scale so that this kinematical piece of information can reliably be used as a proxy for an overall underlying mass distribution (see also Wilkinson et al. 2006a).

5.7 Velocity anisotropy

The mass estimates derived above are based on the assumption of an isotropic velocity distribution, i.e., the velocity anisotropy parameter $\beta = 1 - \langle v_\theta^2 \rangle / \langle v_r^2 \rangle$ was assumed to be zero. However, most of the kinematic studies of dSphs have revealed that a non-negligible amount of anisotropy is required to account for the shapes of the galaxies, and the observed dispersion profiles (Łokas 2001, 2002; Kleyna et al. 2002; Wilkinson et al. 2004). Since the neglect of a non-zero anisotropy has the effect of under- or overestimating the dark halo mass, we also shall consider this problem by solving the Jeans equation

$$\frac{\mathrm{d}\,(\nu \overline{v_r^2})}{\mathrm{d}\,r} + 2\beta\,\frac{\nu \overline{v_r^2}}{r} = -\nu\,\frac{\mathrm{d}\,\Phi}{\mathrm{d}\,r} \tag{5.7}$$

for a varying β. Here, ν and $\overline{v_r^2}$ denote again the 3-dimensional light and dispersion profiles, and Φ is the gravitational potential associated with the underlying mass distribution $M(r)$. The actual

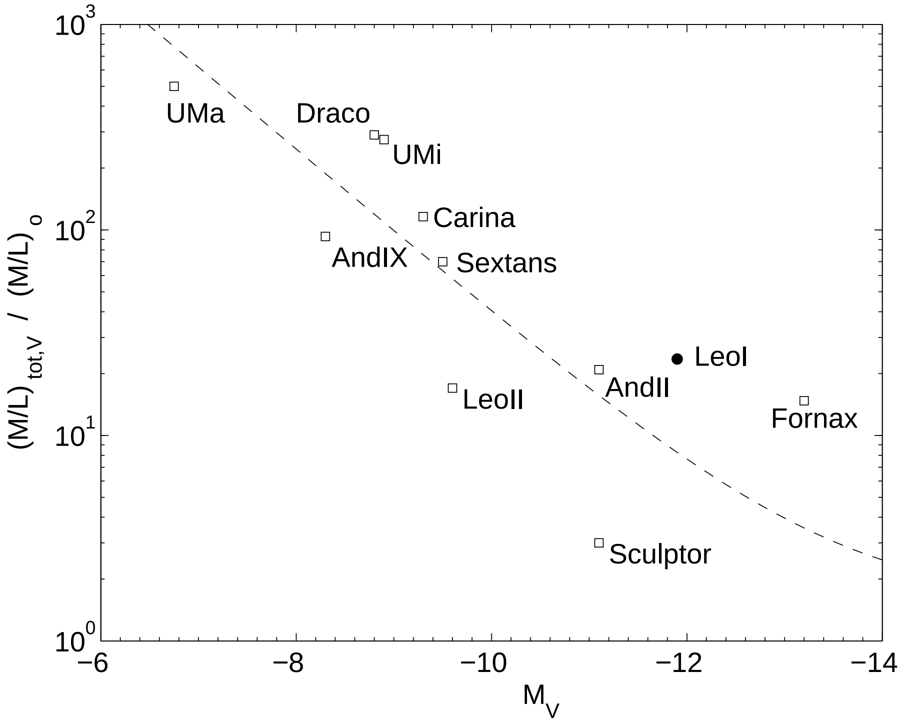

Figure 5.10: Mass-to-light ratios for LG dSphs (after Wilkinson et al. 2006). The most recent individual mass estimates are from the sources cited in the text. The dashed line assumes a stellar $(M/L)_V$ of 1.5 in solar units and a dark matter component of $3.3\times10^7 M_\odot$.

observable quantity, the line-of-sight velocity dispersion σ, is then obtained by direct integration along the line of sight, and under the constraints $\rho\,\overline{v_r^2} \rightarrow 0$ for $r \rightarrow \infty$ and $\beta =$const. This gives rises to the one-dimensional expression

$$\begin{aligned} \sigma^2(R) \;=\; & \frac{2G}{I(R)} \int_R^\infty \quad \mathrm{d}x \quad \nu(x)\, M(x)\, x^{2\beta-2} \\ & \times \int_R^x \quad \mathrm{d}y \quad \left(1-\beta\,\frac{R^2}{y^2}\right)\, \frac{y^{-2\beta+1}}{\sqrt{y^2-R^2}} \end{aligned} \tag{5.8}$$

(Binney & Mamon 1982; Łokas & Mamon 2003; Wilkinson et al. 2004). By adopting analytical prescriptions for the involved functions, one can then proceed to derive σ numerically.

In concordance with the previous section, we chose to describe Leo I's surface brightness profile $I(R)$ and the associated 3D-deprojection with a Plummer-profile using the best-fit parameters to the observations. We then use two different representations of the mass profile $M(r)$, which enters this formalism, spanning the range of plausible mass distributions.

5.7.1 NFW halo mass distribution

Based on high-resolution cosmological simulations, Navarro, Frenk & White (1995, hereinafter NFW) demonstrated that the density profiles of dark matter halos are well fit by a simple function with a single free parameter, the characteristic density. This solution has been applied to a wide range of masses, ranging from galaxy clusters to small scales such as the cosmological dark matter halos associated with the dSphs. Upon transformation of the variables, the density profile corresponds to a mass profile of the form

$$\frac{M(s)}{M_v} = g(c) \left\{ \ln(1+cs) - \frac{cs}{1+cs} \right\}, \tag{5.9}$$

where $s = r/r_v$ denotes the projected distance in units of the virial radius and M_v is the mass enclosed within the virial radius. The latter is generally identified with the total mass of the halo. Finally, the concentration parameter c is used to describe the shape of the profile and defines the amplitude function

$$g(c) = [\ln(1+c) - c/(1+c)]^{-1}. \tag{5.10}$$

For a detailed discussion of these parametrizations and the model, we refer the reader to NFW or Łokas & Mamon (2001). Since the NFW-profile has the unphysical disadvantage of diverging at large radii, it is convenient to consider only radii within a certain cut-off radius. We follow long-standing practice and assume this cut-off to coincide with r_v; beyond this point, the overall density distribution becomes unreliable in most natural cases (e.g., Łokas & Mamon 2001).

The concentration c has been shown to scale with mass. Here we adopt an extrapolation of the formulae derived in the N-body simulations for ΛCDM cosmology of Jing & Suto (2000) to the small masses of dwarf galaxies. Hence,

$$c = 10.23 \left(\frac{h\, M_v}{10^{12}\, M_\odot} \right)^{-0.088}, \tag{5.11}$$

where h denotes the Hubble constant in units of $100\,\mathrm{km\,s^{-1}\,Mpc^{-1}}$. In concordance with current cosmological results, we will use h=0.7 for the remainder of this work. Likewise, the virial radius relates to the virial mass as

$$r_v = 206 \left(\frac{M_v}{10^{12}\, M_\odot} \right)^{1/3} \quad [kpc] \tag{5.12}$$

This leaves M_v and the anisotropy β (assumed constant) as the only free parameters to be determined in a fit of the NFW model profile to the observations.

As Fig. 5.11 (left panel) implies, none of the values for the anisotropy which we have considered yields an adequate fit of the overall dispersion profile.

It rather appears that a progressively radial anisotropy is needed to explain the observations at larger radii, whereas the inner parts of the velocity dispersion are best represented by an isotropic velocity tensor. It is worth noticing that the innermost bin, with a smaller value for the dispersion in the sample after inclusion of the M98 data points, may suggest the presence of some tangential anisotropy in the innermost regions. However, based on the observations, the β is unlikely to fall below -0.5. For the four different β curves that we tested (i.e., -0.5, 0, 0.5 and 1), we obtained reduced χ^2 values of (0.2, 0.16, 0.22, 0.78). The final best fit in terms of a minimized χ^2 was achieved for $\beta = 0.05$ so that the overall profiles are in agreement with an isotropic velocity distribution. The resultant best-fit total virial mass is $M_v = 1.0 \times 10^9\, M_\odot$. Furthermore, the mass within the nominal observed tidal radius amounts to $7.7 \times 10^7\, M_\odot$. It is, unsurprisingly given the near-isotropic distribution deduced, in good agreement with the value obtained under the assumption of a purely isotropic velocity distribution.

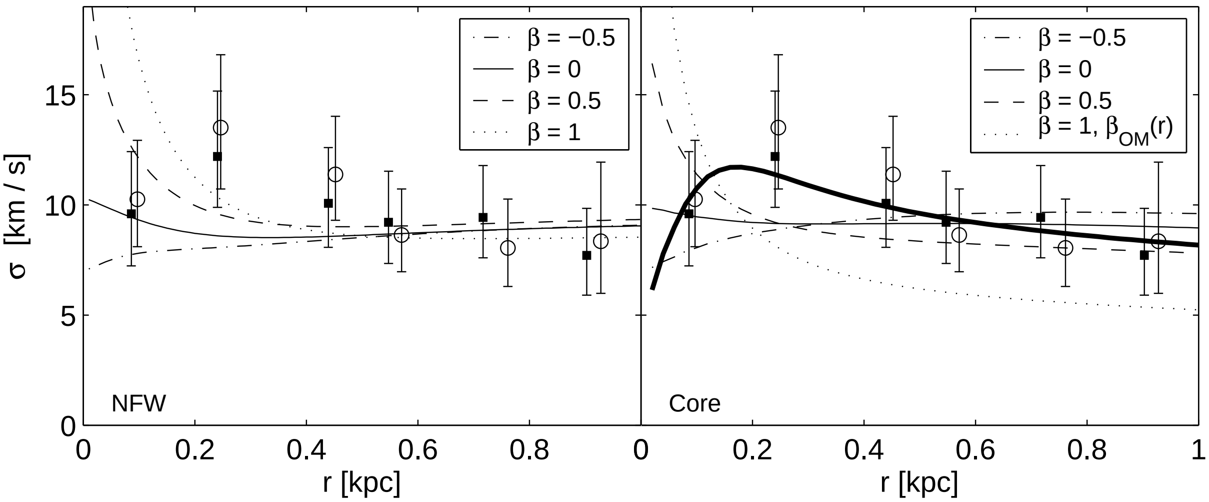

Figure 5.11: Predicted velocity dispersion profiles with varying degree of anisotropy (β) for two different halo density profiles, namely, cuspy ("NFW", top panel) and a cored halo (bottom panel). The inner regions are consistent with isotropic orbits, whereas the outer regions do not rule out a certain amount of radial anisotropy. The lower panel also contains a curve for the case of a radial varying anisotropy parameter, $\beta_{\rm OM}$, after Osipkov (1979) and Merrit (1985), which represents our data reasonably well.

5.7.2 Cored halo profile

The density profile that we obtained under the assumption of velocity isotropy appears to be indicative of a flat, close to uniform density core at small radii (see bottom panels of Fig. 5.9). In conjunction with the observational indications of cored density profiles in low-luminosity galaxies and in particular in some of the dSphs (Łokas 2002; Kleyna et al. 2003; Strigari et al. 2006; Wilkinson et al. 2006a) this prompted us to also build in this particular density distribution in our calculations of Leo I's dispersion profile (eq. 5.7). We parameterize the cored density profile in terms of a generalized Hernquist profile (Hernquist 1990; Zhao 1996; Read & Gilmore 2005) as

$$\rho(r) \,=\, C\left(\frac{r}{r_s}\right)^{-\gamma}\left[1+\left(\frac{r}{r_s}\right)^{\alpha}\right]^{(\gamma-3)/\alpha} \tag{5.13}$$

where C is a normalization constant, r_s is a scale radius, γ is the log-slope of the density profile within r_s and α determines the smoothness of the transition towards the density profile at larger radii. The case of $\alpha \equiv 1$ has often been discussed and fit to dispersion profiles in the literature, since it allows one to envisage a broad class of dark matter halo representations (Jing & Suto 2000; Łokas 2002). A slope of $\gamma > 0$ then corresponds to the cuspy halos, where NFW-like profiles as discussed above are represented by $\gamma = 1$. The opposing class of models with a cored halo is realized by $\gamma = 0$.

It turns out that a least squares fit under the constraint $\alpha = 1$, yields an unsatisfactory representation of our observations. Thus we chose to use the profile according to eq. 5.13 in our fits, leaving C, r_s, α and γ as free parameters. The resulting parameters of $r_s = 0.3\,\text{kpc}$, $\alpha = 1.6$ and $\gamma = 0$ improved the reduced χ^2 from 55 (3-parameter fit) to 13 (4 parameters). It is worth noticing that indeed the best fit was obtained for a pure core profile ($\gamma \equiv 0$). Fig. 5.11 (right panel) displays the resulting radial velocity dispersion profiles for varying degrees of (constant) anisotropy.

As for the case of the cuspy dark halo treated above, we find that our observed velocity dispersion is broadly consistent with an isotropic velocity distribution, where the best fit yielded a β of 0.05. Still, the observations allow for a wider range in the anisotropy, from -0.5 to 0.5. In this context, a slight amount of tangential anisotropy can account for the shape of the profile toward the inner regions, whereas significant radial anisotropy is ruled out at all radii. The values for the associated reduced χ^2 statistics for the cored halo are (0.39, 0.25, 0.40, 1.94) for respective β values of $(-0.5, 0, 0.5, 1)$.

Finally, we also adopted a radially varying anisotropy in our calculations, where we parameterized β according to the traditional prescriptions by Osipkov (1979) and Merrit (1985) as $\beta_{\rm OM}(r) = r^2/(r^2 + r_a^2)$, where r_a denotes the anisotropy radius, at which the transition from isotropic to radial orbits occurs (see also Łokas 2002). Under the assumption of a cored density profile and this particular $\beta(r)$, we can fit our observed line-of-sight velocity dispersion profile fairly well (see the thick solid line in Fig. 5.11, right panel). The best-fit (at a χ^2 of 0.02) is then obtained for an anisotropy radius of $r_a = 0.13\,{\rm kpc}$. In particular, the resulting curve is able to account for the observed raising shape of the profile discussed in Sect. 5.2, albeit by requiring a considerable amount of radial anisotropy at relatively small radii.

In concluding we note that the enclosed mass within the tidal radius amounts to $8.5\times10^7\,M_\odot$ under the assumption of a cored halo in Leo I. This value is larger than under the assumption of a NFW-like mass distribution, but still in agreement with the numbers derived from the Jeans equations above.

5.8 The Metallicity of Leo I

The observed wavelength region in the near-infrared and our spectral resolution, coupled with the S/N of our observations also enabled us to get an estimate of the red giants' metallicities from the equivalent widths (EWs) of the Ca triplet (CaT). This procedure succeeded for 58 of the radial velocity member stars targeted with GMOS, all of which lie well within the nominal tidal radius. For the remainder of our targets, the S/N did not allow us to reliably measure EWs, where a lower limit for these measurements was S/N$\sim$ 10.

5.8.1 Calibration of the metallicity scale

The prominent Ca II feature may be calibrated onto global metallicities since the linestrength is a linear function of metallicity for red giants. By defining a reduced width W', which accounts for the luminosity difference between the targeted star and the horizontal branch (HB) of the system, one can effectively remove any dependence on stellar gravity, effective temperature, and distance. Thus, the CaT has become a well defined calibrator for assessing the metallicity for old, globular cluster-like populations (Armandroff & Da Costa 1990, Rutledge et al. 1997a,b). Consequently, the derived line widths are generally calibrated onto reference scales for globular clusters of known metallicities (Zinn & West 1984; Carretta & Gratton 1997; Kraft & Ivans 2003). Leo I has a prominent old population (e.g., Held et al. 2000), but its dominant populations are of intermediate age (e.g., Gallart et al. 1999a,b). Nonetheless, we can still apply the CaT technique, since Cole et al. (2004) have extended its calibration to younger ages. These authors demonstrated that the CaT technique can be used within an age range from 2.5 to 13 Gyr and for a metallicity range spanning $-2 <$ [Fe/H] < -0.2. Since our Leo I observations aimed primarily at measuring accurate radial velocities, we did not target any globular clusters, which could have been used as calibration standards for the CaT technique. Hence, we had to rely on standard calibrations devised in the literature. Following long standing practice, we employed the definition of Rutledge et al. (1997a, hereafter R97a) for the linestrength of the CaT as the weighted sum of the EWs, giving lower weight to the weaker lines:

$$\Sigma W \;=\; 0.5\,W_{8498} \;+\; W_{8542} \;+\; 0.6\,W_{8662}. \tag{5.14}$$

For a few of the spectra the Ca line at 8498Å was too weak to be accurately measured or was hampered by a too low S/N over the respective bandpass. In this case we used the high S/N spectral measurements of a sample of Galactic globular clusters from Koch et al. (2006):

$$\Sigma W \;=\; 1.13\,(W_{8542} \;+\; 0.6\,W_{8662}) \;+\; 0.04. \tag{5.15}$$

This relation was applied to the low-quality spectra where only the two strongest lines had S/N>10. R97a defined the reduced width as

$$W' \;\;=\;\; \Sigma W + 0.64\,(\pm 0.02)\,(V - V_{HB})\,,$$

where ΣW denotes the CaT linestrength and V_{HB} is the magnitude of the horizontal branch of Leo I. For Leo I, the HB luminosity is (22.60 ± 0.12) mag according Held et al. (2001), who measured it based on this galaxy's RR Lyrae population.

The final calibration of the reduced width in terms of stellar metallicity is then obtained via the linear relation

$$[Fe/H]_{CG} \;\;=\;\; -2.66\,(\pm 0.08) + 0.42\,(\pm 0.02) W'$$

(Rutledge et al. 1997b), where we chose to tie our observations to the reference scale of Carretta & Gratton 1997, hereafter CG97) unless stated otherwise.

The EWs of the calcium lines were determined in analogy to the methods described in Koch et al. (2006), i.e., by fitting a Gaussian plus a Lorentzian profile across the bandpasses defined in Armandroff & Zinn (1990) and summing up the flux in the theoretical profile. The median formal measurement uncertainty achieved in this way, incorporating EW measurement and calibration errors, is 0.12 dex. However, we note that the intrinsic accuracy of the CaT based metallicity measurements may be significantly lower, e.g., due to incompatibilities in the [Ca/Fe] ratio between dSphs and the Galactic calibrators or variations in the HB level of a composite stellar system with both age and metallicity (see discussions in Bosler 2004; Koch et al. 2006).

5.8.2 Metallicity distribution

Fig. 5.12 shows the resulting histogram of our metallicity estimates. The MDF is clearly peaked at a metallicity of −1.31 dex on the scale of CG97 (−1.61 on the scale of Zinn & West 1984; hereafter ZW84). This value is in excellent agreement with the study of Bosler et al. (2004), who derived a CaT metallicity of −1.35 dex (CG97) for a sample of 41 red giants (note, however that the lack of any common targets between the studiesof Bosler [2004] and ours does not allow us to compare measurements of individual stars). Our results also agree well with the low-resolution studies of Suntzeff et al. (1986) and Lee et al. (1993), who obtained −1.8 (ZW84). Moreover they are consistent with the estimates from photometric analyses, which broadly agree on a mean metallicity around −1.6 dex (ZW84 scale; Demers et al. 1994; Bellazzini et al. 2004).

The formal $1\,\sigma$-width of the MDF is 0.25 dex. Taking into account a broadening due to the observational uncertainties, the intrinsic metallicity dispersion amounts to 0.22 dex. With a full

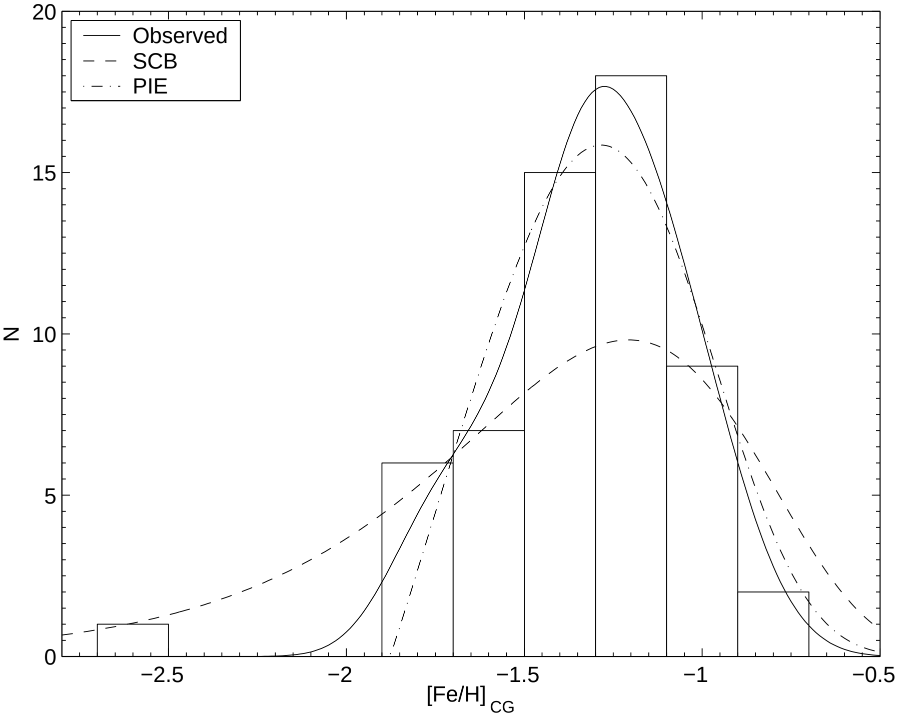

Figure 5.12: Metallicity distribution for the 58 GMOS radial velocity member stars, for which EWs could be measured. These were convolved by observational uncertainties to yield the solid curve. Overplotted are a modified simple closed-box model (SCB, dashed line) and a model using Prompt Initial Enrichment (PIE, dash-dotted line), scaled to the same number of stars.

range in $[Fe/H]_{CG97}$ of approximately one dex between −1.8 and −0.8 dex (note the most metal poor star, which we discuss below) we observe a smaller spread than is seen in a number of other dSphs (Shetrone, Côté, & Sargent 2001; Pont et al. 2004; Tolstoy et al. 2004; Koch et al. 2006), where the MDF may span more than 2 dex and exhibits a well populated metal poor tail. Leo I has been shown to exhibit a rather narrow RGB. By means of detailed modeling of Leo I's CMD and in particular of this narrow feature, Gallart et al. (1999a) suggested that this might be indicative of the absence of any significant chemical enrichment in this dSph. Clearly, the spectroscopic data show that this is not correct and that Leo I underwent considerable enrichment of at least 1 dex in total range.

There is one object in the sample, #774, for which we derived a CaT based metallicity of −2.61 dex. There is no evidence in the spectrum that the linestrength of this target has been underestimated, since its S/N of ∼45 allowed an accurate determination of the triplet's EWs (see Fig. 5.13)[3].

Although weak neutral metal lines around the CaT region do not show up clearly at our nominal spectral resolution and are thus mostly blended, there are still some additional absorption features discernible from the noise (see Fig. 5.13). Among these are for instance the distinct Fe I blend at ∼8514Å and a visible Fe I-line at ∼8689Å. Though clearly present in our stars

---

[3] We note that this metal poor regime was not sampled by the GCs in R97b so that the determination of such metallicities relies on an extrapolation of the existing calibrations.

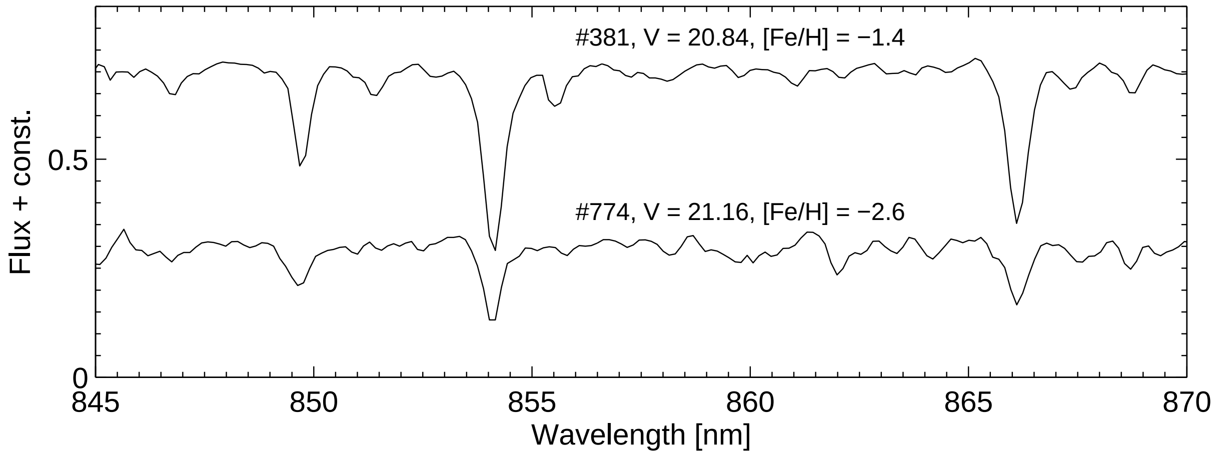

Figure 5.13: Spectra of the most metal poor star in our sample and a typical spectrum of a target around the peak metallicities. Apart from the three dominant Ca lines there are a few weak neutral metal lines detectable, which are not distinguishable from the continuum in the metal poorer target.

with highest metallicities, these features are hardly detectable in the continuum of the metal poor candidate. By assuming appropriate line bandpasses around these two iron features, we employed the same fitting technique as for the CaT described in Section 8.1 in order to derive a rough qualitative estimate of these lines' EWs in each of the stars, where possible. From this point of view, #774 is well consistent with being a rather metal poor object, in which these two EWs are practically governed by the continuum noise. Furthermore, its location well within the galactic boundary (2.5 core radii, 0.67 tidal radii, respectively), its consistency with the systemic velocity (99.9% confidence level) and the low interloper fraction around Leo I's radial velocity make it appear unlikely that this star is a contaminating foreground dwarf.

5.8.3 Radial gradients and implications for evolutionary models

In those dSphs of the Local Group, in which both old and intermediate-age stellar populations have been detected, the younger components often are more strongly centrally concentrated. In a number of dSphs with predominantly old populations, population gradients have been found in the sense that red HB stars are more centrally concentrated than blue HB stars (e.g., Da Costa et al. 1996; Hurley-Keller et al. 1999; Harbeck et al. 2001), a trend that is mirrored also by the presumably more metal-rich red giants. However, as also pointed out by Harbeck et al. (2001), this trend is not seen in *all* dSphs.

Since Leo I hosts dominant intermediate-age populations as well as old populations, one may expect that the more metal-rich and presumably younger stars should then also be more concentrated with respect to a spatially extended metal-poor population. Our data suggest, however, that the metal-rich and metal-poor components in our MDF are drawn from the same spatial distribution. This is reflected by the comparison of the cumulative radial distributions of the more metal-poor ([FeH] < 1.3 dex) versus the metal-rich ([FeH] ≥ 1.3 dex) populations in Fig. 5.14.

Via a K-S test we could underscore this lack of a radial metallicity gradient at the 93% confidence level. This finding is in concordance with the lack of a considerable population gradient in Leo I's CMD. As was reported by Held et al. (2000), both the old HB population and its numerous intermediate-age counterpart exhibit essentially the same spatial distribution (see also

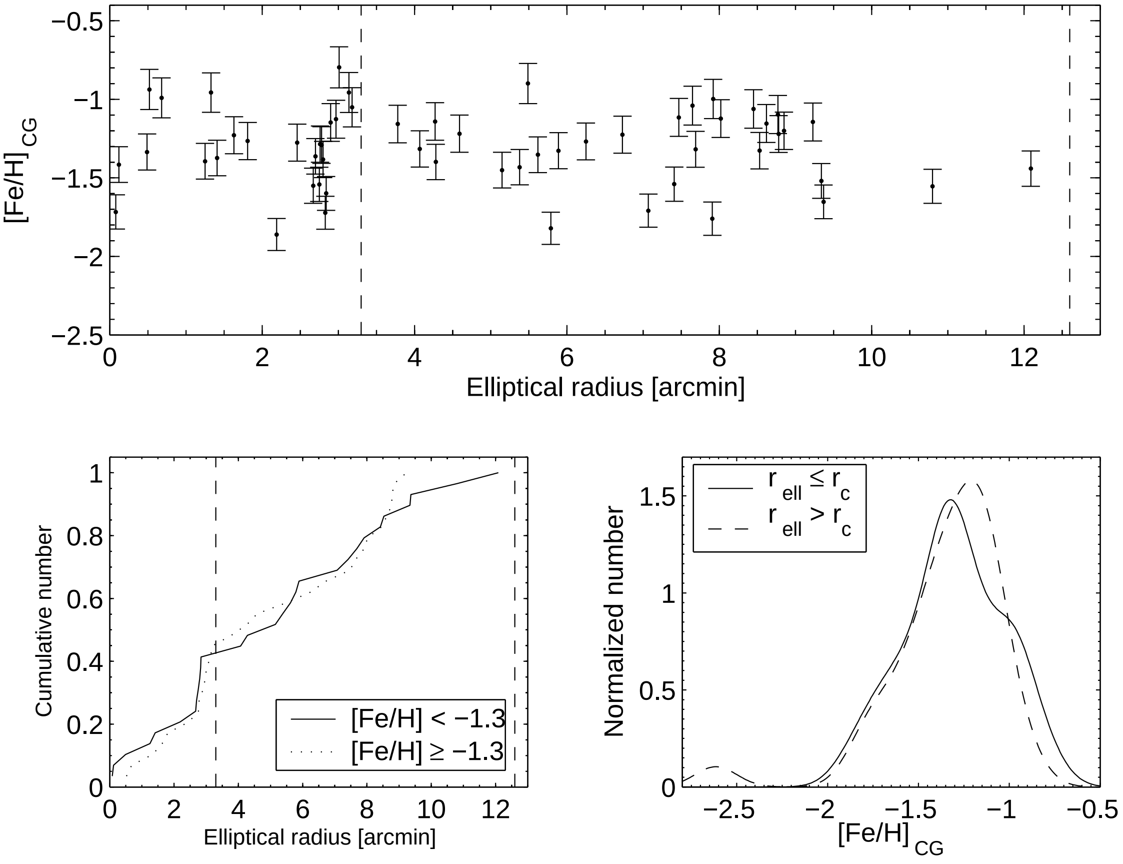

Figure 5.14: CaT metallicities of our radial velocity members vs. their elliptical radius (top). Nominal core and tidal radius are also denoted by vertical lines. The bottom left shows the cumulative number distribution versus radius of the metal richer component (solid line) and the metal poorer population (dotted line). These are practically indistinguishable. MDFs at different radii are displayed in the bottom right panel. These density distributions were convolved by individual measurement errors. No apparent trend of [Fe/H] with radius is discerned.

the right bottom panel of Fig. 5.14). In this respect, Leo I differs from other dSphs with prominent intermediate-age populations such as Carina (e.g., Harbeck et al. 2001; Koch et al. 2006), Fornax (Grebel 1997; Stetson et al. 1998), and Leo II (Bellazzini et al. 2005).

This behavior may indicate that Leo I's star formation occurred from a well mixed reservoir of gas that was little affected by local accretion of material or spatially localized outflows. In this vein, it was suggested by Held et al. (2000) that the size of this galaxy has not significantly changed and that it is unlikely to have undergone severe structural changes in the course of its evolution, i.e., since the first onset of star formation. In such a model one must assume that external effects such as tides, accretion or minor mergers may not have played a significant role in Leo I's history, neither kinematically nor chemically.

5.8.4 Comparison with simple chemical evolution models

Present-day chemical evolutionary models agree on the fact that dSphs are mainly controlled by low SF efficiencies compared to the solar neighborhood, and by strong galactic winds of the order ten times the SF rate (Lanfranchi & Matteucci 2004). For want of a detailed model prediction of Leo I's MDF from its SFH we follow long standing practice in applying basic models of chemical evolution to describe the observations (e.g., Pagel 1997, ch. 8), without employing any deeper nucleosynthetic or physical prescriptions. Such a more detailed modeling is left for future work.

In that spirit, Fig. 5.11 shows the predicted MDFs for two simple models of chemical evolution. To start with, we obtained a best-fit representation of a modified simple closed-box model allowing for outflows, which is exclusively parameterized by the effective yield $p_{\rm eff}$. Basically, this value is proportional to the true nucleosynthetic yield and takes into account effects of the loss of metals. Consequently, the mean metallicity is reduced to below the true yield by the same factor, which relates the outflows and the actual SF rate. A low yield of $0.06\,Z_{\odot}$ is well able to reproduce the metal poor mean location of the peak of the MDF, when compared to the solar neighborhood, which peaks at around -0.2 dex (Nordström et al. 2004 and references therein). However, this prediction tends to overestimate the number of stars below -1.8 dex (note that the most metal poor object in our sample was excluded from the fit), leading to the well-known G-dwarf problem. After allowing for an admixture of a non-zero initial metallicity (prompt initial enrichment, PIE), the overprediction toward the metal poor tail is reduced and it turns out that a pre-enrichment of $Z_0 = 0.013\,Z_{\odot}$ yields a remarkably good representation of the overall shape of the observed MDF. We refer the interested reader to Koch et al. (2006) for a discussion of these standard models.

5.9 Summary and Conclusions

We have obtained radial velocity measurements for 120 red giants in the Leo I dSph. These data not only increase existing samples by more than a factor of three, but also extend in radial distance beyond previous studies of the central regions of the galaxy (M98).

Although the weak velocity gradient that our data exhibit coincides with an apparent rotation about the observed minor axis of Leo I, the associated amplitude has been shown to be insignificant. Supplemented by Leo I's high radial velocity, which we confirmed, and its large distance from the Milky Way, Leo I most likely represents an isolated system, which is currently not affected by Galactic tides. This view is consistent with our detection of nine radial velocity members outside the nominal 'tidal' radius, and emphasises that a failure of the King-model functional fit to surface brightness data at some (outer) radius is not a dynamical proof of a physical effect. 'Tidal' radii, as typically derived from photometry, are labels, and are not proven to be related in any way to gravitational tides. The results of Sohn et al. (2006) indicate that Leo I's surface brightness profile exhibits multiple breaks at large radii, where it deviates from common King models. This argues in favor of the inappropriateness of using King models, but taken on its own says little else. Further, other recent photometric analyses do not provide any such clear evidence of photometric complexity above the noise level (V. Smolčić 2006, private communication). At its large present Galactocentric distance, tidal influences would be plausible only if Leo I's orbit were close to radial. However, our current data set does not allow us to constrain its proper motions and any information about its orbit will have to await future accurate proper motion measurements.

Our derived projected radial velocity dispersion profile is flat out to the nominal tidal radius, a result which is turning out to be a very common feature among the dSphs of the MW system, being established in numerous studies of large radial velocity samples out to and even beyond their nominal tidal radii (Mateo 1997; Kleyna et al. 2001, 2003, 2004; Łokas 2001, 2002; Wilkinson et al. 2004; 2006a,b; Muñoz et al. 2005; Walker et al. 2006a; Westfall et al. 2006). Coupled with the overall high (M/L) ratios, and lack of unambiguous evidence for non-equilibrium effects, the prime explanation of flat dispersion profiles is that dSphs are dark matter supported at all radii.

It turns out that the observed dispersion profiles are largely consistent with an isotropic velocity distribution, but non-negligible amounts of radial (tangential) anisotropy may be needed to account for the shape of the dispersion profile at the largest (smallest) distances.

An apparent rise in the velocity dispersion profile at nearly the core radius was demonstrated not to be a localized dynamical substructure in the galaxy. By using simple prescriptions to describe the shape of the observed velocity dispersion profile we obtain an estimate of the enclosed mass within the nominal 'tidal' radius of 900 pc of $\sim 8\times10^7 M_\odot$ under the assumption of velocity isotropy. Such a mass and the resultant high mass-to-light ratio of $\sim 24\,(M/L)_\odot$ are higher than previously derived values. From their (M/L) of $\sim 13\,(M/L)_\odot$, M98 concluded that Leo I contains a significant dark component. These estimates are in reassuringly good agreement with the values derived from light profiles obtained from high-quality photometric data under the assumption of an extended constant dark matter halo density (V. Smolčić 2006, private communication). Hence, our results strengthen this view and are in concordance with an extended dark matter distribution with a halo mass of a typical scale ($\sim 3\times10^7 M_\odot$), which is shared by the other dSphs of the LG.

By adopting a NFW density profile for Leo I, we estimate its total *virial* mass within its dark matter halo to be $\sim 1\times10^9 M_\odot$. The mass within the tidal radius is estimated to be $\sim 7.7\times10^7 M_\odot$. This does not change much under the assumption of a constant density core in Leo I, where the enclosed mass and best-fit anisotropy are consistent with the values from a cusped profile. Although the isotropically determined density profile indicates a flat central core, this scenario is not significantly preferred against the NFW case if one exclusively argues on the base of the velocity dispersion profile. In general, the shape of the observations seems to indicate that dark matter in fact dominates this dSph at large and small distances. We are aware that analysis only of a dispersion profile $\sigma(r)$ is not sufficient to derive a unique kinematical distribution function of a stellar system. Unless higher moments of the velocity distribution are considered, there remains a degeneracy between anisotropy and density, leading to identical line-of-sight dispersion profiles (e.g., Merrifield & Kent 1990; Łokas & Mamon 2003). While in general such an analysis requires more data than is currently available for Leo I, this will be pursued in future papers dealing with more detailed dynamical modeling (Wilkinson et al., in preparation).

We derived metallicities for 58 of the member stars from the well established CaT calibration. In compliance with previous estimates that were drawn from both photometric and low-number spectroscopic analyses we find a mildly metal poor mean of −1.31 dex (CG97 scale) and a full spread in metallicity covering 1 dex. This is noticeably smaller than the ranges found in dSphs with extended or complex SFHs (Grebel 1997; Pont et al. 2004; Tolstoy et al. 2004; Koch et al. 2006). This spread exceeds the predictions from CMD modeling if one accounts for the narrow RGB and Leo I's existing intermediate-age. Hence, there may be also a large range in ages present in Leo I, as insinuated by the presence of also an old population (Held et al. 2000, 2001) and the preliminary age determinations by Bosler et al. (2004). Practically all dSphs that contain significant intermediate-age populations do show a central concentration of their young components (Stetson et al. 1998; Harbeck et al. 2001; Bellazzini et al. 2005). Intriguingly, Leo I's prominently younger and presumably metal rich population does not exhibit this distinct population gradient, which is witnessed both by its stellar populations (Held et al. 2000) and in the metallicities derived here. In this respect, Leo I is rather unusual among these systems. This property may again point to a negligible role of external influences, such as localized accretion of material, in Leo I's evolution, allowing for good mixing of its gas. Since tides would affect this mixing, it is therefore possible that its current large distance from the MW may be representative for its whole evolution and that it presumably never approached the Galaxy very closely. This view is consistent with the finding, according to which the fraction of intermediate-age populations is closely related to the dSphs' Galactocentric distance. This behavior can be taken as indicative of an increased influence of (e.g., ram pressure) stripping close to the MW (van den Bergh 1994; Grebel 1997; Grebel et al. 2003) and will not have affected Leo I to a major extent. We identified one comparatively metal poor star in our sample, which is unlikely to be a foreground contaminant. With its likely [Fe/H] of $\sim\!-2.6$ (CG97 scale) it lies 0.8 dex below the metal poor tail of our observed MDF. It has been suggested that the explosion of only one massive pregalactic Population III star produces a sufficient amount of energy to expel the entire gas from the first (high-z) cosmological minihalos (Bromm et al. 2003). If the expelled gas falls back afterwards, the subsequently forming generation of stars, which we would observe as the most metal poor and the oldest stars in dSphs, should bear the chemical signature of these Population III stars (e.g., Beasley et al. 2003; Kawata et al. 2006). This makes metal-poor stars in dSph galaxies the prime targets for searches of the signatures of the first stars. However, no star with a metallicity below ~ -3 dex has been detected in a dSph so far (Fulbright, Rich & Castro 2004; Sadakane et al. 2004). The question, whether the lack of any such extremely metal poor objects in the current data is merely due to the low-number statistics of present-day observations, hence reflecting an incomplete sampling, or whether such objects generally do not exist in dSphs remains unsolved. Thus the presence of such a comparatively low metallicity object in our data provides an invaluable testing ground to study the early phases of general galactic evolution.

Acknowledgements These results have been submitted to the ApJ as *Koch et al.* in collaboration with Mark Wilkinson, Jan T. Kleyna, Gerard Gilmore, Eva K. Grebel, N. Wyn Evans, Dougal Mackey and Rosemary F.G. Wyse. I am particularly grateful to Jan Kleyna for providing me his DEIMOS data for this project and to Vernesa Smolčić for sharing her photometric results before publication.

Appendix 5.A
Target stars in Leo I

Table 5.A: Properties of targeted stars in Leo I.

ID^a	α	δ	I	V−I	r_{ell}	v_{HC}	$\delta\, v_{HC}$	R	S/N	$[Fe/H]_{CG}$	$\delta\,[Fe/H]_{CG}$
	(J2000)			[']		[km s^{-1}]					
103	10 08 28	12 18 51	17.77	1.43	0.68	290.52	3.99	59.78	50	−0.99	0.13
132	10 08 48	12 19 44	18.03	1.48	5.15	284.53	6.28	36.12	28	−1.45	0.11
137	10 08 27	12 20 31	17.93	1.56	2.80	295.27	5.33	43.99	40	−1.38	0.12
141	10 09 00	12 18 21	18.09	1.43	7.91	278.98	3.97	58.39	65	−1.76	0.11
143	10 08 32	12 18 34	18.10	1.32	1.18	295.45	14.29	14.10	6	...	...
195	10 08 39	12 17 21	18.28	1.35	3.18	271.78	4.05	54.44	23	−1.05	0.12
208	10 08 38	12 17 55	18.38	1.36	2.67	281.82	10.14	19.54	17	−1.55	0.11
229	10 08 29	12 19 44	18.22	1.46	1.81	312.35	4.08	61.16	32	−1.27	0.12
248	10 09 01	12 16 13	18.50	1.18	8.90	128.58	4.07	64.71	93	−1.81	0.10
251	10 09 05	12 20 11	18.40	1.38	9.34	288.32	3.97	52.86	41	−1.52	0.11
308	10 09 04	12 20 43	18.50	1.35	9.23	286.60	3.89	60.18	31	−1.14	0.12
329	10 08 28	12 18 42	18.47	1.39	0.52	286.10	3.82	62.92	21	−0.94	0.13
345	10 08 37	12 17 47	18.50	1.33	2.46	281.08	4.71	46.13	28	−1.28	0.12
351	10 08 36	12 20 13	18.53	1.39	3.14	295.54	5.11	43.80	39	−0.96	0.13
354	10 08 57	12 22 29	18.55	1.35	8.53	277.73	3.94	56.74	35	−1.33	0.12
360	10 09 00	12 15 49	18.56	1.39	8.85	268.09	4.45	54.28	54	−1.20	0.12
364	10 08 55	12 22 58	18.69	1.29	8.62	286.95	7.94	27.53	56	−1.15	0.12
381	10 08 49	12 18 01	18.66	1.29	5.38	291.22	4.98	45.35	39	−1.43	0.11
393	10 08 58	12 23 11	18.59	1.34	9.37	306.03	4.04	52.95	48	−1.65	0.11
426	10 08 39	12 18 12	18.75	1.28	2.78	270.52	3.34	70.74	12	−1.29	0.12
464	10 08 50	12 15 26	18.89	1.18	6.93	104.11	6.19	39.11	40	−1.49	0.11
512	10 08 48	12 21 29	18.86	1.25	6.25	270.35	4.54	47.65	29	−1.27	0.12
533	10 08 27	12 21 57	19.00	1.19	4.59	303.30	5.70	43.15	13	−1.22	0.12
568	10 08 48	12 16 15	19.02	1.29	5.89	293.85	4.41	56.75	20	−1.33	0.12
577	10 08 28	12 17 27	18.91	1.27	1.10	300.91	20.84	9.68	13	...	...
610	10 08 34	12 21 25	18.94	1.30	4.07	278.44	4.58	50.78	28	−1.32	0.12
616	10 08 39	12 18 54	19.06	1.13	2.97	300.95	6.47	33.99	27	−1.13	0.12
622	10 08 52	12 22 49	19.05	1.26	7.92	285.94	3.98	57.54	32	−1.00	0.12
653	10 08 53	12 20 38	19.07	1.23	6.73	274.34	4.84	50.80	28	−1.23	0.12
655	10 08 33	12 19 02	19.12	1.13	1.63	284.22	3.98	56.65	23	−1.23	0.12
662	10 08 51	12 18 14	19.17	1.15	5.79	281.08	5.37	39.69	41	−1.82	0.10
670	10 08 51	12 14 37	19.05	1.33	7.65	284.90	4.28	54.99	42	−1.04	0.12
674	10 08 52	12 20 21	19.30	1.11	6.28	4.37	5.00	47.53	15	−1.20	0.12
677	10 08 50	12 17 46	19.15	1.18	5.62	291.16	5.93	37.98	25	−1.35	0.11
692	10 08 38	12 17 37	19.09	1.21	2.88	264.46	9.12	23.45	16	...	...
697	10 08 37	12 19 51	19.21	1.14	2.90	270.26	4.84	49.62	23	−1.15	0.12
706	10 08 38	12 19 15	19.17	1.22	2.83	309.99	5.58	41.43	31	−1.72	0.10

Continued on next page

Table 5.A – *Leo I stars, continued*

ID^a	α	δ	I	V−I	r_{ell}	v_{HC}	$\delta\, v_{HC}$	R	S/N	$[Fe/H]_{CG}$	$\delta\,[Fe/H]_{CG}$
716	10 08 54	12 16 51	19.15	1.20	7.07	282.99	8.28	26.72	39	−1.71	0.11
717	10 08 58	12 21 01	19.21	1.18	8.02	287.68	3.71	59.73	39	−1.12	0.12
730	10 08 36	12 18 03	19.13	1.23	2.19	276.73	6.97	32.69	9	−1.86	0.10
752	10 08 48	12 20 31	19.21	1.20	5.49	304.53	5.64	43.03	25	−0.90	0.13
774	10 08 57	12 15 34	19.20	1.14	8.42	288.15	10.60	20.17	46	−2.61	0.09
778	10 08 51	12 23 34	19.27	1.16	8.45	297.28	5.11	41.89	28	−1.06	0.12
827	10 08 36	12 20 04	19.36	1.10	3.01	291.22	5.39	43.20	25	−0.80	0.13
833	10 08 57	12 17 20	19.25	1.23	7.41	302.48	4.74	48.84	39	−1.54	0.11
838	10 08 37	12 17 09	19.28	1.09	2.84	270.62	5.09	37.49	13	−1.60	0.11
846	10 08 39	12 18 26	19.36	1.09	2.75	284.48	6.95	29.76	22	−1.54	0.11
860	10 08 28	12 19 18	19.25	1.26	1.25	274.69	7.06	24.78	34	−1.39	0.11
869	10 08 35	12 21 05	19.34	1.13	3.78	295.38	4.65	43.59	16	−1.16	0.12
870	10 08 27	12 17 54	19.34	1.16	0.49	281.12	4.60	40.10	15	−1.34	0.11
938	10 09 01	12 16 43	19.29	1.29	8.77	295.44	3.64	71.24	58	−1.10	0.12
992	10 08 28	12 19 26	19.44	1.18	1.41	293.61	7.68	25.45	6	−1.37	0.11
1003	10 08 52	12 13 43	19.33	1.26	8.78	271.00	4.28	52.74	37	−1.22	0.12
1013	10 08 31	12 21 41	19.55	1.06	4.27	289.47	10.48	24.55	5	−1.14	0.12
1056	10 08 41	12 21 48	19.45	1.13	5.31	286.78	16.29	6.48	11	...	...
1072	10 08 39	12 19 26	19.58	1.07	2.99	250.76	4.96	45.71	30	−1.30	0.11
1074	10 08 34	12 21 33	19.55	1.13	4.28	305.64	5.97	37.04	11	−1.40	0.11
1086	10 09 03	12 21 34	19.54	1.07	9.30	272.04	9.05	17.19	33	...	...
1092	10 09 04	12 14 8	19.39	1.27	10.80	277.74	7.31	33.08	23	−1.55	0.11
1098	10 08 56	12 16 32	19.45	1.26	7.47	296.44	4.85	47.62	40	−1.12	0.12
1181	10 08 39	12 18 41	19.51	1.10	2.76	284.86	4.18	51.92	8	−1.29	0.12
1183	10 08 29	12 17 17	19.57	1.13	1.33	281.20	9.54	22.02	19	−0.96	0.13
1186	10 08 37	12 19 34	19.59	1.13	2.70	297.99	4.42	49.50	19	−1.36	0.11
1241	10 08 53	12 22 10	19.56	1.20	7.69	281.18	5.56	41.56	21	−1.32	0.11
13062	10 08 27	12 18 12	18.27	1.23	0.12	298.47	2.94	82.16	51	−1.42	0.11
13069	10 08 27	12 18 22	19.58	1.01	0.08	283.44	14.72	13.52	6	−1.72	0.11
16307	10 09 03	12 24 54	18.31	1.46	11.55	−34.30	5.85	36.54	32	−1.65	0.11
16308	10 09 08	12 24 19	18.50	1.34	12.09	286.47	5.26	40.83	40	−1.44	0.11
D1065	10 08 12	12 15 11	19.39	1.42	4.86	259.88	7.64	2.07	6	...	...
D1358	10 07 43	12 13 23	20.93	1.10	11.76	259.07	6.80	0.98	6	...	...
D1395	10 09 11	12 15 11	20.09	0.99	11.30	291.04	5.28	5.28	9	...	...
D1418	10 09 11	12 13 49	20.24	1.13	11.74	261.73	13.21	1.21	6	...	...
D3685	10 08 07	12 23 48	19.50	1.23	7.16	290.66	5.79	4.68	6	...	...
D3737	10 08 07	12 21 49	19.57	1.28	5.96	265.87	5.47	3.53	6	...	...
D3940	10 07 57	12 18 48	18.93	1.33	7.32	273.73	5.07	3.82	9	...	...
D4085	10 07 44	12 17 23	21.28	1.09	10.50	278.44	5.21	3.27	6	...	...
D5535	10 07 42	12 22 50	18.36	1.66	11.81	26.82	3.26	10.55	45	...	...
D5537	10 07 36	12 22 42	19.39	1.31	13.03	280.54	2.67	11.90	21	...	...
D5541	10 07 30	12 22 20	20.78	0.99	14.54	291.00	3.33	6.65	7	...	...
D5544	10 07 40	12 21 32	19.74	1.18	11.95	278.19	2.58	13.44	17	...	...
D5554	10 07 38	12 19 26	20.89	1.03	11.99	280.77	4.10	5.02	7	...	...
D5557	10 07 37	12 19 17	19.98	1.08	12.23	291.22	3.89	5.03	7	...	...
D5559	10 07 38	12 19 09	19.82	1.20	12.03	282.28	3.07	8.42	12	...	...
D5565	10 07 41	12 17 31	20.83	0.97	11.20	287.14	4.64	5.00	8	...	...
D5577	10 07 37	12 17 44	18.51	1.56	12.10	291.62	2.64	11.49	37	...	...
D5579	10 07 41	12 15 20	20.14	1.24	11.57	−49.67	3.95	8.70	9	...	...
D5583	10 07 28	12 14 30	20.64	1.16	14.87	290.32	4.58	4.16	5	...	...
D5588	10 07 38	12 13 10	20.41	1.08	13.06	286.43	3.91	6.55	9	...	...
D5591	10 07 34	12 12 43	19.07	1.41	14.06	287.18	2.65	10.63	26	...	...
D5597	10 07 30	12 11 44	20.43	1.08	15.48	324.22	6.02	1.72	8	...	...
D5885	10 09 18	12 16 44	19.45	1.30	12.60	289.11	3.83	7.05	13	...	...

Continued on next page

Table 5.A – *Leo I stars, continued*

ID^a	α	δ	I	V−I	r_{ell}	v_{HC}	$\delta\, v_{HC}$	R	S/N	$[Fe/H]_{CG}$	$\delta\,[Fe/H]_{CG}$
D5892	10 09 17	12 16 03	20.32	1.19	12.55	286.56	3.69	6.17	6	...	...
D6957	10 07 58	12 26 30	19.82	1.29	10.77	−47.89	11.90	0.86	6	...	...
D6963	10 07 59	12 25 01	19.00	1.31	9.44	−21.78	24.36	0.28	9	...	...
D6966	10 07 46	12 24 15	20.74	1.09	11.60	280.10	7.28	2.07	5	...	...
D6967	10 08 03	12 24 02	18.87	1.44	8.13	297.46	4.06	7.64	15	...	...
D6977	10 08 01	12 23 06	19.04	1.40	7.85	287.24	3.92	8.52	14	...	...
D6986	10 08 03	12 22 32	19.92	1.17	7.21	298.59	4.34	5.96	7	...	...
D7038	10 07 46	12 20 55	18.28	1.64	10.28	298.38	2.30	17.65	48	...	...
D7044	10 07 47	12 20 44	20.64	1.02	10.01	291.33	2.91	8.83	10	...	...
D7019	10 08 01	12 21 19	19.17	1.19	7.01	294.18	4.40	5.20	10	...	...
D7036	10 08 01	12 20 55	19.47	1.36	6.73	297.43	4.17	6.77	10	...	...
D7045	10 08 09	12 20 46	19.78	1.18	4.86	300.93	4.80	4.63	7	...	...
D7057	10 07 59	12 20 35	18.51	1.53	7.21	297.47	3.75	8.18	20	...	...
D7064	10 08 03	12 20 26	18.92	1.40	6.07	290.05	4.39	6.32	11	...	...
D7069	10 08 03	12 20 17	18.24	1.55	6.18	298.99	3.49	9.27	24	...	...
D7085	10 07 47	12 19 53	20.66	1.08	9.86	281.49	3.33	8.71	10	...	...
D7090	10 08 08	12 19 53	18.60	1.47	4.94	281.88	4.38	5.74	18	...	...
D7104	10 08 03	12 19 41	18.90	1.45	5.85	301.67	3.83	7.82	15	...	...
D7154	10 08 05	12 18 59	19.28	1.19	5.44	294.55	4.91	5.96	11	...	...
D7190	10 80 10	12 17 31	19.29	1.34	4.31	276.80	4.86	5.18	9	...	...
D7194	10 07 59	12 17 17	18.22	1.70	7.00	310.55	3.93	7.02	22	...	...
D7218	10 08 01	12 16 14	19.18	1.32	6.77	282.97	4.49	6.28	11	...	...
D7225	10 08 01	12 16 28	19.02	1.26	6.63	262.12	6.52	4.21	11	...	...
D7484	10 08 02	12 13 03	19.34	1.27	8.22	291.37	4.81	3.06	8	...	...
D7493	10 07 46	12 12 15	21.15	1.07	11.78	264.44	6.50	3.47	6	...	...
D8051	10 08 13	12 15 18	18.51	1.37	4.55	288.25	4.41	5.72	14	...	...
D8364	10 09 08	12 24 21	18.48	1.53	11.68	278.84	7.80	2.52	27	...	...
D8384	10 09 08	12 23 08	20.94	1.10	11.16	283.54	3.54	8.61	6	...	...
D8581	10 09 07	12 19 51	20.44	1.11	9.90	276.96	3.07	8.56	7	...	...
D8581	10 09 07	12 19 51	20.44	1.11	9.90	273.62	4.53	4.53	7	...	...
D8677	10 09 10	12 18 43	20.14	1.05	10.55	289.85	3.70	6.54	9	...	...
D8724	10 09 24	12 22 05	18.66	1.46	14.46	298.69	3.55	6.61	23	...	...
D8727	10 09 19	12 21 57	18.24	1.63	13.17	297.88	3.23	9.60	30	...	...
D8728	10 09 19	12 21 22	18.96	1.36	13.07	286.85	4.06	6.94	18	...	...
D8727	10 09 19	12 21 57	18.24	1.63	13.17	305.16	3.17	8.39	6	...	...
D8734	10 09 12	12 20 09	20.50	1.23	11.05	271.37	8.25	4.00	5	...	...
D8738	10 09 12	12 19 04	20.78	0.96	11.03	303.30	5.53	4.21	5	...	...

[a] Star IDs preceeded by a “D” refer to the stars targeted with DEIMOS.

Chapter 6

The Anisotropic Distribution of M 31 Satellite Galaxies: A Polar Great Plane of Early-Type Companions

> “ *What good are Mercator’s North Poles and Equators*
> *Tropics, Zones, and Meridian Lines?*
> *So the Bellman would cry, and the crew would reply*
> *‘They are merely conventional signs.’*”
> — LEWIS CARROLL, *The hunting of the snark.*

Abstract

The highly anisotropic distribution and apparent alignment of the Galactic satellites in polar great planes begs the question how common such distributions are. The satellite system of M31 is the only nearby system for which we currently have sufficiently accurate distances to study the three-dimensional satellite distribution. We present the spatial distribution of the 16 presently known M31 companions in a coordinate system that is centered on M 31 and aligned with its disk. Through a detailed statistical analysis we show that the full satellite sample describes a plane that is inclined by −56° with respect to the poles of M31 and that has an r.m.s. width of 100 kpc. With 88% the statistical significance of this plane is low and it is unlikely to have a physical meaning. We note that the great stellar stream found near Andromeda is inclined to this plane by 7°. Most of the M31 satellites are found within $< \pm 40^\circ$ of M31’s disk, i.e., there is little evidence for a Holmberg effect. If we confine our analysis to early-type dwarfs, we find a best-fit polar plane within 5° to 7° from the pole of M31. This polar great plane has a statistical significance of 99.3% and includes all dSphs (except for And II), M32, NGC 147, and PegDIG. The r.m.s. distance of these galaxies from the polar plane is 16 kpc. The nearby spiral M33 has a distance of only ~ 3 kpc from this plane, which points toward the M81 group. We discuss the anisotropic distribution of M31’s early-type companions in the framework of three scenarios, namely as remnants of the break-up of a larger progenitor, as tracer of a prolate dark matter halo, and as tracer of collapse along large-scale filaments. The first scenario requires that the break-up must have occurred at very early times and that the dwarfs continued to form stars thereafter to account for their stellar population content and luminosity-metallicity relation. The third scenario seems to be plausible especially when considering the apparent alignment of our potential satellite filament with several nearby groups. The current data do not permit us to rule out any of the scenarios. Orbit information is needed to test the physical reality of the polar plane and of the different scenarios in more detail.

6.1 Introduction

As discussed in Chapter 1, all of the Milky Way dSph satellites appear to be located on one or two great planes, which are unlikely to have occurred by chance. Several scenarios to explain such an anisotropy have been brought forth. These have been discussed in detail in Section 1.4 (see also Sect. 6.5). For instance, it was proposed that the Galactic satellites could be remnants of disrupted galaxies, which orbit the Milky Way on the great circles defined by their progenitors (e.g., Lynden-Bell 1976; Kunkel & Demers 1976; Kunkel 1979; Lynden-Bell 1982; Majewski 1994; Fusi Pecci et al. 1995; Kroupa, Theis, & Boily 2005). According to another plausible scenario the satellites can follow their host galaxy's dark matter distribution, which will lead to planar distributions as well (Hartwick 1996, 2000; Kang et al. 2005). In a third possible scenario it was suggested that satellites retain the alignment with the massive primary that they had when they first fell into the group or cluster along a filament (Knebe et al. 2004; Zentner et al. 2005; Libeskind et al. 2005). In this context, cold dark matter (CDM) hierarchical structure formation scenarios lead to highly anisotropic collapse along filaments, naturally resulting in planar configurations aligned with the major axis of the dark matter distribution. All these scenarios have one idea in common: They all suggest that the planar alignment reflects the plane of motion of the satellites.

One may then proceed and ask whether the Milky Way is exceptional in having its satellites located in one or two great planes. If such alignments are common, are they preferentially polar? If one or several of the the above scenarios hold, then similar great planes (possibly even polar great planes) should also be found for the satellite systems of other galaxies. The Holmberg effect in itself is not a sufficient criterion for the existence of polar planes since (with the exception of the Milky Way's surroundings) the observational evidence for it comes from the *projected* distribution of (often very few) satellites around distant primaries. Furthermore, there is some debate as to whether the Holmberg effect really exists (compare, e.g., Sales & Lambas 2004 and Brainerd 2005). If great planes generally exist, this would reveal the orbital planes of the satellite galaxies, it would help to elucidate the origin of the satellites, and could help to understand the accretion history of massive galaxies.

We can investigate these questions by turning to our next closest spiral, M31. M31 has a satellite system that covers the same range of distances as the Galactic satellites. Moreover, the distances of these satellites have been well-determined using mainly observations with the Hubble Space Telescope (HST). In particular, for the majority of these satellites heliocentric distances are available that were measured using a combination of several distance indicators such as the tip of the red giant branch and the horizontal branch, permitting one to derive deprojected distances of these dwarf galaxies from M31 with some confidence (see Grebel 2000 and Grebel et al. 2003, Table 1). This allows us to use the three-dimensional galaxy distribution and to search for possible planes.

M31 is surrounded by three dE galaxies and one dwarf-sized compact elliptical (cE; namely M32). It has at least seven dSph companions, four of which were only discovered and confirmed during the last few years (Armandroff, Davies, & Jacoby 1998, Armandroff, Jacoby, & Davies 1999; Karachentsev & Karachentseva 1999; Grebel & Guhathakurta 1999; Zucker et al. 2004a; Harbeck et al. 2005). Additional very faint satellites may yet to be uncovered. Furthermore, M31 contains one dIrr and dIrr/dSph galaxy within 300 kpc, and two more such dwarfs within a radius of 500 kpc. Altogether there are 13 satellites known within 300 kpc and 15 satellites within 500 kpc, whose spatial distribution can be investigated.

The first search for possible great planes in the distribution of M31 satellites was conducted by Grebel, Kolatt, & Brandner (1999), who at that time had primarily ground-based distance determinations at their disposal. They found that seven (possibly eight) out of 13 satellites appeared to lie within ±15° of a great plane around M31 with a probability for chance alignment of $\leq 5\%$. M33 seemed to lie near an extension of this plane. Grebel et al. (1999) saw little evidence for a Holmberg effect in the distribution of M31's companions.

In this Chapter we carry out a more sophisticated analysis using improved statistical tools and largely homogeneous HST distances wherever available. Distances derived from HST photometry are preferred owing to their superior seeing, resolution, and depth, and because often several distance indicators were combined in determining the distances.

6.2 The definition of a native M31 coordinate system

In order to determine the positions of the M31 satellites relative to M31, we define an absolute coordinate system (CS), which is anchored to the center of M31 and which has two of its vectors lying in the disk place of M31. Coordinates and distances were taken from Zucker et al. (2004a) and Harbeck et al. (2005) for And IX, and from Grebel et al. (2003) and Grebel (2000) for the remaining galaxies. First, each pair of J2000 equatorial coordinates (α, δ) was converted into Galactic longitude and latitude, (l, b), and from that three-dimensional Cartesian (x, y, z) positions relative to the Sun were calculated.

$$\begin{aligned} x &= D_{\odot} \cos b \cos l \\ y &= D_{\odot} \cos b \sin l \\ z &= D_{\odot} \sin b, \end{aligned} \tag{6.1}$$

where $D_{\odot}$ denotes the observed distances from the Sun (see Table 6.1). This right-handed CS (eqs. 6.1) is oriented such that x points towards the Galactic center and z indicates the height above the Galactic plane.

After applying a linear translation to move the origin of this CS to the center of M31, the CS is aligned with this galaxy by rotation around three angles. The first of these affine transformations incorporates the position angle (PA) of M31. Accounting for the inclination of the celestial against the Galactic pole and M 31's PA of $(37.7 \pm 0.2)\,^{\circ}$ (de Vaucouleurs 1958), we rotate the CS clockwise using a transpose rotation matrix around the y-axis[1], $R_y^T(p)$, by the angle $p = 115.17^{\circ}$. In the next step, the resulting CS is rotated around the new x-axis by inclination via the matrix $R_x^T(i)$, where we use the canonical value for the inclination of M31 of $i = -12.5^{\circ}$ (de Vaucouleurs 1959). In this notation, 90° signifies a face-on view. The minus sign arises since the matrices are defined for clockwise rotation. Finally, we rotate the resulting CS, which is now coplanar with the M 31 galactic plane, around its respective z-axis by 180° by means of $R_z^T(\pi)$. Thus consistent with common representations, our CS is oriented such that X_{M31} increases toward the southwest, Y_{M31} increases toward the northwest, and Z_{M31} points toward M 31's galactic pole.

The transformed Cartesian coordinates are thus determined from $(X_{M31}, Y_{M31}, Z_{M31})^T = R_z^T(\pi) \cdot R_x^T(i) \cdot R_y^T(p) \cdot (x, y, z)^T$. The expressions for the individual components read:

$$\begin{aligned} X_{M31} &= -x \cos p - z \sin p \\ Y_{M31} &= -y \cos i - x \sin i \sin p + z \sin i \cos p \\ Z_{M31} &= y \sin i - x \cos i \sin p + z \cos i \cos p. \end{aligned} \tag{6.2}$$

---

[1] Since we rotate the CS rather than the coordinates themselves, the transpose matrix has to be used.

Galaxy	Type	α (J2000)	δ (J2000)	$d_\odot$ [kpc]	X_{M31} [kpc]	Y_{M31} [kpc]	Z_{M31} [kpc]
M 31	Spiral	00 42 44	+41 16 09	773 ± 20	0.0	0.0	0.0
M 32	cE	00 42 42	+40 51 55	770 ± 40	4.7	4.0	0.1
NGC 205	dE	00 40 22	+41 41 07	830 ± 35	3.8	−55.3	16.0
And I	dSph	00 45 40	+38 02 28	790 ± 30	41.0	−0.5	24.7
And III	dSph	00 35 34	+36 29 52	760 ± 70	63.2	23.2	−7.2
NGC 147	dE	00 33 12	+48 30 29	755 ± 35	−85.5	−8.7	−52.4
And V	dSph	01 10 17	+47 37 41	810 ± 45	−104.2	−26.3	45.8
And II	dSph	01 16 30	+33 25 09	680 ± 25	42.2	144.9	53.5
NGC 185	dE	00 38 58	+48 20 12	620 ± 25	−89.3	121.6	−89.4
Cas dSph	dSph	23 26 31	+50 41 31	760 ± 70	−86.3	−50.5	−191.5
IC 10	dIrr	00 20 17	+59 18 14	660 ± 65	−200.0	70.7	−140.7
And VI	dSph	23 51 46	+24 34 57	775 ± 35	243.1	37.6	−100.5
LGS 3	dIrr/dSph	01 03 53	+21 53 05	620 ± 20	149.1	240.6	21.4
Peg DIG	dIrr/dSph	23 28 36	+14 44 35	760 ± 100	355.5	106.5	−174.5
IC 1613	dIrr	01 04 47	+02 07 02	715 ± 35	369.2	334.5	84.8
And IX	dSph	00 52 53	+43 12 00	790 ± 70	−31.6	−12.4	22.0
And X	dSph	00 58 00	+43 59 59	667 ± 30	−48.2	91.5	−37.0
M 33	Spiral	01 33 51	+30 39 37	847 ± 60	87.4	49.8	196.7
G 1	Globular cluster	00 32 47	+39 34 40	773 ± 20	29.4	−2.8	−17.4
B 327	Globular cluster	00 41 35	+41 14 55	773 ± 20	1.3	−0.9	−2.5

Table 6.1: Satellite sample. Coordinates and heliocentric distances from Rich et al. (1996), Grebel (2000), Barmby et al. (2002), Grebel et al. (2003), Zucker et al. (2004, 2006a), Harbeck et al. (2005). X, Y, and Z coordinates are given in our Cartesian coordinate system centered on M31.

A schematic diagram of the satellites' location relative to M 31 in this native M31 CS is shown in Fig. 6.1. The uncertainties in each of the three coordinates were derived by applying the above transformations accounting for the uncertainties in the distances as the only error source. The right panel of Fig. 6.1 seems to suggest the absence of an obvious Holmberg effect in the satellite distribution. Furthermore, by eye one may be tempted to position a possible great circle along the approximate longitudes of +30° and −150°, but this does not look like a very well-defined great circle. Since it is difficult to determine a preferential alignment of the satellite distribution by eye, we now pursue the question of great planes comprising all or subsets of M31's companions via a statistical approach.

6.3 Great planes including all satellites

The most convenient parameterization of a plane is the Hesse form, which describes each point within the plane in terms of the normal vector $\mathbf{n}$ and two vectors, $\mathbf{x}$, $\mathbf{p}$, each pointing from the origin to a point located on the plane. Then $\mathbf{n}\cdot(\mathbf{x}-\mathbf{p})=0$ unambiguously defines the plane. One can determine the closest distance D_p between the origin of the CS and the plane via $D_p=\mathbf{n}\cdot\mathbf{p}$ (see also Kroupa, Theis, & Boily 2005). Since we seek to identify great circles or great planes, the plane needs to intersect the origin (i.e., the center of M31), which allows us to set D_p to zero. Then the Hesse form can be simplified as follows:

$$n_1\,X_{M31}\,+\,n_2\,Y_{M31}\,+\,n_3\,Z_{M31}\,=\,0. \tag{6.3}$$

Here n_i denotes the respective components of the plane's normal vector[2]

---

[2] It is often convenient to give $\mathbf{n}$ in its spherical parameterization, i.e., $l = \arctan(n_2\,/\,n_1)$ and $b = \arctan(n_3/\sqrt{n_1^2+n_2^2})$.

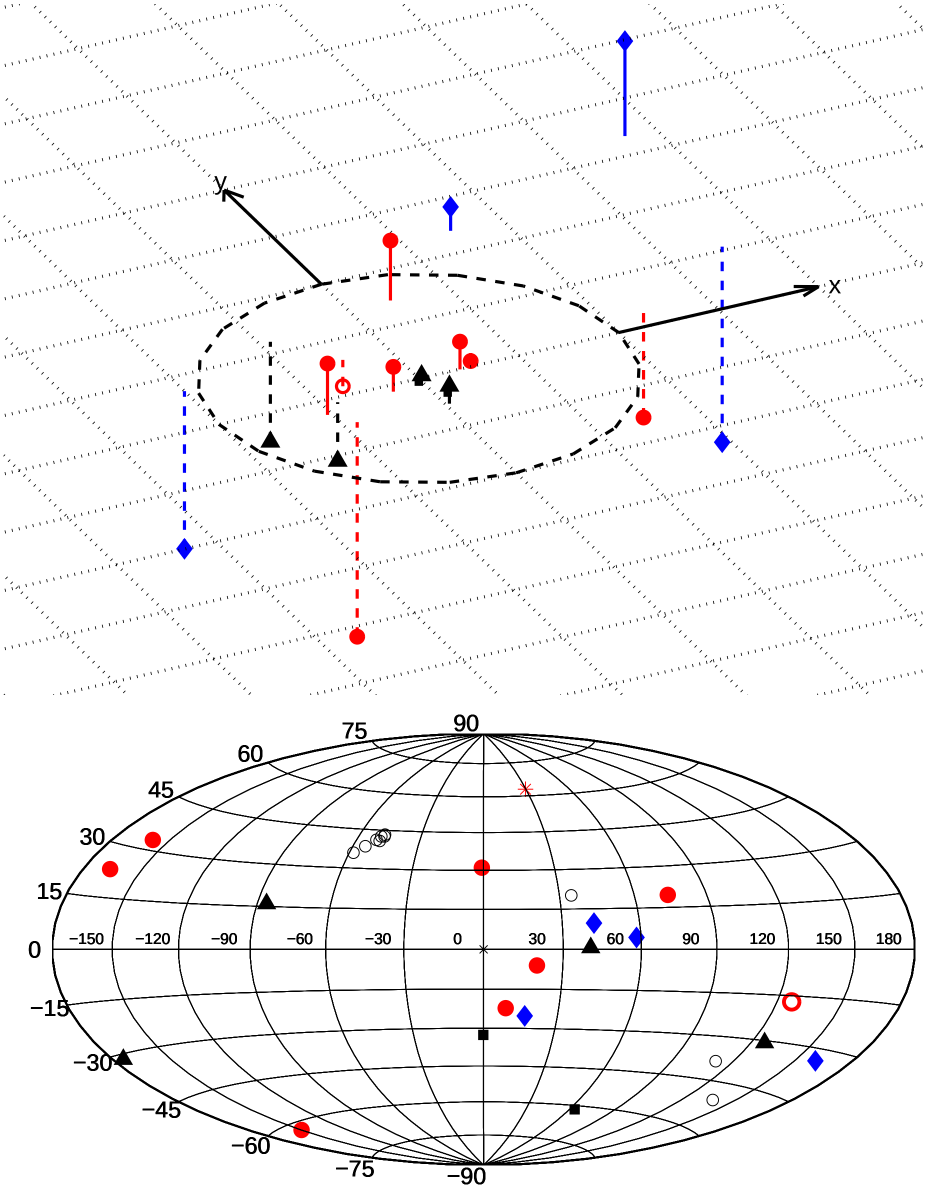

Figure 6.1: Illustration of the position of the M31 satellites relative to the disk plane of M31 (top panel). The dotted grid indicates the location of M31's disk plane, which contains the x- and y-coordinates of our coordinate system centered on M31. Solid (dashed) lines indicate companion galaxies above (below) this plane. The different symbols refer to the morphological types of the M31 companions: dSphs (filled red circles), dEs and cEs (filled black triangles), and dIrrs and dIrr/dSphs (filled blue diamonds). M31 itself is marked with a cross. The axes of each grid have a length of 100 kpc. The dashed circle circumscribes the central 200 kpc around M31. — The bottom panel shows an Aitoff projection of the same data in the M31 reference system, also including the Andromeda stream (open circles), its two most massive globular clusters (black filled squares), M 33 (asterisk) as well as the newly discovered dSph And X (open red circle). Note the lack of an obvious Holmberg effect. Visual inspection suggests a possible great circle of satellites along the latitudes of approximately $+30^\circ$ and -150°.

and $(X_{M31}, Y_{M31}, Z_{M31})$ is the position vector of each satellite, as determined above. From this the distance of any point (x_i, y_i, z_i) to the plane is given by $d_p = (n_1\, x_i + n_2\, y_i + n_3\, z_i)\, /\, \sqrt{n_1^2 + n_2^2 + n_3^2}$. We fit the implicitly defined surface (eq. 6.3) to our data by means of an error-weighted orthogonal distance regression (ODR) using ODRPACK (Boggs & Rogers 1990, Boggs et al. 1992). Instead of minimizing the projected distance to the plane in a given coordinate, as in a traditional least-squares fit, ODR takes into account the perpendicular distance to the curves to be fitted. The individual data points were weighted in the fit by the deprojected uncertainties in the three-dimensional positions, which were calculated from the measurement uncertainties in the galaxies' distances.

6.3.1 The best-fit satellite plane

The formally best-fit plane that we obtained by performing one single ODR fit comprising the entire sample of 15 satellites[3] lies at a normal vector of $l = 171.2°$ and $b = -45.6°$. However, anticipating the statistical method in Section 6.3.3, the significance of this plane is 84%, corresponding to 1.4 Gaussian σ and we cannot reject the possibility that such a plane is a purely random alignment. If we describe the r.m.s. height of an underlying disk distribution for N satellites as $\Delta = \sqrt{(1/N) \sum_{i=1}^{N} d_p^2(i)}$, this value is found to be 99.4 kpc. It is obvious that not all satellites fall onto this plane. Outliers can hamper the determination of a best-fit solution for the simple reason that they are not physically associated with the underlying population that presumably forms such a disk.

6.3.2 Bootstrap tests of best fit planes

When fitting a plane to a set of data points, the influence of outliers can be overestimated and can yield significantly different results. However, since one cannot flag any data point as an outlier *a priori*, we have to use a statistical method to reliably determine a robust solution for estimating best-fit planes. We approach this problem by a bootstrap test (Efron & Tibshirani 1993). That is, we draw any possible combination of a subsample from the satellites, where we covered all possible sample sizes from three to all 15 companions, thus allowing us to run $\sum_{i=3}^{15} \binom{15}{i}$ different tests. For each of the 32647 possible subsamples we performed the plane fit as described above. The resulting distribution of the normal vectors of the best fit planes is shown in the top left panel of Fig. 6.2, where the total of all 15 companions forms the parent sample. Since the direction of the pole is ambiguous due to the lack of actual orbit information, ODR cannot distinguish between normal vectors that are simply inverted in b and shifted by 180° in l. These points are then assigned to the complementary plane exhibiting the mirrored normal vector.

Maxima were determined using methods tailored for the statistical analysis of spherical data (Fisher, Lewis & Embleton 1987). In this approach, the density f of n data points P_i on the unit sphere, which are characterized by their direction cosines $(x_i,\, y_i,\, z_i)$, or in this case the normal vectors of the bootstrapped planes, can be written as a weighted average, w.r.t. all other points present:

$$f(x, y, z) \;=\; \sum_{i=1}^{n} W_n\,(P, P_i). \tag{6.4}$$

Consequently, larger weight is given to closer points. A useful parametrization of the weights W_n

---

[3] The 16th, newly discovered satellite And X will be discussed separately in Sect. 6.4.1.

is the so called Fisher density

$$W_n = \frac{C_n}{4\pi\, n\, \sinh(C_n)} \exp\left\{C_n \left(x\, x_i + y\, y_i + z\, z_i\right)\right\}, \tag{6.5}$$

which is the basic model for directions distributed unimodally with rotational symmetry, and serves more generally as an all-purpose probability model for directions in space and directional measurement errors.

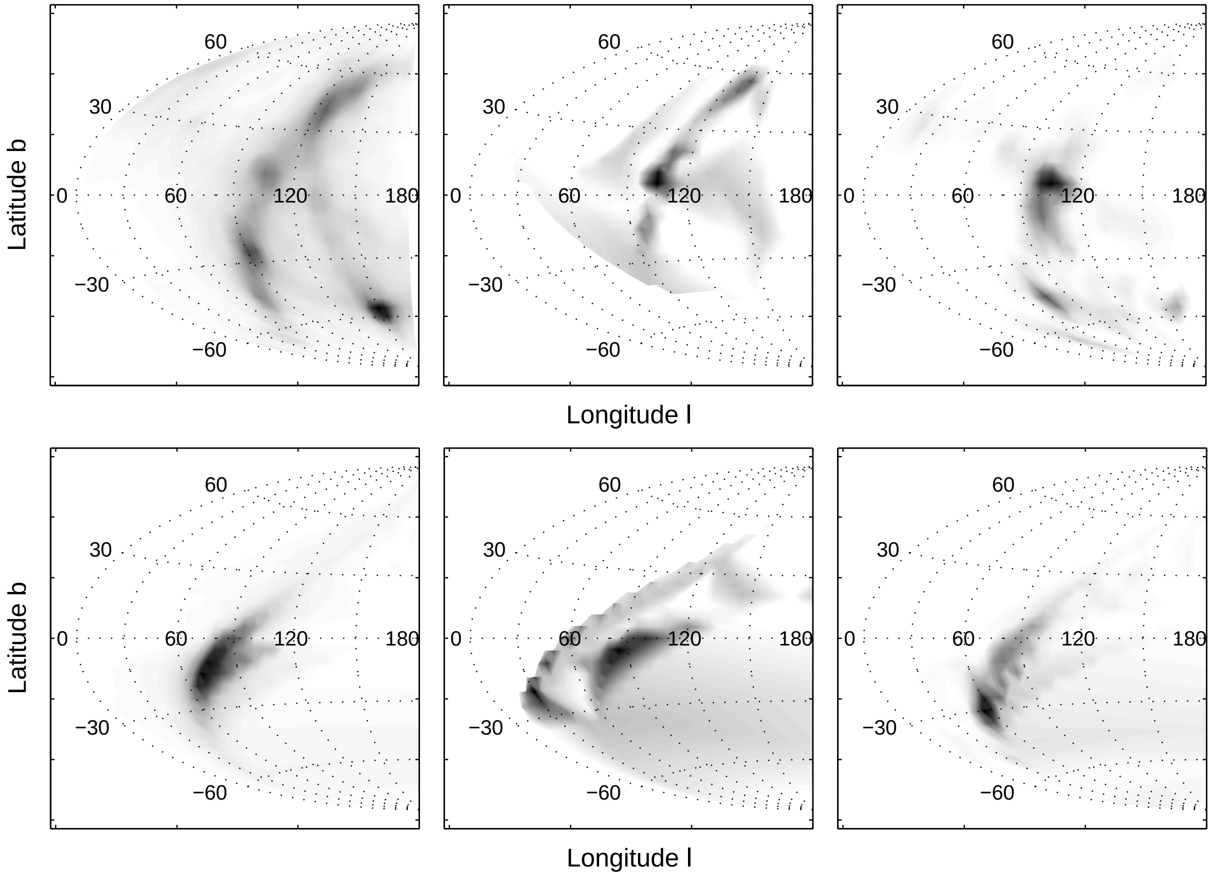

Figure 6.2: Number density distributions of the normal vectors from all bootstrap runs. The top line is drawn from the fits to the observed galaxy sample, whereas the bottom plots show *one* sample each of the large number of tests run on a random distribution. The left panels refer to all possible fits of great planes to galaxies from the entire sample of the 15 M 31 companions. The middle panel shows results for fitting only the seven dSphs. The distribution after exclusion of the And II dSph and inclusion of the dEs and M32 is shown in the right panel. Distinct maxima in the observed plots at ($l = 150.8°$, $b = -56.4°$), ($l = 107.1°$, $b = 6.9°$) and ($l = 102.6°$, $b = 5.2°$) indicate poles of the respective best-fit planes. Maxima in the random distribution do not stand out clearly and appear smeared out.

The C_n-values themselves provide an unbiassed measure of the smoothing of the data set and are here, for convenience, estimated under the assumption that the underlying distribution of vectors is either isotropic or at least close to unimodal. Hence,

$$C_n = \left(\frac{n-1}{n-R}\right) n^{1/3}, \tag{6.6}$$

where R denotes the length of the resultant vector, i.e.,

$$R^2 = \left(\sum_i x_i\right)^2 + \left(\sum_i y_i\right)^2 + \left(\sum_i z_i\right)^2 \tag{6.7}$$

(Fisher, Lewis & Embleton 1987). This representation has the advantage of being *purely* dependent on the deviation of P_i from P and thus the angular separation of the points and not on their direction.

The distinct peak in Fig. 6.2 (left panel) occurs in the direction of $l = 150.8°$ and $b = -56.4°$, which defines a best-fit plane based on a more robust method than obtained by a single fit of all data points. The resultant Δ is 100.0 kpc. It is noteworthy that this is not a polar alignment as would be expected if the Holmberg effect occurred also in M 31.

Fig. 6.3 (left panel) shows the location of all the M31 companions and the great plane that was derived from this ODR fit comprising the entire sample of 15 satellites. The diagram is shown from a viewpoint rotated such that the great plane is seen edge-on. This great plane comprises all dEs, M32, and also all dIrrs except for the transition-type dIrr/dSph galaxy PegDIG (located at a distance of 410 kpc to M31).

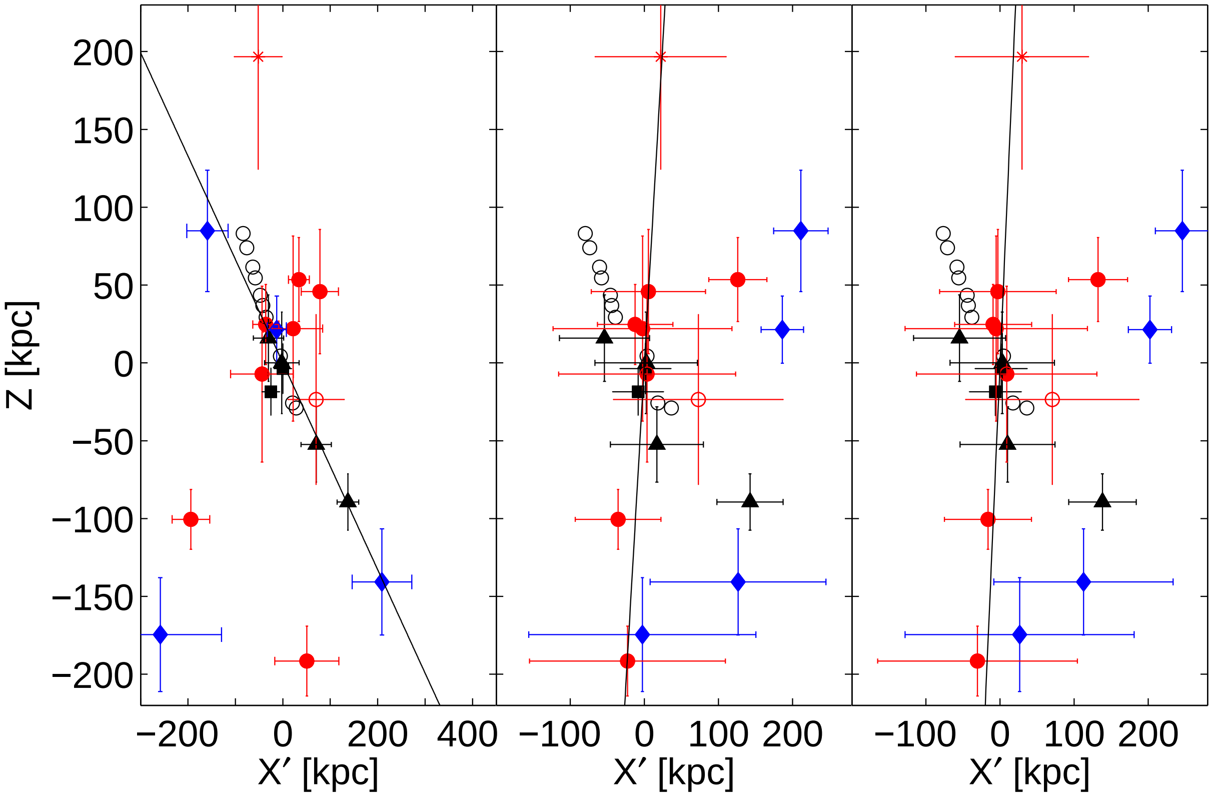

Figure 6.3: The position of the satellite galaxies shown in edge-on projections perpendicular to the best-fit planes. The left plot shows the fit to the entire dwarf sample. The middle panel illustrates the best fit to the dSph subsample. The right panel displays the rotated CS and incorporates the best fit to the combined dE/cE and dSph sample while excluding the outlier And II. The symbols are the same as in Fig. 6.1. Note that the horizontal errorbars in these projections indicate the combined uncertainties of the X_{M31} and Y_{M31} positions.

Although not used in the fits discussed above, we superposed the location of the Andromeda Stream (McConnachie et al. 2003) onto the diagram (Fig. 6.3). This stream has been shown to extend to at least 4.5° southeastward of M31. The ten fields from McConnachie et al. (2003) (errorbars were omitted for clarity) are naturally aligned with respect to each other, but are still located in a separate plane that is inclined against the best-fit plane of our analysis by approximately 7°. We did not attempt to include other features such as And NE (Zucker et al. 2004b), since their three-dimensional position is less well known.

6.3.3 Statistical significance of the planes

In order to assess the statistical significance of the previously determined best-fit plane, we ran a number of additional tests.

First, we generated a random sample of 15 satellites, distributed out to the maximum distance of the observed companions. The radial distribution of the random satellites was taken to follow a power law with an exponent of -2, which is a fairly good approximation of the actual radial distribution of the M31 companions and is also similar to the prediction of cosmological sub-halos (Klypin et al. 1999, Moore et al. 1999, Zentner & Bullock 2003). By means of a KS test it can be shown that the cumulative sample of companions is consistent with such an isothermal density distribution at 99.1%, where the most likely power-law indices fall in the range between -1.6 and -2.3 (see also Kroupa et al. 2005). The innermost satellite was, however, ignored in this procedure, since the central regions of the M31 system are known to be incompletely sampled by observations. Fig. 6.4 shows the radial distribution of the observed satellites relative to M31.

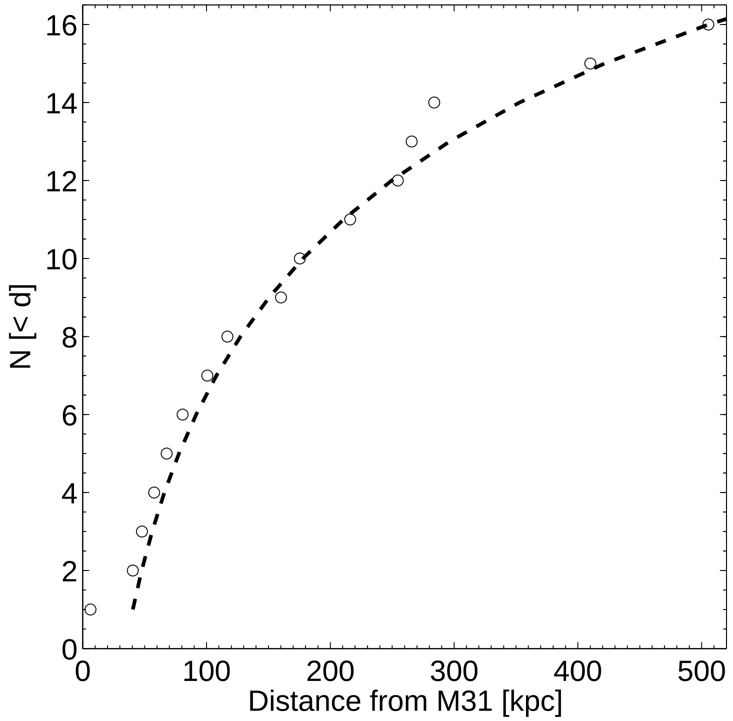

Figure 6.4: Cumulative radial distribution of the M31 satellites. The dashed line is a power-law with an exponent of -2.

Then the entire procedure of bootstrap-fitting planes to this random distribution was carried out analogously to that of the real observed set as described in Sect. 3.2. We determined the best-fit plane from the corresponding density maps (see the bottom panel of Fig. 6.2 for a sample) of the 32647 combinations and calculated the respective r.m.s. distance of the 15 random points to this plane. This procedure was repeated a large number of times (of the order of 10^3) to allow us to assess the probability that the r.m.s. distance Δ originates from a random distribution and to also identify any other potential biases in our method.

For the best-fit plane to the entire satellite sample of 15 companions we find a significance of 87.4%, hence our result is robust at the $1.5\,\sigma$-level. Therefore we cannot reject the hypothesis that such a plane may result from a random distribution and thus may not have any physical meaning. Including McConnachie et al.'s ten fields from the Andromeda stream into the fit routines did not alter the location of the resulting plane much. For this enlarged sample we found a normal vector of ($l = 148.5°$, $b = -53.3°$) with a residual r.m.s of 78 kpc. However, an interpretation of this latter result should be taken with caution, since the sample is biased toward the stream due to the incorporation of ten fields for one contiguous feature (i.e., the stream) versus 15 individual satellites. Hence, stating any significance will not be meaningful as we would produce an artificially increased significance from the large number of fields.

A second test for the robustness of the fitting method employed here comprised the rotation of the real galaxy sample by pairs of random angles. The resulting data were subsequently subjected to the same fitting procedure as above, again repeated for a large number of samples. As a result, we could recover the best-fit plane rotated by the input random angles, where the scatter around the original best-fit angles amounts to approximately 5–10°. This lends further support to the results obtained with the method used here and additionally provides an estimate of typical uncertainties that result from the fits.

6.4 A polar plane of early-type M31 companions

In the previous section we analyzed the entire sample of M31 companions comprising dEs, cEs, dSphs, and dIrrs as well as transition types such as the dIrr/dSph LGS3. Since the dSphs form the most numerous dwarf subsample in a galaxy group, and since the majority of satellite candidates of the massive Local Group galaxies are dSphs (e.g., Grebel 1999), we performed the bootstrap fit procedure including only the seven dSph satellites. It is noteworthy that, while a fit to the full sample of all M31 satellites does not yield a highly significant, unambiguous solution, the majority of dSphs lies within a plane defined by $l = 107.1°$ and $b = 6.9°$ (see middle panel of Fig. 6.2) with an r.m.s. of $\Delta = 46$ kpc. This plane is indicated in the middle panel of Fig. 6.3 after rotation of the viewpoint by the respective longitude. Only one dSph deviates considerably from this plane: And II, located at a distance of 158 kpc to M31 and 112 kpc to the plane, where the latter value is larger than two standard deviations. Excluding this obvious outlier yields a high significance (determined as above by a large number of random samples of seven satellites) of the resulting dSph plane of 99.7%, corresponding to $3\,\sigma$.

As Fig. 6.3 (middle panel) implies, also M31's close companions, the cE M32 and the dE NGC 147 (as well as the transition-type dIrr/dSph PegDIG), lie reasonably close to the best-fit dSph plane. We may thus ask whether an improved fit would result when *all* morphologically similar galaxies are included, i.e., all galaxies of the dSph/dE/cE class. We reran the bootstrap test on this enlarged subgroup. This procedure yields a slightly different plane at $l = 102.5°$ $b = 5.2°$ (see right panels of Figs. 2 and 3) with an r.m.s. of the residuals of $\Delta = 51$ kpc (without

And II). As a result, the significance amounts to 98.7% ($2.5\,\sigma$), again excluding the outlier And II. Hence there is very little difference as compared to the previous fit that included only dSphs. However, if we consider only those galaxies whose positions seem to be in good agreement with the polar great plane of early-type companions, namely M32, NGC 147, PegDIG and the dSphs, but excluding And II, NGC 185, and NGC 205, these nine companions lie within a thin disk with an r.m.s. distance of 16 kpc to this early-type plane.

Based on this best-fit early-type plane, we performed an additional test to assess the bias and uncertainties of the derived best-fit normal vector introduced by the positional uncertainties of the satellite galaxies. For this purpose, each satellite's position was Monte Carlo varied 10^4 times around its error on $(x,\ y,\ z)$ and the normal vector of a plane was determined under the constraint that this plane passes through the new satellite position. As the density contours of the resulting normal vectors in Fig. 6.5 imply, the positional errors lead to smearing out of the best-fit planes' direction cosines of the order of $\pm 10^\circ$ (1σ), which is a measure of the accuracy of our best-fit planes and in good agreement with the uncertainties derived via the statistical test described in Section 6.3.3 (see also Table 6.2). The outlying feature in Fig. 6.5 at $(l,\ b) \sim (155,\ -18)$ is due to And II, which has a large distance of 112 kpc to the plane. Also And X causes a smearing out of the distribution around $\sim (140,\ 0)$ due to its large distance- and resulting position errors in the M31-based coordinate system.

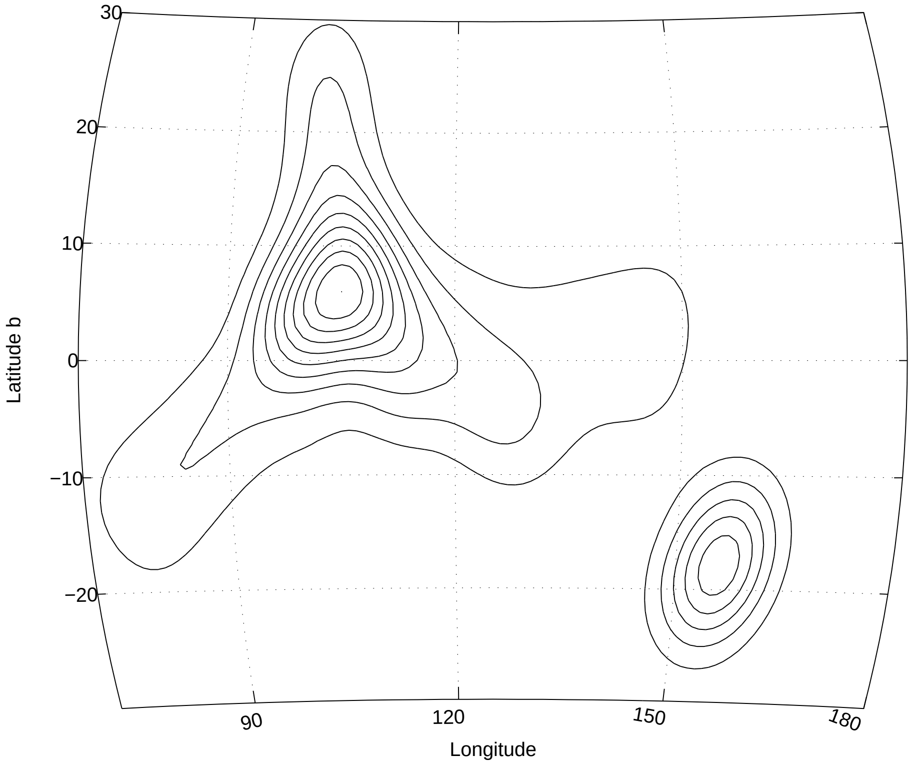

Figure 6.5: Density contours of the normal vectors obtained by Monte Carlo simulations of the satellite positions accounting for the individual distance uncertainties. Each plane was forced to pass through the such varied satellite positions. The outlying structure at $\sim (155,\ -18)$ is due to And II.

Fit sample	Adopted distance to M31 [kpc]	Best-fit plane (l, b)	Significance
All satellites (15)	760 ± 20	$150\overset{\circ}{.}7\,, -56\overset{\circ}{.}5$	86.9 %
	773 ± 20	$150\overset{\circ}{.}8\,, -56\overset{\circ}{.}4$	88.0 %
	783 ± 20	$150\overset{\circ}{.}2\,, -56\overset{\circ}{.}2$	87.1 %
All dSphs (7)	760 ± 20	$100\overset{\circ}{.}3\,, 10\overset{\circ}{.}9$	99.1 %
	773 ± 20	$107\overset{\circ}{.}1\,, 6\overset{\circ}{.}9$	99.7 %
	783 ± 20	$101\overset{\circ}{.}9\,, 6\overset{\circ}{.}5$	98.6 %
dSphs (without And II), dEs, and M32 (10)	760 ± 20	$102\overset{\circ}{.}7\,, 12\overset{\circ}{.}1$	97.8 %
	773 ± 20	$102\overset{\circ}{.}6\,, 5\overset{\circ}{.}2$	98.7 %
	783 ± 20	$102\overset{\circ}{.}8\,, 4\overset{\circ}{.}8$	99.2 %

Table 6.2: Effects of varying M31's distance on the resultant best-fit planes.

Interestingly, also the smaller Local Group spiral M33 is directly encompassed by this great circle (its orthogonal distance to this plane being 2.8 kpc). However, it is not related to the great plane resulting from the fit to *all* M31 satellites – here M33 has a distance of 135 kpc from the plane. Moreover, while the plane comprising all of the M31 satellites is highly non-polar (at -56°), the great plane that includes dSphs, dEs, and the cE exhibits a nearly polar alignment with an inclination of $5 - 7^\circ$ from M31's pole. The most luminous, most massive globular cluster in the Milky Way, ω Cen, shares a number of properties with dwarf galaxies and is often considered to be the stripped remnant of an accreted dwarf (e.g., McWilliam & Smecker-Hane 2005; Hilker et al. 2004; Ideta & Makino 2004; and references therein). The most massive, most luminous globular clusters known in the Local Group are located in M31. One may speculate that these objects might be nuclei or bulges of stripped dwarfs. G1, for instance, also seems to exhibit a metallicity spread (Meylan et al. 2001). If so, the progenitors of these luminous clusters may also have been early-type dwarfs. We have compared the location of the two most luminous M31 globulars, Mayall II or G1 and B 327 (van den Bergh 1968), to the location of our polar plane of early-type galaxies. Although we did not include these objects in any of the fits, we indicate in Figs. 1, 3, and 6 also the positions of these massive globular clusters relative to the M31 system. These clusters have an adopted distance coincident with that of M31 itself (Rich et al. 1996, Barmby et al. 2002). While G1, which is often regarded as the most luminous globular cluster of the Local Group, lies at a distance of merely 8 kpc of this polar great plane and coincides with it to within its errorbars, B 327 is fully encompassed by the early-type great plane[4].

Uncertainties in the analyses presented here result not only from uncertainties in the distances to the satellites of M31, but also from the uncertainty of the distance to M31 itself. Hence we carried out our analysis for three widely used distances to M31 from the literature. The results discussed above rely on the Cepheid distance of 773 kpc (Freedman & Madore 1990). In addition, we also adopted the mean M31 distance of 783 kpc based on several distance indicators discussed by Rich et al. (2005), and the mean distance of 760 kpc resulting from various distance indicators given by van den Bergh (1999). The formal mean uncertainties of these distance measurements are of the order of 10–20 kpc, implying that the different distances agree within their uncertainties. The results for all three M31 distances are listed in Table 6.2. As the values in Table 6.2 demonstrate, the above variation of the distance to M31 does not significantly alter our results. The statistical presence of a polar great plane prevails.

---

[4] Van den Bergh (1968) argues that B 327 is probably the most luminous globular cluster when its reddening is properly taken into account.

6.4.1 A new satellite – And X

Within the framework of large sky surveys, progressively more faint dwarf galaxies are detected and regularly, new companions, both to the Milky Way (e.g., Willman et al. 2005; Belokurov et al. 2006a, 2006b; Zucker et al. 2006b; Zucker et al. 2006c) and to M31 (Zucker et al. 2004a) are reported. Recently, a new dSph candidate in the Andromeda system was discovered by Zucker et al. (2006a) in data from the Sloan Digital Sky Survey (SDSS; Abazajian et al. 2003; Zucker et al. 2004b; Adelman-McCarthy et al. 2006), and consequently named And X. Although this object was not yet included in the analyses described in the previous sections, we added this galaxy to our sample (Table 6.1) and show its position relative to our detected best-fit dSph- and early-type planes in the M31-based coordinate system (indicated as open red circle in Figs. 6.1, 6.3 and 6.6). Subsequently, we performed the identical bootstrap- and statistical tests as described above on the thus enlarged data set, in order to test, whether also this dSph candidate is in compliance with a common plane of morphologically similar satellites.

First of all, it is worth noticing that inclusion of And X in our data set did not alter the poles of the resulting best-fit planes within the uncertainties of our method. Hence, the maximum in the distribution of normal vectors when all (now 16) satellites are considered still lies at $(l,\, b) \simeq (150°,\, -56°)$, in analogy to the top left panel of Fig. 6.2. Likewise, the best-fit dSph- and early-type planes, respectively, maintain their location at $\sim (105°,\, 6°)$ within the uncertainties as discussed in Sections 6.3.3. and 6.4 .

The value of Δ of the full sample w.r.t. the plane that "fits" all companion galaxies now amounts to 97 kpc and is thus slightly smaller than the value obtained before (100 kpc, cf. Sect. 6.3.1). Its distance to this plane itself is a mere 19 kpc and the significance of such an overall alignment is, with 89.4%, comparable to the significance from the previous sample. The main effect of incorporating And X in the statistics of the morphologically distinct samples is a slight smearing out of the distributions of normal vectors. This is reflected in a slightly increased RMS-thickness of the respective planes: Regarding the plane we found to comprise the dSphs only, the RMS distance of the dSphs including And X increases to 51 kpc, where And X is located at a perpendicular separation of 75 kpc from this plane. The resulting significance is found to be 91% ($1.7\,\sigma$, after exclusion of And II as above). Relative to our early-type plane, And X has a orthogonal distance of 72 kpc, yielding a Δ of 53 kpc (after excluding And II), which is significant at 95%, corresponding to $2\,\sigma$. These values are only marginally different from those obtained without incorporation of the newly discovered satellite. Although it is not immediately coincident with the dSph- or early-type planes, its association within such an alignment cannot entirely be ruled out on the ground of statistics.

Despite this only small degradation in the reality of a satellite alignment in terms of slightly reduced statistical significances, one has to keep in mind that And X's distance is yet insecure. Zucker et al. (2006a) give a value of "667 kpc to 738 kpc, ±30 to 35 kpc". Similarly, the resulting position uncertainties in our coordinate system will be underestimated. Consequently, a relationship of And X with the plane we found cannot be ruled out at present.

In a recent paper Martin et al. (2006) announced the discovery of another three faint dSph satellite galaxy candidates in the outer halo of M 31, namely And XI, And XII and And XIII. Since their faintness of $-7.3 \lesssim M_V \lesssim -6.4$ mag prevents an accurate discrimination of the tip of the RGB as a distance indicator, these systems were tentatively assumed to lie at the same Galactocentric distance as M 31 itself in the analyses of Martin et al. (2006). On the other hand, as argued above, distance is a sensitive parameter in our three-dimensional analyses so that we did not account for any of these three newly discovered galaxies in this work.

6.5 Discussion

6.5.1 The break-up or tidal remnant scenario

As mentioned in Section 6.1, one of the scenarios put forward to explain the Galactic polar planes suggests that the dwarf galaxies within such a plane are tidal remnants of a more massive galaxy (e.g., Kunkel 1979; Lynden-Bell 1982). We will refer to this idea as "Scenario I". This scenario leads to the question of whether the properties of the dwarfs, in particular with respect to their stellar populations, are consistent with an origin from a single parent galaxy. We will consider this question first for the Milky Way companions and then for the M31 companions.

A few musings on the Galactic polar great planes

For the Milky Way companions it was shown that each of these dwarfs has its own unique evolutionary history that differs from other dwarfs even when of the same morphological type (e.g., Grebel 1997). This need not contradict an origin from a common, subsequently accreted parent, but would indicate that the separation from this parent should have occurred very early on, followed by continued evolution of the individual tidal fragments. The low metallicities of the old populations of the dSphs (see Table 1 in Grebel et al. 2003) indicate that either the parent galaxy was little evolved when its disruption occurred (supporting the view that this must have happened at ancient times) and/or that the dSphs are tidal fragments of the outer, metal-poor regions of the parent.

All nearby Galactic dwarfs seem to share a common epoch of ancient star formation that is coeval within the present-day measurement accuracy (to within ~ 1 Gyr) and that is indistinguishable from the oldest age-datable stellar populations in the Milky Way (Grebel & Gallagher 2004). The SMC appears to have an old population that is several Gyr younger than the ancient star formation episodes in the other dwarfs and in the Milky Way, but more detailed data are still needed for this galaxy. For the remaining dwarfs, a common epoch of early star formation does not necessitate a common origin, but lends more support to such an idea than would widely differing times for the first significant star formation.

While the *mean* metallicities of the old populations in the various dwarfs tend to differ by a few tenths of a dex, all of these galaxies also show a considerable abundance spread among their old stars. Neither property precludes a common origin from fairly metal-poor regions of a putative common progenitor.

The Galactic dwarfs follow a metallicity-luminosity relation (e.g., Grebel et al. 2003), indicating that intrinsic processes such as their own gravitational potential and hence the ability to retain metals played an important role in their evolution. If these dwarf galaxies are leftovers stripped from a larger satellite, they must once again have been stripped at an early time and must then have continued to form stars after this event in order to produce the observed metallicity-luminosity relation. Clearly, the Galactic dSphs are quite different from more recently formed tidal dwarfs whose departure from the metallicity-luminosity relation readily betrays their nature (e.g., Duc & Mirabel 1998).

It would seem that sustaining the extended star formation histories of the Galactic dSphs (see, e.g., Grebel & Gallagher 2004) would be difficult in low-mass tidal remnants without dark matter unless these galaxies had substantially larger baryonic masses when they condensed than the $\sim 10^5 - 10^6$ $M_\odot$ derived today from their stellar content (see also discussion in Grebel et al. 2003, and for instance the models presented by Wang et al. 2005 and Mashchenko et al. 2005). Other arguments against dSphs being mere tidal remnants without dark matter include the lack of substantial line-of-sight depth (Klessen, Grebel, & Harbeck 2003) and extended, fairly flat radial velocity profiles (Wilkinson et al. 2004). Nonetheless, the question of dark matter in the low-mass dSphs remains yet to be resolved.

Whereas some merger events that are believed to have occurred several Gyr ago have left detectable tidal streams in the Milky Way – for instance, Sagittarius and possibly Monoceros, Canis Major (Ibata, Gilmore, & Irwin 1994; Newberg et al. 2002, 2003; Yanny et al. 2003; Majewski et al. 2003; Martin et al. 2004), and Triangulum-Andromeda (Rocha-Pinto et al. 2004) – no ancient event has so far been identified that could be connected to the origin of the polar great planes. If these planes do indeed have a physical meaning, this unsatisfactory situation may change with the parallax and phase space information for the vast number of Milky Way stars that will be provided by the Gaia mission (Perryman et al. 2001). It has been suggested that the Large Magellanic Cloud may be the main part of a broken-up parent galaxy responsible for the Magellanic Stream of dwarf galaxies and simply has not yet merged with the Milky Way (e.g., Kunkel 1979). Related hypotheses propose that the precursor of today's Sgr dSph may have been deflected into its current orbit by a collision with the LMC (Zhao 1998), and that Fornax might have been stripped of its gas by an encounter with the Magellanic Stream, leading to the H I cloud excess along its inferred orbit (Dinescu et al. 2004).

The strongest evidence in favor or against the reality of orbital planes of dwarf galaxies will come from proper motion measurements. At present, recent measurements reveal a complex picture. Ursa Minor can be ruled out as a member of the Magellanic Stream (Piatek et al. 2005). Fornax, excluded as a stream member by the data of Piatek et al. (2002), is proposed as a likely member of the Fornax–Leo I–Leo II–Sextans–Sculptor stream by Dinescu et al. (2004). For Carina and for Sculptor the situation appears to be ambiguous at present (Piatek et al. 2003; Schweitzer et al. 1995). As more and more epochs are being added, the measurements should yield a clearer picture in the coming years.

A few musings on the M31 polar great plane

The low-mass dSph satellites of M31 are all metal-poor and show hints of metallicity spreads (e.g., Côté, Oke, & Cohen 1999a; Guhathakurta, Reitzel, & Grebel 2000; Harbeck et al. 2001). However, unlike the Galactic dSphs the M31 dSphs are dominated by old populations, lacking prominent intermediate-age or even young populations (e.g., Harbeck et al. 2001; Harbeck, Gallagher, & Grebel 2004). In this sense, they show a much higher degree of homogeneity than the Galactic dSphs. The two elliptical dwarfs that appear to be associated with the polar great plane show considerable enrichment, but NGC 147's globular clusters are old and metal-poor (Da Costa & Mould 1988; Han et al. 1997), and indications of a small old and metal-poor population were recently found in M32 (Alonso-García, Mateo, & Worthey 2004). As for the Milky Way companions, a putative break-up that would have produced the early-type companions of M31 would need to have occurred at very early times.

All of the gas-deficient M31 companions follow the metallicity-luminosity relation of early-type dwarfs (Grebel et al. 2003; Harbeck et al. 2005). In the remnant scenario, this would imply that they should have undergone further chemical evolution to reach a state consistent with their luminosity; hence one may suggest that the remnants should still have contained sufficient gas to continue to form stars for a while after the break-up. If so, then again the break-up must have occurred at very early times considering the observed absence of prominent younger populations.

The cE M32 is a very interesting object in itself: It contains a black hole with a mass of a few times 10^6 $M_\odot$ (e.g., Tonry 1984; Joseph et al. 2001; Van der Marel et al. 1997), it interacts with M31 (King 1962; Choi, Guhathakurta, & Johnston 2002), and may be the remnant of a larger elliptical galaxy (Faber 1973; Nieto & Prugniel 1987) or the bulge of a stripped early-type spiral galaxy (Bekki et al. 2001; Graham 2002). The latter is supported by the detection of what appears to be the remains of a disk in M32 (Graham 2002). This raises the intriguing possibility that M32 may be the remnant of the parent of the dwarf galaxies located in the M31 polar great plane identified in our paper.

One possibility to test this hypothesis is the tight correlation between the mass of the central black holes in nearby galaxies and the physical properties of the surrounding stellar spheroid or bulge, in particular its mass and/or luminosity (Kormendy & Richstone 1995; Magorrian et al. 1998; Marconi & Hunt 2003). If M32's black hole mass were representative of the stripped progenitor's bulge mass, it should clearly deviate from the classical relation after the original bulge has experienced significant mass loss in the course of the tidal disruption. However, it has been demonstrated that the mass of M32's central black hole is in good agreement with its (V-band) spheroid luminosity (van der Marel 1999). Moreover, Marconi & Hunt (2003) showed that its present-day bulge mass and near-infrared luminosity are compatible with such a relation. It is worth noticing, however, that the results of Häring & Rix (2004), who reexamined existing data, indicate a smaller bulge mass for M32, which is too low w.r.t. its black hole mass by a factor of 2–3. Yet, in the light of the uncertainties in such dynamical mass estimates, a possible identification of M32 with the proposed broken-up progenitor of some of the present-day observed dwarf satellites seems to be ruled out.

On the other hand, M32 may be associated with the giant stellar stream around M31 (Ibata et al. 2001), since it appears to be located within the stream; however, its velocity is quite different from that of the stream (Ibata et al. 2004). The stream itself seems to be on a highly radial orbit passing very close to the center of M31. Kinematic studies suggest that its progenitor may have survived until 1.8 Gyr ago (Ibata et al. 2004). Considering this and that the stream stars are metal-rich (Ibata et al. 2001), an immediate association of the stream with the dSphs appears to be unlikely.

The M31 halo differs substantially in its properties from the Galactic halo. The stellar halo appears to extend beyond 150 kpc (Guhathakurta et al. 2005), implying that many of the dwarf satellites considered in our present study are in fact moving through the stellar halo of M31. Apart from a significant old population the halo also contains metal-rich intermediate-age populations with ages in the range of 6–8 Gyr that appear to account for ~ 30 % of the stellar mass (Brown et al. 2003). With ~ -0.5 dex, the mean metallicity is comparatively high (Brown et al. 2003; Durrell et al. 2004) and exceeds that of the dSph satellites by at last one dex in [Fe/H]. Hence a once larger population of M31-dSph-like galaxies may have contributed to the ancient halo of M31, but was not the dominant contributor to its complex halo population structure as a whole.

The proximity of M31's massive globular clusters G1 and B 327 to the plane of early-type satellites raises the question whether these objects should also be considered as the remnants of nucleated dwarf galaxies (e.g., Meylan et al. 2001). If they originate from the same break-up event as the remainder of the dSphs, they must have undergone a different evolution. Primarily, they would then seem to have been dominated by tidal stripping and harassment from their massive host galaxy to leave a nucleus or bulge in its present, globular-cluster-like form.

6.5.2 The prolate dark halo scenario

As outlined in Section 1, this scenario assumes that satellites follow the dark matter distribution of the Milky Way. Polar great planes would result if the dark halo is prolate, as some authors are favoring for disk galaxies (e.g., Hartwick 2000; Navarro et al. 2004) and as has been suggested for our own Milky Way from the kinematics of the Sgr dwarf tidal streams (Helmi 2004). Our finding that most of the *low-mass* satellites within 300 kpc of M31 lie within a polar great plane is consistent with this scenario and supports that triaxial prolate dark halos may be a common occurrence in disk galaxies.

We note, however, that the evidence for a Holmberg effect among the M31 satellites is weak. The majority of the M31 satellites is found within $|\, b_{M31} \,| < 40\,\mathrm{deg}$ of its disk (Fig. 6.1, right).

It would be highly desirable to carry out similar studies also for the satellite populations of nearby groups. While we now have distances for many of the satellites in these systems based on the tip of the red giant branch from HST photometry (see Karachentsev et al. 2000, 2002a, 2002b, 2003a, 2003b, 2003c for details), the uncertainties of these distances including, in particular, those to the massive galaxies in these groups make it difficult to reliably derive the three-dimensional galaxy distribution with sufficient accuracy for a comparable analysis.

6.5.3 The filament scenario

This scenario will also result in planar alignments, which would only be polar if that is the orientation of the major axis of the dark matter distribution. Both this and the preceding scenario have the advantage that they do not require a common origin of the dwarfs and permit the presence of dark matter in the satellites.

An interesting consequence of this scenario is that one may expect to find additional dwarf galaxies when following the great planes out to larger distances since the planes should trace the location of extended cosmological filaments.

Fig. 6.6 shows face-on views on M31's disk: in the top panel of Fig. 6.6, we show the present-day location of several nearby galaxy groups, represented by their brightest object with distances adopted from Karachentsev (2005) and projected onto the plane of M31's disk. It is interesting to note that while the M83 and Cen A groups are located far from the polar plane spanned by Andromeda's early-type companions, the M81 group seems to almost coincide with this great plane (or filament?). Also the extended Sculptor group and presumably the Canes Venatici I Cloud appear to be approximately oriented toward the direction of M31's polar satellite plane, albeit at larger angles. The bottom panel of Fig. 6.6 shows the immediate surroundings of M31. The two arrows indicate the directions toward the Milky Way and M33. Few satellites seem to lie at the far side of M31 as seen from the Milky Way. There is no obvious filamentary structure of M31 satellites extending toward the Milky Way, but the polar plane of early-type companions clearly points toward M33 as we pointed out already earlier.

6.6 Summary

We have presented a Cartesian coordinate system that is centered on M31 and aligned with its disk. We calculated the positions of the galaxies within 500 kpc in this CS. Most (possibly all) dwarf galaxies within this radius are likely satellites of M31. We then investigated the existence of possible great planes encompassing subsets or all of the companions. The great plane that results when trying to account for all 15 M31 companions has low statistical significance (84%) and includes many outliers. While this plane probably has no physical meaning, interestingly the recently discovered Andromeda Stream lies close to it and is inclined with respect to it by $\sim 7^\circ$.

If we restrict our sample selection to only gas-deficient galaxies, i.e., to the dSph, dE, and the cE companions of M31, a *polar* great plane with a statistical significance of 98% results. This sup-

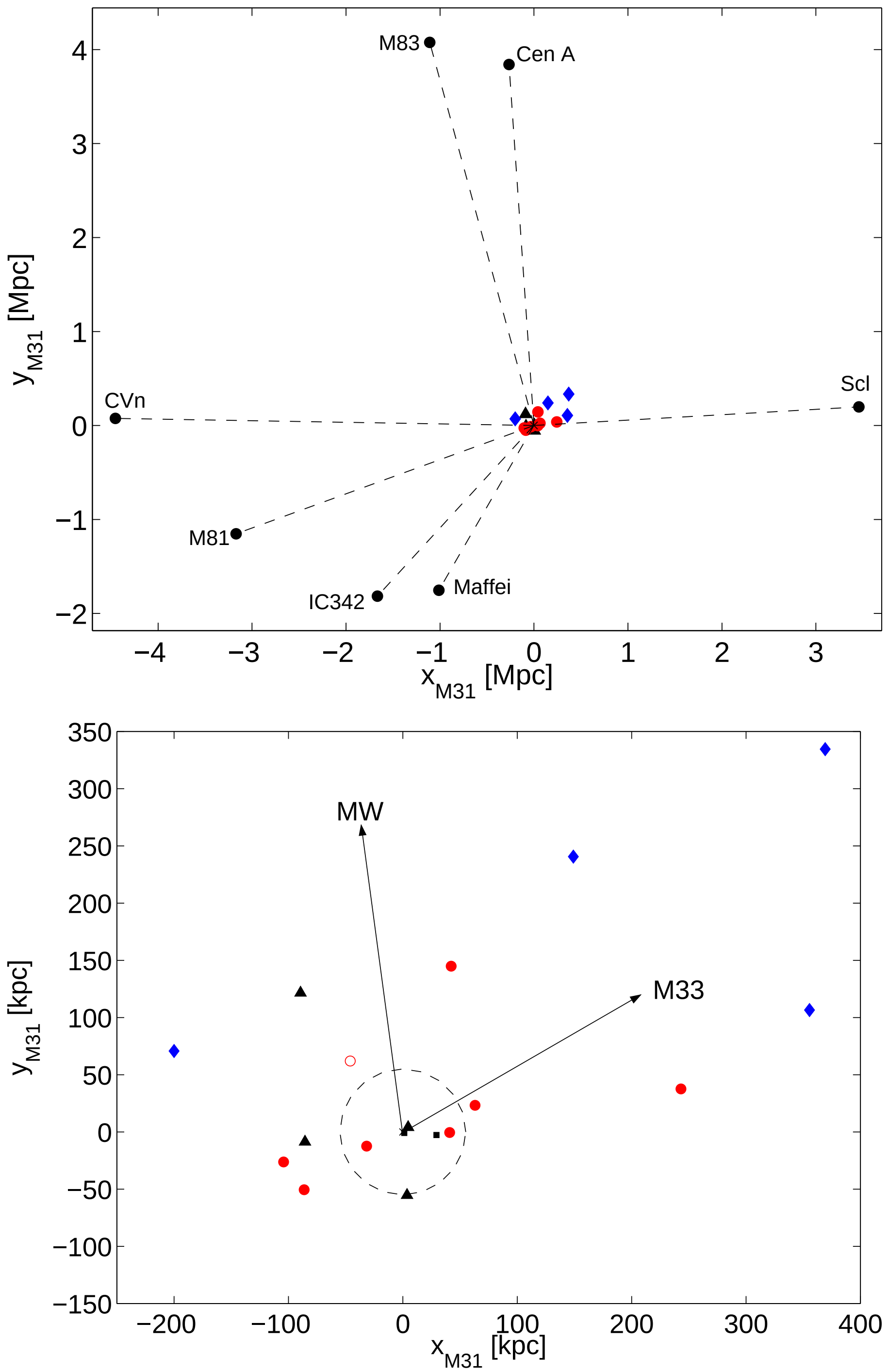

Figure 6.6: Face-on views onto M31's disk plane. The top panel shows the projected location of nearby galaxy groups as given by their most luminous member. The bottom panel is a zoom on M31's immediate vicinity, showing its satellites. The circle designates the central 55 kpc, corresponding to the optical radius of M31's disk. Arrows indicate the direction of the Milky Way (MW) and M33. The symbols are as in Fig. 6.1. The polar great plane of M31's early-type satellites lies along an axis pointing toward the M81 group (top panel) and toward M33 (bottom panel).

ports the earlier claim of the existence of such a plane by Grebel et al. (1999), now based on better and more comprehensive data. M32, NGC 147, PegDIG, and even M33's position are consistent with this great plane. When excluding three deviating early-type dwarfs (And II, NGC 185, and NGC 205) as outliers from the calculation of the statistical significance, the remaining early-type galaxies lie within a mere 16 kpc of this plane, and the resulting statistical significance is 99.7% (3σ). The plane resembles the polar great planes of satellites found around the Milky Way and includes also the more distant dIrr/dSph transition-type galaxy PegDIG and even M33. In total, this polar plane comprises nine out of 16 M31 companions including eight out of 11 of its early-type dwarfs. We note that also the two most luminous globular clusters in the Local Group, both of which are located in M31, are coincident with the plane of early-type companions. The newly discovered dSph And X, however, appears to be not related to this early-type galaxy alignment.

While the plane comprising all of the M31 satellites is clearly non-polar (at -56°), the great plane of gas-deficient satellites shows a nearly polar alignment with an inclination of $6-8^\circ$ from M31's pole. We note that, in contrast to the Milky Way, the M31 companions show little evidence for a Holmberg effect. The majority of these companions is found within $\pm 40^\circ$ of M31's equator. Our findings are relatively insensitive to the adopted distance to M31 itself.

Several scenarios have been suggested to explain the existence of polar planes. A popular scenario suggests that planes originate from the break-up of larger galaxies, keeping smaller fragments in the orbit defined by the progenitor. The fragments may be pure tidal remnants devoid of dark matter. We argue that based on the stellar populations and metallicities of both the Milky Way and the M31 satellites, such a break-up would have to have occurred very early on. A suitable parent progenitor still needs to be identified. Since the satellites follow the luminosity-metallicity relation, they must have continued to form stars after the break-up. There is little evidence so far that the satellites are devoid of dark matter as one would expect from unbound tidal debris. Obviously the best test of this scenario is via proper motions and orbits. The available proper motions for Galactic dwarfs have disproved the association of certain dwarfs with polar orbital planes, but may support this for others.

From a comprehensive set of N-body simulations of galaxy collisions Bournaud & Duc (2006) argued that a small, but non-negligible fraction of satellite dwarf galaxies could have formed in the tidal tails of galaxy mergers. However, as the simulations show, such long lived Tidal Dwarf Galaxies (TDGs) are mostly distributed in the equatorial plane of the progenitor's disk. This finding indicates that the distribution of the MW dSph as well as the alignment of the early-type galaxies in the M 31 system are in conflict with the hypothesis that these dSphs (and presumably dEs) are old TDGs.

The prolate dark halo scenario proposes that satellites follow the dark matter distribution of the massive galaxy they are orbiting, requiring prolate dark halos to create polar great planes. The existence of polar great planes of satellites not only around the Milky Way, but also around M31 would seem to support this scenario, but as noted earlier there is little evidence for a pronounced Holmberg effect in the satellite system of M31. Ultimately, again proper motions and orbits will provide the best test of whether the planar alignments are fortuitous or physical.

The filament scenario suggests that satellites are oriented along cosmological filaments of dark and baryonic matter that is gradually accreted by massive primaries as these continue to grow in hierarchical structure formation. In this case planar alignments not only in the immediate vicinity of massive galaxies are expected, but such filaments should extend over much larger scales. Indeed our polar great plane of M31 satellites points toward the M81 group. On larger scales and for more distant galaxies, this scenario can be statistically tested via weak lensing measurements and large galaxy surveys (e.g., Zentner et al. 2005).

A clear distinction between the different scenarios is not yet possible at present. We can impose constraints based on the known stellar populations and chemical properties of the satellites as discussed before. However, we also need to keep an open mind regarding other possibilities such as that interactions and encounters between companion galaxies may have deflected some of them and altered their orbits, or that we are reading too much into potentially fortuitous planes that may be unconnected with any physical motion of the satellites. All in all, our study underlines the urgent need for orbital information, part of which may be provided by future astrometric missions. Detailed dynamical modeling of the M31 satellite orbits within great planes is underway (Grebel, Koch & Sambhus 2005; Sambhus et al., in preparation) and will aid in assessing the plausibilty of their alignments reality. Clearly, the distribution and motion of satellites provides important tests of galaxy formation and evolution, of the importance of accretion events, of the origin and nature of dwarf galaxies, and of CDM scenarios.

Acknowledgments The results presented in Chapter 6 have been published in collaboration with Eva K. Gebel as *Koch, A. & Grebel, E. K. 2006, AJ, 131, 1405.* I gratefully acknowledge discussions with Helmut Jerjen, Ortwin Gerhard, Niranjan Sambhus, and Sidney van den Bergh for helpful comments.

References

Aaronson, M. 1983, ApJ, 266, L11

Aaronson, M., Olszewski, E. W., & Hodge, P. W. 1983, ApJ, 267, 271

Aaronson, M., & Mould, J. 1985, ApJ, 290, 191 Abazajian, K., et al. 2003, AJ, 126, 2081

Adelman-McCarthy, J. K., et al. 2006, ApJS, 162, 38

Allende Prieto, C., García López, R., Lambert, D. L, & Gustafsson, B. 1999, ApJ, 527, 879

Alonso, A., Arribas, S., & Martínez-Roger, C. 1998, A&AS, 131, 209

Alonso, A., Arribas, S., & Martínez-Roger, C. 1999a, A&AS, 139, 335

Alonso, A., Arribas, S., & Martínez-Roger, C. 1999b, A&AS, 140, 261

Alonso, A., Arribas, S., & Martínez-Roger, C. 2001, AJ, 376, 1039

Alonso-García, J., Mateo, M., & Worthey, G. 2004, AJ, 127, 868

Anders, E., & Grevesse, N. 1989, Geochim. Cosmochim. Acta, 53, 197

Argast, D., Samland, M., Gerhard, O. E., & Thielemann, F.-K. 2000, A&A, 356, 873

Argast, D., Samland, M., Thielemann, F.-K., & Gerhard, O. E. 2002, A&A, 388, 842

Armandroff, T.E., & Zinn, R. 1988, AJ, 96, 92

Armandroff, T.E., & Da Costa, G.S. 1991, AJ, 101, 1329

Armandroff, T. E., Davies, J. E., & Jacoby, G. H. 1998, AJ, 116, 2287

Armandroff, T. E., Jacoby, G. H., & Davies, J. E. 1999, AJ, 118, 1220

Ashman, K.A., Bird, C.M., & Zepf, S.E. 1994, AJ, 108, 2348

Asplund, M., Grevesse, N., & Sauval, A. J. 2005, in: Cosmic Abundances as Records of Stellar Evolution and Nucleosynthesis, ASP Conf. Ser. 336, eds: T.G. Barnes III & F.N. Bash (San Francisco: ASP), 25

Azzopardi, M., Lequeux, J., & Westerlund, B. E. 1985, A&A, 144, 388

Bard, A., & Kock, M. 1994, A&A, 282, 1014

Barmby, P., Perrett, K. M., & Bridges, T. J. 2002, MNRAS, 329, 461

Baumgardt, H., Grebel, E. K., & Kroupa, P. 2005, MNRAS, 359, 1

Beasley, M. A., Kawata, D., Pearce, F. R., Forbes, D. A., & Gibson, B. K. 2003, ApJ, 596, L187

Bekki, K., Couch, W. J., Drinkwater, M. J., & Gregg, M. D. 2001, ApJ, 557, L39

Bell, R. A., Eriksson, K., Gustafsson, B., & Nordlund, A. 1976, A&AS, 23, 37

Bellazzini, M., Gennari, N., Ferraro, F. R., & Sollima, A. 2004, MNRAS, 354, 708

Bellazzini, M., Gennari, N., & Ferraro, F. R. 2005, MNRAS, 360, 185

Bellazzini, M., Correnti, M., Ferraro, F. R., Monaco, L., & Montegriffo, P. 2006, A&A, 446, L1

Belokurov, V., et al. 2006a, ApJL, 647, L111

Belokurov, V., et al. 2006b, ApJL, submitted (astro-ph/0608448)

Bensby, T., Feltzing, S., Lundström, I., & Ilyin, I. 2005, A&A, 433, 185

Bessel, M. S.& Brett, J. M. 1988, PASP, 100, 1134

Binney, J., Mamon, G. A. 1982, MNRAS, 200, 361

Binney, J., & Tremaine S. 1998, "Galactic Dynamics", Princeton University Press

Blackwell, D. E., Petford, A. D., Arribas, S., Haddock, D. J., Selby, M. J. 1990, A&A, 232, 396

Blackwell, D. E., Lynas-Gray, A. E., & Petford, A. D. 1991, A&A, 245, 567

Blackwell, D. E., Smith, G., & Lynas-Gray, A. E. 1995, A&A, 303, 575

Blecha, A., Cayatte, V., North, P., Royer, F., & Simond, G. 2000, Proc. SPIE, 4008, 467

Boggs, P.T., Byrd, R.H., Rogers, J.E., & Schnabel, R.B. 1992, NIST IR 4834, U.S. Government Printing Office.

Boggs, P.T., & Rogers, J.E. 1990, Cont. Math., 112, 183

Bonifacio, P., Sbordone, L., Marconi, G., Pasquini, L., & Hill, V. 2004, A&A, 414, 503

Bosler, T.L., Smecker-Hane, T.A., & McWilliam, A. 2002, in Observed HR Diagrams and Stellar Evolution, ASP Conf. Ser. 274, eds. T. Lejeune, & J. Fernandes (San Francisco: ASP), 252

Bosler, T. L., Smecker-Hane, T. A., Cole, A., & Stetson, P. B. 2004, in Carnegie Observatories Astrophysics Series, Vol. 4: Origin and evolution of the elements, eds. A. McWilliam & M. Rauch (Cambridge: Cambridge University Press)

Bosler, T. L. 2004, Ph.D. Thesis, University of California, Irvine

Bournaud, F., & Duc, P.-A. 2006, A&A, in press (astro-ph/0605350)

Brainerd, T. G. 2005, ApJ, 628, L101

Bromm, V., Yoshida, N., & Hernquist, L. 2003, ApJ, 596, L135

Brown, T. M., Ferguson, H. C., Smith, E., Kimble, R. A., Sweigart, A. V., Renzini, A., Rich, R. M., & VandenBerg, D. A. 2003, ApJ, 592, L17

Busso, M., Gallino, R., & Wasserburg, G. J. 1999, ARA&A, 37, 239

Byrd, G., Valtonen, M., McCall, M., & Innanen, K. 1994, AJ, 107, 2055

Cannon, R. D., Hawarden, T. G., & Tritton, S. B. 1977, MNRAS, 180, 81

Cannon, R. D., Niss, B., Norgaard-Nielsen, H. U. 1981, MNRAS, 196, 1

Cardelli, J. A., Clayton, G. C., & Mathis, J. S. 1989, ApJ, 345, 245

Carigi, L., Hernandez, X., & Gilmore, G. 2002, MNRAS, 334, 117

Carney, B. 1996, PASP, 108, 900

Carney, B. W., Wright, J. S., Sneden, C., Laird, J. B., Aguilar, L. A., & Latham, D. W. 1997, AJ, 114, 363

Carrera, R., Aparicio, A., Martínez-Delgado, D., & Alonso-García, J. 2002, AJ, 123, 3199

Carretta, E., & Gratton, R. 1997, A&AS, 121, 95 (CG97)

Carretta, E. 2006, AJ, 131, 1766

Castelli, F., Gratton, R. G., & Kurucz, R. L. 1997, A&A, 318, 841

Castelli, F., & Kurucz, R. L. 2003, in IAU Symp. 210, Modelling of Stellar Atmospheres, eds.

N.E. Piskunov, W.W. Weiss, & D.F. Gray (San Francisco: ASP), A20 (astro-ph/0405087)

Cayrel, R. 1988, in IAU Symp. 132, The Impact on Very High S/N Spectroscopy on Stellar Physics, G.Cayrel de Strobel & M.Spite (eds.), 345

Chapman, S. C., Ibata, R., Lewis, G. F., Ferguson, A. M. N., Irwin, M., McConnachie, A., & Tanvir, N. 2005, ApJ, 632, L87

Choi, P. I., Guhathakurta, P., & Johnston, K. V. 2002, AJ, 124, 310

Cole, A., Smecker-Hane, T.A., & Gallagher, J.S 2000, AJ, 120, 1808

Cole, A., Smecker-Hane, T.A., Tolstoy, E., Bosler, T.L., & Gallagher, J.S 2004, MNRAS, 347, 367

Cole, A., Tolstoy, E., Gallagher, J.S., & Smecker-Hane, T.A. 2005, AJ, 129, 1465

Coleman, M., Da Costa, G. S., Bland-Hawthorn, J., Martínez-Delgado, D., Freeman, K. C., & Malin, D. 2004, AJ, 127, 832

Côté, P., Oke, J. B., & Cohen, J. G. 1999a, AJ, 118, 1645

Côté, P., Mateo, M., Olszewski, E. W., & Cook, K. H. 1999b, ApJ, 526, 147

Cutri R. M. 2003, Explanatory Supplement to the 2MASS All-Sky Data Release, `http://www.ipac/caltech.edu/2mass/releases/allsky/doc/explsup.html`

Da Costa, G. S., & Mould, J. R. 1988, ApJ, 334, 159

Da Costa, G. S., Armandroff, T. E., Caldwell, N., & Seitzer, P. 1996, AJ, 112, 2576

Da Costa, G. .S., & Hatzidimitriou, D. 1998, AJ, 115, 1934

Da Costa, G. S., Armandroff, T. E., Caldwell, N., & Seitzer, P. 2000, AJ, 119, 705

Dauphole, B., Geffert, M., Colin, J., Ducourant, C., Odenkirchen, M., & Tucholke, H.-J. 1996, A&A, 313, 119

de Blok, W. J. G., McGaugh, S. S., Rubun, V. C. 2001, AJ, 122, 2396

Demers, S., & Harris, W. E. 1983, AJ, 88, 329

Demers, S., & Irwin, M. J. 1993, MNRAS, 261, 657

Demers, S., Irwin, M. J., & Gambu, I. 1994, MNRAS, 266, 7

de Vaucouleurs, G. 1958, ApJ, 128, 465

de Vaucouleurs, G. 1959, ApJ, 129, 521

Dinescu, D. I., Keeney, B. A., Majewski, S. R., & Girard, T. M. 2004, AJ, 128, 687

Dolphin, A. E. 2002, MNRAS, 332, 91

Dong, S., Lin, D. N. C., & Murray, S. D. 2003, ApJ, 596, 930

Dubath, P., & Grillmair, C. J. 1997, A&A, 321, 379

Duc, P.-A., & Mirabel, I. F. 1998, A&A, 333, 813

Duquennoy, A., & Mayor, M. 1991, A&A, 248, 485

Durrell, P. R., Harris, W. E., & Pritchet, C. J. 2004, AJ, 128, 260

Edvardsson, B., Andersen, J., Gustafsson, B., Lambert, D. L., Nissen, P. E., & Tomkin, J. 1993, A&A, 275, 101

Efron, B. & Tibshirani, R.J. 1993, An Introduction to the Bootstrap (London: Chapman & Hall)

Eskridge, P. B., & Schweitzer, A. E. 2001, AJ, 122, 3106

Evans, N. W., Wilkinson, M. I., Guhathakurta, P., Grebel, E. K., & Vogt, S. S. 2000, ApJ, 540, L9

Evans, N. W., Wilkinson, M. I., Perrett, K. M., & Bridges, T. J. 2003, ApJ, 583, 752

Faber, S. M. 1973, ApJ, 179, 423

Ferraro, F.R., Messineo, M., Fusi Pecci, F., De Palo, M.A., Straniero, O., & Limongi, M. 1999, AJ, 118, 1738

Fisher, N. I., Lewis, T., & Embleton, B. J. J 1987, Statistical Analysis of Spherical Data (Cambridge: Cambridge University Press)

Fleck, J. J., & Kuhn J. R. 2003, ApJ, 592, 147

Font, A. S., Johnston, K. V., Bullock, J. S., & Robertson, B. E. 2006, ApJ, 638, 585

Freedman, W. L., & Madore, B. F. 1990, ApJ, 365, 186

Freeman, K. C. & Bland-Hawthorn, J., 2002, ARA&A, 40, 487

Friel, E. D., Jacobson, H. R., Barrett, E., Fullton, L., Balachandran, S. C., & Pilachowski, C. A. 2003, AJ, 126, 2372

Fukugita, M., Ichikawa, T., Gunn, J. E., Doi, M., Shimasaku, K., & Schneider, D. P. 1996, AJ, 111, 1748

Fulbright, J. P. 2002, AJ, 123, 404

Fulbright, J. P., Rich, R. M., & Castro, S. 2004, ApJ, 612, 447

Fulbright, J. P., McWilliam, A., & Rich, R.M. 2006, ApJ, 636, 821

Fusi Pecci, F., Bellazzini, M., Cacciari, C., & Ferraro, F. R. 1995, AJ, 110, 1664

Gallagher, J. S., III, & Wyse, R. F. G. 1994, PASP, 106, 1225

Gallagher, J. S., Madsen, G. J., Reynolds, R. J., Grebel, E. K., & Smecker-Hane, T. A. 2003, ApJ, 588, 326

Gallart, C. 1998, ApJ, 495, L43

Gallart, C., Freedman, W. L., Aparicio, A., Bertelli, G., & Chiosi, C. 1999a, AJ, 118, 2245

Gallart, C., et al. 1999b, ApJ, 514, 665

Gallart, C., Zoccali, M., & Aparicio, A. 2005, ARA&A, 43, 387

Geisler, D., Smith, V. V., Wallerstein, G., Gonzalez, G., & Charbonnel, C. 2005, AJ, 129, 1428

Ghigna, S., Moore, B., Governato, F., Lake, G., Quinn, T., & Stadel, J. 2000, ApJ, 544, 616

Gibson, B. K. 1998, ApJ, 501, 675

Gilmore, G. & Wyse, R.F.G. 1991, ApJ, 367, L55

Gilmore, G., & Wyse, R. F. G. 1998, AJ, 116, 748

Girardi, L., Grebel, E. K., Odenkirchen, M., & Chiosi, C. 2004, A&A, 422, 205

Goerdt, T., Moore, B., Read, J. I., Stadel, J., & Zemp, M. 2006, MNRAS, 368, 1073

Graham, A. W. 2002, ApJ, 568, L13

Gratton, R. G., & Sneden, C. 1991, A&A, 241, 501

Gratton, R., Sneden, C., & Carretta, E. 2004, ARA&A, 42, 385

Grebel, E. K., Roberts, W. J., & van de Rydt, F. 1994, in ESO Conference and Workshop Proceedings, The Local Group: Comparative and Global Properties, ed. A. Layden, R. C. Smith, & J. Storm (Garching: ESO), 148

Grebel, E. K., & Roberts, W. J. 1995, A&AS, 109, 293

Grebel, E. K. 1996, PASP, 108, 1141

Grebel, E. K. 1997, Reviews of Modern Astronomy, 10, 29

Grebel, E. K. 1999, in IAU Symp. 192, The Stellar Content of the Local Group, eds. P. Whitelock & R. Cannon (San Francisco: ASP), 17

Grebel, E. K., Kolatt, T., & Brandner, W. 1999, in IAU Symp. 192, The Stellar Content of the Local Group, eds. P. Whitelock & R. Cannon (San Francisco: ASP), 447

Grebel, E. K. & Guhathakurta, P. 1999, ApJ, 511, L101

Grebel, E. K. 2000, in ESA SP-445: Star Formation from the Small to the Large Scale, eds. F. Favata, A. Kaas, & A. Wilson (Noordwijk: ESA), 87

Grebel, E. K. 2001, A&SSS, 277, 231

Grebel, E. K., Gallagher, J. S., & Harbeck, D. 2003, AJ, 125, 1926

Grebel, E. K., & Gallagher, J. S. 2004, ApJ, 610, L89

Grebel, E. K. 2005, in Near-field cosmology with dwarf elliptical galaxies, IAU Coll. 198, eds. H. Jerjen & B. Binggeli (Cambridge: CUP), 1

Grebel, E. K., Koch, A., & Sambhus, N., 2005, BAAS, 207, 1346

Grebel, E. K., Gallagher, J. S., III, & Harbeck, D. 2006, AJ, submitted

Grevesse, N., & Sauval, A. J. 1999, A&A, 347, 348

Guhathakurta, P., Reitzel, D. B., & Grebel, E. K. 2000, Proc. SPIE, 4005, 168

Guhathakurta, P., Ostheimer, J. C., Gilbert, K. M., Rich, R. M., Majewski, S. R., Kalirai, J. S., Reitzel, D. B., & Patterson, R. J. 2005, Nature, submitted (astro-ph/0502366)

Han, M., Hoessel, J. G., Gallagher, J. S., Holtzman, J., & Stetson, P. B. 1997, AJ, 113, 1001

Harbeck, D., et al. 2001, AJ, 122, 3092

Harbeck, D., Gallagher, J. S., & Grebel, E. K. 2004, AJ, 127, 2711

Harbeck, D., Gallagher, J. S., Grebel, E. K., Koch, A., & Zucker, D. 2005, ApJ, 623, 159

Hargreaves, J. C., Gilmore, G., & Annan, J. D. 1996, MNRAS, 279, 108

Häring, N., & Rix, H.-W. 2004, ApJ, 604, L89

Harrington, R. G., & Wilson, A. G. 1950, PASP, 62, 118

Harris, W.E. 1996, AJ, 112, 1487 (2003 version of the Milky Way globular cluster catalog at http://physwww.mcmaster.ca/ harris/mwgc.dat)

Hartwick, F. D. A., 1976, ApJ, 209, 418

Hartwick, F. D. A. 1996, in Formation of the Galactic Halo...Inside and Out, ASP Conf. Ser. 92, eds. H. Morrison & A. Sarajedini (San Francisco: ASP), 444

Hartwick, F. D. A. 2000, AJ, 119, 2248

Held, E. V., Saviane, I., Momany, Y., & Carraro, G. 2000, ApJ, 530, L85

Held, E. V., Clementini, G., Rizzi, L., Momany, Y., Saviane, I., & Di Fabrizio, L. 2001, ApJ, 562, L39

Helmi, A. 2004, ApJ, 610, L97

Hensler, G., Theis, C., & Gallagher, J. S., III. 2004, A&A, 426, 25

Hernandez, X., Gilmore, G., & Valls-Gabaud, D. 2000, MNRAS, 317, 831

Hernquist, L. 1990, ApJ, 356, 359

Hilker, M., Kayser, A., Richtler, T., & Willemsen, P. 2004, A&A, 422, L9

Hill, V., François, P., Spite, M., Primas, F., & Spite, F. 2000, A&A, 364, L19

Hinkle, K., Wallace, L., Valenti, J., & Harmer, D. 2000, Visible and Near Infrared Atlas of the Arcturus Spectrum 3727-9300Å (San Francisco: ASP), online atlas at ftp://ftp.noao.edu/catalogs/arcturusatlas/visual/

Holmberg, E. 1969, Ark. Astron., 5, 305

Hurley-Keller, D., Mateo, M., & Nemec, J. 1998, AJ, 115, 1840

Hurley-Keller, D., Mateo, M., & Grebel, E. K. 1999, ApJ, 523, L25

Ibata, R. A., Gilmore, G., & Irwin, M. J. 1994, Nature, 370, 194

Ibata, R., Irwin, M., Lewis, G., Ferguson, A. M. N., & Tanvir, N. 2001, Nature, 412, 49

Ibata, R., Chapman, S., Ferguson, A. M. N., Irwin, M., Lewis, G., & McConnachie, A. 2004, MNRAS, 351, 117

Ideta, M., & Makino, J. 2004, ApJ, 616, L107

Ikuta, C., & Arimoto, N. 2002, A&A, 391, 55

Irwin, M., & Hatzidimitriou, D. 1995, MNRAS, 277, 1354

Jing, Y. P., & Suto, Y. 2000, ApJ, 529, L69

Johnson, J. A. 2002, ApJSS, 139, 219

Johnson, J. A., Ivans, I. I., & Stetson, P. B. 2006, ApJ, 640, 801

Johnston, K. V., Spergel, D. N., & Hernquist, L. 1995, ApJ, 451, 598

Jordi, K., Grebel, E. K., Ammon, K. 2006, A&A, submitted

Joseph, C. L., et al. 2001, ApJ, 550, 668

Kang, X., Mao, S., Gao, L., & Jing, Y. P. 2005, A&A, 437, 383

Karachentsev, I. D. & Karachentseva, V. E. 1999, A&A, 341, 355

Karachentsev, I. D., et al. 2000, A&A, 363, 117

Karachentsev, I. D., et al. 2002a, A&A, 383, 125

Karachentsev, I. D., et al. 2002b, A&A, 385, 21

Karachentsev, I. D., et al. 2003a, A&A, 398, 467

Karachentsev, I. D., et al. 2003b, A&A, 404, 93

Karachentsev, I. D., Sharina, M. E., Dolphin, A. E., & Grebel, E. K. 2003c, A&A, 408, 111

Karachentsev, I. D. 2005, AJ, 129, 178

Karaali, S., Bilir, S., & Tunçel, S. 2005, PASA, 22, 24

Kawata, D., Arimoto, N., Cen, R., & Gibson, B. K. 2006, ApJ, 641, 785

King, I. R. 1962, AJ, 67, 471

King, I. R. 1966, AJ, 71, 64

Klessen, R. S., & Kroupa, P. 1998, ApJ, 498, 143

Klessen, R. S., & Zhao, H. 2002, ApJ, 566, 838

Klessen, R. S., Grebel, E. K., & Harbeck, D. 2003, ApJ, 589, 798

Kleyna, J. T., Wilkinson, M. I., Evans, N. W., & Gilmore, G. 2001, ApJ, 563, L115

Kleyna, J. T., Wilkinson, M. I., Evans, N. W., Gilmore, G., & Frayn, C. 2002, MNRAS, 330, 792

Kleyna, J. T., Wilkinson, M. I., Gilmore, G., & Evans, N. W. 2003, ApJ, 588, L21

Kleyna, J.T., Wilkinson, M.I., Evans, N.W., & Gilmore, G.F. 2004, MNRAS, 354, 66

Klypin, A., Kravtsov, A. V., Valenzuela, O., & Prada, F. 1999, ApJ, 522, 82

Knebe, A., Gill, S. P. D., Gibson, B. K., Lewis, G. F., Ibata, R. A., & Dopita, M. A. 2004, ApJ, 603, 7

Koch, A., & Edvardsson, B. 2002, A&A, 381, 500

Koch, A., Grebel, E. K., Odenkirchen, M., & Caldwell, J. A. R. 2004a, The Messenger, 115, 37

Koch, A., Odenkirchen, M., Grebel, E. K., & Caldwell, J. A. R. 2004b, AN, 325, 299

Koch, A., Grebel, E. K., Wyse, R. F. G., Kleyna, J. T., Wilkinson, M. I., Harbeck, D. R., Gilmore, G. F., & Evans, N. W. 2006a, AJ, 131, 895

Koch, A., Grebel, E. K., Wyse, R. F. G., Kleyna, J. T., Wilkinson, M. I., Harbeck, D. R., Gilmore, G. F., & Evans, N. W. 2006b, The ESO Messenger, 123, 38

Kochanek, C. S. 1996, ApJ, 457, 228

Kormendy, J., & Richstone, D. 1995, AR&A, 33, 581

Kormendy, J., & Freeman, K. C. 2004, in: "Dark matter in galaxies", S. F. Ryder, D. J. Pisano & K. C. Freeman (eds.), IAU Symposium 220, 377

Kraft, R. P., & Ivans, I.I. 2003, PASP, 115, 143

Kroupa, P. 1997, New Ast., 2, 139

Kroupa, P., Theis, C., & Boily, C. M. 2005, A&A, 431, 517

Kuhn, J. R. 1993, ApJ, 409, L13

Kunkel, W. E., & Demers, S. 1976, The Galaxy and the Local Group, Roy. Green. Obs. Bull., 182, 241

Kuhn, J. R., Smith, H. A., & Hawley, S. L. 1996, ApJ, 469, L93

Kunkel, W. E. 1979, ApJ, 228, 718

Lambert, D. L. 1987, J. Astrophys. Astron., 8, 103

Landolt, A. U. 1992, AJ, 104, 340

Lanfranchi, G. A., & Matteucci, F. 2003, MNRAS, 345, 71

Lanfranchi, G. A., & Matteucci, F. 2004, MNRAS, 351, 1338

Lanfranchi, G. A., Matteucci, F., & Cescutti, G. 2006a, MNRAS, 365, 477

Lanfranchi, G. A., Matteucci, F., & Cescutti, G. 2006b, A&A, 453, L67 (LMC06)

Langer, G. E., Hoffmann R. D., Sneden, C. 1993, PASP, 105, 301

Langer, G. E., & Hoffmann R. D. 1995, PASP, 107, 1177

Larson, R. B. 1972, Nat. Phys. Sci., 236, 7

Layden, A. C., & Sarajedini, A. 2000, AJ, 119, 1760

Lee, G. L., Freedman, W., Mateo, M., Thompson, I., Roth, M., & Ruiz, M. -T. 1993, AJ, 106, 1420

Lee, M. G. 1995, AJ, 110, 1155

Lee, M. G., et al. 2003, AJ, 126, 284

Letarte, B., Hill, V., Jablonka, P., Tolstoy, E., & Meylan, G. 2006, A&A, 453, 547

Libeskind, N. I, Frenk, C. S, Cole, S., Helly, J. C, Jenkins, A., Navarro, J. F, & Power, C. 2005, MNRAS, 363, 146

Lin, D.N.C., & Murray, S.D. 1998, in Dwarf Galaxies & Cosmology, XXXIIIrd Rencontres de Moriond, eds. T.X. Thuan et al. (Paris: Editions Frontières), 433

Łokas, E. L., & Mamon, G. A. 2001, MNRAS, 321, 155

Łokas, E. L. 2001, MNRAS, 327, L21

Łokas, E. L. 2002, MNRAS, 333, 697

Łokas, E. L., & Mamon, G. A. 2003, MNRAS, 343, 401

Luck, R. E., & Bond, H. E. 1985, ApJ, 292, L559

Lynden-Bell, D. 1975, Vistas Astron., 19, 299

Lynden-Bell, D. 1976, MNRAS, 174, 695

Lynden-Bell, D. 1982, Observatory, 102, 202

Lynden-Bell, D., & Lynden-Bell, R. M. 1995, MNRAS, 275, 429

Mackey, D., & Gilmore, G. 2003, MNRAS, 345, 747

Mac Low, M., & Ferrara, A. 1999, ApJ, 513, 142

Magorrian, J., et al. 1998, AJ, 115, 2285

Majewski, S. 1994, ApJ, 431, L17

Majewski, S. R., Siegel, M. H., Patterson, R. J., & Rood, R. T. 1999, ApJ, 520, L33

Majewski, S. R., Ostheimer, J. C., Patterson, R. J., Kunkel, W. E., Johnston, K. V., & Geisler, D. 2000, AJ, 119, 760

Majewski, S. R., Skrutskie, M. F., Weinberg, M. D., & Ostheimer, J. C. 2003, ApJ, 599, 1082

Majewski, S.R., et al. 2005, AJ, 130, 2677

Marconi, A., & Hunt, L. K. 2003, ApJ, 589, L21

Martin, N. F., Ibata, R. A., Bellazzini, M., Irwin, M. J., Lewis, G. F., & Dehnen, W. 2004, MNRAS, 348, 12

Martin, N. F., Ibata, R. A., Irwin, M. J., Chapman, S.,. Lewis, G. F., Ferguson, A. M. N., Tanvir, N., & McConnachie, A. W. 2006, MNRAS, in press (astro-ph/0607472)

Martínez-Delgado, D., Alonso-Garcia, J., & Aparicio, A. 2001, ApJ, 549, L63

Mashchenko, S., Couchman, H. M. P., & Sills, A. 2005, ApJ, 624, 726

Mateo, M., Olszewski, E.W., Pryor, C., Welch, D.L., Fischer, P. 1993, AJ, 105, 510

Mateo, M. 1997, in The Nature of Elliptical Galaxies, ASP Conf. Ser. Vol. 116, eds. M. Arnaboldi, G. S. Da Costa, & P. Saha (San Francisco: ASP), 259

Mateo, M. 1998, ARA&A, 36, 435

Mateo, M., Hurley-Keller, D., & Nemec, J. 1998, AJ, 115, 1856

Mateo, M., Olszewski, E. W., Vogt, S. S., & Keane, M. J. 1998b, AJ, 116, 2315 (M98)

Mateo, M. 2005, in: "Near-field cosmology with dwarf elliptical galaxies", H. Jerjen & B. Binggeli (eds.), IAU Colloquium 198, 52

Matteucci, F. 2003, Ap&SS, 284, 539

McConnachie, A.W., Irwin, M.J., Ibata, R.A., Ferguson, A.M.N., Lewis, G.F., & Tanvir, N. 2003, MNRAS, 343, 1335

McNamara, D. H. 2000, PASP, 112, 1096

McWilliam, A., Preston, G. W., Sneden, C. & Searle, L. 1995, AJ, 109, 2757

McWilliam, A. 1997, ARA&A, 35, 503

McWilliam, A., & Smecker-Hane, T. A. 2005, ApJ, 622, L29

Mégessier, C., 1994, A&A, 289, 202

Merrifield, M. .R., & Kent, S. M. 1990, AJ, 99, 1548

Merrit, D. 1985, AJ, 90, 1027

Meylan, G., Sarajedini, A., Jablonka, P., Djorgovski, S.G., Bridges, T., & Rich, R.M. 2001, AJ, 122, 830

Mighell, K. J. 1990a, A&AS, 82, 207

Mighell, K. J. 1990b, A&AS, 82, 1

Mighell, K. J., & Rich, R. M. 1996, AJ, 111, 777

Mighell, K.J. 1997, AJ, 114, 1458

Milgrom, M. 1983, ApJ, 270, 371

Monelli, M., et al. 2003, AJ, 126, 218

Moore, B. 1996, ApJ, 461, L13

Moore, B., Ghigna, S., Governato, F., Lake, G., Quinn, T., Stadel, J. & Tozzi, P. 1999, ApJ, 524, 22

Mould, J. R., Cannon, R. D., Frogel, J. A., & Aaronson, M. 1982, ApJ, 254, 500

Mould, J. R., & Aaronson, M. 1983, ApJ, 273, 530

Muñoz, R. R., et al. 2005, ApJ, 631, L137

Muñoz, R. R., et al. 2006, ApJ, in press (astro-ph/0605098)

Nadaraya, E. A. 1964, "On estimating regression", in: Theory of Probability and its Applications, 141

Navarro, J. F., Frenk, C. S. & White, S. D. M. 1995, MNRAS, 275, 720 (NFW)

Navarro, J. F., Abadi, M. G., & Steinmetz, M. 2004, ApJ, 613, L41

Newberg, H. J., et al. 2002, ApJ, 569, 245

Newberg, H. J., et al. 2003, ApJ, 596, L191

Nieto, J.-L., & Prugniel, P. 1987, A&A, 186, 30

Nonino, M., et al. 1999, A&AS, 137, 51

Nordström, B., et al. 2004, A&A, 418, 989

O'Brian, T. R., Wickliff, M. E., Lawler, J. E., Whaling, W., & Brault, J. W. 1991, J. Opt. Soc. Am. B., 8, 1185

Odenkirchen, M., et al. 2001, AJ, 122, 2538

Oh, K. S., Lin, D. N. C., & Aarseth, S. J. 1995, ApJ, 442, 142

Olszewski, E. W., Pryor, C., Armandroff, T. E. 1996, AJ, 111, 750

Osipkov, L. P. 1979, Pis'ma Astron. Zh., 5, 77

Osterbrock, D. E., Fulbright, J. P., Martel, A. R., Keane, M. J., Trager, S. C., & Basri, G. 1996, PASP, 108, 2770

Osterbrock, D. E., Fulbright, Bida, T. A. 1997, PASP, 109, 614

Pagel, B. E. J. 1997, Nucleosynthesis and chemical evolution of galaxies (Cambridge: Cambridge University Press)

Palma, C., Majewski, S. R., & Johnston, K. V. 2002, ApJ, 564, 736

Palma, C., Majewski, S. R., Siegel, M. H., Patterson, R. J., Ostheimer, J. C., & Link, R. 2003, AJ, 125, 1352

Pasquini, L., et al. 2002, The ESO Messenger, 110, 1

Paunzen, E., Pintado, O. I., Maitzen, H. M., & Claret, A. 2005, MNRAS, 362, 1025

Perryman, M. A. C., et al. 2001, A&A, 369, 339

Peterson, R. C, Dalle Ore, C. M., & Kurucz, R. L. 1993 ApJ, 404, 333

Piatek, S., & Pryor, C. 1995, AJ, 109, 1071

Piatek, S., et al. 2002, AJ, 124, 3198

Piatek, S., Pryor, C., Olszewski, E. W., Harris, H. C., Mateo, M., Minniti, D., & Tinney, C. G. 2003, AJ, 126, 2346

Piatek, S., Pryor, C., Bristow, P., Olszewski, E. W., Harris, H. C., Mateo, M., Minniti, D., & Tinney, C. G. 2005, AJ, 130, 95

Piatek, S., et al. 2006, AJ, 131, 1445

Pont, F., Zinn, R., Gallart, C., Hardy, E., & Winnick, R. 2004, AJ, 127, 840

Poretti, E. 1999, A&A, 346, 487

Prantzos, N., Hashimoto, M., & Nomoto, K. 1990, A&A, 234, 211

Press, W. H., Teukolsky, S. A., Vetterling, W. T., & Flannery, B. P. 1992, Numerical Recipes in FORTRAN: The Art of Scientific Computing (2nd ed.; Cambridge: Cambridge University Press)

Pritzl, B. J., Venn, K. A., & Irwin, M. I. 2005, AJ, 130, 2140

Prochaska, J. X., Naumov, S. O., Carney, B. W., McWilliam, A., & Wolfe, A. M. 2000, AJ, 120, 2153

Pryor, C., McClure, R.D., Fletcher, J. M., & Hesser, J. E., 1991, AJ, 102, 1062

Pryor, C., J. 1990, AJ, 100, 127

Quian, Y. Z., & Wasserburg, G. J. 2001, ApJ, 559, 925

Read, J. I., & Gilmore, G. 2005, MNRAS, 356, 107

Read, J. I., Wilkinson, M. I., Evans, N. W., Gilmore, G., Kleyna, J. T. 2006a, MNRAS, 366, 429

Read, J. I., Wilkinson, M. I., Evans, N. W., Gilmore, G., Kleyna, J. T. 2006b, MNRAS, 367, 387

Rich, R. M., Mighell, K. J., Freedman, W. L., & Neill, J. D. 2005, AJ, 129, 2670

Rich, R. M., Corsi, C. E., Cacciari, C., Federici, L., Fusi Pecci, F., Djorgovski, S. G., & Freedman, W. L. 2005, AJ, 129, 2670

Richstone, D. O., & Tremaine, S. 1986, AJ, 92, 72

Rizzi, L., Held, E. V., Bertelli, G., & Saviane, I. 2003, ApJ, 589, L85

Robertson, B., Bullock, J. S., Font, A. S., Johnston, K. V., & Hernquist, L. 2005, ApJ, 632, 872

Robin, A. C., Reylé, S., Derrière, S., & Picaud, S. 2003, A&A, 409, 523

Rocha-Pinto, H. J., Majewski, S. R., Skrutskie, M. F., Crane, J. D., & Patterson, R. J. 2004, ApJ, 615, 732

Royston, P. 1995, Appl. Stat., 44, 547

Rutledge, G.A., Hesser, J.E., Stetson, P.B., Mateo, M., Simard, L., Bolte, M., Friel, E.D., & Copin, Y. 1997a, PASP, 109, 883

Rutledge, G.A., Hesser, J.E., Stetson, P.B. 1997b, PASP, 109, 907

Sadakane, K., Arimoto, N., Ikuta, C., Aoki, W., Jablonka, P., & Tajitsu, A. 2004, PASJ, 56, 1041

Saha, A., Monet, D. G., & Seitzer, P. 1986, AJ, 92, 302

Sales, L., & Lambas, D. G. 2004, MNRAS, 348, 1236

Sandage, A. 1965, in ‘The Structure & Evolution of Galaxies’, Solvay 1964 (London: Interscience), p83

Sarajedini, A., & Layden, A. 1997, AJ, 113, 264

Schaye, J., & Aguirre, A. 2005, in IAU Symp. 228, From Lithium to Uranium: Elemental Tracers of Early Cosmic Evolution, ed. V.Hill, P. François, & F. Primas, 557

Schlegel, D.J., Finkbeiner, D.P., & Davis, M. 1998, ApJ, 500, 525

Schweitzer, A. E., Cudworth, K. M., Majewski, S. R., & Suntzeff, N. B. 1995, AJ, 110, 2747

Schweitzer, A. E., Cudworth, K. M., & Majewski, S. R. 1997, in Proper Motions and Galactic Astronomy, ASP Conf. Ser. 127, ed. R. M. Humphreys (San Francisco: ASP), 103

Searle, L., & Zinn, R., 1978, ApJ, 225, 357

Shetrone, M. D., Côté, P., & Sargent, W. L. W. 2001, ApJ, 548, 592

Shetrone, M. D., Venn, K. A., Tolstoy, E., Primas, F., Hill, V., & Kaufer, A. 2003, AJ, 125, 684

Siegel, M. H., & Majewski, S. R. 2000, AJ, 120, 284

Siegel, M. H., & Majewski, S. R. 2005, AAS, 207, 188.14

Silk, J., Wyse, R.F.G. & Shields, G. 1987, ApJ, 322, L59

Sivarani, T., et al. 2004, A&A, 413, 1073

Smecker-Hane, T.A., Stetson, P.B., Hesser, J.E., & Lehnert, M.D. 1994, AJ, 108, 507

Smecker-Hane, T. A., Stetson, P. B., Hesser, J. E., & Vandenberg, D. A. 1996, in From Stars to Galaxies: the Impact of Stellar Physics on Galaxy Evolution, ASP Conf. Ser. Vol 98, eds. C. Leitherer, U. Fritze-von Alvensleben, & J. Huchra (San Francisco: ASP), 328

Smecker-Hane, T.A., Mandushev, G.I., Hesser, J.E., Stetson, P.B., Da Costa, G.S, & Hatzidimitriou, D. 1999, in Spectrophotometric Dating of Stars and Galaxies, ASP Conf. Ser. Vol. 192, eds. I. Hubeny, S. Heap, & R. Cornett (San Francisco: ASP), 159

Smith, G. & Drake, J.J. 1990, A&A, 231, 125

Sneden, C. 1973, ApJ, 184, 839

Sohn, S. T., et al. 2006, ApJ, submitted (astro-ph/0608151)

Spekkens, K., Giovanelli, R., & Haynes, M. P. 2005, AJ, 129, 2119

Stetson, P. B., Hesser, J. E., & Smecker-Hane, T. A. 1998, PASP, 110, 533

Stetson, P.B. 2000, PASP, 112, 925

Stoughton, C., et al. 2002, AJ, 123, 485

Strigari, L. E., Bullock, J. S., Kaplinghat, M., Kravtsov, A. V., Gnedin, O. Y., Abazajian, K., & Klypin, A. A. 2006, ApJ, submitted (astro-ph/0603775)

Suntzeff, N., Aaronson, M., Olszewski, E. W., & Cook, K. H. 1986, AJ, 91, 1091

Suntzeff, N.B., Mateo, M., Terndrup, D.M., Olszewski, E.W., Geisler, D., & Weller, W. 1993, ApJ, 418, 208

Swope, H. H. 1967, PASP, 79, 439

Thévenin, F., & Idiart, T. P. 1999, ApJ, 521, 753

Thielemann, F.-K., Nomoto, K., & Hashimoto, M. 1996, ApJ, 460 408

Thielemann, F.-K., et al. 2001, PrPNP, 46, 5

Timmes, F. X., Woosley, S. E., & Weaver, T. A. 1995, ApJS, 98, 617

Tinsley, B.M. 1975, ApJ, 197, 159

Tonry, J. L. 1984, ApJ, 283, L27

Tolstoy, E., Irwin, M.J., Cole, A.A., Pasquini, L., Gilmozzi, R., & Gallagher, J.S. 2001, MNRAS, 327, 918

Tolstoy, E., Venn, K. A., Shetrone, M. D., Primas, F., Hill, V., Kaufer, A., & Szeifert, T. 2003, AJ, 125, 707

Tolstoy, E., et al. 2004, ApJ, 617, L119

Travaglio, C., Gallino, R., Busso, M., Ferrini, F., & Straniero, O. 1999, ApJ, 521, 691

Truran, J., Cameron, 1971, Ap&SS, 14, 179

van den Bergh, S. 1968, The Observatory, 88, 168

van den Bergh, S. 1994, ApJ, 428, 617

van den Bergh, S. 1999, ARA&A, 9, 273

van den Bergh, S. 2000, The galaxies of the Local Group, Cambridge Astrophysics Series no. 35, Cambridge University Press

Vandenberg, D. A., Swenson, F. J., Rogers, F. K., Iglesias, C. A., & Alexander, D. R. 2000, ApJ, 532, 430

van der Marel, R. P., de Zeeuw, P. .T., & Rix, H. W. 1997, ApJ, 488, 119

van der Marel, R. P. 1999, AJ, 117, 744

Venn, K. A., & Lambert, D. L. 1990, ApJ, 363, 234

Venn, K. A., Irwin, M. I., Shetrone, M. D., Tout, C. A., Hill, V., & Tolstoy, E. 2004, AJ, 128, 1177

Vogt, S. S., Mateo, M., Olszewski, E. W, & Keane, M. J. 1995, AJ, 109, 151

Vogt, S. S., Mateo, M., Olszewski, E. W., & Keane, M. J. 1995, AJ, 109, 151

Walker, M. G., Mateo., M., Olszewski, E. W., Bernstein, R. A., Wang, X., & Woodroofe, M. 2006a, AJ, 131, 2114

Walker, M. G., Mateo, M., Olszewski, E. W., Bernstein, R., Wang, X., Woodroofe, M. 2006b, ApJ, 642, L42

Wang, X., Woodroofe, M., Walker, M. G., Mateo, M., & Olszewski, E. 2005, ApJ, 626, 145

Watson, G. S. 1964, “Smooth regression analysis”, The Indian Journal of Statistics, 359

Westfall, K. B., Ostheimer, J. C., Frinchaboy, P. M., Patterson, R. J., Majewski, S. R., &Kunkel, W. E. 2006, AJ, 131, 375

Wilkinson, M. I., & Evans, N.W. 1999, MNRAS, 310, 645

Wilkinson, M. I., Kleyna, J. T., Evans, N. W., Gilmore, G. F., Irwin, M. J., & Grebel, E. K. 2004, ApJ, 611, L21

Wilkinson, M. I., Kleyna, J. T., Evans, N. W., Gilmore, G. F., Read, J .I., Koch, A., Grebel, E. K., & Irwin, M. 2006a, in: "Mass Profiles and Shapes of Cosmological Structures", G. Mamon, F. Combes, C. Deffayet & B. Fort (eds.), EAS Publication Series, 20, 105

Wilkinson, M. I., Kleyna, J. T., Gilmore, G. F., Evans, N. W., Koch, A., Grebel, E. K., Wyse, R. F. G., & Harbeck, D. R. 2006b, The Messenger, 124, in press

Willman, B., et al. 2005, ApJ, 626, L85

Woosley, S. E. 1986, in Nucleosynthesis and Chemical Evolution, 16th Advanced Course Swiss Society of Astrophysics and Astronomy, ed. B. Hauck, A. Maeder & G. Meynet (Geneva: Geneva Observatory), 74

Woosley, S. E., Wilson, J. R., Matthews, G. J., Hoffman, R. D., & Meyer, B. S. 1994, ApJ, 433, 229

Woosley, S. E., & Weaver, T. A. 1995, ApJS, 101, 181

Wylie, E. C., Cottrell, P. L., Sneden, C. A., & Lattanzio, J. C. 2006, ApJ, in press (astro-ph/0605538)

Wyse, R. F. G., Gilmore, G., Houdashelt, M. L., Feltzing, S., Hebb, L., Gallagher, J. S., III, & Smecker-Hane, T. A. 2002, NewA, 7, 395

Wyse, R. F. G., Gilmore, G., Norris, J. E., Wilkinson, M. I., Kleyna, J. T., Koch, A., Evans, N. W., & Grebel, E. K. 2006, ApJ, 639, L13

Yanny, B., et al. 2003, ApJ, 588, 824

Yi, S. K., Kim, Y., & Demarque, P. 2003, ApJs, 144, 259

Zaritsky, D., Olszewski, E. W., Schommer, R. A., Peterson, R. C., & Aaronson, M. 1989, ApJ, 345, 759

Zentner, A. R., & Bullock, J. S. 2003, ApJ, 598, 49

Zentner, A. R., Kravtsov, A. V., Gnedin, O. Y., & Klypin, A. A. 2005, ApJ, 629, 219

Zhao, H. 1996, MNRAS, 278, 488

Zhao, H. 1998, ApJ, 500, L149

Zinn, R., & West, M.J. 1984, ApJS, 55, 45

Zucker, D. B., et al. 2004a, ApJ, 612, L121

Zucker, D. B., et al. 2004b, ApJ, 612, L117

Zucker, D. B., et al. 2006a, ApJL, in press (astro-ph/0601599)

Zucker, D. B., et al. 2006b, ApJL, 643, L103

Zucker, D. B., et al. 2006c, ApJ, submitted (astro-ph/0606633)

Acknowledgements

"Here's a sigh to those who love me,
And a smile to those who hate;
And, whatever sky's above me,
Here's a heart for every fate."
— LORD BYRON, *To Thomas Moore*

At this stage I would like to thank all the people who have made possible this work and accompanied me throughout these years:

In the first place I am grateful to my supervisor Eva K. Grebel for her excellent support at all times. She constantly provided me with interesting ideas and projects, which were the base for many "small and short" papers.

I would like to thank Mark Wilkinson for his second expertise, but also for many illuminating discussions and involving me in many absorbing projects. Furthermore, he was always helpful and patient in leading my way through obscure kinematical calculations.

I am extremely grateful to ANdy McWilliam for the great amount of hospitality during my stays at the Carnegie Observatories, where I learned a lot about data reduction and humour.

I would also like to thank Gerry Gilmore for sharing the ESO Large Programme and the resulting data with us as well as rendering possible a fruitful stay at the IoA Cambridge.

Jan Kleyna is gratefully acknowledged for plenty of discussions about data reduction and interpretation, Rosie Wyse for her tutorial on chemical evolutionary models, and Jay S. Gallagher III and Daniel Harbeck for their inspiring input into this work.

A major Thank You goes to my befriended colleagues and collegial friends at the AIUB for enduring my lingering presence during my perpetual coffee breaks: Karin Ammon, Andi Immeli, Stefan Kautsch, Andrea Kayser, Thorsten Lisker, Niranjan Sambhus and Piet Westera.

Of course I do have to mention my colleague Matt Lab – without your help all my calculations and beautiful plots wouldn't have come into life.

Finally I would like to thank my parents for making studies worth studying through their support and interest in my work.

Publication list

1. Refereed Articles

- **Koch, A.**, Wilkinson, M.I., Kleyna, J.T., Gilmore, G.F., Grebel, E.K., Mackey, D.A, Evans, N.W., & Wyse, R.F.G. 2006, ApJ, submitted: '*Stellar kinematics and metallicities in the Leo I dwarf spheroidal galaxy – wide field implications for galactic evolution*'
- **Koch, A.**, Grebel, E.K., Kleyna, J.T., Wilkinson, M.I., Harbeck, D.R., Gilmore, G.F., Wyse, R.F.G., & Evans, N.W. 2006, AJ, in press (astro-ph/0609700): '*Complexity on Small Scales II: Metallicities and Ages in the Leo II Dwarf Spheroidal Galaxy*'
- **Koch, A.** & Grebel, E.K. 2006, AJ, 131, 1405: '*The anisotropic distribution of M 31 satellite galaxies: A polar great plane of early-type companions*'
- Wyse, R.F.G., Gilmore, G.F., Norris, J.E., Wilkinson, M.I., Kleyna, J.T., **Koch, A.**, Evans, N.W., & Grebel, E.K. 2006, ApJ, 639, L13: '*Further evidence for a merger origin for the Thick disk: Galactic stars along line-of-sight to dwarf spheroidal galaxies*'
- **Koch, A.**, Grebel, E.K., Wyse, R.F.G., Kleyna, J.T., Wilkinson, M.I., Harbeck, D., Gilmore, G.F., & Evans, N.W. 2006, AJ, 131, 895: '*Complexity on small scales: The metallicity distribution of the Carina dwarf spheroidal galaxy*'
- Harbeck, D., Gallagher, J.S., Grebel, E.K., **Koch, A.**, & Zucker, D.B. 2005, ApJ, 623, 159: '*Andromeda IX: Properties of the smallest M 31 dwarf satellite galaxy*'
- **Koch, A.**, Grebel, E.K., Odenkirchen, M., Martínez-Delgado, D., & Caldwell, J.A.R. 2004, AJ, 128, 2274: '*Mass segregation in the globular cluster Palomar 5 and its tidal tails*'
- **Koch, A.**, Odenkirchen, M., Grebel, E.K., & Caldwell, J.A.R. 2004, AN, 325, 299: '*A calibration map for Wide Field Imager photometry*'
- **Koch, A.**, & Edvardsson, B. 2001, A&A, 381, 500: '*Europium abundances in F and G disk dwarfs*'

2. Non-refereed Articles & Conference Proceedings

- Gilmore, G., Wilkinson, M., Kleyna, J., **Koch, A.**, Evans, W., Wyse, R.F.G., Grebel, E. 2006, in 7th UCLA Symposium, Sources and Detection of Dark Matter and Dark Energy in the Universe, eds. NN, in press (astro-ph/0608528): '*Observed Properties of Dark Matter: dynamical studies of dSph galaxies*'
- Kayser, A., Grebel, E.K., Cole, A. A., Harbeck, D.R., **Koch, A.**, Gallagher, J.S., & Da Costa, G.S. 2006, in: 'Globular Clusters – Guides to Galaxies', ed. T. Richtler, & S. Larsen, ESO/Springer Verlag, in press (astro-ph/0607047): '*The Age-Metallicity relation of the Small Magellanic Cloud*
- Glatt, K., Grebel, E.K., & **Koch, A.** 2006, in: 'Globular Clusters – Guides to Galaxies', ed. T. Richtler, & S. Larsen, ESO/Springer Verlag, in press: '*Star clusters in the Small Magellanic Cloud*'
- Wilkinson, M.I, Kleyna, J.T, Gilmore, G.F., Evans, N.W., **Koch, A.**, Grebel, E.K., Wyse, R.F.G., & Harbeck, D.R. 2006, The Messenger, 124, 25: '*Probing the dark matter content of Local Group dwarf spheroidal galaxies with FLAMES*'

- **Koch, A.**, Grebel, E.K., Wyse., R.F.G., Kleyna, J.T., Wilkinson, M.I., Harbeck, D., Gilmore, G.F., & Evans, N.W. 2006, The Messenger, 123, 38: '*The age-metallicity degeneracy in the dwarf spheroidal Carina as seen by FLAMES*'

- **Koch, A.**, Wilkinson, M.I., Kleyna, J.T., Gilmore, G.F., Evans, N.W., & Grebel, E.K. 2005, BAAS, 37, 1345: '*Stellar kinematics in the Leo I dwarf spheroidal galaxy – wide field implications for galactic mass profiles*'

- Grebel, E.K., **Koch, A.**, & Sambhus, N. 2005, BAAS, 37, 1346: '*Satellite Anisotropies: A Polar Great Plane of M31 Early-Type Companions*'

- Wyse, R.F.G., Gilmore, G.F., Norris, J.E., Wilkinson, M.I., Kleyna, J.T., **Koch, A.**, Evans, N.W., & Grebel, E.K. 2005, BAAS, 37, 1368: '*Further evidence for a merger origin for the Thick disk: Galactic stars along line-of-sight to dwarf spheroidal galaxies*'

- Wilkinson, M.I., Kleyna, J.T., Evans, N.W., Gilmore, G.F., Read, J.I., **Koch, A**., Grebel, E.K., & Irwin, M. 2005, in 'Mass Profiles and Shapes of Cosmological Structures', G. Mamon, F. Combes, C. Deffayet, B. Fort (eds.), EAS Publication Series, 20, 105: '*The internal kinematics of dwarf spheroidal galaxies*'

- Glatt, K., Grebel, E.K., & **Koch, A.** 2005, AN, 326, 651: '*Star clusters in the Large Magellanic Cloud*'

- **Koch, A.**, Wilkinson, M.I., Grebel, E.K., Harbeck, D., Kleyna, J.T., Wyse, R., Gilmore, G.F., & Evans, N.W. 2005, in 'Near-field Cosmology with Dwarf Elliptical Galaxies', H. Jerjen, B. Binggeli (eds.), IAUC, 198, 134: '*The chemical evolution of subpopulations in the Carina dwarf spheroidal galaxy*'

- Wilkinson, M.I., Kleyna, J.T., Evans, N.W., Gilmore, G.F., Grebel, E.K., **Koch, A.**, Read, J., & Young, R. 2005, in 'Near-field Cosmology with Dwarf Elliptical Galaxies', H. Jerjen, B. Binggeli (eds.), IAUC, 198, 240: '*Substructure in Dwarf Spheroidals – a Star Cluster Connection?*'

- Harbeck, D., Gallagher, J.S., Grebel, E.K., **Koch, A.**, & Zucker, D.B. 2005, AAS, 205, 9301: '*WIYN observations of And IX: A metal poor, low-mass dSph Galaxy*'

- **Koch, A.**, Grebel., E.K., Harbeck, D., Wilkinson., M.I., Kleyna, J.T., Gilmore, G.F., Wyse, R.F.G, & Evans, N.W. 2005, in ESO-Arcetri Workshop, 'Chemical Abundances and Mixing in Stars',eds. L. Pasquini & S. Randovich, Springer Verlag, 249 (astro-ph/0410435): '*Chemical evolution in the Carina dSph*'

- **Koch, A.**, Grebel., E.K., Harbeck, D., Wilkinson., M.I., Kleyna, J.T., Gilmore, G.F., Wyse, R.F.G, & Evans, N.W. 2004, ANS, 325, 44: '*The Metallicity and Age Distribution of the Carina Dwarf Spheroidal Galaxy*'

- **Koch, A.**, & Grebel, E.K. 2004, STScI May 2004 Symposium, 'Planets to Cosmology: Essential Science In Hubble's Final Years', M. Livio (ed.) (Cambridge University Press, astro-ph/0407212): '*R-process and α-elements in the Galactic disk: kinematic correlations*'

- **Koch, A.**, Odenkirchen, M., Grebel, E.K., & Caldwell, J.A.R. 2004, The Messenger, 115, 37: '*Correcting spatial gradients: The case of Wide Field Imager Photometry*'

- **Koch, A.**, Odenkirchen, M., Grebel, E.K., Martínez-Delgado, D., & Caldwell, J.A.R. 2004, 'Satellites and tidal streams', IAC/ING Joint Conference, A.S.P. Conf Ser. 327, 333, F. Prada, D. Martínez-Delgado & T.J. Mahoney eds.: '*The luminosity function of Palomar 5 and its tidal tails*'
- **Koch, A.**, Odenkirchen, M., Caldwell, J.A.R., & Grebel, E.K. 2003, ANS, 324, 144: '*A retrospective of r-process and α-element abundances in the Galactic disk – correlations with rotational velocity*'
- **Koch, A.**, Odenkirchen, M., Grebel, E.K., Martínez-Delgado, D., & Caldwell, J.A.R., 2003, ANS, 324, 144: '*Mass segregation in the low-concentration globular cluster Palomar 5*'
- **Koch, A.**, Odenkirchen, M., Caldwell, J.A.R., & Grebel, E.K. 2002, ANS, 324, 95: '*A calibration map for the Wide Field Imager*',
- **Koch, A.**, Odenkirchen, M., Caldwell, J.A.R., & Grebel, E.K. 2002, ANS, 324, 79: '*The mass function of the globular cluster Palomar 5 and its tidal tails*'

3. Theses

- **Koch, A.** 2006, Ph.D. Thesis, University of Basel: '*Chemical and kinematical evolution in nearby dwarf spheroidal galaxies*'
- **Koch, A.** 2003, Diploma Thesis, University of Heidelberg: '*The luminosity function of the globular cluster Palomar 5 and its tidal tails*'

Ich erkläre, dass ich die Dissertation “Chemical and Kinematical Evolution in Nearby Dwarf Spheroidal Galaxies” nur mit der darin angegebenen Hilfe verfasst und bei keiner anderen Fakultät der Unversität Basel eingereicht habe.

. . . .

Binningen, den 22. August 2006